



UNIVERSITÀ DEGLI STUDI DI PAVIA

**DOTTORATO IN SCIENZE CHIMICHE
E FARMACEUTICHE**

XXX CICLO

Coordinatore: Chiar.mo Prof. Mauro Freccero

Multimodal Molecular Tools Targeting

G-Quadruplex Nucleic Acids

Tutore

Chiar.mo Prof. Mauro Freccero

Tesi di Dottorato di

Alberto Lena

Anno Accademico 2016 – 2017

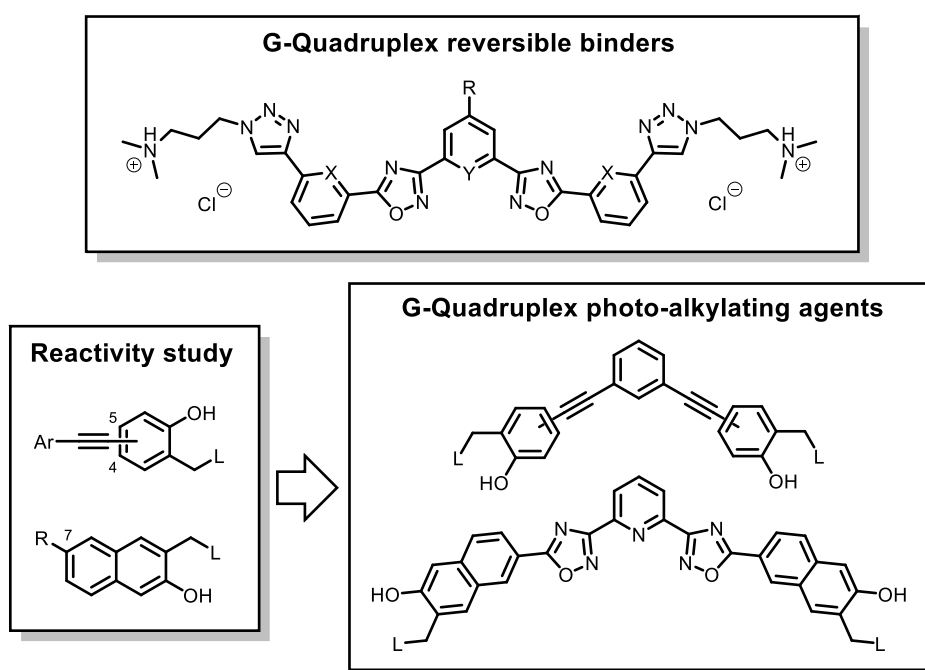
Dedicated to my family.

Abstract

G-quadruplexes (G4s) are non-canonical nucleic acid (NA) structures adopted by single strands rich in guanine^[1]. The basic constituent of such structures is the guanine quartet, formed by four of such nucleobases interconnected in a peculiar hydrogen bond net. Two or more of such quartets pile on top of each other, interacting via π - π stacking. Monovalent cations such as K^+ and Na^+ greatly stabilize such assemblies, by sitting in the inner channel^[2]. Despite these common features, G4s are highly polymorphic and differ for example in molecularity – number of single strands involved in the folding – and topology, which is defined by the mutual orientation of the G tracts at the tetrads corners^[3]. In the last two decades increasing attention has been focused on the search of small molecules able to stabilize such structures, yielding cores with extremely varied characteristics. Such great deal of effort is justified by the distribution of putative G4 sequences in key genomic regions. In fact, after the identification of the basic G4 motif in the telomeric repeats, increasing number of reports demonstrated their location in the transcription promoters of genes, in replication origins and 5'-UTRs of mRNA^[4]. This specific distribution led to the hypothesis, supported by several experimental evidences, that G4s regulate biological processes involving genome manipulation, such as replication, transcription, translation and alternative splicing, as well as telomere maintenance. As these findings extend to viruses^[5], parasites^[6] and bacteria^[7], the leading idea is that these mechanisms might be evolutionarily conserved. This also suggests that the G4 folding state control might be a valuable approach to tackle a wide variety of pathologies associated to these processes and organisms. However, many questions remain to date unaddressed, regarding for example the clarification of their biological roles and folding state along the cell cycle. The panel of tools available to date for such investigation could thus be profitably expanded to help shedding light on these aspects and to possibly provide additional ligands for therapeutic strategies implementation^[8].

For the task, two strategies have been proposed and described in this thesis (Scheme 1). The first concerns the implementation of a new family of oligo-heteroaromatic ligands for G4 binding. These could in fact mimic the structure of Telomestatin^[9], an extremely potent natural occurring G4 ligand, while rendering the synthetic access and diversification easier.

Moreover, the use of acyclic derivatives instead of a macrocyclic one like Telomestatin itself, might shift the interaction of the ligands to the grooves, instead of the end tetrads. This interaction mode has often been regarded as more selective for specific topologies over others, while possibly maintaining the selectivity over duplex DNA, and might thus prove extremely beneficial^[10]. The second strategy is based on G4 alkylation with photo-activatable moieties. These would in fact enable to form covalent and thus more stable adducts, with the advantage that the insertion and removal of the alkylating moiety might be thoroughly controlled in time and space. This would pave the way for a number of applications besides the mere therapeutic targeting. In fact, permanent fluorescent tagging and G4 forming sequences pull-down might be envisaged in live cells.



Scheme 1: General structure of the main multimodal tools targeting G-quadruplex nucleic acids developed in this thesis.

Concerning the first strategy, a family of eight heptacyclic compounds were designed and synthesized with the aim to improve the characteristics of the previously reported oligo-heteroaromatic ligands. In particular, the heptacyclic design, presented as more performing with respect to the pentacyclic one, was combined with the lower steric hindrance of oxadiazoles with respect to oxazoles, which allow higher conformational flexibility^[11]. Moreover, the novel compounds were decorated with water-solubilizing tertiary amines and

the effect of the six-membered rings nature (pyridine vs benzene) was assessed. The central ring was also functionalized with a primary amine group, so as to provide a possible tethering point for functional moieties. For the scope an optimized synthetic strategy was set up and was easily adapted to obtain considerable structural variety upon tuning of the starting building blocks. Thus, the compounds were tested as G4 ligands with standard biophysical assays. In particular, FRET experiments revealed good stabilization of quadruplex DNA, with remarkable selectivity over ds-DNA. Higher stabilizations were measured for compounds featuring pyridine rings, in particular in the central position. The interaction was confirmed by means of CD experiments, which revealed the formation of an induced CD band, ascribable to the ligand. Interestingly, FID revealed only partial displacement of TO, even at high ligand concentration. However, the analysis of analogous G4-TO-ligand mixtures by native MS highlighted the presence of ternary complexes, suggesting that the two compounds might target different binding sites. Analysis of the signals ratio suggested that the ligands binding mutually affect each other's interaction. Such aspect was also supported by docking studies, which suggested a mixed binding mode for the heptacyclic compounds, accommodating one half of the structure in the groove while protruding the other half on the end quartet.

In the second part, the feasibility of the photo-alkylation strategy was first assessed, as little information is available on effective application of such tools to G4s. Particular care was put onto the absorption wavelengths of the alkylating moieties, trying to red-shift them in the visible region. More in detail, the study focused on naphtho- and benzo- quinone methide precursors (QMP). The former already absorb in the visible region due to the extended aromatic systems, while the latter needed the functionalization with arylethynyl moieties to obtain the required red-shift. QM photo-generation efficiency was hence assessed for both building blocks, featuring a variety of substituents. For arylethynyl QMPs^[12], the QM generation was proven by laser flash photolysis and trapping with a number of nucleophiles. Analysis of the process efficiency highlighted a performance improvement with aryl moieties positioned in *para*- to the hydroxyl groups and featuring electron-donating substituents, besides the expected advantages of holding a good leaving group. Naphtho-QMPs were found to absorb up to 450 nm at physiological pH and to be particularly performing in photo-generation when an ester functionality is present at position 7. These moieties were then

used to construct putative G4 ligands, containing at least two alkylating moieties. This would in fact provide higher alkylation efficiency and prevent off-target migration due to the thermal and photochemical reversibility of the process. Three ligands featuring naphtho-QMPs and six containing benzo-QMPs were synthesized. Assessment of their G4 binding activity by FRET-melting assays revealed modest but selective stabilization. Again, the interaction was confirmed by CD titrations, in which an ICD band was sometimes observed, and absorption titrations, displaying moderate K_a values (10^5 - 10^6 M⁻¹ per binding site). Negative FID likely suggested a different binding mode with respect to the end tetrad. G4 photo-alkylation was then attempted, irradiating the DNA-compounds complexes at 365 nm. Gel electrophoresis analysis showed that all compounds alkylate the G4s at some extent. The three most performing compounds were analysed in more detail, confirming that the covalent complex is formed in varying quantities depending on both the peculiar G4 and nature of the ligands. Moreover, the G4 alkylating activity was retained also in the presence of a duplex competitor. Notably, the covalent adducts had remarkable thermal stability, showing little degradation even at 95°C. Unfortunately, due to this intrinsic stability the alkylation sites could not be identified with simple experiments.

- [1] Neidle, S., *Curr Opin Struct Biol* (2009) 19, 239-250.
- [2] Largy, E. *et al.*, *The Alkali Metal Ions: Their Role for Life*, Springer International Publishing: Cham, (2016) pp 203-258.
- [3] Burge, S. *et al.*, *Nucleic Acids Res* (2006) 34, 5402-5415.
- [4] Rhodes, D., and Lipps, H. J., *Nucleic Acids Res* (2015) 43, 8627-8637.
- [5] Perrone, R. *et al.*, *J Med Chem* (2013) 56, 6521-6530.
- [6] Leeder, W. M. *et al.*, *Sci Rep* (2016) 6, 29810.
- [7] Beaume, N. *et al.*, *Nucleic Acids Res* (2013) 41, 76-89.
- [8] Di Antonio, M. *et al.*, *Methods* (2012) 57, 84-92.
- [9] Kim, M.-Y. *et al.*, *Journal of the American Chemical Society* (2002) 124, 2098-2099.
- [10] Hamon, F. *et al.*, *Angew Chem Int Ed Engl* (2011) 50, 8745-8749.
- [11] Petenzi, M. *et al.*, *Chemistry* (2012) 18, 14487-14496.
- [12] Doria, F. *et al.*, *J Org Chem* (2016) 81, 3665-3673.

Table of Contents

ABSTRACT	V
TABLE OF CONTENTS	IX
CHAPTER 1 : INTRODUCTION	1
1.1 Structure and biology of G-Quadruplex nucleic acids	3
1.1.1 Quadruple helix DNA and RNA	4
1.1.2 Biological significance of G-Quadruplexes	7
1.1.3 Small molecules targeting G-Quadruplexes	13
1.1.4 Targeted covalent modifications of G4	31
1.1.5 Biophysical evaluation of small molecule – G4 affinity	37
1.2 DNA alkylation	47
1.2.1 Classical alkylating agents	47
1.2.2 Quinone methides as masked electrophiles	49
1.2.3 Photochemically generated QMs	54
1.2.4 QM detection.....	58
AIM OF THE THESIS	61
CHAPTER 2 : G4 REVERSIBLE TARGETING	65
2.1 Heptacycles for selective G4 targeting	67
2.1.1 Facile synthesis of a water-soluble heptacyclic ligand	67
2.1.2 Structural variations in the heptacyclic scaffold	72
2.1.3 Heptacyclic scaffolds adapted for conjugation	74
2.1.4 Biophysical binding assays towards G4 structures	76
CHAPTER 3 : PHOTOINDUCED G4 ALKYLATION	87
3.1 Conjugation and substituent effects on the photogeneration of prototype arylethynyl o-QMs	89
3.1.1 Synthesis of arylethynyl QM precursors	90
3.1.2 UV-vis absorption of QMPs	91
3.1.3 Photoreactivity and QM trapping	93

3.1.4 Laser flash photolysis QM and T ₁ detection.....	96
3.1.5 Conjugation, leaving group and solvent effects	99
3.1.6 Substituent effect on QM photogeneration	103
3.1.7 Substituent and conjugation effect on QM reactivity	108
3.1.8 Singlet oxygen photosensitization	109
3.2 Design of a naphtho-QMP functional tool.....	113
3.2.1 Synthesis of 6-substitued <i>o</i> -NQMPs	114
3.2.2 Absorption and emission proprieties of a prototype NQMP	120
3.2.3 LFP detection of a naphtho-QM	122
3.2.4 Photoreactivity and QM trapping	124
3.2.5 Substituent effect on NQMP photoreactivity	128
3.3 Towards selective G4 photo-alkylation	131
3.3.1 Synthesis of V-shaped bifunctional <i>o</i> -QMPs.....	132
3.3.2 Synthesis of V-shaped bifunctional NQMPs.....	133
3.3.3 Synthesis of trifunctional <i>o</i> -QMPs.....	136
3.3.4 QMPs as G-quadruplex reversible ligands	136
3.3.5 Photoalkylation of G-quadruplex	145
3.3.6 Assessment of the alkylation site	151
CONCLUSIONS AND REMARKS	157
CHAPTER 4 : EXPERIMENTAL SECTION	159
4.1 Materials and methods	161
4.1.1 Purification	161
4.1.2 Characterization.....	162
4.1.3 Reactivity studies and transients detection	162
4.1.4 Biophysical assays	164
4.1.5 Biochemical assays.....	166
4.1.6 Molecular docking	172
4.2 Synthetic protocols.....	173
4.2.1 Synthesis of heptacycles	173
4.2.2 Synthesis of 4- and 5-Arylethynyl-ortho-QMPs.....	185
4.2.3 Synthesis of 7-substitued NQMPs	191
4.2.4 Preparative phototrapping of prototype QMPs.....	201
4.2.5 Synthesis of QMPs for G4 binding	208
APPENDIX A – DNA SEQUENCES	217

APPENDIX B - FITTING EQUATIONS	219
BIBLIOGRAPHY.....	225
LIST OF ABBREVIATIONS	235
ACKNOWLEDGEMENTS	237

CHAPTER 1 : Introduction

1.1 Structure and biology of G-Quadruplex nucleic acids

About 60 years ago, DNA double helical structure was unveiled by Franklin, Watson and Crick. This way of assembling the two strands is governed by precise nucleobase pairing rules. In turn, these depend on the complementary hydrogen bonding patterns of the pairs cytosine-guanine and thymine-adenine. However, the double helix can be described as the dormant form of DNA. In fact, whenever a biological process involving DNA has to take place, the two strands need to be separated. This is true, for example, for replication and transcription. Moreover, RNA, the ribonucleotide copy of DNA, carries out its functions as a single strand or, at least, not in the canonical double helix form.

It is however unlikely for this single stranded “active” form of nucleic acids to simply be linear. In fact, a wealth of hydrogen-bond interactions, canonical or not, can be established between nucleobases of the same strand or of more strands normally unpaired, when positioned at the right distance. This results in the folding into various secondary structures, profoundly different from the renowned double helix (Figure 1). These comprehend, among others, G-quadruplexes, i-motifs, triplexes, hairpins and Holliday junctions^[1].

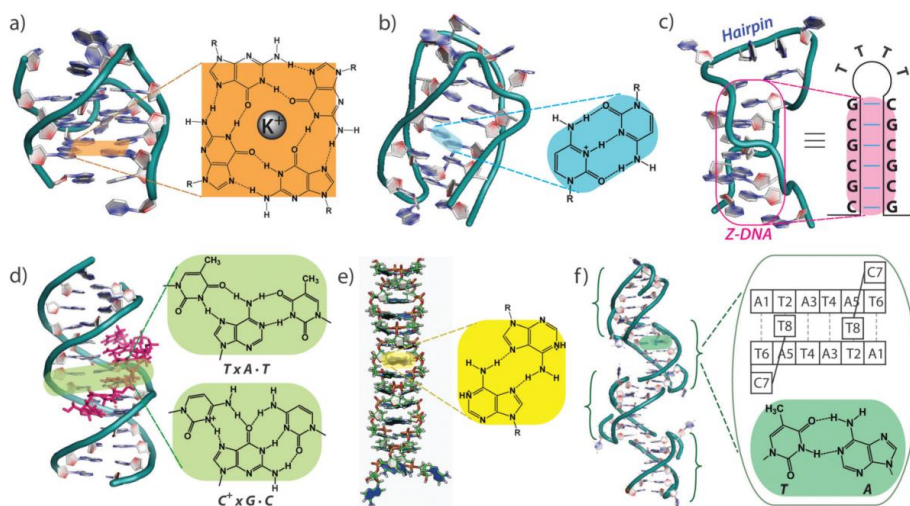


Figure 1: Representative non-B DNA structures and their molecular structures. (a) G-Quadruplex. (b) i-motif. (c) Hairpin. (d) Parallel triplex. (e) A-motif. (f) Hoogsteen-type non-canonical duplex structure.

G-quadruplexes (G4s) have gained a lot of attention in the last fifteen years for two main reasons: their location in ‘hot’ genomic regions and their putative biological functions. Before

discussing in more detail these two aspects, a brief introduction on the constitutive elements of these structures will be given.

1.1.1 Quadruple helix DNA and RNA

G-quadruplexes can be formed by nucleic acids strands rich in guanine, at high alkaline cations concentration and physiological pH^[2]. When such strands contain at least four guanine tracts separated by a certain number of nucleobases, the assembly of guanine quartets is favoured. As the name already suggests, these are formed by four guanines each, binding through an unconventional hydrogen bonds net^[3]. This is possible thanks to the peculiar nature of guanine structure, which has appropriate hydrogen bond donor and acceptor groups on opposite faces of the molecule (Figure 2). Through the pairing of O⁶ and N⁷ acceptors on one guanine with N¹ and N² donors of the following one, a square structure is assembled. Two or more quartets can then pile on top of each other, via π - π stacking interactions.

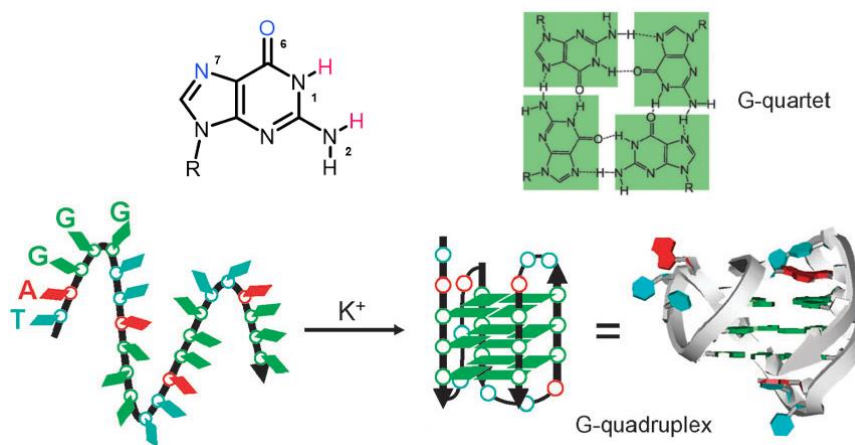


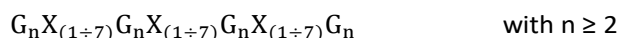
Figure 2: Folding of a single strand DNA oligonucleotide into a G-quadruplex structure.

Thus, an empty channel is formed in the middle of the resulting 3D structure. As each guanine has an oxygen atom, O⁶, pointing towards such channel, a considerable negative electron density is accumulated. The resulting repulsion is relieved by positioning positively charged alkaline cations on the inside, notably K⁺ and Na⁺ ^[4]. Depending on the specific cation's size, this can sit at different heights in the channel. For example, K⁺ has the right size to insert between two quartets, coordinating as high as eight oxygen atoms. Conversely, Na⁺ is small

enough to lie in the middle of a quartet and form a complex with the four carbonyl groups involved. Other cations have the right size to stabilize G quartets. These include monovalent NH_4^+ , Rb^+ and Cs^+ , as well as bivalent cations, such as Sr^{2+} , Ba^{2+} , and Pb^{2+} . Other cations are instead unable to interact with the quartet. The most relevant in this sense is Li^+ , which is too small to interact with the internal channel constituents^[5].

Apart from the G quartets, G4s contain constitutive elements which are not strictly involved in the non-covalent bonds but contribute to the overall 3D structure^[6]. These are the loops, which are constituted by the nucleobases connecting the different G tracts, and the flanking regions, the sequences preceding and following the first and last G tract. Moreover, the spaces located between two corners of the G4 3D structure are named grooves.

Because of this peculiar structure requiring four guanine tracts to be positioned at the right distance, a model sequence has been proposed as the minimal one needed to form a G4^[7].



In particular, G4 stabilization increases with the number of guanine quartets piling up. Therefore, although two is the minimum number, three quartets are often found to interact. Moreover, it was thought that only G4s with loops of moderate and similar length were stable enough to actually fold. Algorithms were thus implemented based on these features so as to screen genomes looking for putative G4 sequences (PQS) and estimate the likelihood of their folding^[8]. However, experimental evidences have shown that this is not true and that G4s with longer loops and even structures displaying loops of very different length can in principle be formed *in vitro*^[9]. In the same way, also bulged G4, that is structures in which guanine tracts are interrupted by another nucleobase, can actually fold. Therefore, more complex algorithms which aim at better describing these features and reduce false negative results have been developed in the last decade^[10, 11].

Despite sharing these structural features and a minimal sequence, G4s are highly polymorphic. The main distinction that can be made is based on G4s molecularity^[12]. This is defined as the number of single strands that compose the structure. Therefore, although the most investigated structures are monomolecular, and thus intramolecular, also bi- and tetramolecular G4s have been observed, forming intermolecular assemblies.

Moreover, G4s differ in topology^[13]. This is determined by the orientation that the G tracts adopt with respect of each other (Figure 3). Therefore, if all the G tracts run in the same direction, the resulting topology is classified as parallel. Conversely, if the four G tracts are divided in pairs with opposite orientation, the G4 is antiparallel. The intermediate situation, with three G tracts running in one direction and the fourth running in the opposite one leads to a hybrid G4. Of course, the adoption of a certain topology affects the loops geometry. In fact, in a parallel topology, all the three loops must connect the top end tetrads to the bottom ones, hindering the grooves. Loops with such characteristics are called propeller-type. In an antiparallel topology, instead, the loops connect guanines of the same tetrad. However, depending on the disposition of the connected guanines, either adjacent or at opposite corners of the tetrad, the loops will be lateral or diagonal and the resulting G4s will be called either chair- or basket-type. Hybrid G4s contain a mix of these kinds of loops.

The folding into a particular topology of a certain sequence is ultimately governed by thermodynamics. Factors affecting the stability of the possible topologies are for example the available cations, the loops conformation etc. Different environmental conditions can lead to very different topologies even for the same conformation (e.g. telomeric sequence 22AG has a mixed conformation in K^+ rich buffer and an anti-parallel one in Na^+)^[14] and often more than one are present at the same time in defined ratios.

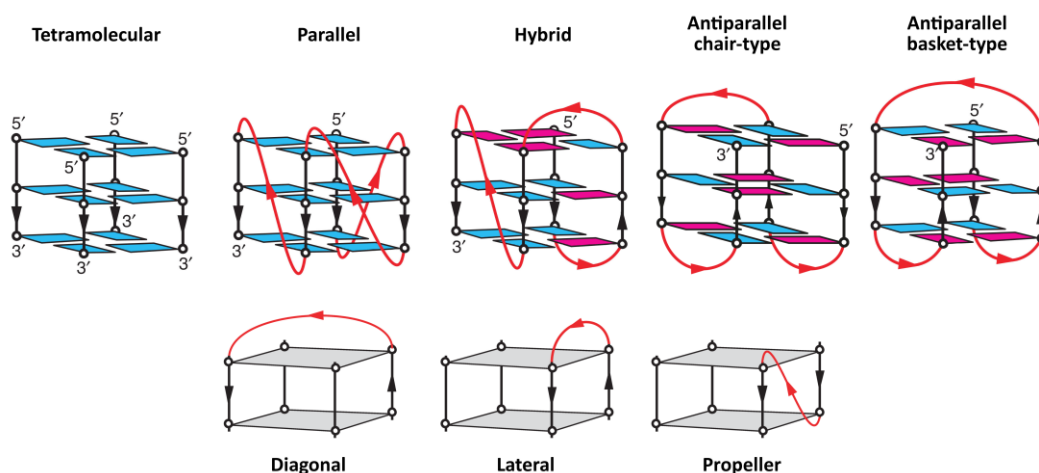


Figure 3: Schematic representation of different G4 topologies and loop geometries. *Anti*-guanines are depicted in cyan, *syn*-guanines in magenta.

The facing of guanines involved in adjacent tetrads is also particularly important for the free energy of the conformation. This depends primarily on the glycosidic bond angle (GBA) adopted by each guanine^[4]. GBA is defined as the angle between the sugar moiety, lying in the plane, and the guanine, disposed perpendicularly to it. If the nucleobase points away from the sugar, the disposition is called *anti*, whereas it is called *syn* in the opposite case (Figure 4). Upon G4 folding, guanines of directly stacked quartets face each other in *syn/syn*, *anti/anti* and *syn/anti* or *anti/syn* dispositions. As the *syn* disposition is more hindered and thus less stable than the *anti* one, *anti/anti* facings are preferred^[15]. *Anti/syn* and *syn/syn* facings are higher and higher in energy. However, specific facings are needed, depending on the particular topology. *Anti/syn* dispositions are observed at guanine tracts polarity inversion points, that is when tracts running in opposite directions are present. Therefore, parallel G4s, which do not need such turning points, only display *anti* guanines and *anti/anti* dispositions (*syn/syn* facings are too unstable and sterically demanding), whereas the necessary *syn* monomers are observed at specific positions in anti-parallel and hybrid G4s, involved in *syn/anti* pairs.

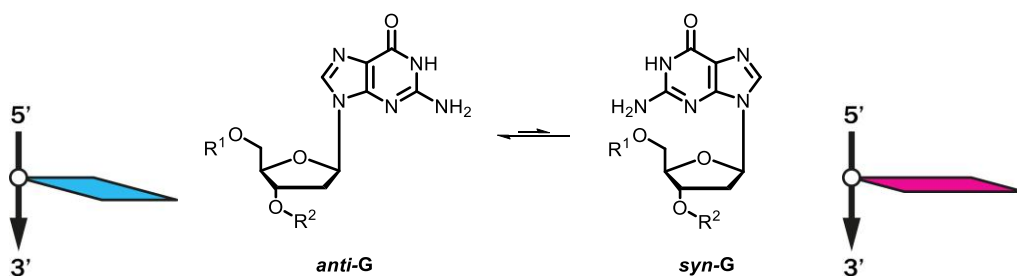


Figure 4: Guanine *anti* and *syn* glycosidic bond conformations.

1.1.2 Biological significance of G-Quadruplexes

As previously stated, G4s catalysed the attention in the last two decades due to their distribution throughout the genome. In fact, bioinformatic and empirical screenings led to identify up to 700.000 PQS in the human genome^[9], localized mainly at telomeres^[16], replication origins^[17], transcription starting sites of multiple genes^[18], 5'UTR regions of mRNA^[19], etc. As such regions are apparently highly conserved^[20], the resulting G4s are likely to have some kind of biological significance. Interestingly, these findings extend to genomes

other than the human one. In fact, PQS have been identified also the genetic information of viruses^[21], bacteria^[22], yeasts^[23], parasites^[24] etc., suggesting not only a general relevance but also that some kind of evolutionary pressure is in place to retain the mechanisms associated to these sequences.

Despite research has flourished on G4s, in terms of PQS identification, association to biological processes and implementation of small molecules able to target them^[3], an overview of such investigations cannot overlook the pending biological questions about G4s. For the sake of this dissertation, these will be mentioned only briefly, but their importance and the urgent need of biological and chemical tools to answer them must be kept in mind. The main source of discussion, which even precedes the clarification of the biological roles of these structures, is whether G4s can actually fold in living cells. This question was partially answered with the implementation of fluorescent monoclonal antibodies able to specifically stain such structures in fixed cells^[25, 26]. This was in fact the first direct visualization in the cellular environment, even though a number of issues (e.g. G4 folding induction, biases introduced with chromatin fixation, etc.) and the reported high cross-reactivity for one of the antibodies^[27] make them only a partial solution to the issue. These experiments however added up to a number of less direct evidences, such as the identification of protein partners, both with chaperone and unwinding activity^[28, 29]. Therefore, although a conclusive proof is still missing, all these empirical findings suggest that G4 folding might actually happen *in vivo*.

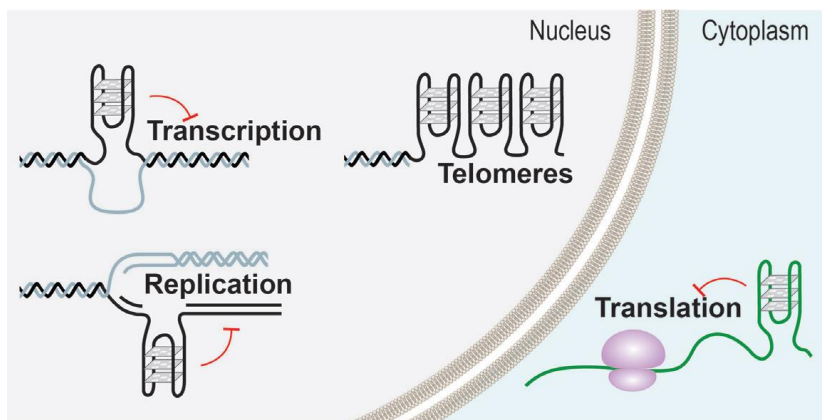


Figure 5: Possible locations of G-quadruplex structures in cells. G4 formation can occur in double stranded G-rich regions when DNA becomes transiently single stranded, during transcription, replication and at the single stranded telomeric G-rich overhangs. Outside the nucleus, G-quadruplexes can also form in mRNA and are involved in translational control.

However, G4s, in order to fold, need to compete with the corresponding double strand. It is thus fair to assume that the folding process is facilitated only when the duplex splits up in the corresponding single strands. Clearly, this situation is not prevalent, although it is observed during specific processes, such as transcription and replication. Therefore, the question of whether G4s actually fold *in vivo* must be complemented with a thorough detailing of where and when these processes take place, which is mainly missing to date and constitutes an open question in the field.

Clarification of G4s biological roles comes on top of these open issues. However, investigations and results on this aspect are more consistent, to the point that multiple putative functions associated with the specific genomic locations have been identified (Figure 5). These are supported by a number of indirect evidences, that is not obtained in live cells. Although some functions are very general and possibly common to various organisms, others have been postulated for specific sequences in specific species (e.g. promotion of RNA dimerization in HIV-1)^[30]. Due to the purpose of this discussion, the following overview on G4 functions will be limited to the general ones.

- **Telomeres**

PQS in the telomeric regions were the first to be identified and since then they have kept a prominent position in G4 research. Telomeres are repetitive non-coding sequences located at the end of chromosomes in eukaryotes. Their purpose is to be sacrificed during replication, so as to prevent the polymerase machinery to cleave valuable genetic information. In fact, the enzyme is unable to proceed until the very end of the DNA sequence and, by stopping in advance, produces the loss of the last nucleobases. As cleavage of coding genes would likely result in unviable cells, telomeres are sacrificed in their place. This process gradually consumes the sequences and ultimately leads to cell ageing and death.

Interestingly, telomeres contain a sequence which is potentially able to fold into a G4 structure. For humans the repetitive motif is 5'-d(TTAGGG)_n, although some variations are detected depending on the specific species. Four of these repeats can assemble into a G4, as it was demonstrated *in vitro*^[16]. As telomeric regions end with a 3' overhang which is single stranded, it is possible for G4s to spontaneously fold at such sites. It has been suggested that G4s role in this context might concern telomere maintenance^[3]. In fact, they might prevent

recognition of chromosomes ends as strands breaks by repair enzymes, which would lead to inter-chromosomes fusion events.

However, and possibly more interestingly, it was also observed that G4s stall telomerase activity^[31]. Telomerase is an enzyme with reverse transcriptase activity. Through a multicomponent machinery it replicates an RNA template and elongates telomere ends. This ultimately leads to cells immortalization, as it helps escaping natural ageing. However, such an enzyme is expressed and active only in few cell lines. Besides normal stem cells, these mostly comprehend tumour cells. Stabilization of telomeric G4s might thus constitute a valuable approach to contrast cancer cells immortalization and trigger DNA damage, ultimately leading to apoptosis. For this reason, a wealth of studies has been focussed on the clarification of telomeric G4s effective folding and on finding small molecules able to target them, as a novel therapeutic strategy^[32, 33].

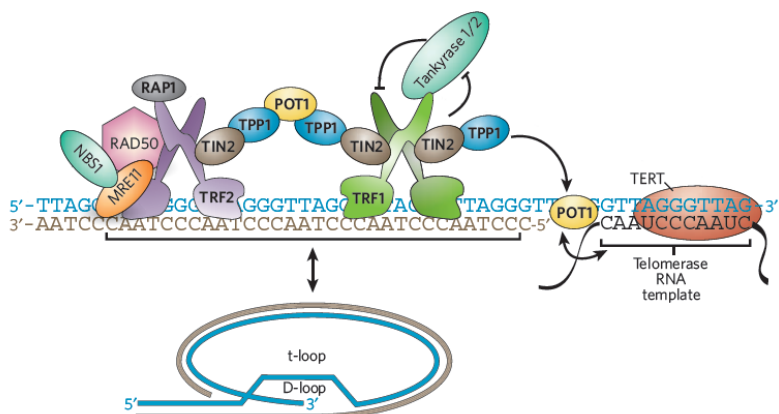


Figure 6: Protein complexes binding to the double- and single-stranded telomeric DNA. The telomerase complex interacts with the telomeric overhang and is regulated by shelterin and other telomeric proteins. The single-stranded overhang can invade the double-stranded portion of the telomere, forming protective loops at the invasion site.

This whole research is not based on mere *in vitro* evidences of telomeric G4 folding, but is instead substantiated by evidences collected in the cellular context. In fact, a number of proteins have been identified, which specifically interact telomeric G4s exclusively upon folding. Therefore, it is likely that such folded G4 structures are the real molecular partners also in cells. Among these, there are some chaperone proteins (e.g. TEBP β in ciliates)^[34] and proteins with helicase activity^[28]. Moreover, the shelterin complex^[35], which contributes to telomere capping and t-loop maintenance exerting a protecting effect from degradation, seems to have some subunits interacting with G4s, namely RAP1, TRF2 and POT1 (Figure 6).

- **Transcription starting sites**

Bioinformatic analysis revealed that many genes, and interestingly many proto-oncogenes, contain PQS upstream of their transcription start sites, in regions where transcription factors and other regulatory elements bind to initiate the process^[18]. Therefore, the folding state of such sequences is likely to affect the transcription process (Figure 7). In particular, experimental evidence suggests that G4s have a suppressing activity on transcription when they are folded^[36-38]. In fact, when introducing point mutations in the sequence which impede G4 formation, overexpression of the controlled genes is observed. This was experimentally demonstrated for the MYC gene, for example.

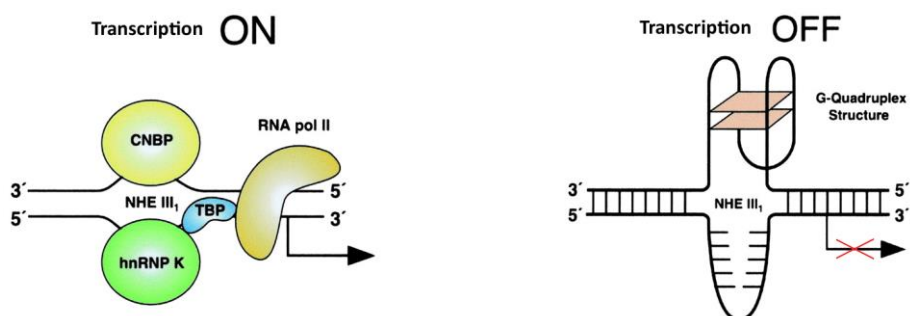


Figure 7: Model of MYC transcriptional regulation by a G-quadruplex in the promoter region NHE III. The binding of hnRNP K and CNBP to single-stranded DNA induced by negative supercoiling leads to activation of MYC transcription.

An additional empirical evidence regarding G4 involvement in transcription regulation is the effect of G4 binding ligands on genes expression. In fact, upon treatment of live cells with such small molecules, a considerable decrease in the levels of transcription products is observed for genes that contain PQS in the upstream sequence^[23]. These evidences led to develop tailored assays, in which the transcription regulation by a certain PQS is monitored through the expression of reporter genes, cloned downstream, such as that coding for luciferase^[39]. In this way, either the G4 involvement in transcription regulation or the activity of putative ligands can be assessed.

Transcription regulation is of particular interest, as a number of the putatively involved genes code for proteins associated to cancer hallmarks and other pathologies. Concerning cancer, overexpression of such proteins leads to dysregulation of the related processes, such as uncontrolled proliferation, enhanced tumour vascularization and apoptosis escape^[40-42]. Another example is that of HIV-1. When the viral genome is integrated in that of the host

cells, expression of its gene is apparently controlled by specific G4s in the promoter region, which impede transcription when folded^[21]. Therefore, G4 folding regulation in these contexts might constitute a novel approach to tackle a wide number of pathologies.

- **Translation regulating sites**

PQS have been identified not only in DNA, but also in RNA transcripts. In particular, comprehensive screening of mRNA products revealed an interesting prevalence of PQS at 5'UTR (untranslated regions) of such RNA sequences^[19], although their distribution also extends to other locations, such as alternative splicing regulating sites and TERRA RNA transcript of the telomeric sequence^[43]. 5'UTR of mRNA play pivotal roles in regulating the translation process, similarly to the regions upstream of the transcription starting sites. Therefore, PQS located at such RNA sites are believed to have some role in this and in particular to suppress translation (Figure 8). This is the case for example of NRAS^[44], which was the first of such RNA PQS to be identified. Similarly, PQS associated to fragile X mental retardation seem to suppress translation and promote their toxic accumulation of RNA transcripts^[45].

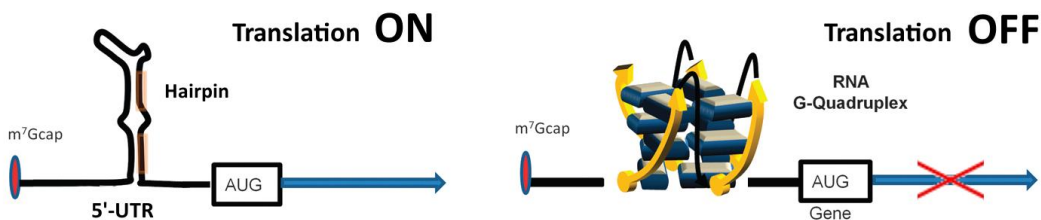


Figure 8: Proposed translation inhibition by RNA G-quadruplex formation.

Although, at least intuitively, G4 folding should be easier in RNA than in DNA, as RNA does not occur under a double helical form, recent empirical evidence suggested that RNA PQS are mostly unfolded in the cellular context^[46]. These findings were quite surprising when considering the number of evidences of RNA G4s regulatory roles. Therefore, additional investigation is needed to thoroughly understand under which specific circumstances these structures actually form in live cells.

- **Replication associated sequences**

Similarly to transcription and translation, PQS have often been hypothesized to regulate DNA replication in a suppressive way. In fact, *in vitro* experimental evidences show that folded G4

structures can stall the polymerase activity, impeding the progression of the replication fork^[47]. Contextually, a number of enzymes with helicase activity have been identified with high affinity for G4s, such as FANCI and Pif1^[28]. This suggests that their peculiar role is to unwind such secondary structures in order to remove impediments to the replication machinery when necessary (Figure 9). Interestingly, inactivation of such helicases results in rearrangement of the genetic information. In fact, deletions are observed at sites where PQS should be present, indicating that the DNA polymerase is stalled at such sites and needs to by-pass them^[48]. G4s might thus fold in sequences related to replication in a time-resolved manner, possibly controlled by specific enzymes.

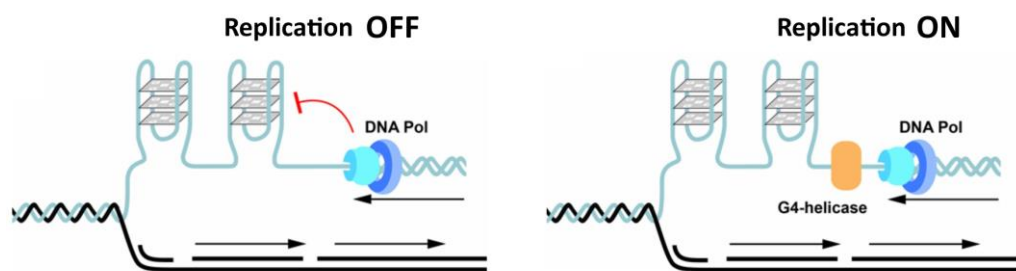


Figure 9: Schematic representation of replication inhibition by G-quadruplex sequences. G4-helicases such as FANCI and Pif1 could resolve them and promote DNA polymerase advancement.

Interestingly, though, this suppressive role does not seem to be the only one associated to replication. In fact, genome wide studies highlighted a considerable abundance of PQS at replication origins. Notably, these consist in up to 80% of the total origins number^[17] and, more interestingly, they seem to be the most active. Such a prevalence again suggests an active role of PQS in regulating the process, which probably is not a suppressive one.

1.1.3 Small molecules targeting G-Quadruplexes

Since Zahler and co-workers demonstrated in 1991 that G4 structures stabilized by K^+ are able to inhibit telomerase activity^[31], G4s have emerged as a significant target for anticancer drug development. The first evidence for a biological application of a small molecule stabilizing a G-quadruplex was indeed the *in vitro* inhibition of telomerase activity by a 2,6-diamidoanthraquinone in 1997^[49]. Ever since, there has been an astounding emergence of small molecules able to interact efficiently and selectively with such peculiar DNA secondary

structures. These compounds appeared to selectively inhibit the growth of cancer cells, and drew the attention towards the attracting perspective of developing novel potent anti-cancer drugs. Initially it was shown that small molecules able to induce or stabilize G-quadruplexes could provoke the uncapping of proteins in the shelterin complex as well as telomerase downregulation, leading to telomere disorganization and genomic instability, eventually causing apoptosis^[50]. More recently, G4 imaging^[25, 26] together with bioinformatic mapping studies^[10] and last generation sequencing^[9, 51] have provided new insights on the biology of G4s in non-telomeric regions^[52], suggesting their involvement in a broad range of biological processes, from replication^[53] to gene expression^[54] and genomic instability^[55]. Several G4-targeting small molecules were found to affect the mRNA levels of genes containing G4 motifs within the promoter region, e.g. the proto-oncogenes MYC^[38] and KRAS^[37]. A reduction in the level of their transcripts was obtained upon treatment with PDS, a known G4 ligand, although it is still unclear whether transcription repression is a direct consequence of G4 stabilization or is indirectly caused by DNA damage. Accordingly, the opportunity of designing novel anti-cancer therapeutic strategies by G4 targeting has become very appealing.

It is not surprising, therefore, that the last 20 years have seen the multiplication of reports on new molecules in the field of G4 binders^[56]. Initially inspired to classical DNA intercalators, their structure has been refined to gain selectivity over other DNA forms. In most cases, the quadruplex stabilization occurs *via* π stacking and electrostatic interactions. The essential feature often considered when designing a new ligand is a large flat aromatic system that can fit onto the external face of the quadruplex (Figure 10). This binding mode, normally referred to as end stacking, represents the most straightforward distinctive tract of quadruplex recognition if compared to alternative DNA structures. Given the remarkable wide area of the G-quartet, a good G4 ligand should embed a large aromatic surface, much larger than that of a classical duplex intercalator, to maximize the overlap and provide the best selectivity. Additional features include an electron-poor core and positively charged moieties, which could both participate in the stabilization through electrostatic interactions and ensure reasonable water solubility to the compound. However, due to ubiquitous presence of negatively charged backbone and the absence of a strict peculiar geometrical arrangement, such interactions are potentially much less specific. In some cases it has been

shown that an additional cation could intercalate between the ligand and the end tetrad, although little information is available concerning its actual contribute. Sometimes, nucleobases in the loops could participate through specific hydrogen bonding or stacking interactions, but these are hardly predictable due to loose geometric constraints in this regions.

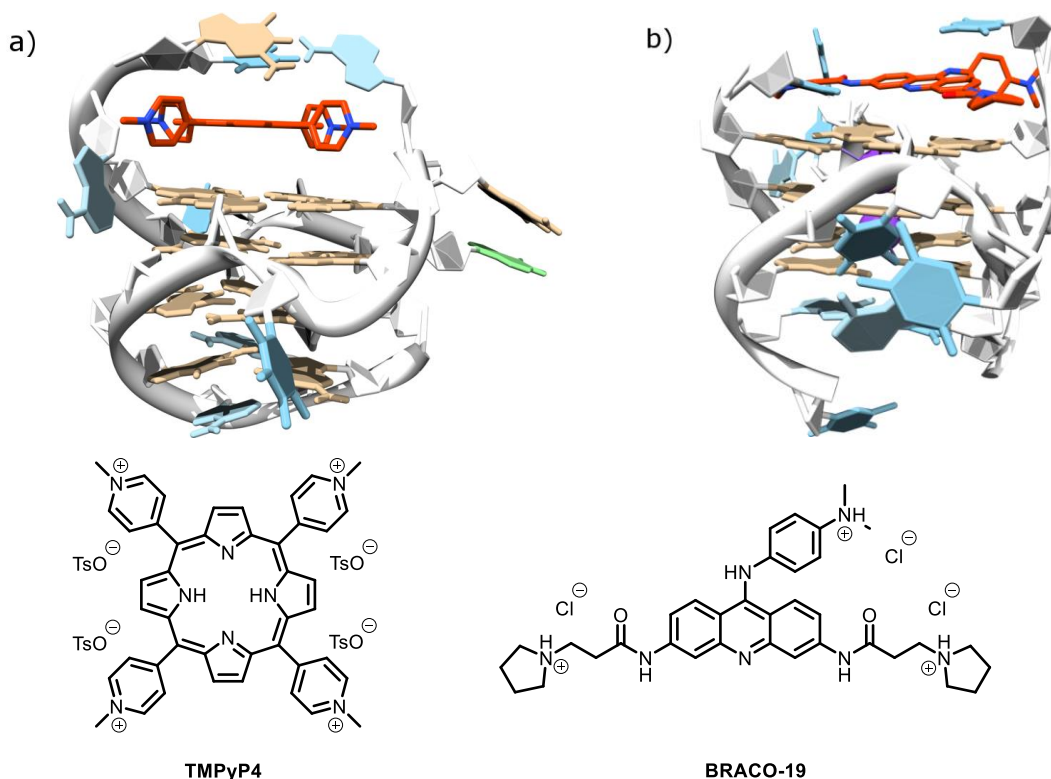


Figure 10: (a) NMR structure of the complex between porphyrin **TMPyP4** and c-myc derived quadruplex Pu24I (PDB ID: 2A5R). (b) XRD structure of the complex between acridine derivative **BRACO-19** and bimolecular parallel-stranded human telomeric G-quadruplex [d(TAGGGTTAGGGT)]₂ (PDB ID: 3CE5)^[57].

When the experimental evidences are not consistent with an end stacking binding mode, the common rationale point out to the interaction with the lateral grooves of G-quadruplex. However, despite the large number of such claims, so far only **Distamycin A**^[58, 59] and related derivatives^[60] have been univocally identified as G4 groove binders by solving the NMR solution structure for some of their complexes. Interestingly, besides the observed dimeric binding in two opposite grooves for the tetramolecular [d(TGGGGT)]₄ quadruplex (Figure 11), another study suggested that two distamycin molecules could stack on the terminal G-tetrad of certain intramolecular quadruplexes^[61]. Unfortunately, there is no general rule and the

structural polymorphism of G4 backbone arrangement, which shapes the four grooves, justifies the lack of knowledge on which structural features might take advantage of such interactions while maintaining poor recognition of *ds*-DNA major and minor grooves.

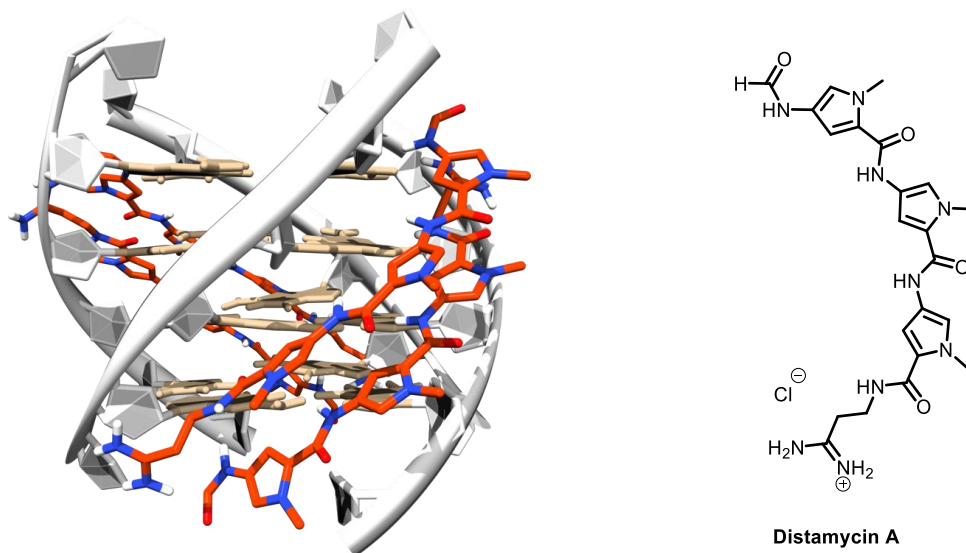
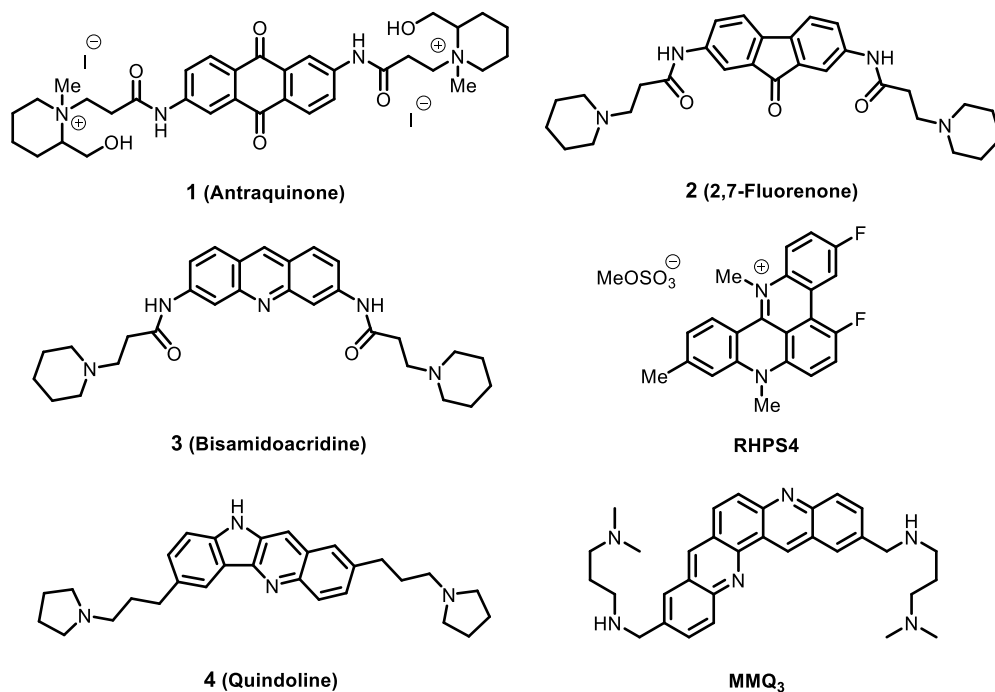


Figure 11: NMR structure of the 4:1 complex of **Distamycin A** with tetramolecular [d(TGGGGT)]₄ quadruplex (PDB ID: 2JT7)^[59].

To date, the structure-based design of G-quadruplex targeting compounds has been directed by two predominant criteria, namely large planar aromatic surfaces and positively charged structures, but also empirical approaches have proved to be fundamental. Hence, the most representative classes of G4 ligands are described below.

Anthraquinones, fluorenones, acridines, quindolines and quinacridines

The first G4-interacting compound was the 2,6-disubstituted aminoalkylamido anthraquinone **1** (Scheme 1), which exhibited good telomerase inhibitory activity ($T^{el}IC_{50}=23 \mu M$)^[49]. Molecular modeling was used to establish the DNA G4–AQ complexes based on a “threading” intercalation binding mode. This molecular model indicates that tetrad–ligand π – π overlap is feasible, and that any flexible pendant side chains can be accommodated in the wider G4 grooves. Subsequently, 2,7-fluorenone analogues have been designed to prevent quinone related redox activity and decrease the observed cytotoxicity^[62]. These compounds were found to be 10-fold less cytotoxic than the related anthraquinones, preserving a good inhibitory activity ($T^{el}IC_{50}=9 \mu M$ for **2**).



Scheme 1: Examples of antraquinone, fluorenone, acridine, quindoline and quinacridine G4 binders.

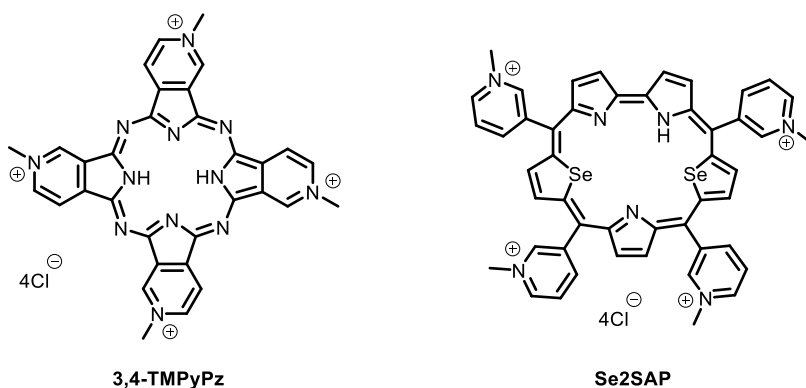
To introduce a positive charge in the central ring as a complementary electronic feature with respect to the negative electrostatic potential formed at tetrad center, the synthesis of a series of 3,6-bisamidoacridines (e.g. **3**) was accomplished. However, due to the weak basicity of the acridine nitrogen atom, the inhibitory activity was substantially unaffected^[33]. Still, **BRACO-19** (Figure 10), which belongs to the family of 3,6,9-trisubstituted acridines, has received great attention and is still considered one of the G4 reference ligands^[63]. Pentacyclic acridine **RHPS4** has also been identified as a potent telomerase inhibitor ($T^{\text{el}}IC_{50}=0.33 \mu\text{M}$). Notably, this compound was found to inhibit cell proliferation within 2–3 weeks at non-cytotoxic concentrations^[64].

Molecular modeling revealed that a tricyclic aromatic structure might be further extended to maximize stacking interactions with the surface of the terminal quartets. Accordingly, quindoline^[65] and quinacridines^[66] tetra- and penta-cyclic ligands such as **4** and **MMQ₃** have been identified as G4 ligands. Bent-shaped arrangement of the five fused aromatic rings was found to be much convenient. More than one sp^2 nitrogen was embedded to maintain the electron-deficient properties of the scaffold. These ligands were found to bind to the human

intramolecular G4, as evidenced by the melting temperature measurements. The most active compound of this class is **MMQ₃** ($\Delta T_m = 19.7$ °C and $^{Tel}IC_{50} = 0.028$ μM).

Cationic porphyrins

The macrocyclic planar arrangement of the aromatic rings in porphyrin and analogues make them good candidates for binding G4s by stacking with the terminal tetrads. Unfortunately, porphyrins are well-established binding agents for *ds*-DNA, and therefore are poorly selective ligands. The porphyrin analogue **TMPyP4** (Figure 10) was found to bind both parallel and antiparallel G4 structures, but with only two-fold selectivity for quadruplex over duplex DNA. Interestingly, besides showing intercalation between adjacent tetrads and stacking onto the external quartet (Figure 10), X-ray studies of the complex between **TMPyP4** and the bimolecular parallel-stranded human telomeric G-quadruplex [d(TAGGGTTAGGG)]₂ described an alternative and unprecedented binding mode based on the stacking onto the TTA nucleotides without any direct contact with G-quartets^[67].

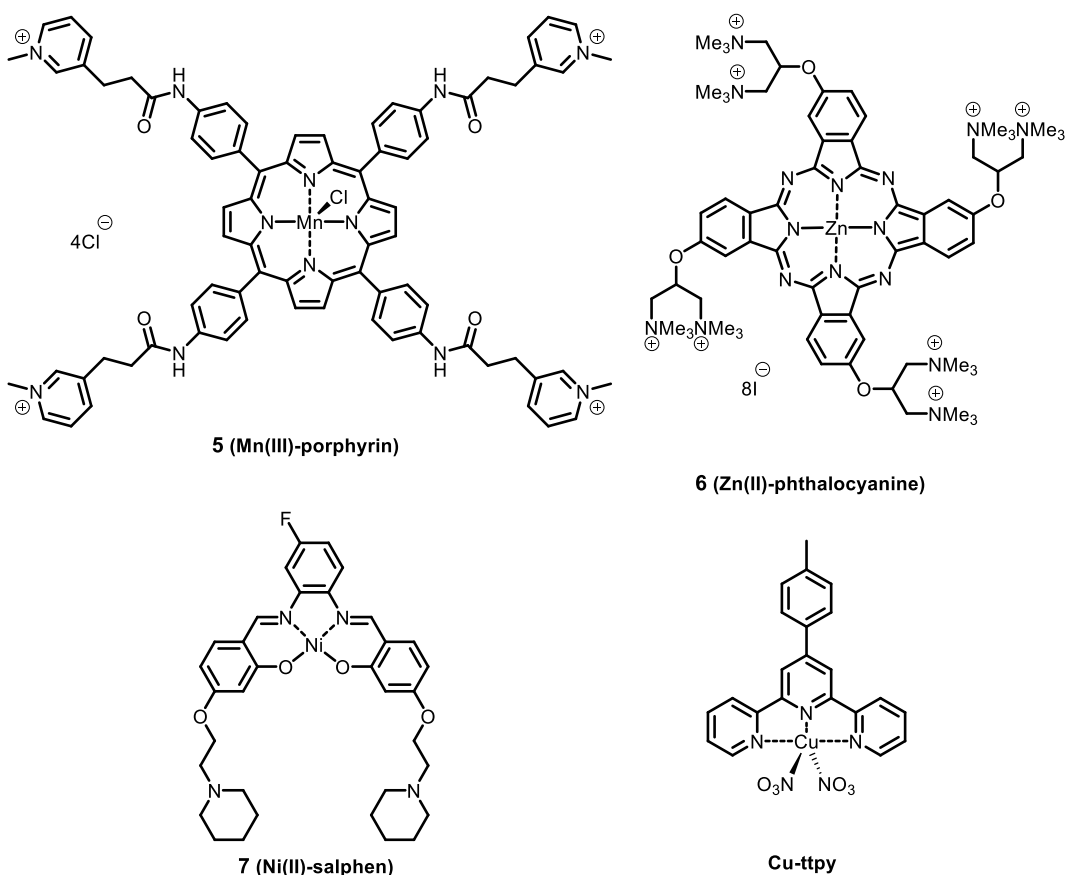


Scheme 2: Structure of selective porphyrin derivatives targeting G4s.

Several structurally related compounds have been described such as the porphyrazine **3,4-TMPyPz** (Scheme 2), which has shown a 100-fold increase in affinity as compared to **TMPyP4**, but also a significant improvement of the specific recognition of G4 over *ds*-DNA^[68]. Notably, diselenosapphyrin **Se2SAP**, embedding an expanded porphyrin core, was shown to bind strongly and selectively to quadruplex DNA and displaying high topological preference^[69]. In detail **Se2SAP** converted parallel (e.g. Myc-22) and anti-parallel (e.g. hTel21) topologies into a mixed anti-parallel/parallel hybrid structure.

Metal complexes

While initially most G4 binders were based on mere organic molecules, more recently metal complexes have shown their potential to be used as excellent quadruplex binders^[70]. Besides their cationic and highly polarized nature is a clear advantage for promoting the association with the negatively charged DNA, the right positioning of a metal ion over the cation channel of the quadruplex should enhance the stacking interactions of the organic portion and give a positive contribute to the overall complex stability.



Scheme 3: Metallo-organic compounds used as efficient and selective G4 binders.

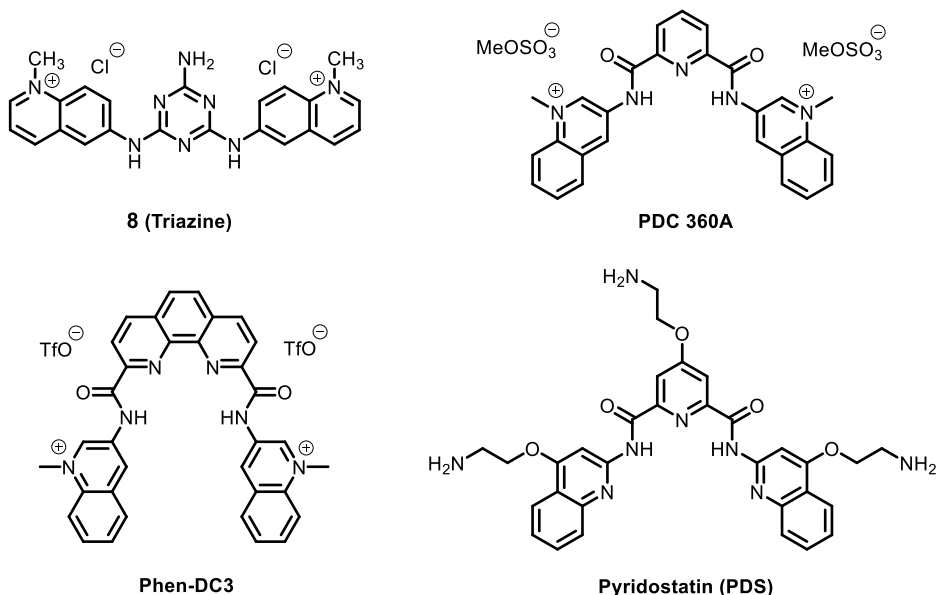
Metal-porphyrins have been successfully used for targeting G-quadruplexes (Scheme 3). In particular, Mn(III)-porphyrin **5**, containing four flexible bulky cationic arms was found to be able to differentiate between G4 and *ds*-DNA with a 10000-fold selectivity thanks to the central cation and the bulky substituents^[71], making it one of the most selective G-

quadruplex ligands. Zn(II)-phthalocyanine **6** revealed potent G4 affinity and displayed strong inhibitory activity against telomerase ($^{Tel}IC_{50}=0.23 \mu M$)^[72].

Other selective organometallic complexes include Ni(II)-salphen **7** ($\Delta T_m=33^\circ C$)^[73] and Cu(II)-terpyridine **Cu-ttpty** ($\Delta T_m=15^\circ C$)^[74], but a variety of polypyridyl and phenanthroline based complexes gave also promising biological activity^[75]. The geometry of metal centre is a key parameter to consider as it was shown to have a remarkable effect on governing the selectivity. For instance, the copper atom in **Cu-ttpty** displayed a square pyramidal geometry, with a nitrate anion at the apical position, thus disfavouring intercalation between *ds*-DNA nucleobases.

Bisquinoline and bisquinolinium compounds

In 2002 Mergny identified by FRET-melting experiments a new class of G-quadruplex ligands containing both quinoline and triazine structural motifs that also exhibited potent and specific *in vivo* anti-telomerase activity with $^{Tel}IC_{50}$ lying in the nanomolar range of concentrations^[76]. Among these, triazine **8** was the most studied. Telomerase downregulation was found to be mediated by G4 formation in hTert RNA, the transcript of the telomerase-coding gene, inducing an alternative splicing pattern^[77]. Triazines were rapidly replaced by the emergence of a structurally-related bisquinolinium series containing a 2,6-pyridodicarboxamide (PDC) core. In particular, **PDC 360A** exhibited a high G4 stabilization ($\Delta T_m=21^\circ C$), excellent selectivity (> 150-fold) and efficient telomerase inhibition ($^{Tel}IC_{50}=300 \text{ nM}$)^[78]. The accepted explanation for the outstanding recognition ability displayed for quadruplex DNA accounts for the preferred *syn-syn* conformation adopted by the central PDC unit which benefits of two intramolecular hydrogen bonds. The geometry of the ligand is therefore locked in a V-shaped structure, which is highly favorable to maximize the overlap with G-quartets. The high affinity of PDC derivatives for quadruplex DNA was confirmed by their remarkable ability to induce the challenging formation of tetramolecular G4s, suggesting the possibility of acting as molecular chaperones^[79]. Moreover, **PDC 360A** was found to localize preferentially at telomeric regions of chromosomes, providing one of the first evidences of quadruplex existence in a cellular context^[80].



Scheme 4: Bisquinoline and bisquinolinium compounds used as selective G4 binders.

Closely related to this family is the nonmethylated bisquinoline derivative **Pyridostatin** (sometimes abbreviated with **PDS**), reported by Rodriguez in 2008^[81]. Three primary amine moieties ensured water solubility and additional electrostatic interactions, while isomeric quinolines were attached to the PDC core. The compound showed both exceptional affinity and selectivity for quadruplex DNA. The *in vitro* ability of promote POT1 uncapping from telomeric overhangs ($^{POT1}IC_{50}=200$ nM) was accompanied by an impressive $\Delta T_m=35^\circ\text{C}$ in 60 mM K⁺ at 0.18 μM of ligand. For comparison $\Delta T_m=30^\circ\text{C}$ in 60 mM K⁺ at 1.2 μM of **Telomestatin**, the most potent natural occurring G4 small molecule^[82]. The great success of this small molecule is demonstrated by the large amount of studies that have used **Pyridostatin** and its conjugates for both *in vitro*^[83] and *in vivo*^[84] applications, pull-down^[85] and G4-sequencing^[9]. It is currently used as a benchmark compound for unravelling G4s biological role^[3, 86, 87].

The natural extension of this family of ligands was achieved by substitution of the central pyridine ring with a phenanthroline, yielding the compound known as **Phen-DC3**^[88], whose structure is strongly resembling that of a G-quartet (Figure 12). Remarkably, this is still one of the strongest G4-interacting small molecule available, as it exhibits exquisite *in vitro* potency. Moreover, the selectivity of **Phen-DC3** is higher than that of **Telomestatin**,

confirming the great potential of the bisquinolinium compounds, which represent an ideal compromise between rapid synthetic access and efficient target recognition.

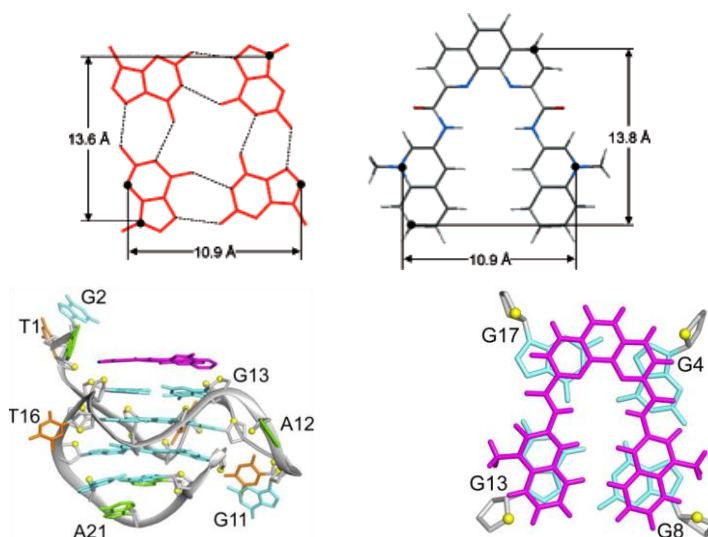


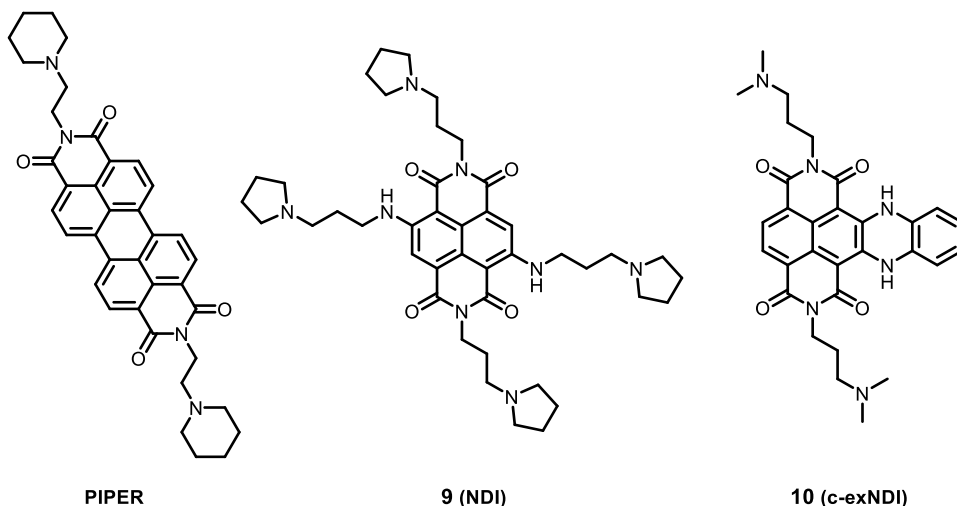
Figure 12: (above) Dimensions of a G-quartet (determined from X-ray structure) and **Phen-DC3** (after molecular mechanics MM2 calculations). (below) Lateral and top view of the NMR solution structure of the complex between **Phen-DC3** and c-myc derived G-quadruplex Pu24T (PDB ID: 2MGN)^[89].

Perylene and naphthalene diimides

In 1998, Hurley reported the perylene diimide **PIPER**^[90] (Scheme 5), characterized by an extended hydrophobic aromatic core with two external protonable side chains, as an effective telomerase inhibitor ($T^{el}IC_{50}=20\ \mu\text{M}$). An NMR structure indicated that **PIPER** binds by stacking onto the terminal tetrads. Moreover, it has shown to induce the formation of a quadruplex from the hybridized double stranded sequence Pu27 of the c-myc promoter region^[91].

Due to the severe aggregation properties of perylenes water solubility was a major issue. Conversely, smaller arylene naphthalene diimides (NDIs), like tetrasubstituted NDI **9**, found a wider application as G4 binders. First reported by Neidle^[92] and later extensively studied by Freccero^[93], those compounds are excellent G4 binders, although they suffer of lack of specificity with increasing the number of positively charged moieties. Compared to the twisted conformation of perylene diimide cores, NDIs are planar, an important feature for G4 end stackers. Additionally, the NDI scaffold is easily functionalized and a number of

different heteroatoms can be directly attached in the naphthalene core. These substituents exert a marked effect on the electronic energy levels of NDI and provide the means to fine tune its optoelectronic properties. In particular, donor substituents decrease the HOMO–LUMO gap while increasing both HOMO and LUMO energies. This, combined with the high structural variability and their intrinsic fluorescent properties, made NDIs a powerful tool to efficiently target quadruplex DNA and design new G4 selective probes^[94–96].



Scheme 5: Structure of selective perylene and naphthalene diimides

More recently, Freccero reported a new class of core-extended naphthalene diimides (c-exNDIs), such as c-exNDI **10**, with a peculiar selectivity for the G4 found in the LTR promoter of HIV-1 retrotranscript^[97]. The same derivatives have been also used as aggregation mediated G4 light up probes^[98, 99].

Telomestatin and related oligo-heteroaromatic ligands

Telomestatin is a natural product, isolated from *Streptomyces anulatus*, which possesses a unique structure incorporating one thiazoline and seven oxazole rings in a macrocyclic oligomeric array. Currently it is one of the most potent and specific inhibitors of telomerase ($IC_{50} = 5 \text{ nM}$)^[100]. The observation that its structure might behave similarly to a G-tetrad and efficiently stack on the top of it led to the discovery that **Telomestatin** selectively stabilizes the formation of an intramolecular G-quadruplex from the human telomeric d[TTAGGG] repeat sequence ($\Delta T_m = 24^\circ\text{C}$)^[32] and suggested that stabilization of ss-DNA alternative structure could sequester telomerase natural substrate. In addition, owing to its neutral

macrocyclic nature, this compound displays almost no affinity for ds-DNA, and a 70-fold selectivity for intramolecular telomeric G4^[101]. Additionally, long-term treatment of different telomerase-active cancerous cell lines with **Telomestatin** at non-cytotoxic concentrations induced telomere shortening and growth arrest, eventually causing apoptosis^[102, 103]. Outstandingly, **Telomestatin** exerted anti-cancer activity also in telomerase-negative tumor cell lines by triggering the uncapping of proteins such as POT1 and TRF2 in the shelterin complex, and exposing telomers to degradation^[104].

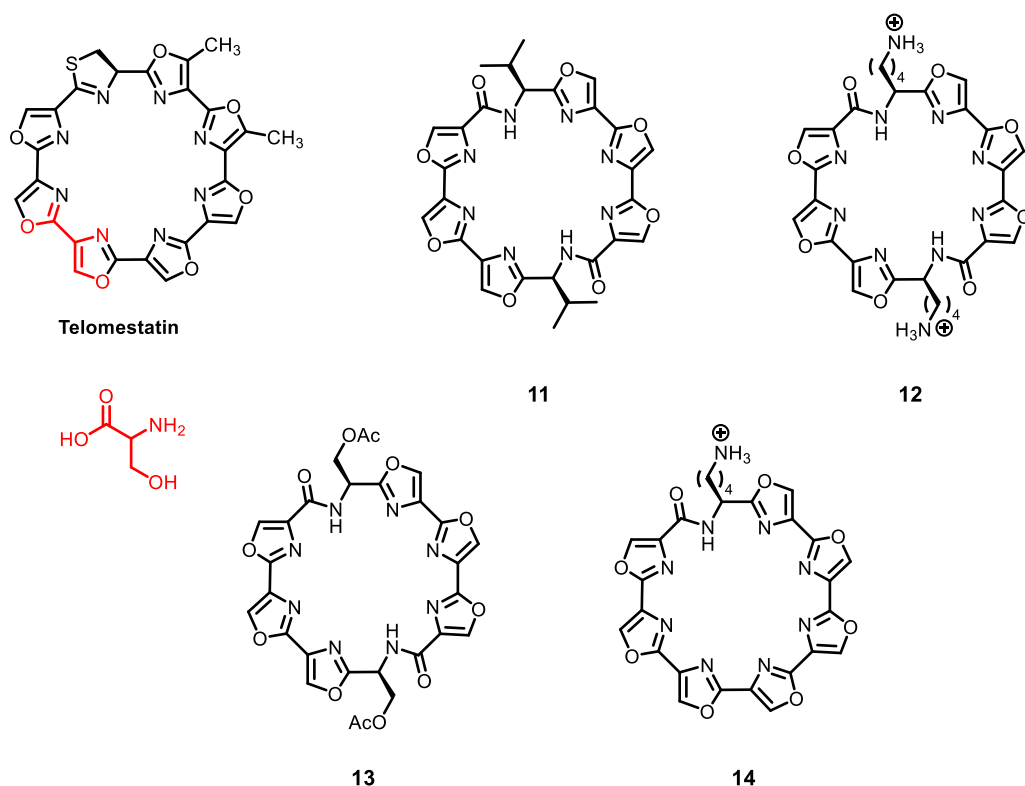


Figure 13: Structure of **Telomestatin** and its macrocyclic hexa- and heptaioxazole analogues **11-14**.

Up to now, **Telomestatin** still represents one of the most selective and powerful G4 ligands, which combines excellent *in vitro* G4 binding capacity with high *in vivo* biological potency. Recently, its total synthesis was achieved^[105-107], yet the low yield of the multi-step procedure makes a large-scale production process cost prohibitive. However, thanks to its synthesis, (S)-telomestatin interestingly exhibited enhanced potency compared to the natural enantiomer, (R)-telomestatin^[108].

The unique 24-membered hepta-oxazole structure has spawned effort on the synthesis of a number of macrocycles containing from three to seven oxazole rings, either linked directly or via amide bonds^[109-113]. Macrocyclic hexaoxazoles **11-14** (Figure 13) have been synthesized starting from amino acids, as it was noticed that connected oxazole rings embedded a serine backbone^[114]. Two trioxazole units were thus linked and cyclized with two peptide bonds through L-valine, L-acetylserine and L-lisine residues^[111], respectively. Detailed studies on the complex between **11** and d(T₂AG₃)₄ telomeric G4 uncovered an unusual, entropically driven end stacking binding mode^[115]. The driving force reflected favorable drug-induced alterations in the configurational entropy of the host quadruplex, as loop adenine nucleobases commonly engaged in stacking interactions were effectively displaced.

Moreover, NMR studies of the complex between **12** and d(T₂AG₃)₄ telomeric G4 highlighted a mixed binding-mode^[116]. In particular, the structure (Figure 14) evidenced an optimal fitting between the aromatic surface of the ligand and the external quartet, the ionic interaction of the protonated lysine-residues and the phosphatidic-backbone, and the additional accommodation of a potassium ion coordinated by the end tetrad and the nitrogen binding cavity of the ligand. All these observations accounted for the impressive affinity of **12** for telomeric G4 ($\Delta T_m=49^\circ\text{C}$)^[111], which still maintained good selectivity over ds-DNA even though the added electrostatic interactions could potential be a source of unspecificity.

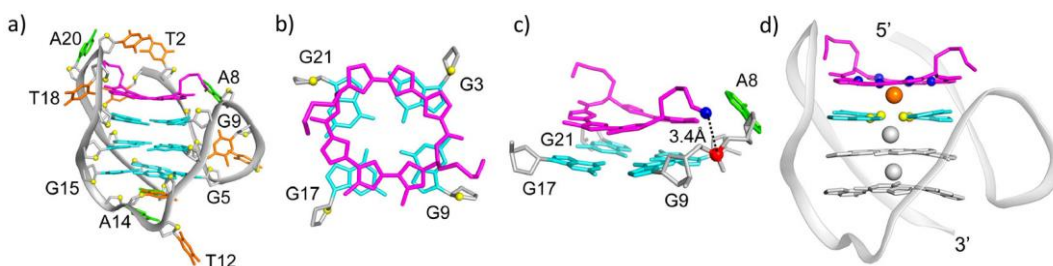
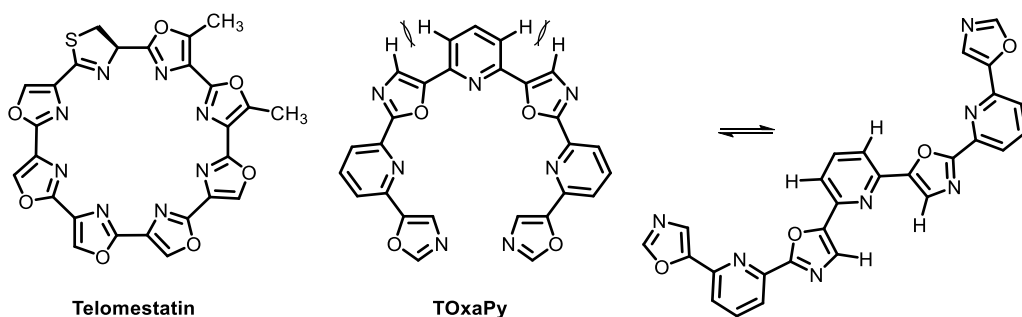


Figure 14: Solution structure of the complex between **12** and human telomeric G4^[116]. (a) Side view of a representative structure. (b) Top view showing the effective stacking. (c) Magnified side view showing the close proximity between one cationic side chains of **12** (shown as blue sphere) and the anionic phosphate group of A8 (shown as red sphere). (d) Side view showing the accommodation of an additional K⁺ ion between the ligand and the end tetrad. Color legend: magenta, **12**; cyan, Guanine; green, Adenine; orange, Thymine; gray, backbone and sugars; blue, nitrogen atom; red, phosphorus atom; yellow, oxygen atom.

However, despite the structural similarity, the *in vitro* potency of these macrocyclic analogues is still far from being comparable to that of telomestatin. In fact, hexaoxazole **13**

and heptaoxazole **14** revealed inhibition of telomerase with $IC_{50}=2\mu M$ and $IC_{50}=0.67\mu M$ ^[117] respectively.

Although the macrocyclic nature of **Telomestatin** is recognized to dominate the interaction with quadruplex structures and to determine its selectivity, Teulade-Fichou developed a class of compounds featuring a neutral nonmacrocylic oligomeric scaffold with alternate oxazole and pyridine motifs^[118, 119]. Interestingly, the heptacyclic derivative **TOxaPy** (Scheme 6) displayed no affinity for duplex DNA and exhibited an unprecedented binding preference for antiparallel quadruplex topologies (Figure 15a vs b).



Scheme 6: Structures of **Telomestatin** and derived open-chain **TOxaPy** analogue.

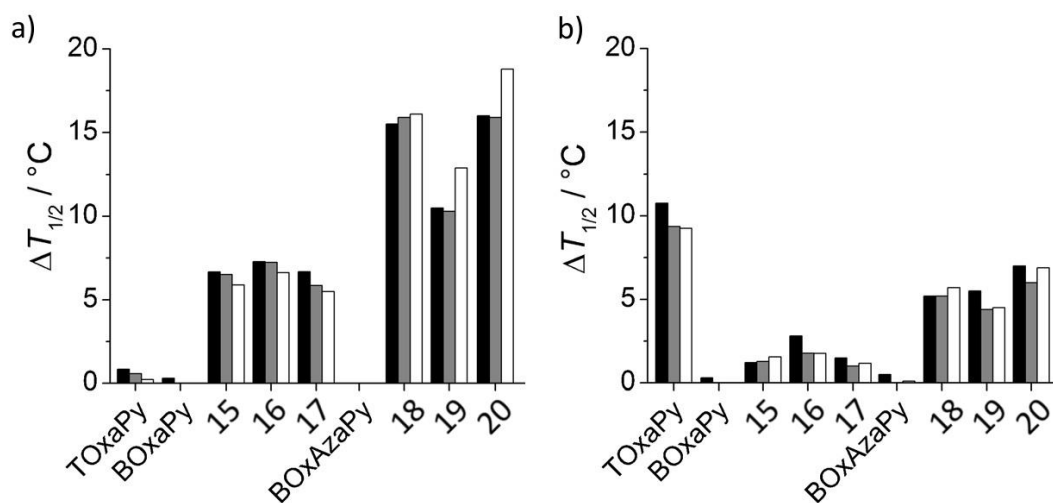


Figure 15: FRET-melting assay results for some open-chain oligoetheroaryls and telomeric quadruplex (F21T). Melting stabilisation in the absence (black bars) or presence of double-stranded DNA (ds26) at 3 μM (grey bars) or 10 μM (white bars) in (a) K^+ and (b) Na^+ .

Notably, docking studies supported a probable groove binding mode for the compound in its open conformation (Figure 16). Besides the high flexibility distinctive of the oligoaryl scaffold, the energy of the bent conformer was raised by the steric repulsions experienced by 2-2' aryl hydrogens (Scheme 6), thus prejudicing π stacking with the external tetrads. Considering the high diversity of grooves for shape and dimension within different G4 classes, such an unusual binding mode was addressed as the essential source of the observed topological selectivity.

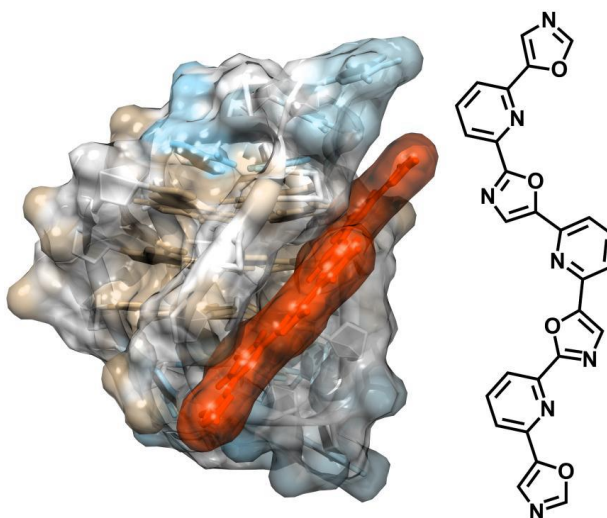
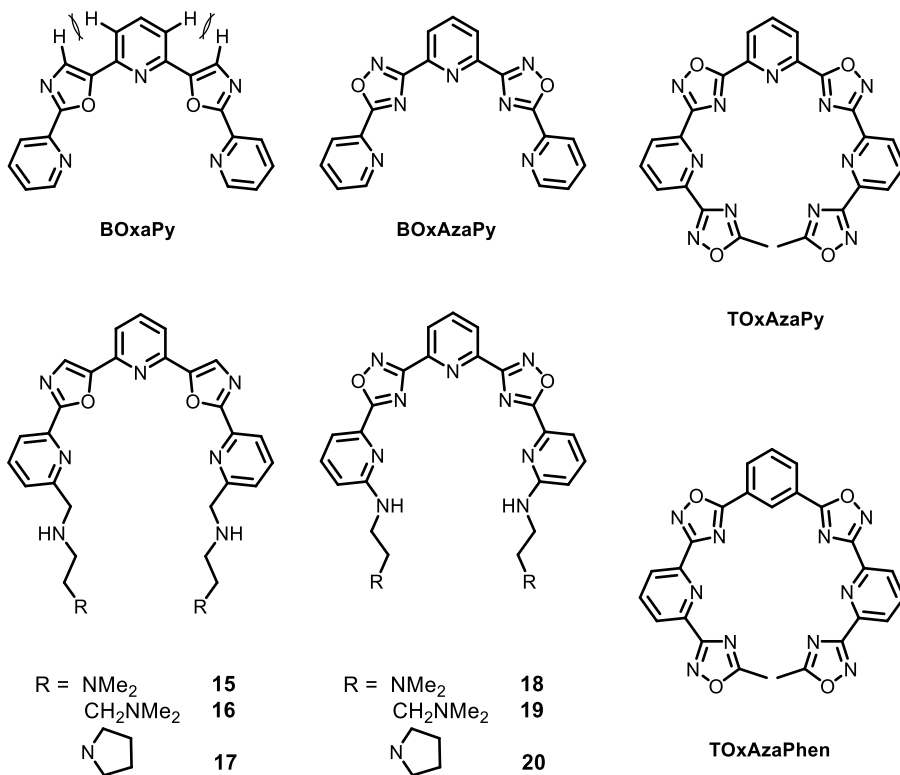


Figure 16: Proposed binding mode of **TOxaPy** with antiparallel 22AG (Na⁺-rich buffer) after docking optimization, and structure of the bound conformer. PDB coordinates: 143D.

The potential of such acyclic derivatives raised the interest on establishing which structural features were controlling their binding properties. For instance, it was shown that the length of the oligomeric scaffold was a factor strongly affecting target recognition, as the shorter pentacyclic **BOxaPy** (Scheme 7) did not bind to the quadruplex at all (Figure 15). However, a remarkable improvement in the binding of the pentacyclic scaffold was observed by incorporation of cationic side-chains. Substitution of the oxazole rings with 1,2,4-oxadiazoles yielded the pentacyclic derivative **BOxAzaPy**. This compound was designed to erase the H-H steric repulsions of the bent conformer, and to mimic the nitrogen binding cavity of telomestatin. Paralleling its oxazole analogue, the neutral pentacycle showed substantially no affinity for quadruplex structures, whereas derivatization with cationic pendals improved the binding properties of the scaffold. Overall, the **BOxAzaPy** family **18-20** proved to be best

performing than the BOxaPy family **15-17** in terms of quadruplex melting stabilization, and both classes manifested an opposite preference for quadruplex topology when compared to **TOxaPy**. However, based on the FID assays it was concluded that the binding mode of all the oligoaryls synthesized differed from the usual π stacking. The suggested rationale for these findings was the highly flexible structure, which is well-suited for good accommodation and interaction with grooves and loops.

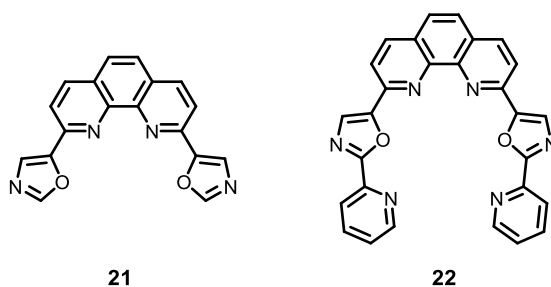


Scheme 7: Structures of oligo-heteroaromatic penta- and heptacyclic derivatives.

The benefits observed in the oxazole–oxadiazole exchange in the pentacyclic compounds prompted the synthesis of heptacyclic analogues **TOxAzaPy** and **TOxAzaPhen** (Scheme 7). The compounds still showed high selectivity for G4s over duplex DNA, but the observed enhancement in the melting stabilization temperature for the mixed topology of 22AG in K⁺ ($\Delta T_m=11.6$ and 10.8 respectively) was less pronounced than for the antiparallel conformation of 22AG in Na⁺ ($\Delta T_m=14.1$ and 16.9 respectively)^[120].

Despite the general improvement of target affinity, such a substitution led to a detrimental effect on the topological selectivity. Unfortunately, as the binding mode was not unraveled, it is not clear yet if this was a consequence of a change in the targeted G4 feature or the formation of specific bond interactions. Curiously, substitution of the central pyridine ring with a benzene did not affect the binding, meaning that the nitrogen atom was not playing a fundamental role in the binding.

More recently, similar phenantroline-bis-oxazole ligands **21** and **22** were shown to discriminate among various quadruplex topologies, although an end-stacking binding mode was proposed^[121].



Scheme 8: Structure of phenantroline-bis-oxazole ligands **21** and **22**.

Additionally, inspired to the linked monocyclic aromatic concept, Moses reported the synthesis of a family of triazole-containing ligands which exhibited excellent selectivity and good (although low) quadruplex stabilizing properties (Figure 17). Molecular modeling studies showed that bifunctional compounds like **23** display a cooperative mixed binding mode, in which the central planar system interacts with the external tetrad, while the side chains lie in the grooves created by the loops^[122, 123]. Conversely, π stacking interactions with C₃-symmetrical tris-triazole ligands like **24** are prevented by hindering hydrogens on sp³ carbons, but suggested groove binding interactions with the three side chains have been supported by modelling studies^[124].

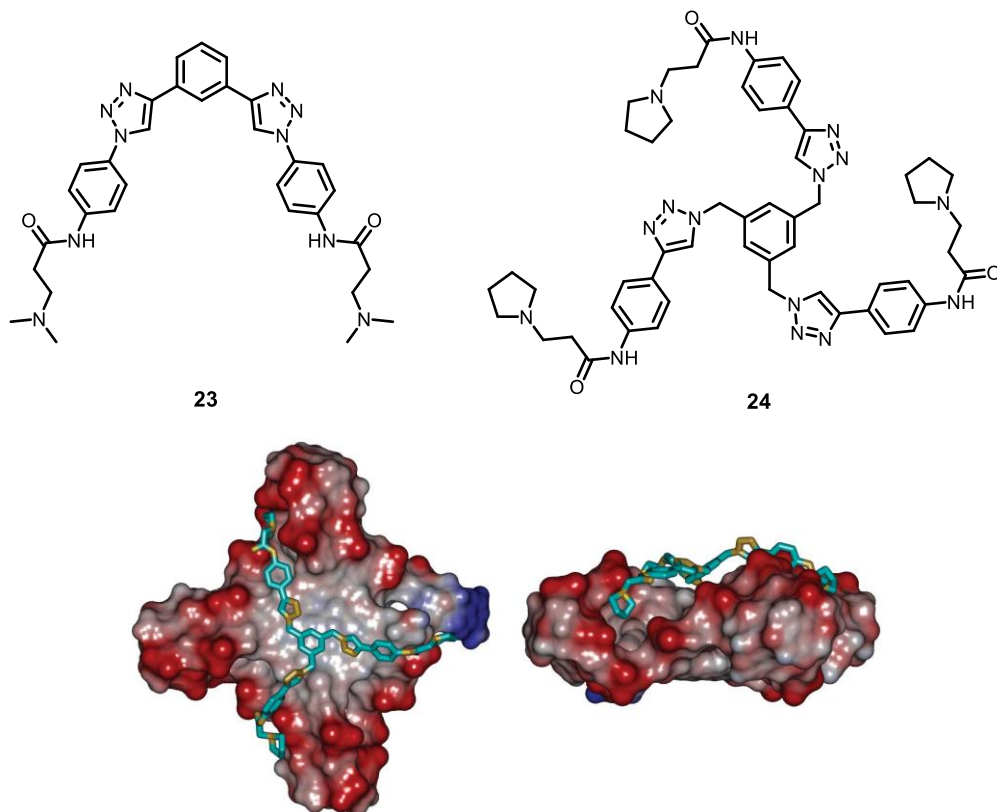
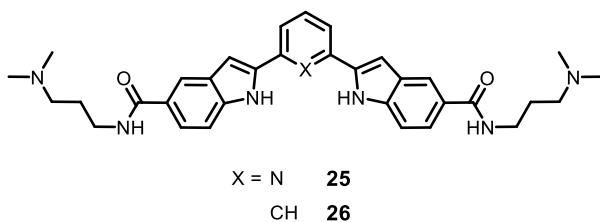


Figure 17: Structure of triazole-containing ligands **23** and **24**. Top and side view of a molecular model of the complex between **24** and parallel human telomeric G-quadruplex.

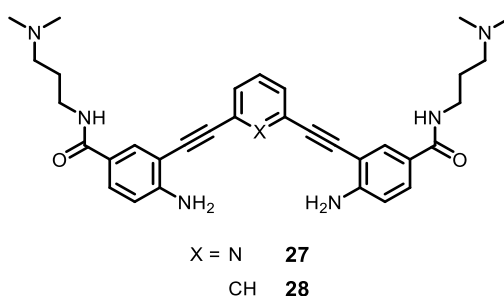
Two bis-indole carboxamides reported by Balasubramanian^[125] **25** and **26** can be included in the same category of oligo-heteroaromatic scaffolds. These compounds exhibited high stabilization of quadruplex DNA sequences associated with the c-kit2 and c-myc promoters. Also in this case the experimental evidences were discarding an end stacking binding mode for both compounds.



Scheme 9: Structures of bis-indole carboxamides.

Arylethynyl derivatives

Two synthetic intermediates of indoles **25** and **26** were the two bis-phenylethynyl amide derivatives **27** and **28**. Besides the rather different structural motif, these compounds showed good affinity for quadruplex DNA and unexpectedly exhibited a preference for the parallel conformation^[126]. Owing to the free rotation around their triple bonds, the high conformational flexibility of these compounds enabled G4 recognition through groove binding, as confirmed by NMR titrations. Besides the excellent selectivity for the quadruplex over the duplex, the uncommon binding mode was confirming a potentially promising discrimination between different G4 topologies.



Scheme 10: Structures of bis-phenylethynyl amide groove binders.

1.1.4 Targeted covalent modifications of G4

Although the great number of compounds that have been designed and used to effectively target G-quadruplex DNA, structural recognition is almost exclusively achieved through intrinsically weak noncovalent secondary interactions, which means that the binding is reversible. As a consequence, these ligands must be particularly selective to maintain the interaction with their target in a complex biological environment^[127]. Reasonably, a substantial improvement of the biological response is expected from compounds which, besides the capacity of targeting the G-quadruplex, own the ability of forming a covalent bond with it, giving rise to an irreversible immobilization on the structure. Moreover, selective alkylation could trigger the population of a single G4 conformer in a polymorphic sequence^[128] and have a strong impact on the biological response. Also, it should not be excluded the possibility of creating a damage that is not efficiently repaired by DNA repair

enzymes, which would promote strand breaks, gene deletion and eventually cause apoptosis^[129].

The first G-quadruplex irreversible ligand was described by Teulade-Fichou^[130] in 2007. **Pt-MPQ** was inspired on known DNA platinating agents and consisted in a quinacridine scaffold embedding a monofunctional platinum moiety. Such a study provided the first example of *in vitro* selective platination of quadruplex DNA over duplex DNA. Subsequent studies on platinum complexes derived from the terpyridine structure showed that the platination can be non-specific and generate off-target reactivity^[70]. Indeed, while the compound **Pt-tpty** selectively platinated adenines present in one of the G-quadruplex loops resulting from the human telomeric sequence 22AG^[131] and at the 5'-end overhanging region of short propeller-type parallel Myc-22^[132], the compound **Pt-tpty** platinated indifferently the most reactive base of the sequence without particular recognition of the structure, and the extended complex **Pt-BisQ** shown no covalent reactivity, probably being too congested to interact with the G-quadruplex structure^[131].

Another example of G4 metalation was described by Mergny^[128], who obtained a mercury (II) – thymine crosslink (T-Hg-T) between two lateral loops. However, the use of selective targeting complexes using mercury chemistry was not shown.

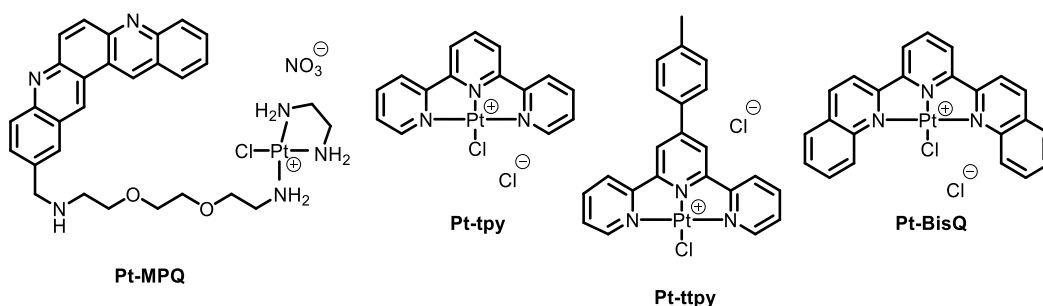
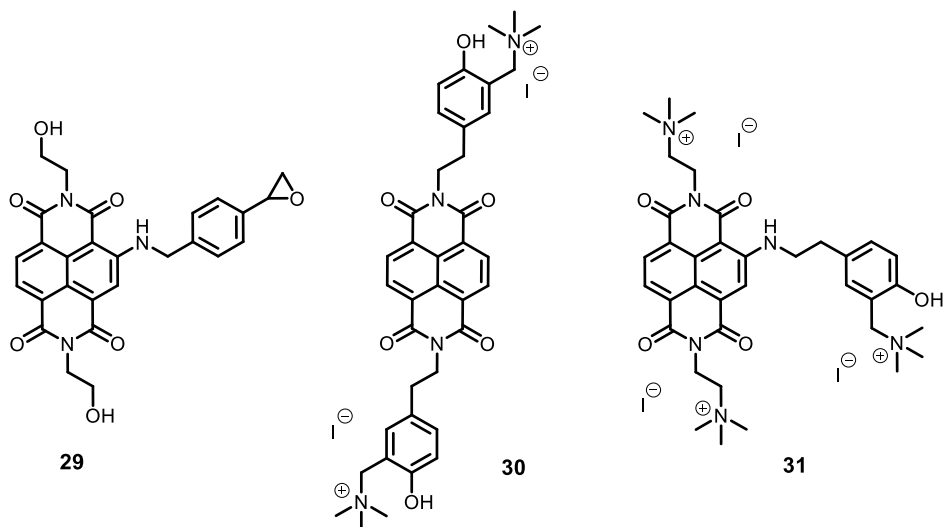


Figure 18: Platinum complexes with dual reversible/irreversible binding mode targeting G4.

An important class of ligands with covalent activity combines a G-quadruplex selective ligand with an alkylating agent. Belonging to this class are the hybrids ligand-alkylating agent developed by Freccero, which possess a binding naphthalene diimide core tethered to an electrophile, such as an epoxide^[133] (Scheme 11), or a chemically activatable electrophile precursor, such as quinone methide precursors^[134, 135] (for a detailed discussion on quinone

methides see Section 1.2). However, such derivatives did not exceed 15% of capture efficiency, a feature that has been associated to thermal reversibility of the covalent adducts with DNA.



Scheme 11: Structure of NDI–electrophile conjugates for G4 alkylation investigated by Freccero.

Based on the same idea, Balasubramanian combined **Pyridostatin** to a nitrogen mustard, namely chlorambucil, a well-known DNA alkylating agent that inhibits cell proliferation (Figure 19)^[129]. The typical reactivity of chlorambucil is characterized by highly toxic inter-strand cross links (ICLs) that induce double strand break formation and lead to inhibition of cancer cell proliferation, but can cause undesirable secondary malignancies in healthy cells. Additionally, poor DNA recognition accounts for its off-target alkylation. These features were shown to be strongly influenced by the targeting properties of the PDS core. In fact, the PDS-chlorambucil compound **32** was shown to form stable covalent adducts with the G4 structures Myc-22 and 22AG *in vitro* and at very low concentrations (< 5 μM), with good selectivity over double-stranded DNA. Overall, the addition of the targeting unit prevented the generation of toxic ICLs by preferential intrastrand cross-linking of single-stranded DNA *via* selective G4 recognition. As a dominating DNA damage which is efficiently repaired by a dedicated nucleotide excision repair (NER) enzyme, this molecular tool has been proposed to enable depletion of cell proliferation in NER-deficient cancers.

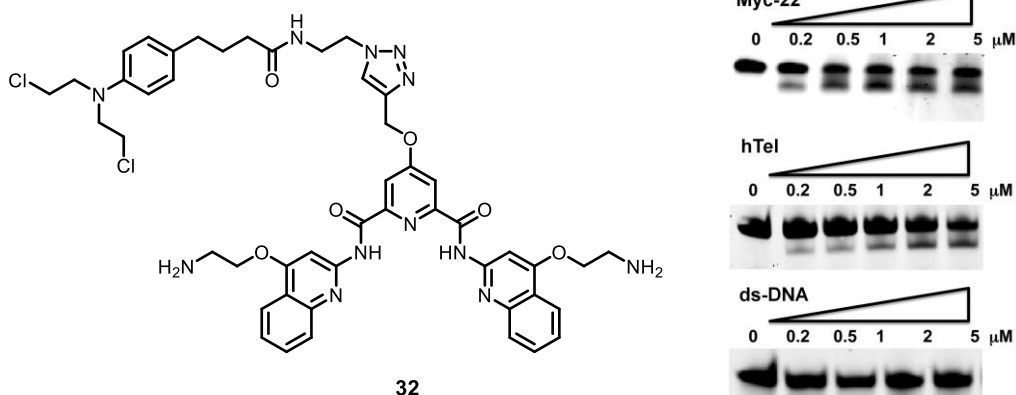


Figure 19: Structure of PDS-Chlorambucil conjugate **32** and *in vitro* selective alkylation of Myc-22 and hTel versus ds-DNA.

An innovative strategy following these models is based on the conjugation of a G-quadruplex ligand to a photoactivatable alkylating agent, which could allow spatial and temporal control over the effective alkylation event. Such photoactivatable G-quadruplex ligands were first obtained by Teulade-Fichou by tethering the PDC binding motif to a photomarker, benzophenone or tetrafluoroarylazide, through various spacers (Figure 20)^[136].

The conjugates **33-38** retained high quadruplex vs duplex selectivity, and alkylation of 22AG and Myc-22 G-quadruplexes was effectively achieved *in vitro*, leading to their irreversible trapping. Moreover, selective alkylation of specific nucleobases depended on G4 sequence and topology and appeared to be strongly influenced by the spacer length and the nature of the photomarker used. The cellular assays were also promising since toxicity was triggered by near-UV/vis irradiation, although there is no proof that the actual target is a G4. Besides its potential use in the development of next generation highly selective therapeutic drugs, the strategy was shown to be exploitable to generate effective G4 photolabelling tools.

Following the same photochemical strategy, Freccero developed a photoreactive molecular dye (Scheme 12) targeting the human telomeric G4 sequence hTel22 by green light activation (532 nm)^[137]. Highly selective covalent modification of G4 versus ss-DNA and ds-DNA was achieved with an outstanding efficiency of 64%. Generation of a reactive phenoxy radical was detected by LFP, and was promoted by electron transfer from the light-harvesting NDI.

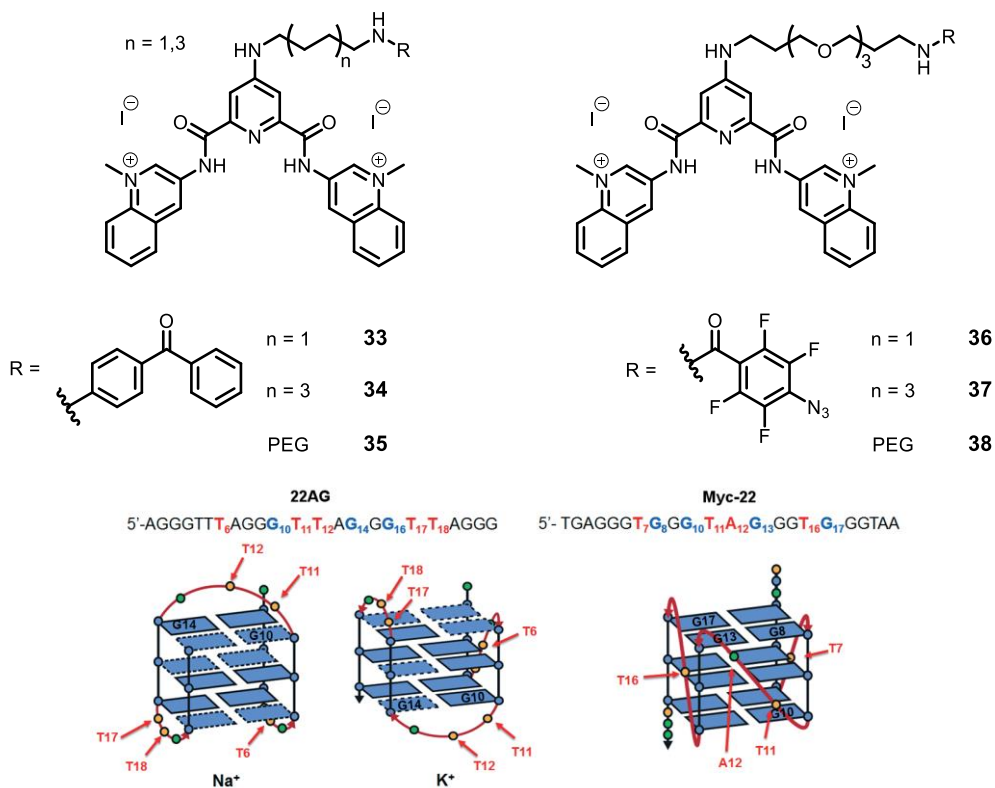
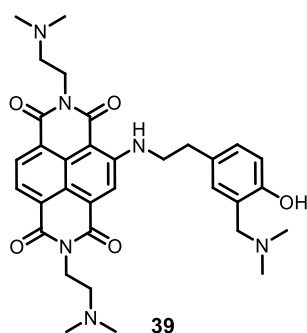


Figure 20: Structure of PDC-photomarker conjugates studied. Schematic structure of 22AG in Na^+ and in K^+ buffers and Myc-22. In each case it is shown the alkylation sites targeted by PDC-photomarker derivatives. Legend: guanine = blue, thymine = yellow, adenine = green; syn = dashed square, anti = plain square; alkylated guanine residues are labeled in black, while alkylated nucleobases in the loops are highlighted with red arrows.



Scheme 12: Green light harvesting photo-alkylating agent.

Besides the intrinsic contribute to the overall stabilization of the G4 structure, the development of such irreversible binders can also be exploited for other in cell applications. For instance, fluorescent labelling of covalent adducts has been suggested as a strategy to

get more precise cellular imaging^[84]. Else, isolation of G4–DNA directly from cellular genome could be achieved by affinity pull-down, provided that the covalent link can be reverted.

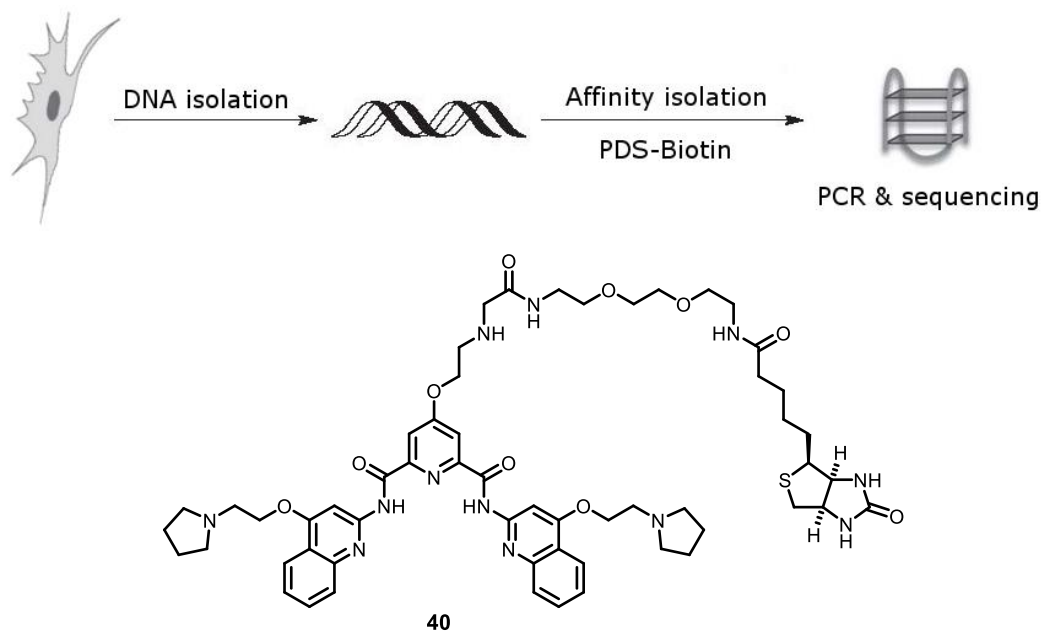


Figure 21: Validation of G4-folding sequences found in genomic DNA with biotin-PDS conjugate **40**. In principle, a reversible covalent binder could allow the isolation of actual G4-forming sequences under the strict cellular context.

Recently it has been proposed that mapping of G4-folding DNA sites could be achieved by means of affinity isolation. The concept has been demonstrated *in vitro*, as G4-folding sequences could be isolated from a mixture of different oligonucleotides including ss-DNA, ds-DNA and hairpin RNA (Figure 21). In particular, the mixture was incubated with biotin-PDS conjugate **40** and separated by means of streptavidin-coated magnetic beads^[85]. The use of a G4 reversible binder was fundamental to assure the possibility to disrupt the complex upon thermal or chemical denaturing and recover intact DNA for PCR analysis and sequencing. So far, however, the method has been used with cell extracts only, a limit that could be overcome by using a covalent binder with a residual reversible character. Platinating agents would fail in the intent, as DNA could not be recovered due to the strength of the newly formed covalent bond^[130]. Conversely, the use of small molecules targeting G4 embedding reversible (e.g. by heating) alkylating agents would offer the best solution to the encountered technical limits.

1.1.5 Biophysical evaluation of small molecule – G4 affinity

A number of biophysical methods have been employed to characterize ligand-G4 complexes and study the interactions of natural and synthetic compounds with quadruplex DNA [138]. These techniques span from high throughput simple methods, used for a quick screen and for obtaining a qualitative information on ligand affinity, to more sophisticated and time-consuming ones, from which kinetic, thermodynamic, stoichiometric and structural information could be derived and used for fine structure-activity correlations.

The key challenge of G4 nucleic acid targeting is the selectivity for quadruplex structures in comparison to duplex DNA. Hence, the biophysical and biochemical methods that are commonly used to investigate ligand-DNA interactions need to take this fundamental aspect into account. In the case of qualitative screening assays the most reliable way to achieve such an information often implies to perform competition experiments, in which the assay output is evaluated in the absence and in the presence of a competitor *ds*-DNA.

Each technique has its own advantages and disadvantages and the right choice depends on the individual case. Often more than one method are needed to obtain a complete picture of the G4-ligand interactions.

In the following paragraphs some of the most frequently used techniques and assays to characterize G4 ligands are described.

NMR and XRD

Because of the high degree of structural polymorphism that characterize quadruplex DNA, it is important to determine the actual ligand binding site and its mode of interaction at molecular level. A number of NMR spectroscopy and X-ray diffraction studies have been successfully performed to resolve the structures of various G4s and their complexes with ligands, allowing fine structural analysis of the interactions involved in the recognition.

Ligand complexes with quadruplex DNA and RNA have been solved by X-ray diffraction spectroscopy and their structures are available in the RCSB protein data bank (PDB)^[139, 140]. The crystals are commonly produced by vapor diffusion with sitting or hanging drops in a solution that contains the cacodylate salt of a monovalent cation, 3–6 mM spermine, and 5–15% (v/v) of polyethylene glycol at pH 6.0–7.0. X-ray crystal structures are unambiguous, and

provide a definitive view of the location of the cations within the structure, the hydration within the grooves, and the binding mode of the ligand with the G4. However, it is possible that the crystal structure is not representative of the primary species in solution due to crystal packing forces and the crystallization conditions that may influence the structure.

Conversely, NMR spectroscopy provides the most complete structural data of G-quadruplexes and their complexes in solution^[141]. The dynamics of the interactions involved in the recognition process can be studied. In particular, NOESY experiments are used to determine the correlations between signals due to ligands and those attributable to nucleic acid, in order to determine the contact area. However, the complete structural determination requires a long and rigorous work, and its application is not always possible since it requires the prevalence of just one conformer in solution.

Even so, free G4 structural data together with *in silico* docking or molecular modeling analysis provide an important tool for the fast screening of compound libraries and could support the design of new interacting small molecules.

ITC and SPR

Only few techniques provide direct quantitative information on the thermodynamics and kinetics of interaction. Among these, the most extensively used methods are the isothermal titration calorimetry (ITC) and the surface plasmon resonance (SPR).

ITC is a powerful technique that allows the direct monitoring of many bimolecular binding interactions^[142]. Binding isotherms are used to determine thermodynamic parameters of interaction such as the binding enthalpy (ΔH) and entropy (ΔS) along with the binding constant (K_a) and the stoichiometry (n). However, it usually requires substantially more material than most spectrophotometric methods and may not be suitable for determining large binding constants.

Surface plasmon resonance (SPR) is a sensitive technique for characterizing G4-ligand interactions. In general, an intramolecular G4-forming oligonucleotide sequence is immobilized onto a thin metal film coated sensor chip. Upon interaction of a small ligand with a G4, a change in refractive index at the sensor surface occurs. The variation of the angle at which the minimum of reflected light density occurs is related to the interactions involving

the free species in solution and the G4 which is covalently bound to the surface. Based on this principle, SPR has been successfully used as a rapid and powerful tool for screening small molecule libraries allowing the measurement of both kinetic (k_{ass} and k_{diss}) and thermodynamic (K_a) parameters of interaction^[69, 143].

FRET-melting assay

The classical high throughput survey for studying small molecule – G4 interactions is the FRET-melting assay. In this experiment, pre-annealed oligonucleotide sequences capped with a couple of FRET fluorophores, commonly a carboxyfluorescein reporter (FAM, $\lambda_{\text{max,exc}} = 495 \text{ nm}$, $\lambda_{\text{max,em}} = 520 \text{ nm}$) and a carboxytetramethylrhodamine quencher (TAMRA, $\lambda_{\text{max,exc}} = 546 \text{ nm}$, $\lambda_{\text{max,em}} = 583 \text{ nm}$) are incubated with the putative ligand. The emission is then monitored as the temperature is risen in the range between 25 and 95 °C. In the folded structure the two fluorophores are close in space, therefore FRET is effective and quenching is maximized. Conversely, in its unfolded structure, the mean distance between the two fluorophores is higher, FRET is less effective and quenching is minimized. By plotting the reporter emission *versus* temperature, a growing sigmoid is obtained and the curve's inflection point is defined as the melting temperature (Figure 22). The affinity of the ligand for its target is then related to the difference in the melting temperature (ΔT_m) of that particular structure in the presence or in the absence of the added compound.

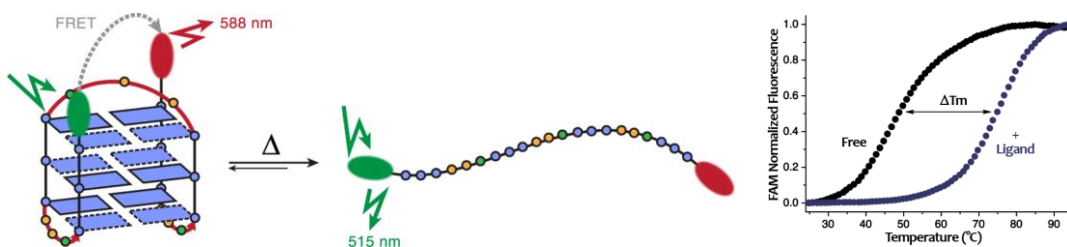


Figure 22: FRET-melting assay and definition of melting stabilization temperature. Legend: green dye = reporter = FAM; red dye = quencher = TAMRA.

Importantly, it is erroneous to relate the thermodynamics of a ligand-DNA complex (e.g. the binding constant, the enthalpy of formation) to the absolute value of melting stabilization temperature. The output response is a semi-quantitative measure of how much the guest stabilizes the host by their interaction, but it does not tell any information on the stoichiometry, the binding sites, or the actual energies of interaction. Moreover, different

structures have distinct stability, which is related to the absolute value of the melting temperature. In principle, the same binding interaction should have rather different impact on DNA motifs with diverse intrinsic stability. Therefore, the only straightforward conclusion that can be derived is the comparison between the affinity of different compounds for a given structure, and the effect of an added competitor to the selectivity of the tested compound for its target. Even so, the potency of this technique has to be assigned to its ease implementation in a microplate automated system and its employment as a high-throughput screening assay.

Fluorescent Intercalator Displacement

A simple method that aims at evaluating G4 binding affinity and quadruplex- over duplex selectivity of putative ligands is the fluorescence intercalator displacement (FID) assay, first described by Teulade-Fichou^[144]. This assay is based on the displacement of a fluorescence probe, namely thiazole orange (TO), from quadruplex and duplex DNA structures by increasing amounts of a putative ligand (Figure 23). Thiazole orange is virtually non-fluorescent in free solution, as a result of double bond isomerization and free rotor efficient excited state deactivation mechanisms. When it intercalates within *ds*-DNA nucleobases or stacks on the external quartets of a G-quadruplex these quenching mechanisms are no more available due to the planar geometry constriction and, as a result, the compound becomes strongly fluorescent with up to 1000-fold increase.

Provided that the binding mode of the putative ligand should be the same of thiazole orange (i.e. end-stacking), the addition of increasing concentrations of a candidate compound induces the displacement of TO, and hence a related decrease of its fluorescence. Therefore, by means of simple fluorescence titration, the affinity of the compound for a G4 can be evaluated through its ability to displace TO. Additionally, by comparing the ability of the ligand to displace TO from various G4s and *ds*-DNA structures a measure of its selectivity could be inferred. Moreover, substitution of TO with related cyanine analogue TO-PRO-3 or Hoechst 33258 enables the screening of compounds with optical properties overlapping those of TO and may interfere with the assay^[145].

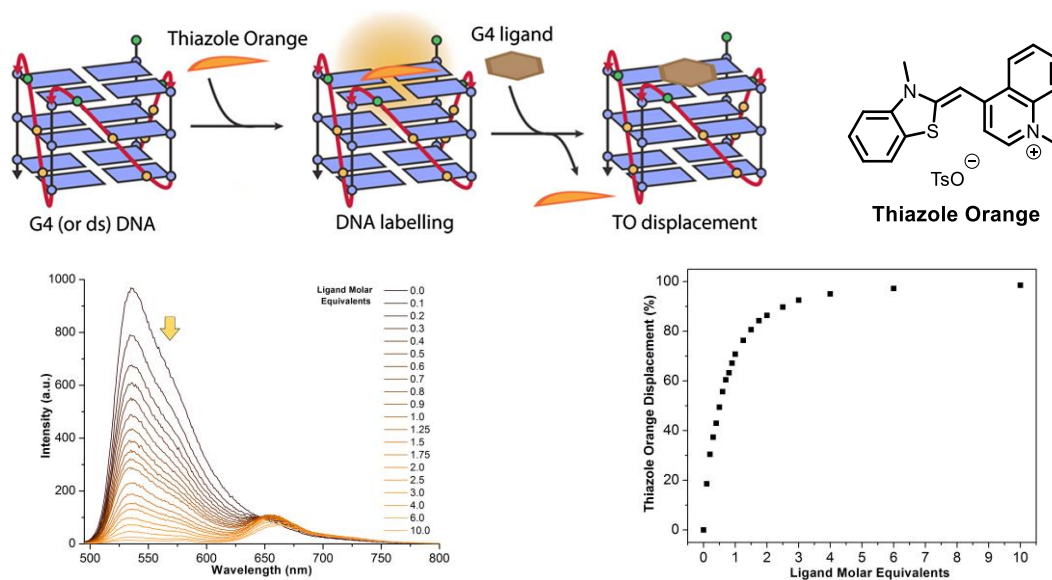


Figure 23: Principle of G4-FID assay. Thiazole orange fluorescence quenching upon competitive ligand addition.

Based on this concept, high throughput modifications of the FID assay have been derived and used to screen large libraries of compounds^[146-148]. Unfortunately, the higher limitation of this technique is its susceptibility to false positives or negatives due to indirect competition and quenching effects not relevant to G4-binding. Particularly, false negatives are frequently encountered when the compound binding mode is not well defined and differs from that of TO. For this reason, the use of FID often should be corroborated by other techniques (e.g. FRET-melting, ITC, SPR or CD titrations).

Recently, a new turn-off fluorescent quadruplex DNA probe has been designed as a fluorescent indicator. Its fluorescence is strongly quenched when bound to G4 DNA and fully restored when it is displaced by ligand^[149]. This probe improves the sensitivity of the G4-FID assay, as the read out relies on increased fluorescence instead of quenching observed with the classical probes. Moreover, the higher affinity for quadruplex DNA compared to TO makes this probe far more discriminating, resulting in a useful tool to distinguish good binders from excellent ones.

UV-Vis Spectroscopy

A simple method for studying ligand-G4 interactions involves the use of UV-Vis spectrophotometry. In fact, both DNA and ligand UV-vis spectra change in terms of band

shape and intensity. Usually melting temperatures are measured, providing a measure of the stabilization of the quadruplex structure induced by compound binding. Besides, these methods also provide useful information about the actual DNA-ligand interactions. For instance, a remarkable bathochromic shift and a hypochromic effect on the Soret band of cationic porphyrin **TMPyP4** was observed upon binding of a G4^[150]. This optical response has been proposed to arise from the strong interaction between the electronic states of the chromophore and DNA bases, indicating a stacking interaction between the **TMPyP4** molecule and the G4 structure.

However, the ligand spectrum often overlaps to that of DNA and this limits the use of absorption spectroscopy for measuring binding constants only by exploiting neat ligand absorption bands changes, which is definitely not a general remark. In addition, melting measurements are also often complicated by ligand superimposition. Therefore, absorption spectroscopy has been overcome by polarized light spectroscopy, which offers a more powerful tool for distinguishing between different supramolecular conformations and for which achiral small molecules are normally inactive.

CD Spectroscopy

Circular dichroism (CD) is a valuable tool to inquire the secondary structure of large biomolecules, especially proteins and nucleic acids^[151]. Optical activity arises when parallel molecular electric and magnetic transition moments (i.e. within a chiral molecule) can interact to produce a helical charge–redistribution path that can couple with the oscillating electric field of a circularly polarized light beam^[152]. DNA nucleobases are themselves achiral, but become chiral when placed within the framework of the chiral sugar–phosphate backbone, and CD signal arises from stereospecific coupling of near-degenerate electronic transitions (exciton coupling) of neighboring base chromophores. The quantum mechanical description of CD spectroscopy for molecules as large as DNA is very complex, and to date it is not possible to provide structural information at atomic level. For this reason, CD spectroscopy has been primarily used as an empirical technique to study DNA, but has received great attention for its high sensitivity, as sample concentration can be as low as 20 mg/mL^[151].

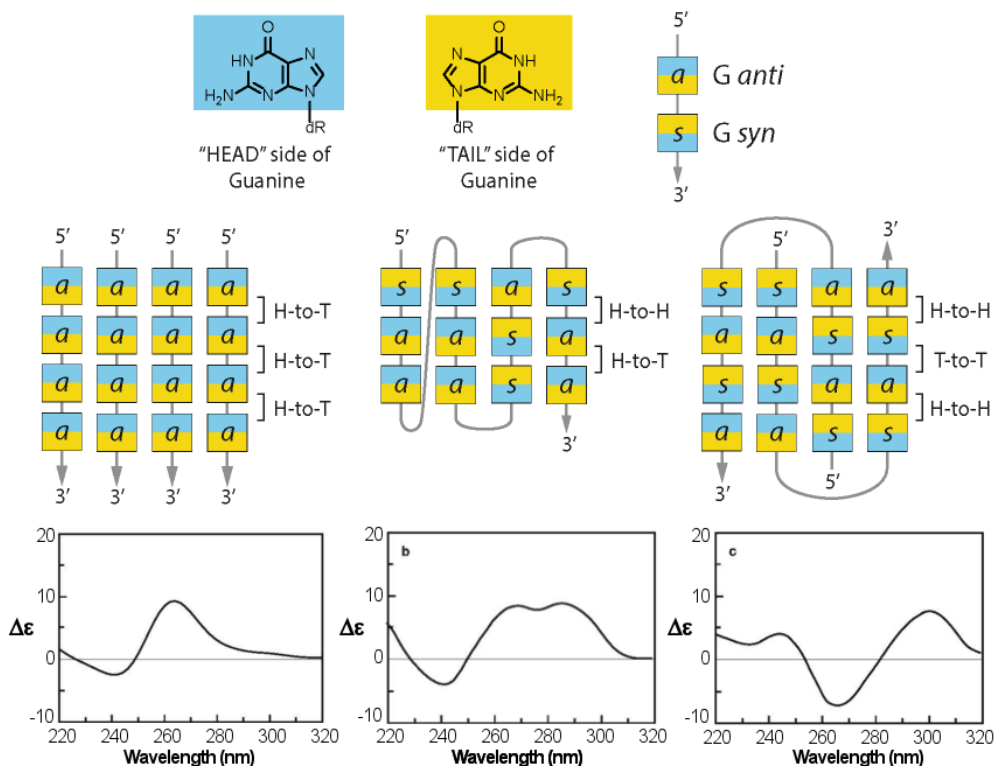


Figure 24: CD spectra resulting from different orientation of *syn*- and *anti*- guanines stacking interactions. All H-to-T stacking of the first type is characteristic for parallel G4 topologies (e.g. Myc-22). Alternate H-to-H and T-to-T stacking of the third type is characteristic for antiparallel topologies (e.g. 22AG in Na⁺ buffer). Mixed H-to-H and H-to-T stacking of the second type can be observed in hybrid topologies (e.g. 22AG in K⁺ buffer). Adapted from [153].

Circular dichroism has been extensively used for studying G-quadruplex folding topologies, ligand binding, the effect of cations, the kinetics of G4 formation and melting^[153, 154]. The sign and position of minima and maxima in a CD spectrum has been related to the relative orientation of guanine *syn* and *anti* conformation around the glycosyl bond in consecutive G-quartets (Figure 24)^[153]. However, most often in the literature CD spectra are interpreted empirically, on the basis of comparison with spectra of known G-quadruplex structures. Quite simplistically, for instance, a negative peak at 265 nm and a positive peak at 300 nm has been related to an antiparallel topology, while a negative peak at 240 nm and a positive peak at 265 nm has been reported to be the typical signature of parallel G4 structures. This have to be considered a rough approximation and must be handled with awareness on its limitations. Even so, regardless of conformational analysis speculations, melting experiments can be performed to obtain the melting stabilization temperature (ΔT_m) as a qualitative

measure of ligand affinity. Moreover, titrations of quadruplex DNA with ligand can be monitored at DNA ellipticity maxima yielding to binding constants extrapolation (Figure 25).

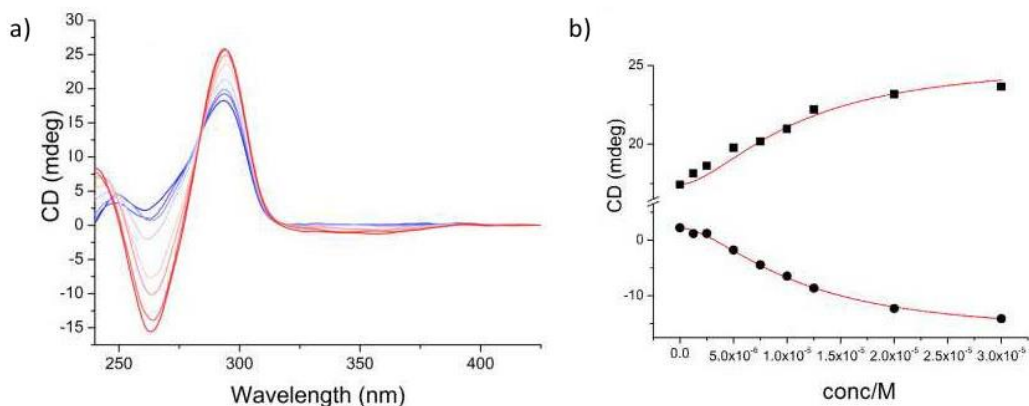


Figure 25: Change in CD spectra of a G4 observed upon addition of increasing concentration of ligand. Derived titration plots representing the change in ellipticity monitored at 292 nm (circles) and 260 nm (squares).

Induced Circular Dichroism

Since dichroism is a propriety that arises from supramolecular chirality, any achiral molecule should in principle be inactive by CD spectroscopy. However, as a consequence of binding, even an intrinsically achiral ligand could be affected by the surrounding chiral environment, so that an electronic transition that is localized on such molecule could become CD active. The dichroic signal is said to be induced by the host-guest complex formation and it is commonly referred as an induced CD (ICD)^[155]. For obvious reasons, to observe an ICD the molecule must absorb at that specific wavelength. Also, it is hard to assign an ICD signal below 310 nm due to nucleobase signal overlap. From a mechanistic point of view, the ICD signal can be caused by the stereospecific coupling of electric transition moments of the ligand and neighboring DNA bases^[156] or, much less frequently, can be due to an electronic transition which is delocalized over at least two fused ring systems arranged in a helical fashion^[82, 157] (Figure 26). The most intense ICD signals have commonly been associated with a binding mode that interests G-quadruplex grooves rather than the planar end quartets^[156]. However, it is now widely accepted that a variety of well-established stackers can give rise to ICD signals, and misinterpretation is often a risk.

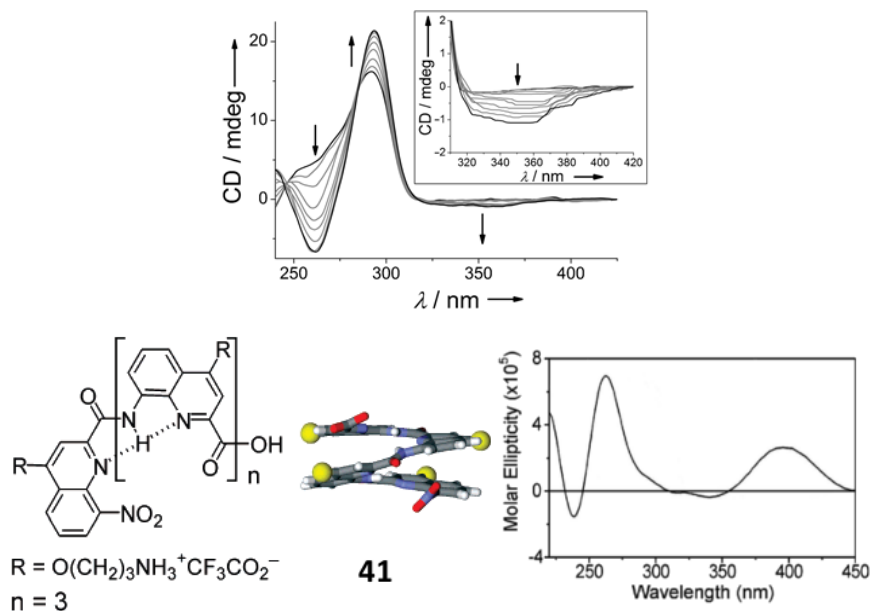


Figure 26: (above) Example of CD titration of a G4 with increasing concentration of ligand showing an induced CD signal at 360 nm. (below) Induced preferential handedness in helical oligomer **41** upon G4 binding, resulting in an intense CD signal at 400 nm.

Fluorescence Spectroscopy

Considering highly rigid large planar aromatic structures commonly needed to obtain selective targeting of G4s, the same compounds are quite often fluorescent. A number of studies take advantage of the intrinsic fluorescent properties of these ligands to extract binding constants.

Conversely, the intrinsic fluorescence of nucleobases is too low to exploit it for structural studies. Therefore, a suitable fluorescent reporter group needs to be incorporated in the polynucleotide structure to impart fluorescent properties. Highly fluorescent 2-aminopurine, an adenine analogue, has been widely used for this purpose by incorporating it in the loops of G4s. Its quantum yield, in fact, is highly sensitive to environmental conditions and can be used to probe for interactions between the quadruplex and a small molecule^[158]. In particular, its fluorescence intensity is affected by environment polarity and tends to increase with solvent exposure and decrease with base stacking. Accordingly, the overall fluorescence changes upon small molecule interaction in the proximity of the fluorescent modified base.

Mass Spectrometry

Electrospray ionization mass spectrometry (ESI-MS) is another useful technique for the characterization of non-covalent interactions between native DNA structures and small molecules^[159]. The studies are carried out using negative ion polarity in the presence of ammonium acetate buffer. Low source and capillary temperatures and low acceleration voltages in the transfer optics prevent disruption of the non-covalent interactions. Even though the actual measure is carried out in the gaseous phase, the qualitative results obtained are consistent with the interaction in solution. From a simple titration, with minimal sample consumption, it is possible to determine both the stoichiometry and the binding constant. Also, the selectivity for quadruplex DNA can be easily obtained by competition experiments with *ds*-DNA or even with different quadruplex structures. Competition of the compound under study with established ligands for the G-quadruplex can be used to assess its binding mode. In addition, this technique can be used to investigate binding kinetics.

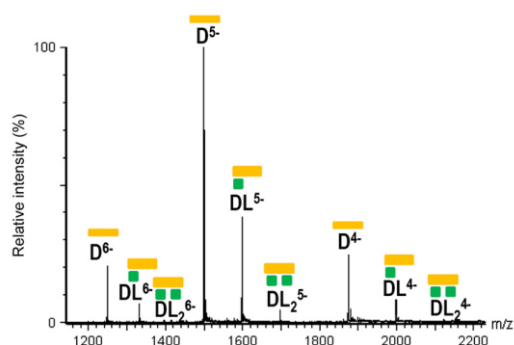


Figure 27: Typical electrospray MS spectrum of a DNA (D) – ligand (L) mixture, showing the presence of three species D, DL and DL₂ at three different charge states.

1.2 DNA alkylation

Drugs that form a covalent bond with their target have been extensively studied by molecular biology. For instance, a number of irreversible inhibitors targeting specific enzymes have been approved as treatments for diverse clinical indications and have made a major positive impact on human health^[160].

Since the initial application of such covalent modifications in early 1900's, DNA has played a central role in the range of cellular targets, and the use of alkylating agents to irreversibly modify DNA nucleobases represents the oldest anticancer strategy^[161]. In fact, nucleobase alkylation is a genotoxic event as it affects basic cellular processes such as replication and transcription^[162]. In this section some general aspects of DNA alkylation will be introduced. Among the various classes of electrophiles, the focus will be centred on last generation alkylating compounds activatable by external stimuli.

1.2.1 Classical alkylating agents

Alkylating agents behave as electrophilic traps for macromolecular nucleophiles including cysteine, lysine, tyrosine, and threonine amino acids, as well as DNA and RNA nucleobases. The first report on DNA alkylation was the use of a nitrogen mustard in 1946^[163]. Following this, many carbon electrophiles have been studied as antineoplastic agents, based on nitrogen and sulphur mustards^[164], epoxides^[165], N-nitrosoureas^[166], triazines^[167], and alkyl sulfonates^[168] (Figure 28). Besides not being included in the class of alkylating agents, cisplatin and related organometallic complexes^[169] also found a wide application as DNA covalent modifiers. Despite commonly being considered an irreversible event, DNA alkylation could sometimes display a reversible nature even under physiological conditions.

Alkylating agents can be further classified as mono- and bifunctional (Figure 28). The latter, which are also known as crosslinking agents, may react with two nucleobases within the same DNA strand (intrastrand cross-link) or form a joint between complementary strands (interstrand cross-linking, ICL). In general, the formation of ICL represents the most toxic of all alkylation events as it prevents strand separation in a DNA double helix causing replication stalling and subsequent double strand breaking^[170]. Conversely, intrastrand cross-linking and

simple DNA adducts are considered less cytotoxic damages and cellular repair machinery can efficiently overcome most of them.

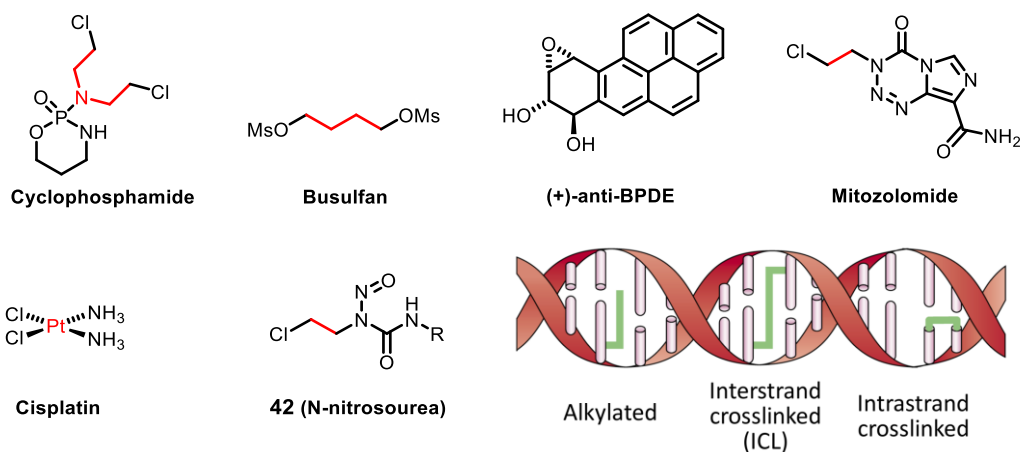
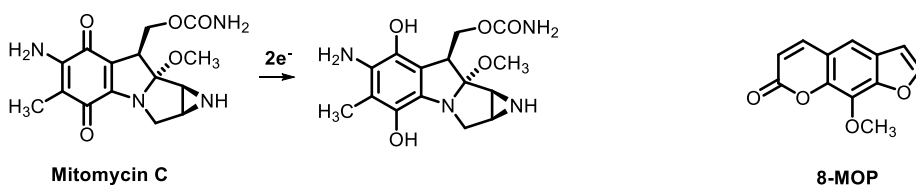
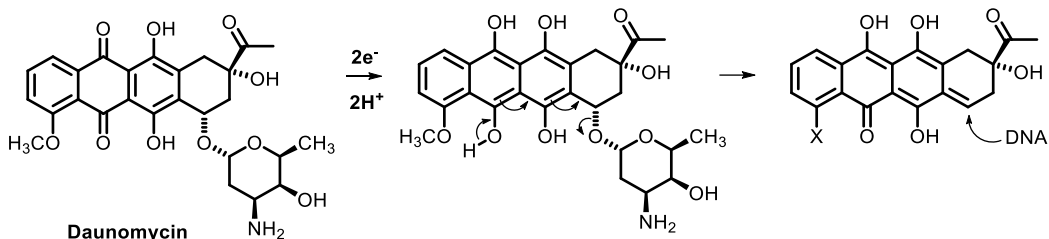


Figure 28: Examples of some classical mono- and bifunctional alkylating or platinating agents. Schematic representation of monoalkylation adduct with DNA nucleobases (e.g. **(+)-anti-BPDE**), interstrand crosslink (e.g. **Cyclophosphamide**) and intrastrand crosslink (e.g. **Cisplatin**). The crosslinking backbones are shown in red.

Despite many reports successfully employing such covalent drugs, the lack of target specificity and premature degradation has often represented a major drawback for the therapeutic opportunities, limiting their development in discovery programs in the recent past. To overcome this issue, a challenging but promising strategy may rely on the use of masked electrophiles which require an “in situ” activation rather than intrinsically reactive alkylating agents. Such electrophiles may be induced by heat, light or a chemical signal, thus allowing a spatial and temporal control of the alkylation event upon application of an external stimulus. Belonging to this family, **Mitomycin C**^[171] is a crosslinking agent which is activated upon enzymatic or chemical reduction of the quinone (Scheme 13), while psoralens (e.g. **8-MOP**) owe their crosslinking ability to the presence of two double bonds that can give rise to [2+2] photocycloadditions upon UV irradiation^[172].



Scheme 13: Two masked DNA alkylating agents activated by reduction and light stimuli respectively.

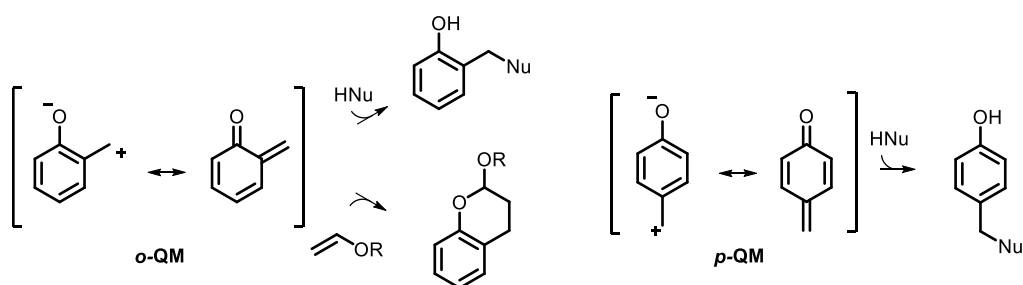


Scheme 14: Proposed mechanism for the observed DNA alkylation by anthracycline derivative **Daunomycin**.

Similar to Mitomycin C, the anticancer activity of some natural occurring anthracycline derivatives has been related to the generation of alkylating intermediates by bioreduction *in vivo* and subsequent elimination of the amino-sugar functionality (Scheme 14)^[173]. Inspired by these electrophilic Michael acceptors, which can be generated by elimination reactions from phenolic systems, several groups have focused their attention towards the use of reactive quinone methides to accomplish smart DNA alkylation.

1.2.2 Quinone methides as masked electrophiles

Quinone methides (QMs) are very reactive intermediates in many chemical and biological processes^[174]. Structurally they consist in a quinone analogue, in which one of the carbonyl oxygens is replaced by a methylene group (Scheme 15). Not surprisingly, QMs reactivity resembles that of α,β -unsaturated ketones, as they typically undergo nucleophile addition at the exocyclic methylene group. However, QMs are far more electrophilic than other Michael acceptors as a consequence of an enhanced charge separation character. The latter can be explained considering that the zwitterionic resonance form is greatly stabilized by aromatic conjugation.

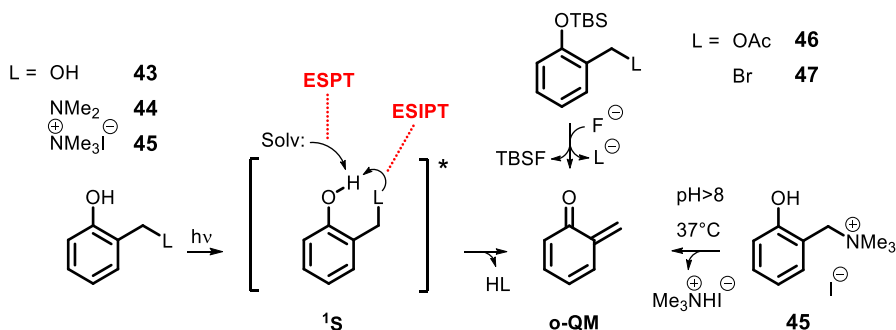


Scheme 15: General structure of ortho- and para-QMs and their typical reactivity: as electrophile in conjugate addition and as heterodienophile in [4+2] cycloaddition (only σ -QMs).

More properly, the aromaticity gain in the conjugate addition is responsible for both the thermodynamic driving force and fast reaction kinetics. Moreover, the *ortho*-QM isomer (*o*-QM) can also be engaged in [4+2] cycloadditions with electron-rich alkenes to give chromans.

The high reactivity of quinone methides makes their isolation normally impossible, with rare exceptions^[175]. In fact, their lifetime is usually no longer than fractions of a second, and even in the absence of any nucleophile they tend to undergo self-reactions. Nonetheless, these transient species were found to be involved in the biosynthesis of lignin^[176] and are useful reaction intermediates in organic synthesis^[177, 178]. Additionally, the reactivity of QMs have also been exploited to create useful protecting groups^[179] and self-immolative linkers^[180], to make bioorthogonal ligations^[181], and to achieve the alkylation of biological targets such as proteins^[182] and nucleic acids^[183]. This widespread applications account for the number of studies available on QM generation and reactivity.

Concerning their generation from stable precursors, disparate mild protocols have been successfully employed for both *o*- and *p*-QMs starting from stable *ortho*- and *para*- benzyl substituted phenols^[184]. Above all, the photochemical^[185-187], fluoride^[188-190] and pH-mediated^[191] procedures have been the most thoroughly applied (Scheme 16). Interestingly, the generation of an intermediate phenolate anion seem to be a common key mechanistic step. In the photochemical activation protocol, the formation of the phenolate is in fact induced by excited state proton transfer either intramolecularly or solvent-mediated (ESIPT and ESPT respectively).



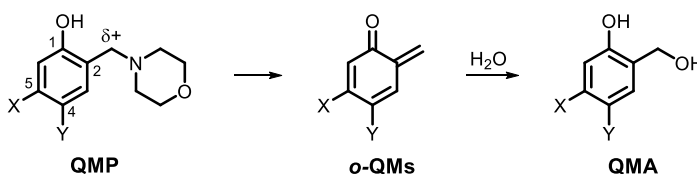
Scheme 16: Activation protocols for the generation of *o*-QMs: base catalysis, fluoride activation and photochemical activation.

While photogeneration of *o*-QMs has been successfully achieved from benzyl alcohols (e.g. **43**), Mannich base of phenols (e.g. **44**) and their quaternary ammonium salts (e.g. **45**), potassium fluoride (KF) has been widely used as a non-physiological chemical trigger for the generation of *o*-QMs starting from *O*-(tert-butyldimethylsilyl) acetates or bromides (e.g. **46** and **47**). Quaternary ammonium salts have also been used to generate *o*-QMs by thermal annealing in water under almost physiological conditions (38 °C and pH 7.8).

Notably, whichever the protocol employed, the electronic properties of the aromatic precursor greatly affect the efficiency of QM generation^[192]. In more detail, electron-withdrawing groups (EWGs) have shown to strongly suppress QM formation, while electron-donating groups (EDGs) facilitate it (Table 1). Moreover, direct comparison between 4- and 5-substituted *o*-QMPs showed that the same group shows its maximum influence when it is directly conjugated with the nascent exocyclic methylene. This behaviour reflects the intrinsic electron-deficient nature of the QM intermediate. EDGs favour leaving group detachment by weakening the benzylic bond, especially when directed conjugated with the benzylic position. The opposite is expected for EWGs, for which a strengthening hyperconjugation effect could be invoked.

Additionally, the substituent strongly affects the reactivity of the transient QM^[192]. As expected, EWGs greatly enhance QM electrophilicity and thus second order reaction rates with nucleophiles. Conversely, EDGs lowers QM electrophilicity extending its lifetime.

Table 1: Effect of the aromatic substituents on the half-life time of *o*-QMPs in water^[192].



QMP	X	Y	QMA	T (°C)	t _{1/2} (min)
48	COOMe	H	53	100	stable
49	H	COOMe	54	100	149
50	H	H	55	50	115
51	H	OMe	56	22	11
52	OMe	H	57	22	4

Since QM adducts (QMA) have a notoriously reversible nature^[193], the above-described substituent effect has strong consequences on the stability of QM nucleophilic adducts. For the same reasons, in fact, the presence of an EDG makes also the alkylating adduct thermodynamically less stable. This translates into a faster rate of QM regeneration eventually leading to easier reversion of the nucleophilic addition.

Rokita took advantage of reversible QMA formation to improve target specificity. The idea relies on the conjugation of a QMP to an efficient sequence or structure recognizing moiety^[194-197] to push the reaction towards the thermodynamically favoured products. For instance, a PNA-QMP self-adduct was successfully employed to obtain sequence specific DNA alkylation (Figure 29).

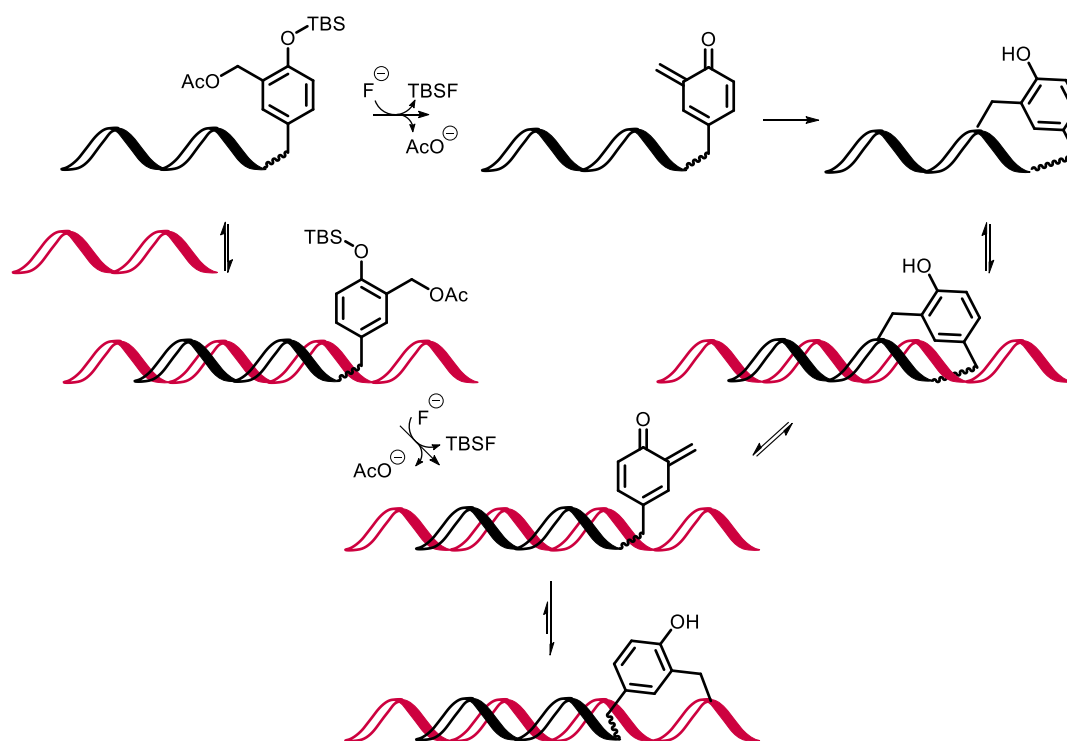


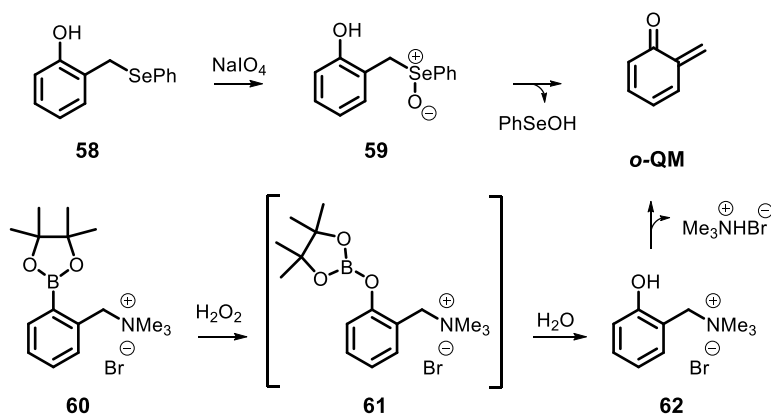
Figure 29: Possible equilibria controlling target-specific alkylation of a PNA-QMP conjugate. PNA sequence is shown in black, ss-DNA is represented in red.

Although reversible alkylation can be advantageous to overcome kinetic traps that limit both potency and selectivity of alkylating agents, sometimes it might pose some hurdles. In fact, detection and structural characterization of the primary adducts with the target could be

very challenging. Moreover, their potency as DNA alkylating agents may be easily underestimated due to the loss of metastable adducts during chromatographic and electrophoretic separations or enzymatic digestions.

Recently, selective oxidation of QM-DNA adducts was proposed as a method to rapidly quench their reactivity and prevent QM regeneration^[198]. As the resulting derivatives persist through standard enzymatic digestion, chromatography, and mass spectral analysis, this method would allow the observation of the kinetic products, those which are responsible for inducing the first cellular response.

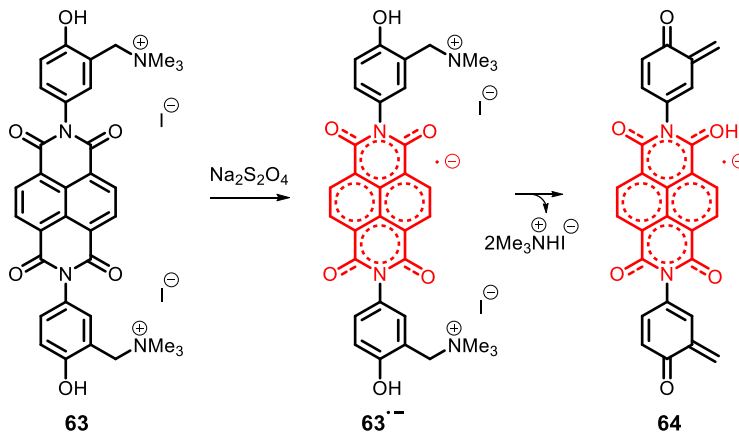
Besides the widely used protocols described so far, the activation of QMs by means of oxidative and reductive methods have also been reported. In particular, Zhou^[199, 200] successfully achieved *o*-QM generation under mild oxidative conditions starting from phenol selenides (e.g. **58**), through spontaneous decomposition of the corresponding selenoxide **59** (Scheme 17). Moreover, Peng^[201] exploited the oxidation of arylboronic ester derivatives (e.g. **60**) for the release of reactive QMs in the presence of H₂O₂, a stable ROS that is commonly present at higher level in oxidatively stressed cancer cells^[202]. Oxidation of the carbon-boron bond, followed by hydrolysis of the borate **61** under physiological conditions, leads to the precursor **62** which spontaneously decomposes to yield the corresponding *o*-QM.



Scheme 17: Oxidative methods towards the generation of *o*-QMs starting from selenides and arylboronic esters.

Conversely, Freccero^[203] designed the NDI-QMP conjugate **63**, which act as an activatable precursor of the bis-alkylating agent **64** under reductive conditions (Scheme 18). In fact,

naphthalene diimide derivatives are known to be easily reduced to their radical anion^[204]. The resulting switch of the NDI electronic properties, from strongly electron-poor (**63**) to electron-rich (**63^{•-}**), is thus reflected on the activation of the QMP reactivity.

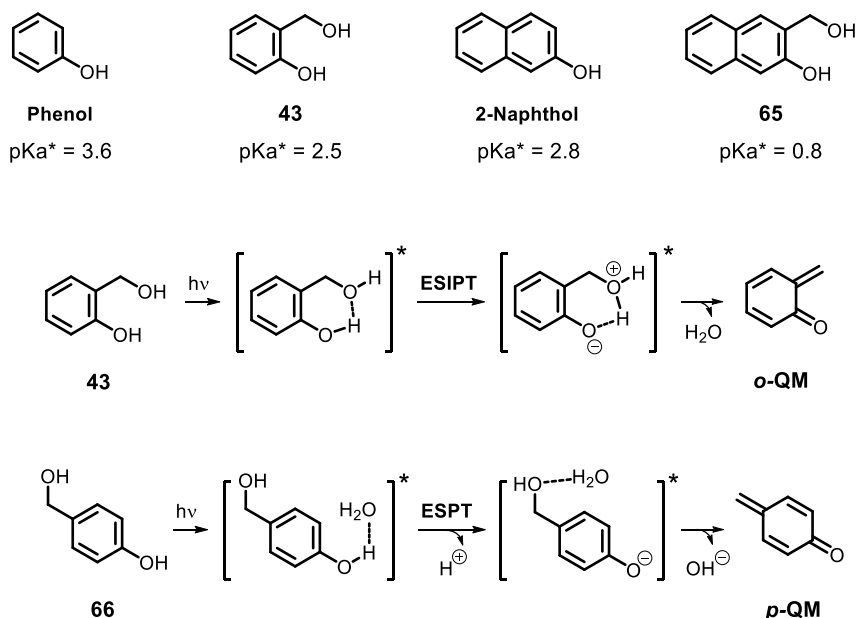


Scheme 18: Reductive activation process for the generation of NDI-QM conjugate **63^{•-}**. While NDI behave as an electron-withdrawing substituent disfavouring QM generation, its electron-rich radical anion triggers it.

1.2.3 Photochemically generated QMs

Photogeneration of QMs was first achieved by photolysis of benzyl alcohols^[185] and their naphtho-derivatives^[205]. Detailed mechanistic studies showed that the dehydration occurs from the singlet excited state and is usually complete within a nanosecond^[185]. It was thus proposed that the excitation of *o*-hydroxybenzyl alcohols (e.g. **43** and **65**) results in an excited state intramolecular proton transfer (ESIPT) of the phenolic proton to the proximal oxygen atom, provoking its detachment. In fact, phenols and naphthols are known to be very strong acids in their excited states, and can even undergo proton transfer to poorly basic sp^2 carbon^[206, 207]. Moreover, intramolecular hydrogen bond between negatively charged phenolate oxygen and the benzylic hydroxy group further enhance S_1 acidity (Scheme 19). Following proton transfer, polar or ionic intermediates are therefore to be expected. Notably, benzylic alcohol displays good propensity to lose a hydroxide ion or a water molecule, whereas it is reluctant to form a hydroxyl radical. This is clearly the opposite situation with respect to other leaving groups such as halides and acetate, which tend to be homolytically cleaved upon irradiation.

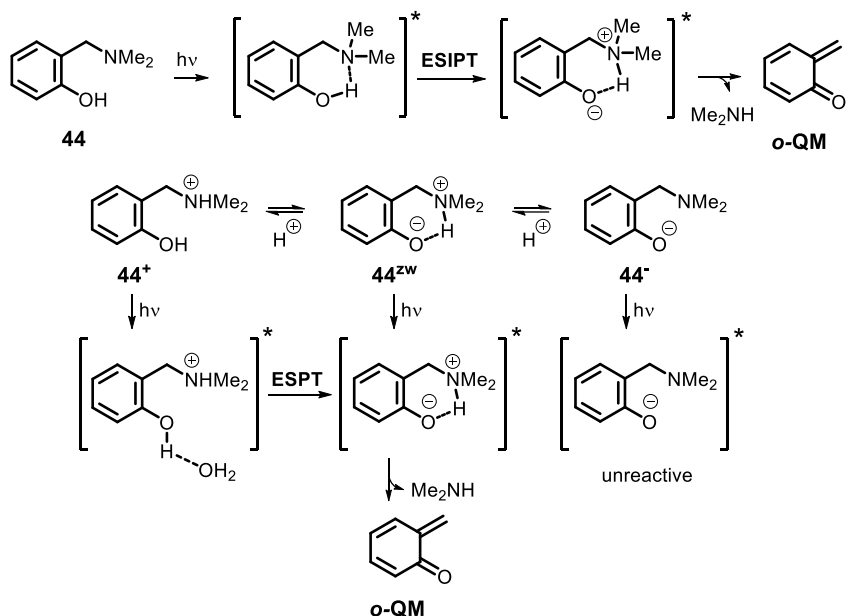
In the case of *p*-QMPs (e.g. **66**) the distance between the phenol and the hydroxyl group is too large to undergo ESIPT, and although excited state proton transfer (ESPT) can occur in the presence of a protic solvent, the efficiency for the *p*-QM photogeneration is often much lower^[185, 208].



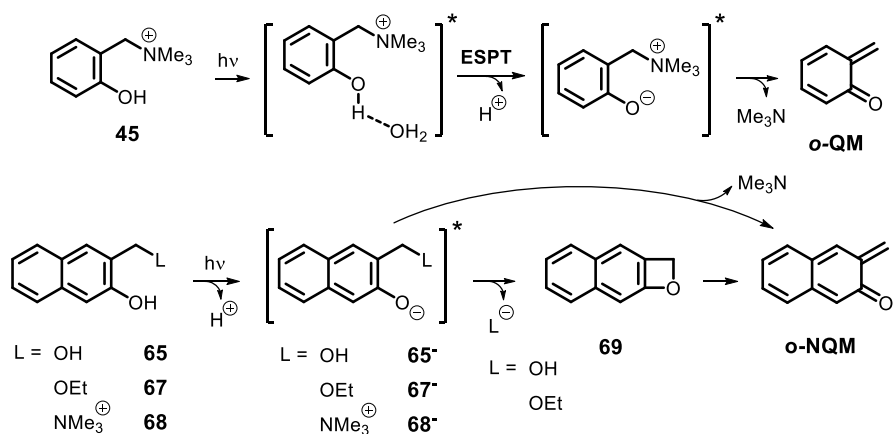
Scheme 19: Measured pK_a s for phenol and naphthol prototype systems in their excited state^[209-212], and mechanism of photogeneration of *o*- and *p*-QMs from benzylic alcohols.

Following studies showed that QMs can also be generated by photochemical elimination of amines from *o*-hydroxybenzylamines^[186, 213] (Scheme 20). The advantage of such modified functionalization is the enhanced water-solubility of the resulting precursors. However, in aqueous solution, the QMPs are not merely present as a neutral species, but protonation equilibria are in place. In these conditions, Basarić reported that the zwitterionic form of the Mannich base is the most photoreactive species^[213].

Subsequently, quaternary ammonium salts of phenolic Mannich bases were shown to be better and preferable QMPs (Scheme 21), since they display an increased generation quantum yield ($\Phi_R = 0.98$ for **45** vs $\Phi_R = 0.23$ for **43** in 1:1 aqueous ACN), a much higher solubility in water, and neglectable nucleophilicity^[191]. This last feature prevents the undesired nucleophilic attack of the precursor on the newly generated QM.



Scheme 20: Mechanisms of *o*-QM photogeneration from Mannich base **44** in organic solvents *via* ES IPT. In water, this mechanism is no longer available and the most reactive species is the zwitterionic **44^{zw}**, which does not need any proton transfer.

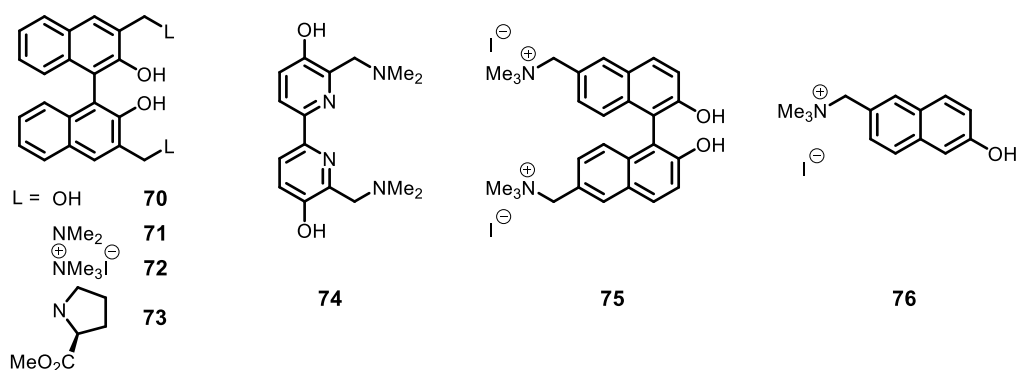


Scheme 21: Mechanisms of *o*-QM photogeneration from quaternary ammonium salt **45**. In the case of *o*-NQMPs, formation of naphthoxete **69** precedes *o*-NQM generation when the leaving group is water or an alcohol.

Naphthoquinone methide precursors (NQMPs) display an almost identical behaviour, both in terms of photogeneration and subsequent NQM reactivity. In fact, the rate of the addition of various nucleophiles to *o*-NQMs is close to that of the parent *o*-QMs. The only remarkable difference was the observation of naphthoxete **69** as a kinetic precursor of *o*-NQMs when the leaving group is an alcohol or water^[209] (Scheme 21).

The possibility to photogenerate QMs from this type of precursors has attracted a great deal of attention for its postulated application in a biological context. In fact, most of the reported generation protocols require the use of a chemical additive for in situ activation of the reactive species (e.g. fluoride or a redox active reagent). Conversely, the photogeneration of QMs does not require any additive, hardly supplied in the cellular environment. Besides water solubility, though, one of the basic prerequisite for such cellular applications is the presence of an absorption band at wavelengths higher than 350 nm to prevent light-induced direct or sensitized DNA damage. However, this is not trivial, as the prototype *o*- and *p*-QMPs (**43** and **66**) exhibit negligible absorptivity above 300 nm. A proposed strategy to address this issue is to extend the system conjugation. In fact, naphtho-^[214], byaryl-^[215-217], and binol-QMPs^[214, 218-220] all display a reasonable absorption above 350 nm (Scheme 22).

In particular, *o*-binol-QMPs (*o*-BQMPs) can be photoactivated upon irradiation at wavelengths as high as 360 nm. The resulting bis-QM can react twice and produce promising DNA crosslinking. Various versions of these *o*-BQMPs were prepared encompassing alcohols (**70**), Mannich bases (e.g. **71**), quaternary ammonium salts (e.g. **72**), amino acids and amino esters (e.g. **73**) functionalizations^[218, 220]. Besides displaying all remarkable photoreactivity, amino acids and amino esters containing precursors exhibited photocytotoxicities comparable to psoralens in human colorectal adenocarcinoma cell lines (IC₅₀=130-230 nM).



Scheme 22: Structure of some mono- and bifunctional QMPs employed as DNA photoalkylating and crosslinking agents.

Similar absorption properties and reactivity were displayed by biphenyl^[216] and bipyridyl^[215] bis-*o*-QMPs (e.g. **74**), which could again effectively react to bis-alkylate nucleophiles of interest.

Mono- and bi-functionalized para-naphtho-QMPs (p-NQMPs) were also reported to be activated at wavelengths higher than 350 nm. Despite ESIPT is not available in contrast to the previous examples, these derivatives (e.g. **75** and **76**) showed pretty high photoreactivity and promising alkylation of single- and double-stranded DNA with significant purine selectivity^[214].

1.2.4 QM detection

Laser flash photolysis (LFP) spectroscopy is the technique of choice for studying light-induced fast chemical processes such as the formation and the reactivity of short-living transient species^[221]. In flash photolysis experiments a short but intense laser pulse initiate the formation of transient species, which is usually accompanied with a change of the sample optical density (ΔOD). This change is spectroscopically monitored by measuring the transmittance of a probe beam before and after the laser excitation (Figure 30). Particularly, in nanosecond LFP the experimental time-scale is limited by the pulse duration (about 2-10 ns) and the stability of the electronic/optical components (few tens of ms), making it a suitable technique to detect quinone methides, triplet excited states, radicals, carbenes and so on.

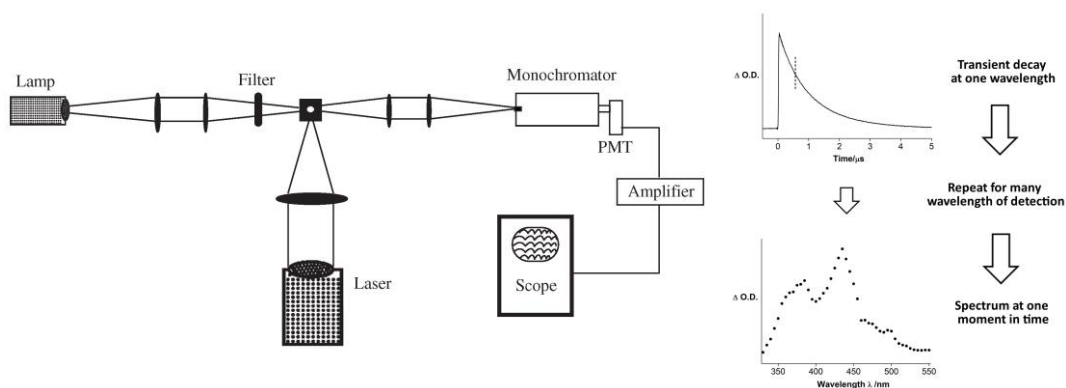


Figure 30: (left) Typical LFP system configuration and (right) instrumental output.

The LFP instrumental output is normally a plot of ΔOD versus time at a given probe wavelength. Transient spectra are then obtained by collecting time-resolved traces at different probe wavelengths, and extracting the signal at a given time from each of them.

The direct information that could be gathered from these time-resolved measurements is the kinetics of the formation and decay processes. In mostly all the cases, the former occurs in the ps-ns time-scale, and could only be detected with a picosecond LFP system. The simplest situation often encountered in nanosecond LFP is an instantaneous raise of signal contextually to the pulse and the observation of a slow decay, with the signal that might or might not be returning to the preexcitation level (e.g. by formation of stable photoproducts or photobleaching). A first or pseudo-first order kinetics is generally observed, since even for many second-order reactions the concentration of the reactive intermediate lies in the micromolar range, while that of the molecule with which it reacts is several orders of magnitude larger. In this context, the effect of different quenchers could add a better insight on the nature of the transient species and its reactivity. For instance, a faster rate of transient consumption in the presence of molecular oxygen is a typical feature of triplet excited states, which are sensitive to T-T annihilation. Conversely, quenching by nucleophiles (such as a thiol) is characteristic of a highly electrophilic species, while quenching by an electron-rich dienophile (such as ethylvinylether) is normally associated with the generation of a quinone methide.

Finally, quantum yields of formation could be derived from nanosecond LFP measurements. For equal laser delivered energy (normally 5-25 mJ per pulse), in fact, the signal right after the pulse is proportional to the product of the quantum yield of formation times the extinction coefficient difference between the transient and its precursor. As a consequence, when structurally related species are compared, assuming a roughly similar transient extinction coefficient would imply that the initial ΔOD is only proportional to the quantum yield of transient formation.

Aim of the Thesis

The importance of G-quadruplex structures in telomere biology, transcription regulation (of cancer genes) and genomic instability has been established by a broad range of corroborating evidences. Moreover, their presence in precise genomic *loci* has been proposed to be a result of an evolutionary selection process, suggesting that they may feature fundamental genomic regulatory switches. Their central role in phenotype expression has stimulated strong efforts to develop selective G4-targeting small molecules for the treatment of cancer and genetically mediated diseases^[97, 222].

Even though they share some common structural features, G-quadruplexes exhibit a notable polymorphism, making sequence and structure recognition theoretically possible. Still, topological selectivity is not achievable by the ordinary and wide accepted stacking recognition, since the external G-tetrads are ubiquitous and their well-defined structure cannot be a discriminating factor, thus making the selectivity issue a very arduous task. Recently, telomestatin derived non-macrocyclic oligo-heteroaromatic compounds have shown to preferentially bind some topology, suggesting that the recognition process might be associated with a groove binding mode^[118].

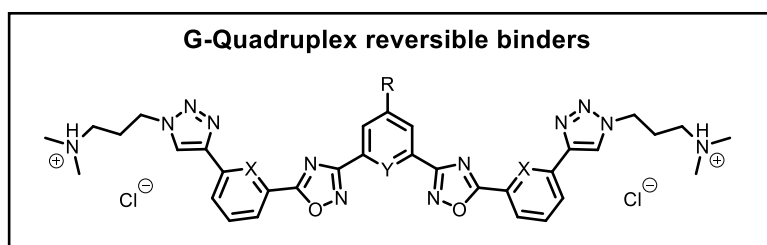


Figure 31: Conceptual design of water-soluble heptacyclic compounds as G4 selective binders.

The first purpose of this thesis is to further inquire the still unexplored field of oligo-heteroaromatic ligands by extending the available studies with a new family of water-soluble heptacyclic compounds (Figure 31). The development of a straightforward reliable and flexible synthetic protocol is of particular importance. The structural elements needed for good *in vitro* affinity need to be investigated by thoughtful substitution of strategic atoms. Additionally, the introduction of an easily tetherable functional group is convenient for

engineering conjugated molecular tools exploiting the targeting proprieties of the new G4 ligand. Finally, elucidation of the binding mode would be desirable in view of further scaffold optimization.

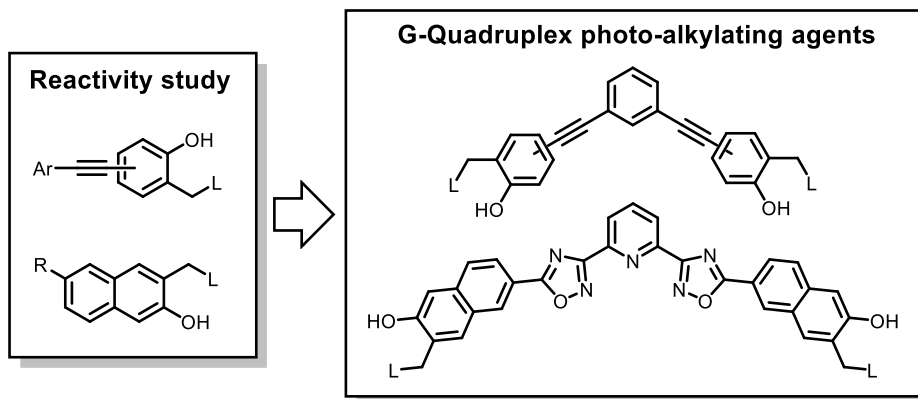
As extensively depicted^[131, 135, 136], the formation of a covalent link would add a major contribute to the compute of the overall energetics of G4 binding. The higher stabilization of the quadruplex structure might in turn improve the related biological effect. The poor evidences available to date, however, do not allow to univocally prove the validity of such a hypothesis. The unique advantage of creating covalent links in close proximity to a particular genomic area of interest brought about by selective ligand interaction could be exploited to obtain more defined cell imaging with negligible off-target blurring. Moreover, affinity isolation of G4 structures forming within cellular genome could be achieved only after formation of a strong covalent link between the targeted structure and the biotin affinity tag. In this specific case, the alkylation process should ideally be reversible to enable the release of the alkylated sequence after the pull-down.

For all these reasons, further investigation on targeted covalent modification of G-quadruplexes are mandatory. In this context, phototriggerable electrophiles – and among them quinone methide precursors – are convenient alkylating agents for biological applications as they allow spatial and temporal control over their tethering activity. Moreover, the intrinsic reversibility of light-induced QM generation could allow trap and release of the G4 structure depending on the conditions (e.g. release under simultaneous denaturing and competition trapping).

The second aim of this thesis is the synthesis of water-soluble extended aromatic compounds embedding two or three QMPs as a strategy to obtain selective G4 recognition and anchoring and avoid off-target migration related to the reversible nature of QM adducts (Scheme 23). To address the issue of preventing potential direct or sensitized target photodamage, it is essential to develop QM precursors activated by near UV-visible light (above 350 nm). Direct thymine-thymine cross-linking occurs below 310 nm, while UVA radiation acts indirectly by photosensitization reactions producing ROS^[223]. Red-shifted absorption with respect to ortho-benzoquinone methide precursors can be achieved by electronic conjugation. Concerning this aspect, preliminary studies are needed to investigate the photoreactivity of

extended conjugated prototype systems in order to find the optimal structural features that maximize QM generation. Two strategies should be considered, taking into account that the putative ligand should be an extended V-shaped planar aromatic compound: (a) substitution of ortho-QMP with an arylolethynyl moiety and (b) exploitation of a naphtho-QMP system. Substituent effects must also be considered in the attempt of tuning their reactivity.

Subsequently, the rational design and the synthesis of water-soluble V-shaped putative G4 ligands embedding two or more red-shifted QMP systems must be accomplished. Affinity as reversible binders needs to be first evaluated to assure effective non-covalent interactions with the target and selectivity over duplex DNA. Furthermore, the photoreactivity towards G4 nucleic acids must be assessed. The fraction of alkylated oligonucleotide should be quantified and optimized by varying the compound loading and the irradiation time. Finally, retention of selectivity over *ds*-DNA during the alkylation process should be checked. Thermal reversibility of alkylated DNA adducts has to be examined to establish the actual formation of a stable covalent bond. Identification of the alkylation site would also provide insights on the actual binding site and mode of the ligand.



Scheme 23: Schematic route towards the development of selective G4 photoalkylating agents.

CHAPTER 2 : G4 Reversible Targeting

2.1 Heptacycles for selective G4 targeting

Inspired by the remarkable biological activity and the unique selectivity for G4 structures of telomestatin, a number of synthetic analogs have been designed. Based on the previous works of Teulade-Fichou^[118-120], open form of macrocycles represented a valuable choice, not only because low yield cyclization process can be avoided, and a symmetric synthesis can be used as well, but mainly because the flexible oligoaryl system has been recognized as an important structural element conferring high topological selectivity.

Following the previous efforts made in recognition of the structural elements controlling target recognition, changing the nature of the six-membered rings has not been a matter of thorough investigation yet. In particular the potential role of the three pyridine nitrogen atoms as hydrogen bond acceptors and coordination sites needs to be clarified. Additionally, by analogy to the observed beneficial effect in **BOxApy** and **BOxAzaPy** families, evaluation of the effect of cationic side-chains addition on the heptacyclic scaffold is compelling.

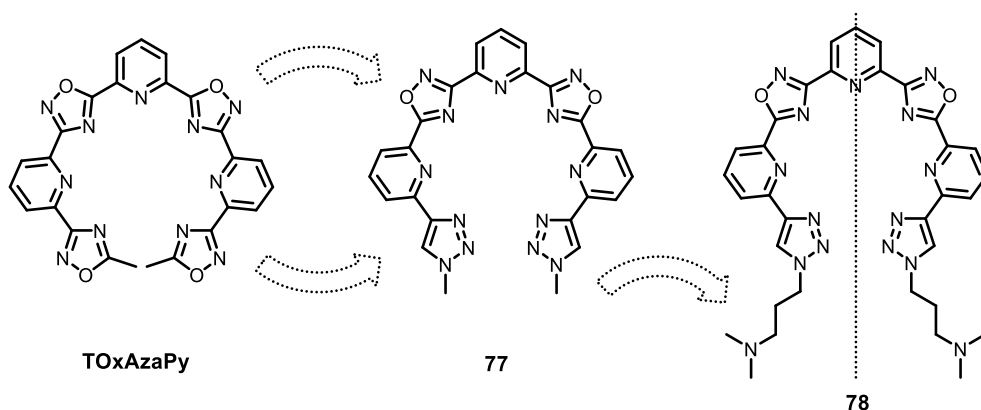
In this section, the synthesis of water-soluble heptacyclic oligoaryls will be shown. 1,2,3-triazoles will be proposed as a convenient alternative to the lateral 1,3,4-oxadiazole rings. Hence, the synthetic versatility will be exploited for the smooth preparation of carbo-analogues and the incorporation of an aromatic primary amino group for further scaffold derivatization. The *in vitro* G4 stabilization of the new family of oligo-heteroaromatic compounds will be evaluated by FRET-melting, CD-melting and FID biophysical assays to establish the best performing scaffold. Furthermore, MS competition experiments will be presented as an evidence to support some conclusions on the binding mode.

2.1.1 Facile synthesis of a water-soluble heptacyclic ligand

Despite the number of methods available for the synthesis of substituted 1,2,4-oxadiazoles^[224-227], fairly low reaction yields were commonly associated with the synthesis of bifunctional oligoaryl systems^[119] as a consequence of the relatively drastic reaction conditions needed for the ring closure step. Therefore, substitution of the terminal 5-membered rings in the heptacyclic scaffold with 1,2,3-triazoles was a highly agreeable choice (**77**). Copper(I)-catalyzed 1,3-dipolar cycloaddition between azides and terminal alkynes has

widely been used in the recent literature^[228] as a click reaction as it affords with high yield and regioselectivity 1,2,3-triazoles. Besides its huge scope, the reaction is compatible with water media, proceeds under mild reaction conditions and is orthogonal to most functional groups. Moreover, both oxadiazoles and triazoles are well known pharmacophores^[229] in medicinal chemistry for their thermal and chemical stability in water, the presence of several heteroatoms that can be involved in coordination events, and the absence of protonable nitrogens at physiological conditions.

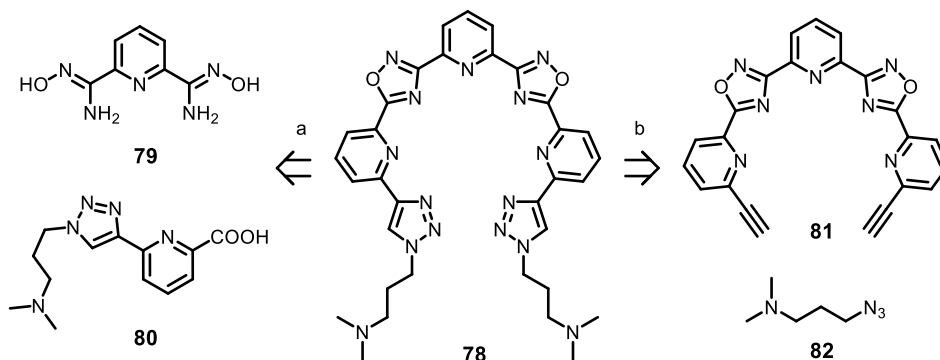
Such a modification also allowed the addition of cationic side-chains at the two extremities to improve water-solubility and target affinity, by means of ready available aminoalkyl azides (Scheme 24). By analogy with the alternating 6- and 5-membered rings oligomeric scaffolds already described (e.g. **TOxAzaPy**), an internal plane of symmetry was maintained in order to simplify the overall synthetic process.



Scheme 24: Design of a water-soluble symmetric heptacyclic scaffold with a simplified synthetic approach, inspired by the known **TOxAzaPy** structure.

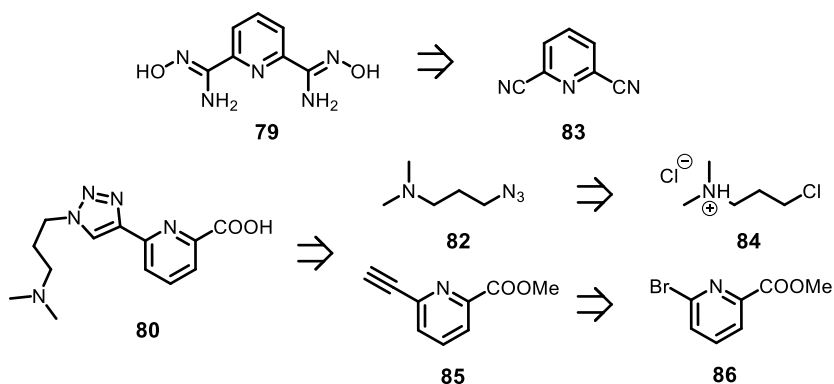
According to the recommended disconnection of 5-membered rings, retrosynthetic analysis of **78** leads to two alternative pathways (Scheme 25). The choice of first disconnecting central 1,2,4-oxadiazoles reflected the convenience of a more convergent synthetic process. Maximizing symmetry reduction in early retrosynthetic steps was highly recommended as it minimized the number of bifunctional reactions, which intrinsically involve lower yields. As thoroughly described in the literature^[230], the 1,2,4-oxadiazoles could be formed by condensation between a carboxylic acid (or activated derivatives) and an amidoxime followed by intramolecular cyclodehydration, oxidative condensation between an aldehyde

and an amidoxime, or 1,3-dipolar cycloaddition between a nitrile oxides to a nitrile. The latter had to be avoided due to the self-oligomerization of the bifunctional reagent^[231]. The choice of election was, therefore, the condensation of the amidoxime **79** on the carboxylic acid **80**.



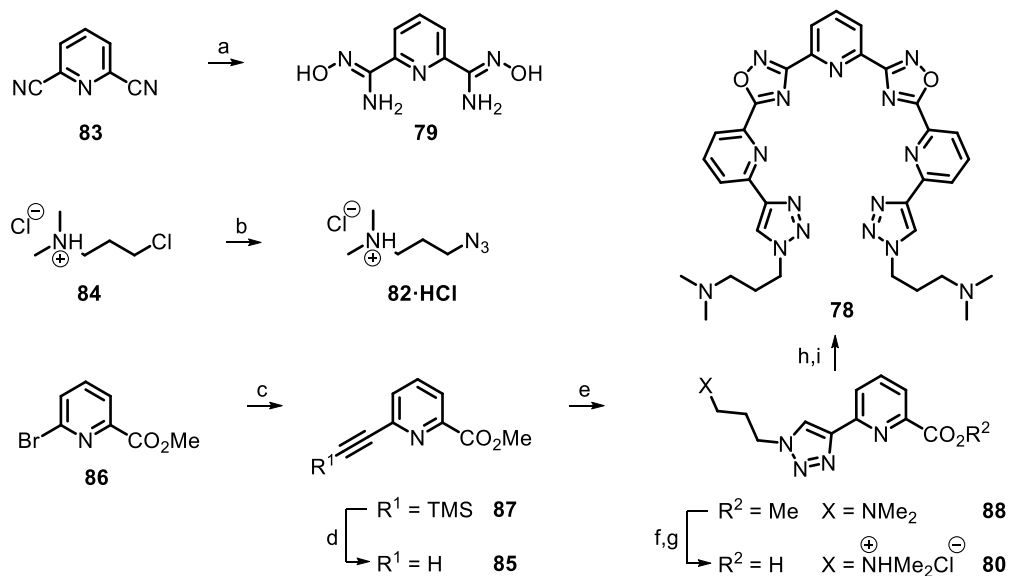
Scheme 25: Retrosynthetic analysis of **78**. Disconnection (a) is more simplifying than (b).

Following the retrosynthetic analysis, amidoxime **79** was obtainable from nitrile **83**, which was commercially available (Scheme 26). Carboxylic acid **80** was disconnected along the triazole, through a CuAAC disconnection, to yield azide **82** and alkyne **85**. Both the compounds were ready obtainable from commercially available halides **84** and **86**.



Scheme 26: Retrosynthetic analysis of building blocks **79** and **80**.

Based on previous reports^[119], diamidoxime **79** was obtained from pyridine-2,6-dicarbonitrile (**83**), by addition of two equivalents of hydroxylamine in 1:1 aqueous ethanol (Scheme 27). Precipitation of the rather insoluble diamidoxime simplified the work up. In parallel, azide **82** was obtained as its hydrochloride by nucleophilic substitution of the corresponding alkyl chloride **84** with sodium azide, in the presence of catalytic NaI^[232].



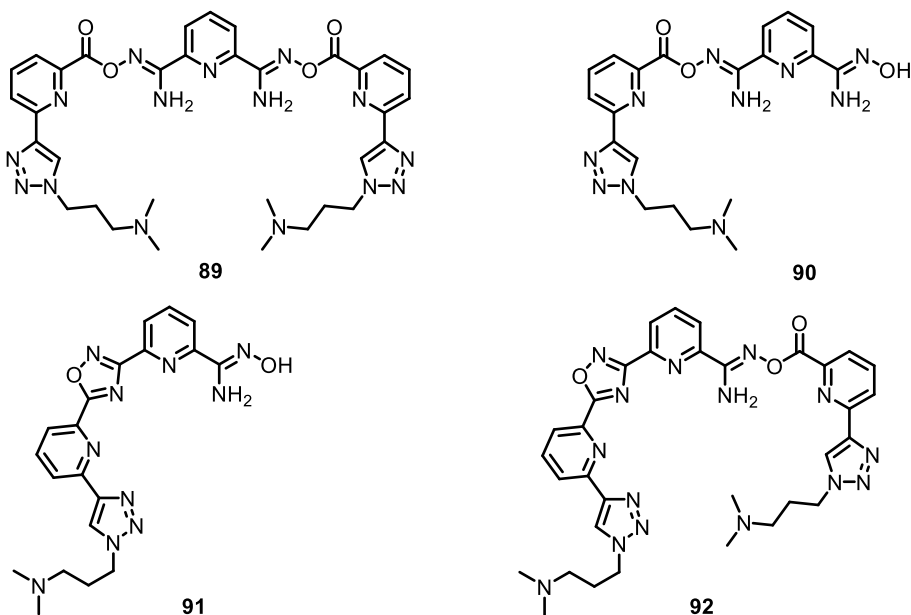
Scheme 27: Synthesis of water-soluble heptacyclic oligo-heteroaryl **78**. (a) $\text{NH}_2\text{OH} \cdot \text{HCl}$, Na_2CO_3 , $\text{EtOH}/\text{H}_2\text{O}$, rt, 16 h (yield: 78%); (b) NaN_3 , H_2O , 80°C , 16 h (yield: 91%); (c) $\text{Pd}(\text{PPh}_3)_2\text{Cl}_2$ 2%, PPh_3 4%, CuI 2%, $i\text{Pr}_2\text{NH}$, TMS-CCH , PhCH_3 , 80°C , 1 h (yield: 92%); (d) K_2CO_3 , MeOH , rt, 2 h (yield: 87%); (e) **82**· HCl , $\text{CuSO}_4 \cdot 5\text{H}_2\text{O}$, sodium ascorbate, $\text{H}_2\text{O}/t\text{-BuOH}$, rt, 24 h (yield: 90%); (f) K_2CO_3 , $\text{THF}/\text{H}_2\text{O}$, reflux, 2 h; (g) HCl , H_2O (yield over 2 steps: 98%); (h) CDI , **79**, DMF , rt, 16 h; (i) K_2CO_3 , DMF , 60°C , 2 h (yield over 2 steps: 34%).

Sonogashira cross-coupling between methyl 6-bromopicolinate **86** and ethynyltrimethylsilane in toluene, and subsequent TMS protecting group removal upon basic methanolysis^[233], smoothly allowed the introduction of a terminal alkyne at the right position (**85** *via* **87**). Notably, low catalytic loading was sufficient as only 2 mol% of both Pd and Cu were used. The cross-coupling was performed on the methyl ester, as the carboxylic acid is usually not tolerated^[234]. Surprisingly, trimethylsilyl group removal with fluoride (TBAF) in anhydrous THF afforded **85** in nearly 40% yield only, while more than a 2-fold improvement was achieved by basic methanolysis.

The CuAAC reaction between **85** and **82** was performed in aqueous *tert*-butanol to dissolve both reagents and catalyst, and cleanly afforded methyl ester **88**. Subsequent basic hydrolysis and acidic work up yielded amino acid **80**, as its hydrochloride, quantitatively.

Condensation between amidoximes and carboxylic acids are achieved upon activation of the acid with the usual protocols and coupling reagents commonly employed in peptide chemistry. Although acyl chlorides^[235], mixed anhydrides^[236], and activated esters^[225] have been widely used for the scope, the imidazolide^[226] was chosen in this case due to both

proper reactivity and reagent inexpensiveness. Therefore, carboxylic acid **80** was activated *in situ* with 1,1'-carbonyldiimidazole (CDI) and reacted with diamidoxime **79** in DMF to yield the intermediate bis-O-acyldiamidoxime **89** (Scheme 28). Eventually, one-pot addition of catalytical K_2CO_3 and heating at $60^\circ C$ yielded ring closing dehydration to the desired heptacyclic compound **78**.



Scheme 28: Structures of the intermediates **89-92** identified in the steps (h) and (i) in Scheme 27.

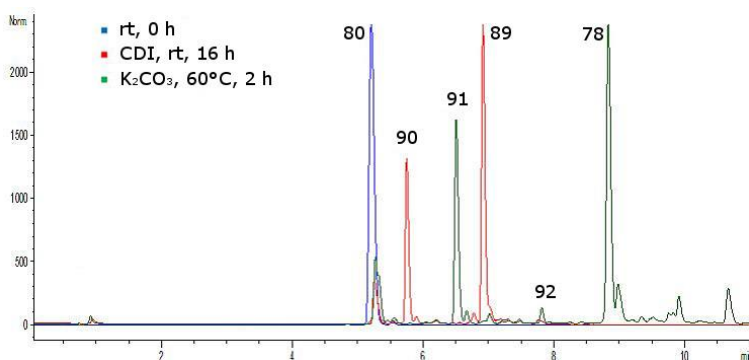
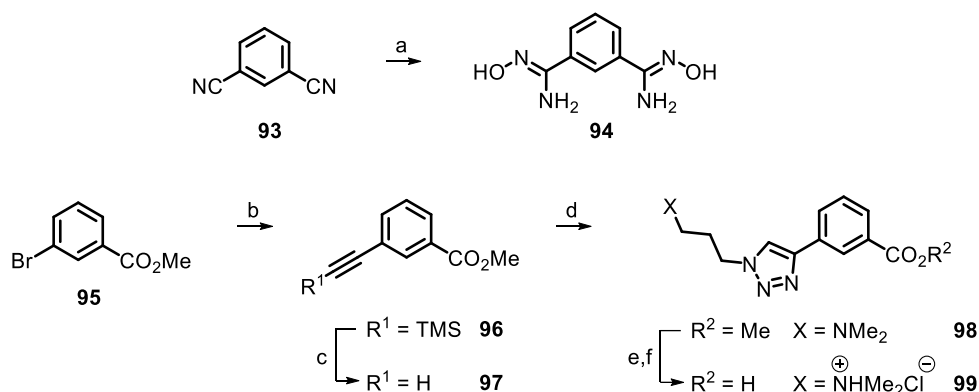


Figure 32: Superimposed HPLC chromatograms relative to steps (h) and (i) in Scheme 27.

Optimization of the aforementioned condensation/cyclodehydration reaction started with the identification of the intermediates **89-92** in the reaction mixture (Figure 32). One-pot base promoted cyclodehydration proved to be the best alternative in terms of final yield.

2.1.2 Structural variations in the heptacyclic scaffold

The aforementioned synthetic process was designed to be convergent and highly flexible, an important feature which is frequently exploited in medicinal chemistry to easily implement single structural modifications and quickly screen different combinations of those elements. This approach was used to investigate structural variability in the nature of the 6-membered rings, as no evidence proving or disproving the involvement of pyridine nitrogen in G4 selective targeting for this class of open-chain oligo-heteroaryl ligands was available yet.

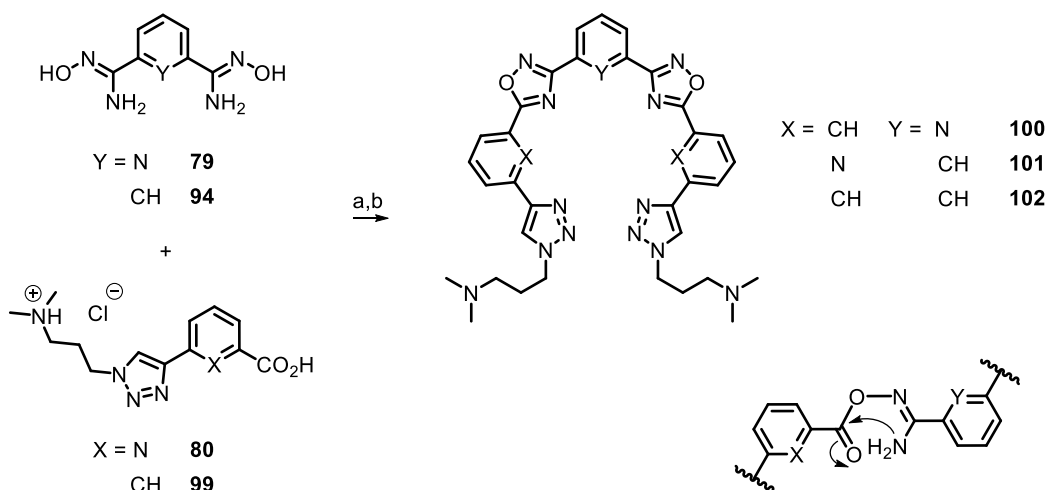


Scheme 29: Synthesis of carbon analogue building blocks **94** and **99**. (a) $\text{NH}_2\text{OH}\cdot\text{HCl}$, Na_2CO_3 , $\text{EtOH}/\text{H}_2\text{O}$, reflux, 16 h (yield: 78%); (b) $\text{Pd}(\text{PPh}_3)_2\text{Cl}_2$ 2%, CuI 1%, Et_3N , TMS-CCH , ACN , 50°C , 24 h (yield: 88%); (c) K_2CO_3 , MeOH , rt, 2 h (yield: 86%); (d) **82-HCl**, $\text{CuSO}_4\cdot 5\text{H}_2\text{O}$, sodium ascorbate, $\text{H}_2\text{O}/t\text{-BuOH}$, rt, 24 h (yield: 95%); (e) K_2CO_3 , $\text{THF}/\text{H}_2\text{O}$, reflux, 24 h; (f) HCl , H_2O (yield over 2 steps: 97%).

The carbon analogue building blocks were synthesized following the same synthetic scheme with some adaptations for the reaction conditions (Scheme 29). Therefore, benzene-1,3-diamidoxime (**94**) was obtained from commercially available isophthalonitrile (**93**), by addition of two equivalents of hydroxylamine in aqueous ethanol^[237]. Substitution of electron-poor pyridine with benzene lowered the electrophilic nature of the nitrile, thus requiring heating at the reflux temperature for 16 hours for the reaction to be complete.

Analogously, terminal alkyne **97** was obtained through Sonogashira cross coupling on aryl bromide **95**, following a published procedure^[238], and subsequent basic methanolysis of the TMS-protected alkyne **96**. Hence, basic hydrolysis of methyl ester **98**, which was obtained by CuAAC with **82-HCl**, afforded amino acid **99**. Despite the latter reaction was performed under the same conditions described for compound **88**, the reaction rate was much lower, reflecting the lower electrophilicity of benzoate with respect to picolinate.

The synthesis of the three carbon analogues **100-102** was obtained by the right combination of building blocks (Scheme 30). Again, the substitution of pyridine with benzene had strong impact on the cyclodehydration step. Apparently, the most important feature controlling this step was the nature of the group X (Scheme 30), considering that if X = N (**78** and **101**) the ring-closing reaction proceeded smoothly, while if X = CH (**100** and **102**) long reaction times were necessary (48 and 96 hours respectively). Such a marked effect was explained in terms of electrophilicity of the carboxylate and, to a lesser extent, nucleophilicity of the nitrogen in the O-acyl-amidoxime. In fact, benzene (X = CH) consistently lowers the electrophilic nature of the carboxylate and therefore its reactivity; conversely, benzene itself (Y = CH) has only a slight effect on incrementing the nucleophilic nature of the nitrogen in the amidoxime. Overall, the worst combination of diamidoxime **79** and carboxylic acid **99**, led to at least a 50-fold decrement of reactivity in the base promoted cyclodehydration. Unfortunately, if the temperature was raised, an increment in side-products formation was observed as a consequence of competing amidoxime hydrolysis, diacylation of the intermediates and DMF decomposition.

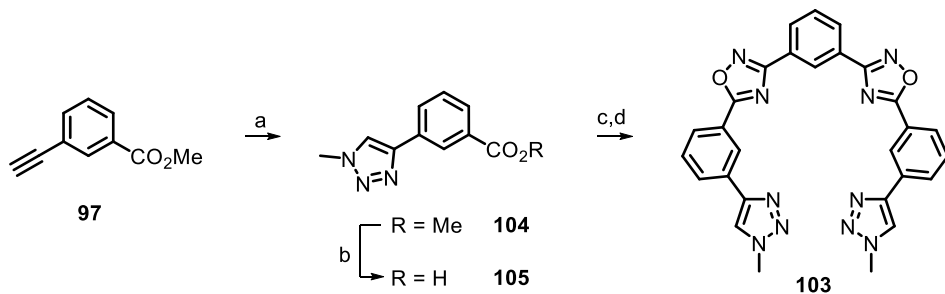


Scheme 30: Synthesis of heptacyclic carbon analogues **100-102**. (a) CDI, DMF, rt, 16 h; (b) K₂CO₃, DMF, 60°C, 2 h – 4 d (yields over 2 steps: 30-40%). Intramolecular nucleophilic attack of O-acyl-amidoxime on carboxylate is shown.

Though the designed synthesis leads to symmetric oligoaryl ligands, desymmetrization would be theoretically possible, even though the number of possible derivatives would escalate rapidly.

Since direct comparison between **TOxAzaPy** and heptacycle **78** *in vitro* affinities for their target would have not allowed the discernment between the effect of the cationic side-chains and that of the triazole for oxadiazole substitution, the synthetic protocol was used to obtain heptacycle **103** (Scheme 31), which was missing the cationic pendals.

Considering that low molecular weight alkylazides are not stable and hazardous, a modified protocol^[239] was exploited for the synthesis of N-methyl-triazole **104**, consisting on *in situ* generation of methylazide and subsequent copper (I) promoted cycloaddition with alkyne **97** (Scheme 31). Hydrolysis of ester **104** afforded the carboxylic acid **105**. Condensation with diamidoxime **94** and cyclodehydration under the usual conditions afforded the desired product, which precipitated as a white solid in the reaction vessel. The rather impressive insolubility of the heptacyclic compound in both polar and non-polar solvents, including aromatic ones, complicated its characterization. Eventually, NMR analysis of **103** was achieved in deuterated trifluoroacetic acid (CF₃COOD). Indeed, the very low solubility of **103** in polar aprotic solvents, which become neglectable in water (< 10⁻⁷ M), made impossible its employment in biological assays.



Scheme 31: Synthesis of heptacycle **103**. (a) MeI, NaN₃, Cu, CuSO₄, H₂O/*t*-BuOH, MW, 125°C, 10 m (yield: 39%); (b) K₂CO₃, THF/H₂O, reflux, 16 h (yield: 98%); (c) CDI, **94**, DMF, rt, 16 h; (d) K₂CO₃, DMF, 60°C, 8 h (yield over 2 steps: 49%).

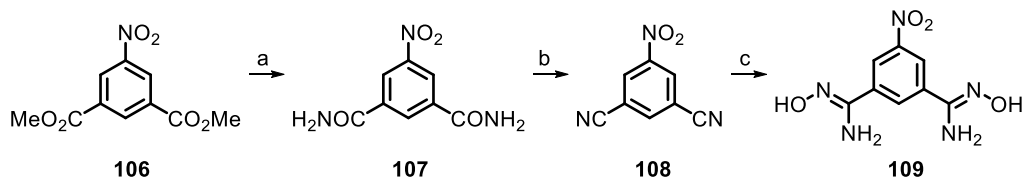
2.1.3 Heptacyclic scaffolds adapted for conjugation

The simplest selective molecular tools commonly exploit the conjugation of a vector, that is a target specific recognition unit (e.g. a ligand or a substrate selectively targeting a DNA structure or a protein), with one or more functional tags (e.g. a fluorophore, biotin, an alkylating agent, a radionuclide, a secondary recognition unit). The assumption on which

such engineered tools rely is that each module does not affect the function of the other. This is commonly guaranteed by proper separation in space by the interposition of spacers of appropriate length. Certainly, to create conjugates on a preformed scaffold it is mandatory the presence of a reactive functional group for derivatization under conditions orthogonal to any other functional group already present. Conveniently, such a functional group should be inserted during the latest stages of compound synthesis, or be protected to prevent it from interfering.

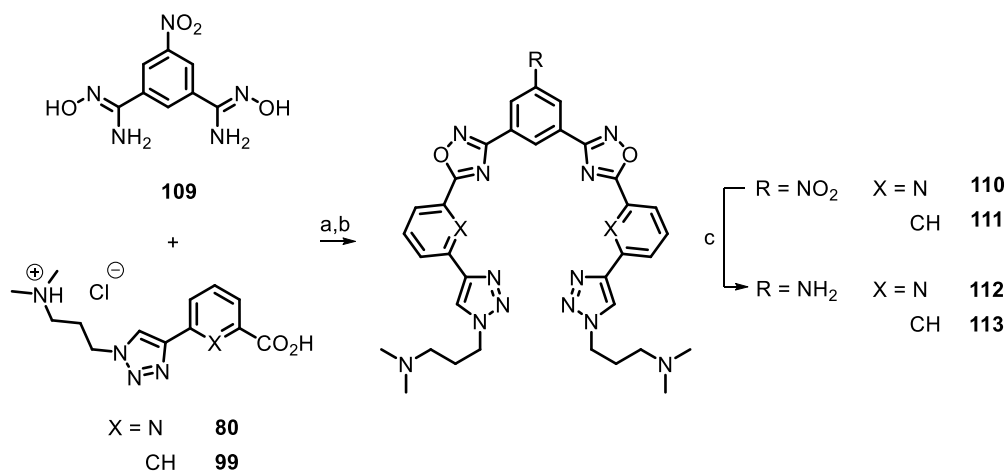
In this specific case, to exploit the targeting proprieties of the heptacyclic scaffold, both or one of the terminal side chains might be replaced with a suitable unit, through CuAAC reaction with the corresponding azide. However, this approach would have needed the addition of protecting/deprotecting steps, since triazoles synthesis preceded oxadiazoles formation. Instead, to fully exploit the power and versatility of the synthetic design described so far, an aromatic primary amino group was introduced in the central 6-membered ring. Conveniently, this rather nucleophilic group was not interfering with the synthesis of the heptacyclic derivative since it was masked as a nitro-group.

By adaptation of a known procedure^[240], commercially available dimethyl 5-nitroisophthalate (**106**) was converted into isophthalonitrile **108** by amidation with ammonia and subsequent dehydration of the intermediate diamide **107** with trifluoroacetic anhydride (Scheme 32). Subsequent addition of hydroxylamine was effective at room temperature and afforded diamidoxime **109** in 71% yield over the three steps. Compared to isophthalonitrile (**93**), for which the reaction was effective only at reflux temperature, the added nitro substituent had an enhancing effect on the addition of hydroxylamine. The increased electrophilic nature of aryl cyanides was in fact comparable to pyridine-2,6-dicarbonitrile (**83**).



Scheme 32: Synthesis of the NO₂-containing building block **109**. (a) NH₃, MeOH, rt, 16 h (yield: 94%); (b) trifluoroacetic anhydride, Et₃N, THF, rt, 3 h (yield: 87%); (c) NH₂OH·HCl, Na₂CO₃, EtOH/H₂O, rt, 16 h (yield: 86%).

The synthesis of nitro-substituted heptacycles **110** and **111** was obtained by condensation and ring-closing dehydration of diamidoxime **109** with carboxylic acids **80** and **99**, under the same reaction conditions described above. Eventually, the nitroaryl was effectively reduced with SnCl₂ in ethanol to afford the NH₂-substituted heptacyclic compounds **112** and **113**.



Scheme 33: Synthesis of substituted heptacyclic oligo-heteroaryls **110-113**. (a) CDI, DMF, rt, 16 h; (b) K₂CO₃, DMF, 60°C, 2 h – 4 d (yields over 2 steps: 30-45%) (c) SnCl₂, HCl, EtOH, reflux, 6 h (yield: 82-86%).

Accordingly, further scaffold derivatization has been proved to be possible by exploiting the reactive primary arylamine, e.g. by peptide bond formation with a carboxylic acid counterpart.

2.1.4 Biophysical binding assays towards G4 structures

Remarkably, all the compounds in the family benefited of the two tertiary amine side-chains in terms of solubility in water under physiological conditions (.ca 10⁻² M). This feature differentiated them from all the known non-macrocyclic oligo-heteroaromatic G4 ligands and could be a fundamental advantage in terms of drug bioavailability and permeability to cell and nucleus membranes.

To screen the *in vitro* affinity of the heptacyclic compounds for quadruplex DNA, FRET-melting assays were first performed on three G4-folding sequences, namely human telomeric F21T and HIV-1 viral quadruplexes LTRIII and LTRIV. The data, summarized in Figure

33, agreed with the assignment of good though not exceptional binding affinity to the new scaffold. If compared to **TOxAPy** and **TOxAzaPy** heptacyclic analogues, the water-soluble family exhibited similar and in some cases higher performances. Interestingly, the data suggested a clear influence of the nature of the 6-membered rings on target affinity. In particular, by replacing each pyridine with benzene the melting stabilization temperature (ΔT_m) decreased systematically. Moreover, the role of the central pyridine seemed to be more important than the two side 6-membered rings (cf. **100** vs **101**).

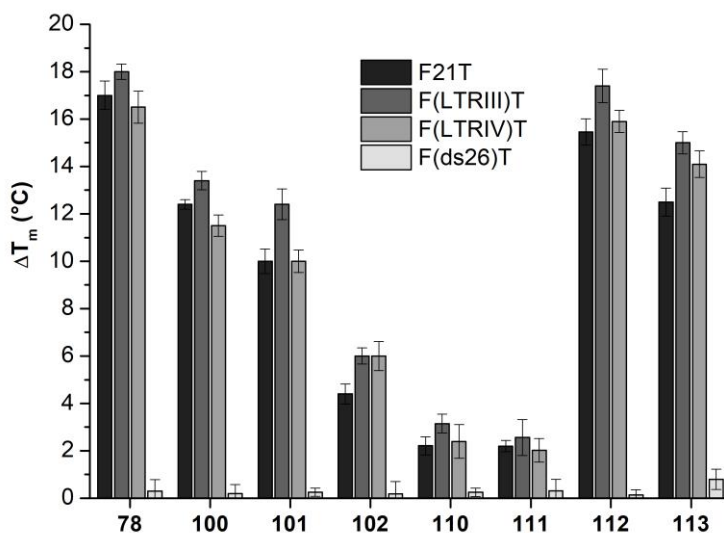


Figure 33: FRET-melting stabilization temperatures of heptacycles **78**, **100-102**, **110-113** with three selected G4s (Human telomeric F21T and viral retrotransposons LTRIII and LTRIV) and one ds-DNA control sequence (ds26). Conditions: DNA 0.25 μ M, compounds 1 μ M, LiCaco 10 mM (pH 7.2), LiCl 99 mM and KCl 1 mM (LiCl 90 mM and KCl 10 mM for F21T).

Notably, the change in the electronic distribution due to benzene for pyridine central ring substitution was not accounting for the observed binding reduction, as the introduction of strong electron-withdrawing nitro substituent in the benzene ring was negatively affecting the affinity for quadruplexes (cf. **101** vs **110** and **102** vs **111**). Conversely, electron-donating primary amino group strongly improved the binding proprieties (cf. **101** vs **112** and **102** vs **113**), which were substantially comparable to their pyridine-containing analogues (cf. **78** vs **112** and **100** vs **113**). However, it was not clear the actual role of pyridine nitrogen and primary amino substituents, and even a change in the binding mode could not be rule out. Two main hypotheses have been proposed, in which the pyridine nitrogen was promoting the coordination of a potassium ion and thus favoring the bent conformer and an end tetrad

stacking binding mode, or the same atom could be involved in some specific hydrogen bond within the target grooves. In both cases, the effect of the amino group in the carbon-analogues was not consistent, hence a different stabilizing effect had been adduced in this case, whether it resulted from electrostatic or hydrogen bonding interactions.

Overall, the central pyridine nitrogen seemed to be mandatory for getting high affinity, and the only way to overcome its substitution with benzene was the introduction of an EDG primary amine in position 4. An additive or synergistic effect is not to be neglected but probing this hypothesis would have needed additional synthetic efforts since 2,6-disubstituted-4-nitropyridines were not commercially available. Even so, such results were encouraging on further exploring the structural variability. Conjugation of the scaffold with functional moieties containing an acid group would be appealing even by exploiting the carbon derivatives **112** and **113**, as recently demonstrated by their N-acetyl derivatives, whose ΔT_m showed to be poorly affected^[241].

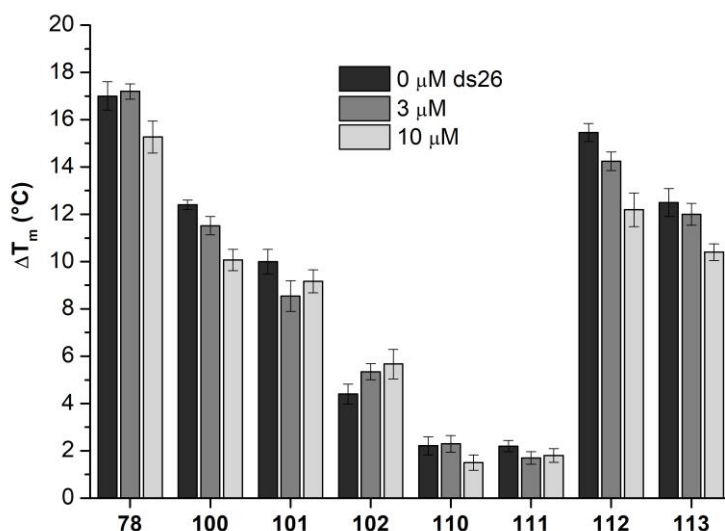


Figure 34: FRET-melting competition assay for heptacycles **78**, **100-102**, **110-113** and the human telomeric F21T sequence in the absence and in the presence of double-stranded DNA competitor (ds26). Conditions: DNA 0.25 μM, compounds 1 μM, ds26 0, 3, or 10 μM, LiCaco 10 mM (pH 7.2), LiCl 90 mM and KCl 10 mM.

Despite the two charged conformationally free side chains, which are usually associated with unspecific electrostatic interactions with phosphate backbone, all the ligands showed little interaction with double-stranded DNA (ds26 in Figure 33). A FRET-melting based competition

assay with telomeric F21T sequence confirmed this finding, as little perturbation of the ΔT_m value was observed after addition of 100 base-pair equivalents of ds-DNA (Figure 34).

The CD spectra of two of the G4s used in the FRET–melting assay (hTel21 is the untagged version of F21T) changed sensibly upon addition of the heptacyclic ligand **112** (Figure 35), meaning that, as a consequence of guest accommodation, the host conformation was altered. This is another typical signature of a strong binding interaction between a ligand and the quadruplex that can overcome the loss of stability resulting from geometry distortion.

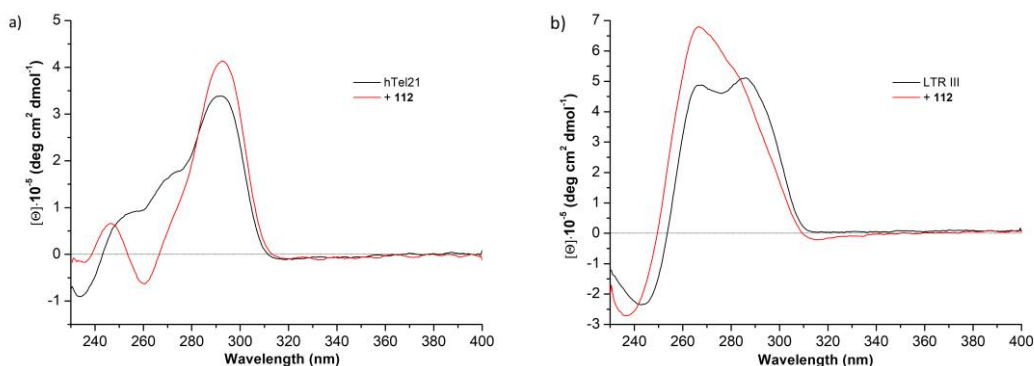


Figure 35: Circular dichroic spectra of (a) hTel21 and (b) LTRIII G4 sequences before and after addition of heptacycle **112**. Conditions: DNA 4 μ M, compounds 16 μ M, LiCaco 10 mM (pH 7.2), KCl 100 mM.

To ensure that the observed raising of melting temperature as a consequence of G4 stabilization was not biased by the use of fluorophore modified oligonucleotides, melting curves were independently obtained by means of circular dichroism measurements on the unmodified DNA sequences (Figure 36) and overall confirmed the FRET-based data mentioned above. Notably, the isothermal CD spectra in the presence of heptacyclic ligand **112** undoubtedly showed the formation of a small negative circular dichroic signal at 320–340 nm, which was decreasing upon melting (Figure 37a), that could not be coupled with any electronic transition located in DNA nucleobases. Rather, the new CD signal was clearly associated with a ligand absorption band and was arising from ligand–G4 interaction. The induced-CD (ICD) could be extending far beyond 310 nm, being a significant contribute to the observed decrease in the absolute value of the peak centered at 284 nm (Figure 37a). This evidence, however, could support both end stacking and groove binding modes.

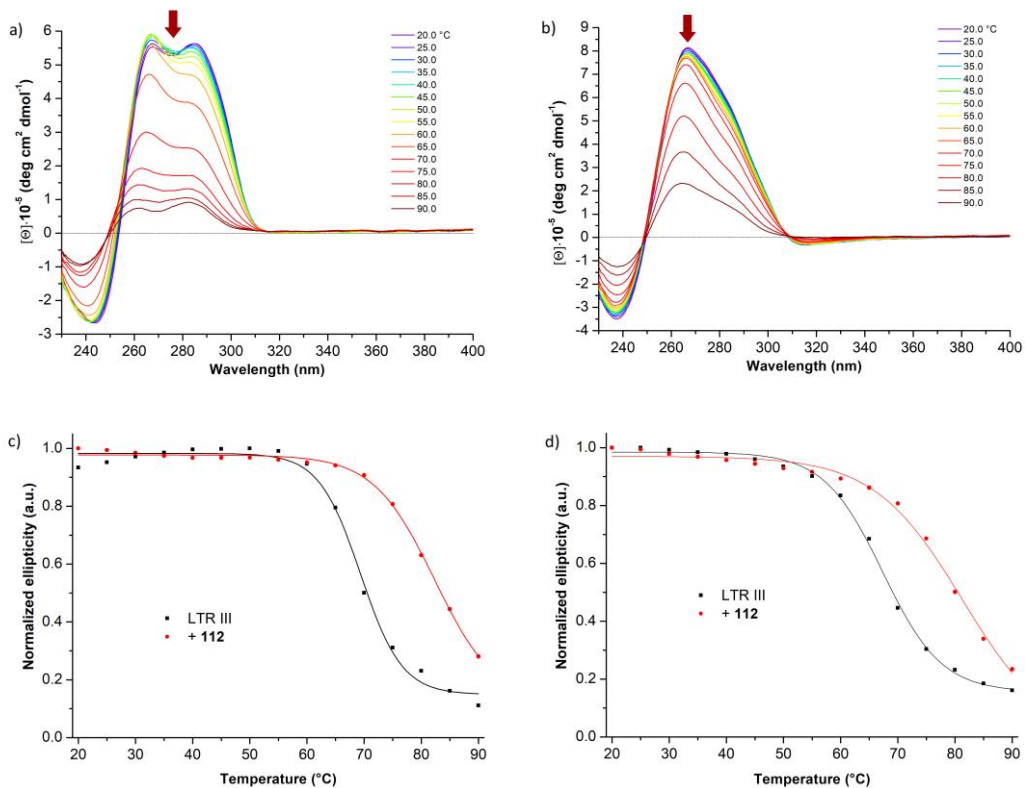


Figure 36: Isothermal CD spectra of LTRIII (a) before and (b) after addition of heptacycle **112**. Melting curves obtained from monitoring the change in the ellipticity at (c) 267 nm and (d) 289 nm (mean $\Delta T_m = 13.4$ °C), normalized to the maximum value assumed during the melting. Conditions: DNA 4 μ M, compounds 16 μ M, LiCaco 10 mM (pH 7.2), KCl 100 mM.

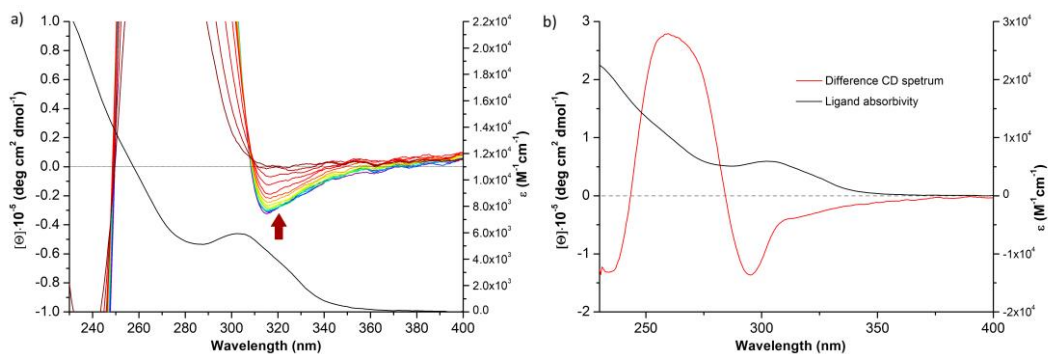


Figure 37: (a) Enlargement of Figure 36b showing the induced dichroic signal on the ligand absorption band; ligand molar absorptivity has been superimposed for a clearer comparison. (b) Comparison between the difference CD spectrum of LTRIII in the presence and in the absence of **112**, and the molar absorptivity of the ligand.

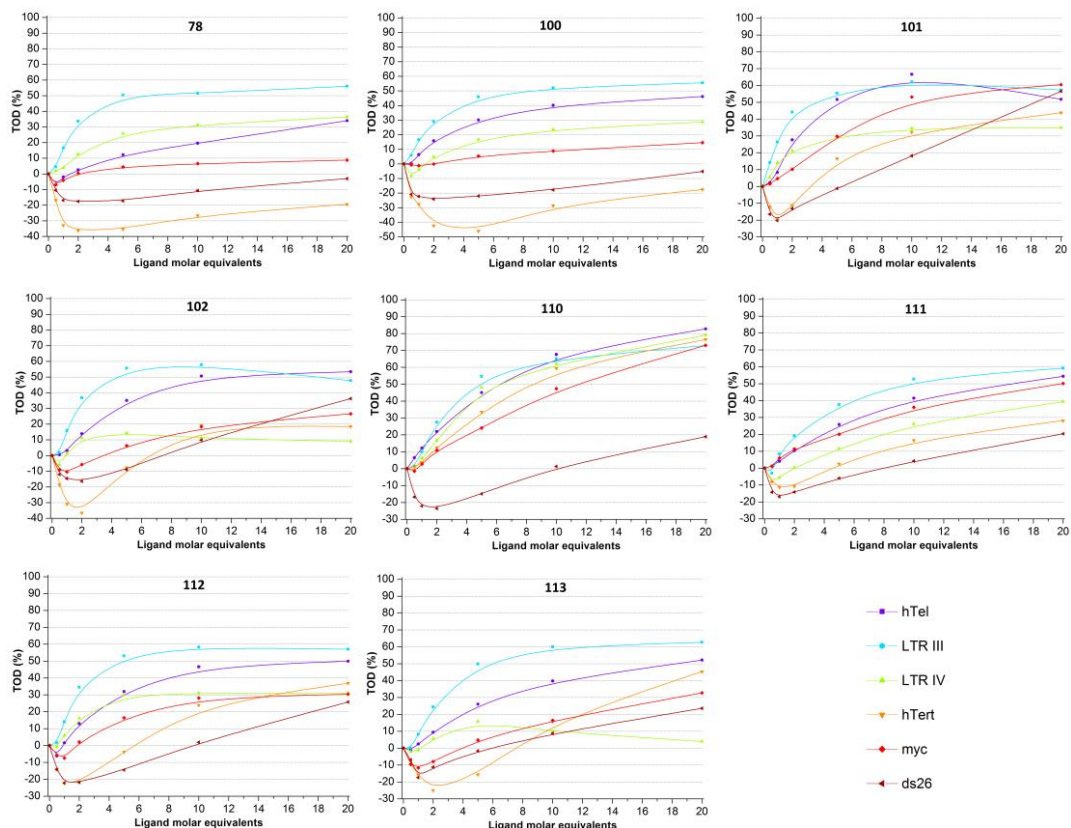


Figure 38: FID titration assay of heptacycles **78**, **100-102**, **110-113** with five selected G4s (hTel, LTRIII, LTRIV, hTert, and myc) and one ds-DNA control sequence (ds26). Conditions: DNA 1 μ M, TO 2 μ M, compounds 0–20 μ M, LiCaco 10 mM (pH 7.2), KCl 100 mM.

Fluorescence intercalator displacement (FID) was used as a further G4 affinity screening assay. The ability to displace thiazole orange, a fluorescent dye that intercalates in the DNA and binds to G4 end quartets, was probed for all the synthesized heptacyclic compounds and a panel of five G4 (Figure 38).

Remarkably, despite the good binding properties displayed in the FRET–melting assays, poor TO displacement was observed in every case, even upon addition of a large excess of ligand. In the best cases, 60% of TO was displaced as plateau was reached and, even then, the addition of 10 or more equivalents of ligand was required. Such behavior was markedly in contrast with the almost quantitative displacement observed with effective end stackers (e.g. **PhenDC3** and tetrasubstituted **NDI 9**) after addition of just 2 equivalents of ligand (Figure 39). Additionally, parallel myc quadruplex, which exhibits rigid and fairly accessible tetrads

and hence should experience the higher TO displacement, was found to be one of the least affected G4 structures.

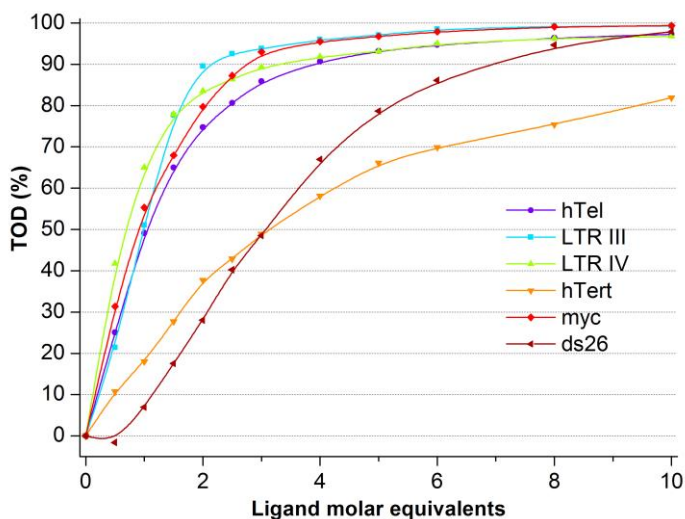


Figure 39: FID titration assay on reference tetrasubstituted NDI 9.

To gain a better perspective on the FID assay outcome, some TO–ligand competition experiments with Pu24T (a variant of myc G4) were analyzed by soft ionization MS-spectrometry. First, the mass spectrum of the sequence alone was registered in the negative mode (**Error! Reference source not found.**). Formation of three stacked tetrads was confirmed by the presence of two K^+ ions along the oligonucleotide sequence.

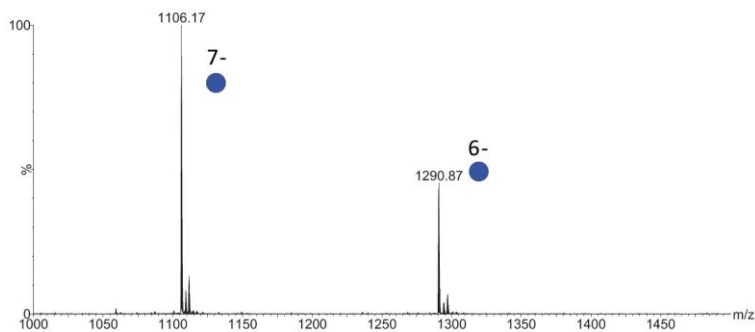


Figure 40: MS analysis of neat Pu24T G4 sequence 2 μ M. Conditions: H_2O/i -PrOH 8:2, HFIP 120 mM, TEA (pH 7.4), KCl 80 μ M. Legend: blue circle = myc. Ion total charge is displayed.

Addition of an excess of TO was accompanied by the formation of G4–TO complexes with one, two and three molecules of guest (Figure 41). Coherently, the 3:1 complex was far less abundant than the 2:1 and 1:1, and most likely arose from unspecific interactions.

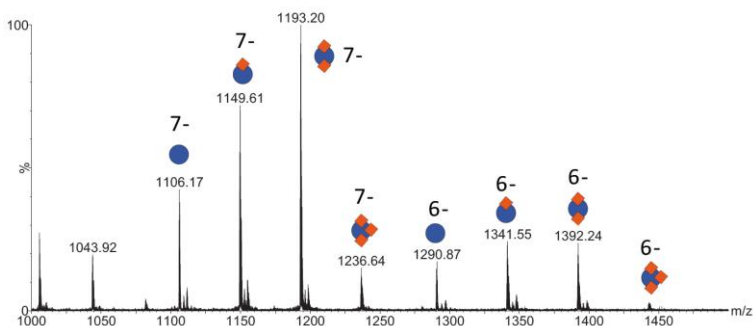


Figure 41: MS analysis of Pu24T 2 μ M incubated with TO (a) 0 μ M and (b) 16 μ M. Conditions: H₂O/*i*-PrOH 8:2, HFIP 120 mM, TEA (pH 7.4), KCl 80 μ M. Legend: blue circle = myc; orange diamond = TO. The ion total charge is displayed.

When the G4 was added with the heptacyclic ligands **110** or **100**, formation of 1:1 and 2:1 complexes was observed, the 1:1 being the most abundant species in both cases (Figure 42a and Figure 43a). As expected, when both TO and the ligand were mixed and incubated with the quadruplex, more complicated spectra were obtained (Figure 42b and Figure 43b). Several mixed complexes were formed along the already identified peaks associated to TO-G4 and ligand-G4 complexes. Thus, by comparing the fraction of TO_n-G4 which was bound by the ligand for the different TO_n-G4 complexes (Table 2), it was possible to establish that, despite the binding sites for the heptacyclic compounds and thiazole orange are different (the fraction is not dropping to 0 for either n=1 and n=2), the two ligands mutually affect each other's interaction with the G4 (*cf.* n=0 vs n=1 vs n=2).

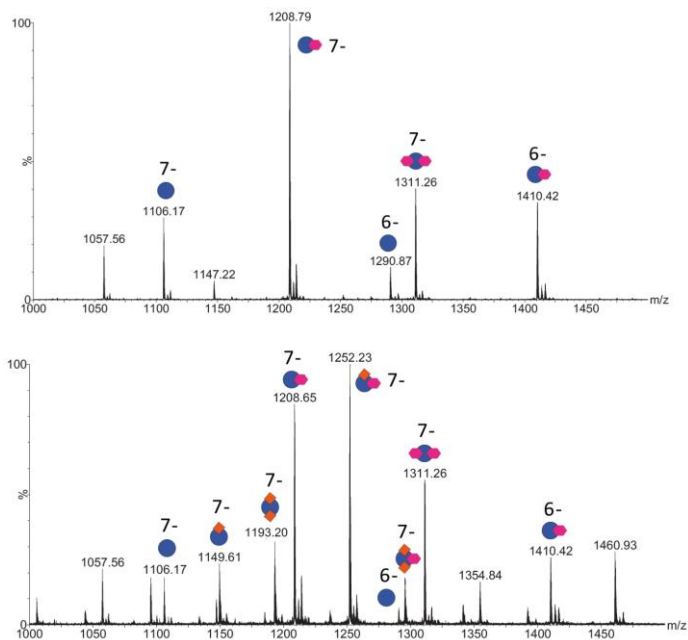


Figure 42: MS analysis of Pu24T 2 μM incubated with heptacyclic ligand 110 20 μM and TO (top) 0 μM and (bottom) 16 μM . Conditions: $\text{H}_2\text{O}/i\text{-PrOH}$ 8:2, HFIP 120 mM, TEA (pH 7.4), KCl 80 μM . Legend: blue circle = myc; purple hexagon = ligand; orange diamond = TO. The ion total charge is displayed.

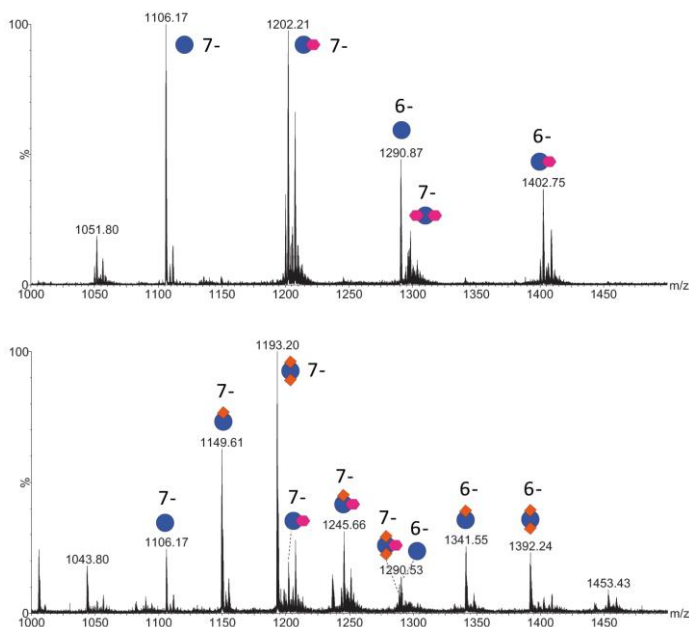


Figure 43: MS analysis of Pu24T 2 μM incubated with heptacyclic ligand 100 20 μM and TO (top) 0 μM and (bottom) 16 μM . Conditions: $\text{H}_2\text{O}/i\text{-PrOH}$ 8:2, HFIP 120 mM, TEA (pH 7.4), KCl 80 μM . Legend: blue circle = myc; purple hexagon = ligand; orange diamond = TO. The ion total charge is displayed.

Table 2: Fraction of TO_n-G4 bound with heptacyclic ligands **110** and **100**.

n		110	100
0		0.83	0.42
1		0.79	0.30
2		0.38	0.08

Interestingly, the binding of heptacycle **100** increased the affinity for the coordination of one more K⁺ ion (Figure 44), a feature normally ascribed to end stackers with a coordinating cavity.

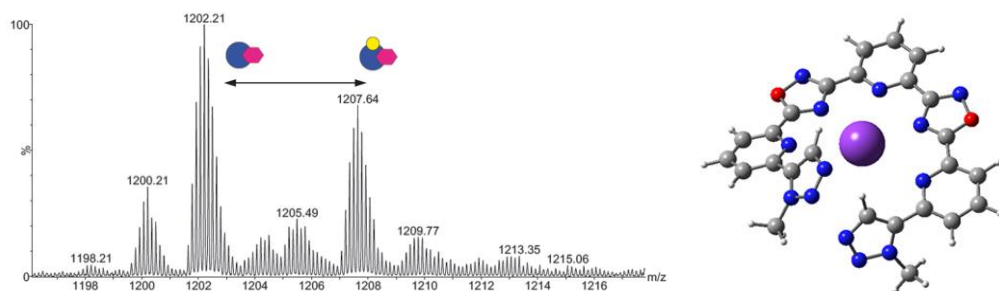


Figure 44: Enlargement of peak at $m/z = 1200$ of Figure 43a, showing an additional K⁺ coordination. Legend: blue circle = myc; purple hexagon = ligand; yellow circle = K⁺ ion. Proposed coordinating mode.

Overall, the data suggested a mixed binding mode where the ligand is more easily accommodated in a different site with respect to the end tetrads, but could also worsen or inhibit their access. A docking study performed on Pu24T and heptacyclic ligands **100**, **110** and **112** supported this statement, as the energy minima were found to coincide with an open conformer of the ligand which was accommodating one half of its oligoaryl structure into one groove of the G4, while the second half was protruding on the top tetrad and effectively hindering it (Figure 45).

The proposed substitution of pyridine with benzene aimed at understanding the role of those nitrogen atoms in providing coordination, preferential geometry and electronic affinity with the G4. Even if their actual role still needs to be fully clarified, they do provide an important recognition feature. The preliminary results are fairly encouraging into exploring the potential of these new heptacyclic structures and the flexibility of the proposed synthesis.

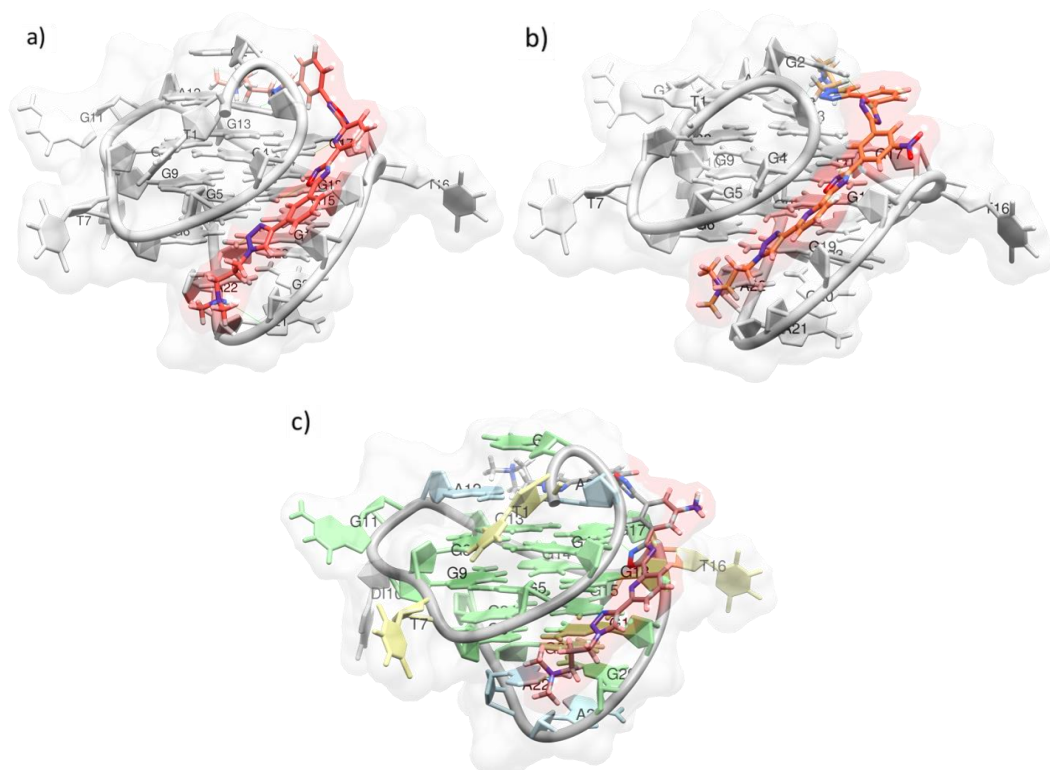


Figure 45: Docking of (a) 100, (b) 110 and (c) 112 with Pu24T (PDB: 2A5P), showing a mixed groove-loop binding mode. One half of the heptacyclic scaffold is effectively hindering one end tetrad.

CHAPTER 3 : Photoinduced G4 Alkylation

3.1 Conjugation and substituent effects on the photogeneration of prototype arylethynyl *o*-QMs

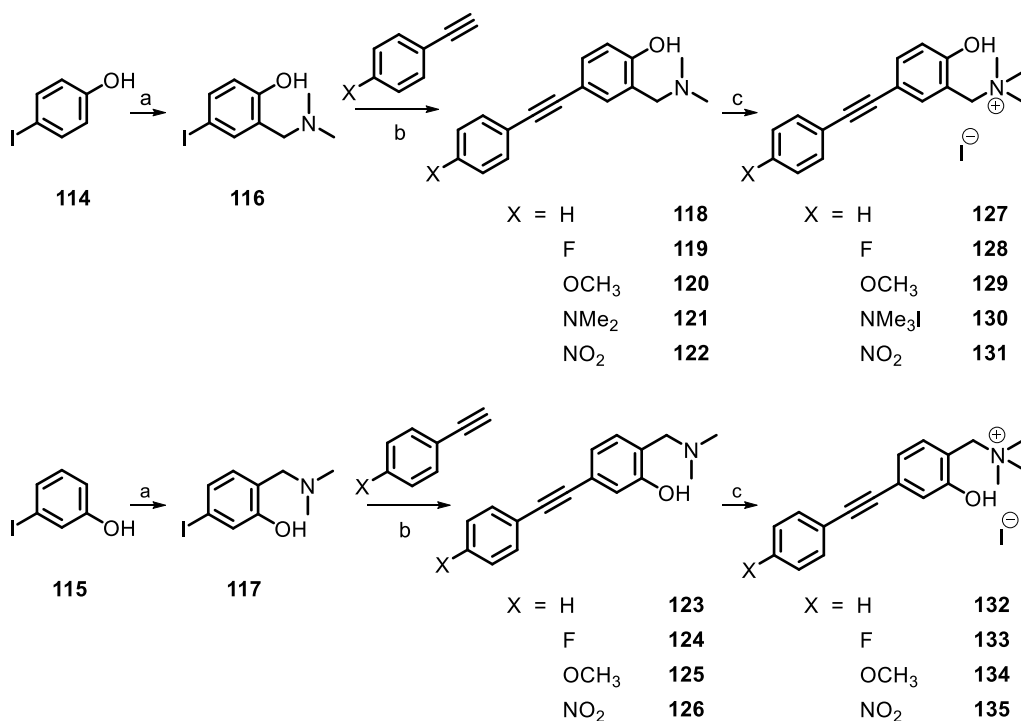
An issue often encountered when considering the *in vivo* application of any photoactive molecule is the need of long excitation wavelength ($\lambda \geq 350 - 400$ nm), in order to limit damage of the biological matrix through direct or photosensitized reactions^[242]. The thoroughly studied *o*-QMPs and *p*-QMPs systems display low absorptivity above 310 nm, making them not suitable as photoactivable alkylating agents for biological applications. At the current state of the art, few examples of systems capable of generating quinone methides through excitation with light of such wavelengths have been reported. These include naphthol derivatives^[214], BINOLs^[218, 220], bis-aryls^[215], anthrol^[243], and naphthalene diimide^[135, 244, 245] QM derivatives. Interestingly, these mono- and bis-alkylating agents exhibit similar and in some case higher photoinduced antiproliferative activity compared to psoralenes. However, the observed efficiencies of photochemical generation of these QMs are sensibly lower to those associated with benzo-QM derivatives, as demonstrated by their generally good fluorescence. Yet, extended conjugation of the original ortho-benzo-QMP as an alternative strategy to achieve the required red-shift has not been examined yet. In view of exploiting QM-like electrophiles to design new G-quadruplex covalent binders and considered that some of the best performing G4 reversible ligands (e.g. **PDS**^[81], **PDC**^[79], **PhenDC3**^[88], **Cu-ttpty**^[246], **Cbz-2Py**^[247]) benefit of a planar structure containing multiple aromatic systems that can interact with the external quartets, or less frequently with the grooves, it was interesting to investigate the effect of a conjugated aromatic moiety on benzo-QMP photoreactivity.

In this section, the effect of several arylethynyl conjugated moieties on the photogeneration of quinone methides from water-soluble Mannich bases and related quaternary ammonium salts is presented. The aim of this study was understanding how the moiety position and additional electronic substituents may affect the efficiency of *o*-QM generation in a prototype system that can be adapted to an extended planar molecule. First, the synthetic approach to the precursors will be presented. Hence, laser flash photolysis detection, characterization of the transient QM species and reactivity studies will be shown. From the

overall data, some general conclusions will be drawn on how the different structural features act to tune the photoreactivity of the precursor. Moreover, the exploitation of less reactive alkylating agents as singlet oxygen sensitizers will be proposed. Most of the data described in this section have been published in Journal of Organic Chemistry^[248].

3.1.1 Synthesis of arylethynyl QM precursors

To avoid any photoisomerization, typical in stilbenes^[249] and azobenzenes^[250], that would eventually lower the QM generation quantum yield, an alkynyl unit was chosen as an electronically conjugating spacer between two aryl groups. Consequently, a library of 4'-substituted 4- and 5-arylethynyl Mannich bases and quaternary ammonium salts have been synthesized following a two steps protocol (Scheme 34), starting from the commercially available *p*- and *m*-iodophenol **114** and **115**.



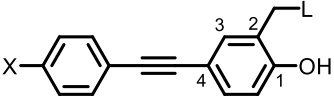
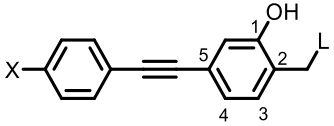
Scheme 34: Synthesis of 4- and 5-arylethynyl Mannich bases and quaternary ammonium salts **118-135**. (a) PFA, NHMe₂ 33% in EtOH, EtOH, reflux, 2 h (yields: 30-35%); (b) Pd(PPh₃)₄ 3%, CuI 17%, TEA, rt, 2.5 h (yields: 70-94%); (c) MeI, ACN, rt, 24 h (yields: 95-99%).

These phenols were first converted into their Mannich bases **116** and **117**, *via* a published procedure^[251]. Subsequently, the iodo-derivatives were coupled with commercially available 1-ethynyl-4-substitutedbenzenes through Sonogashira cross-coupling in neat triethylamine (TEA) with Pd(PPh₃)₄ (3% mol) and CuI (17% mol), providing derivatives **118-126** from good to excellent yields (62-97%). The presence of free hydroxyl groups is hardly compatible with the reaction conditions needed for Sonogashira cross-couplings; therefore, an additional protection step is normally necessary for the reaction to take place. Yet, in the presence of such Mannich bases, the cross-coupling was effective on the free phenol derivatives (**116** and **117**). Likely, this has to be ascribed to the formation of an intramolecular H-bond between the OH and the amino moiety which ensures a self-protective effect. Methylation of the tertiary amine was accomplished by treating with excess MeI in acetonitrile, and quantitatively yielded the quaternary ammonium salts **127-135** (Scheme 34).

3.1.2 UV-vis absorption of QMPs

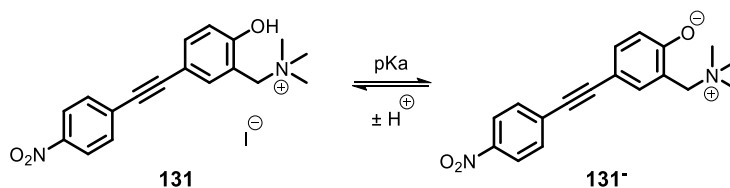
UV-vis spectra were measured in 1:1 aqueous ACN, showing bands maxima ranging from 285 nm to 348 nm (Table 3).

Table 3: Absorption maxima in ACN:H₂O 1:1 of 4- and 5-arylethynyl Mannich bases and their quaternary ammonium salts.

	X	L=NMe ₂	λ _{max} (nm)	L=NMe ₃ ⁺ I ⁻	λ _{max} (nm)
	H	118	308	127	292
	F	119	305	128	285, 302
	OCH ₃	120	313	129	320
	NMe ₂	121	326	-	-
	NMe ₃ ⁺	-	-	130	296, 308
	NO ₂	122	335	131	348
	H	123	289	132	290
	F	124	285	133	285, 301
	OCH ₃	125	317	134	320
	NO ₂	126	340	135	330

Compared to the unsubstituted o-QMP^[252], the addition of an arylethynyl conjugating moiety shifted the absorption of the precursor by about 20-30 nm, regardless of the substitution position. Moreover, the position of the maximum in the absorption spectra was strongly affected by the substituent X. The most intense bathochromic shift was observed for the pale-yellow nitro-derivatives **122**, **126**, **131**, and **135**). The presence of a push-pull motif caused, in fact, the appearance of an absorption tail up to 450 nm.

Much attention has been focused to the absorption properties of quaternary ammonium salt **131** conjugate base (Scheme 35), the zwitterion **131**⁻, which exhibits a maximum at 405 nm and a 500 nm absorption tail. Spectrophotometric titration revealed that the acidic proton has a pKa of 7.55 ± 0.01 (Figure 46). This means that under physiological conditions (pH = 7.2) 31% of the molecules are ionized, therefore providing a true visible light harvesting QMP. For comparison, the pKa of 1-(2-hydroxyphenyl)-N,N,N-trimethylmethanaminium iodide is 8.74^[253], leading to the presence of only 3% of zwitterionic species at pH 7.2, still absorbing in the UV region.



Scheme 35: Protonation equilibrium for **131**.

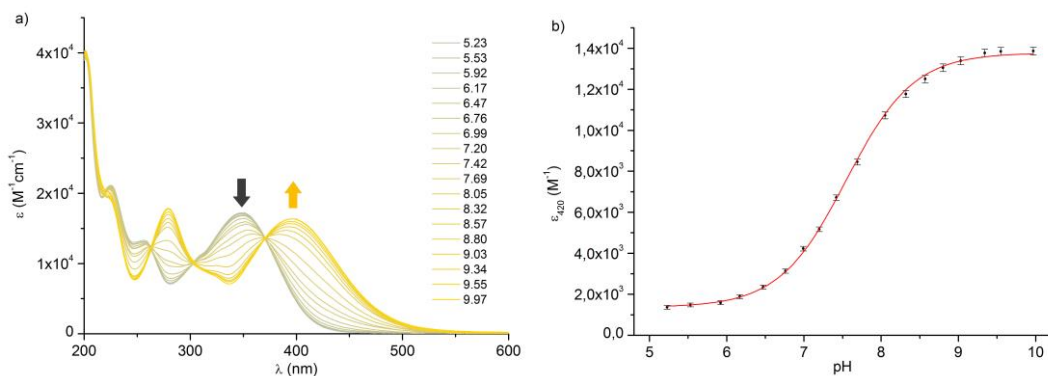
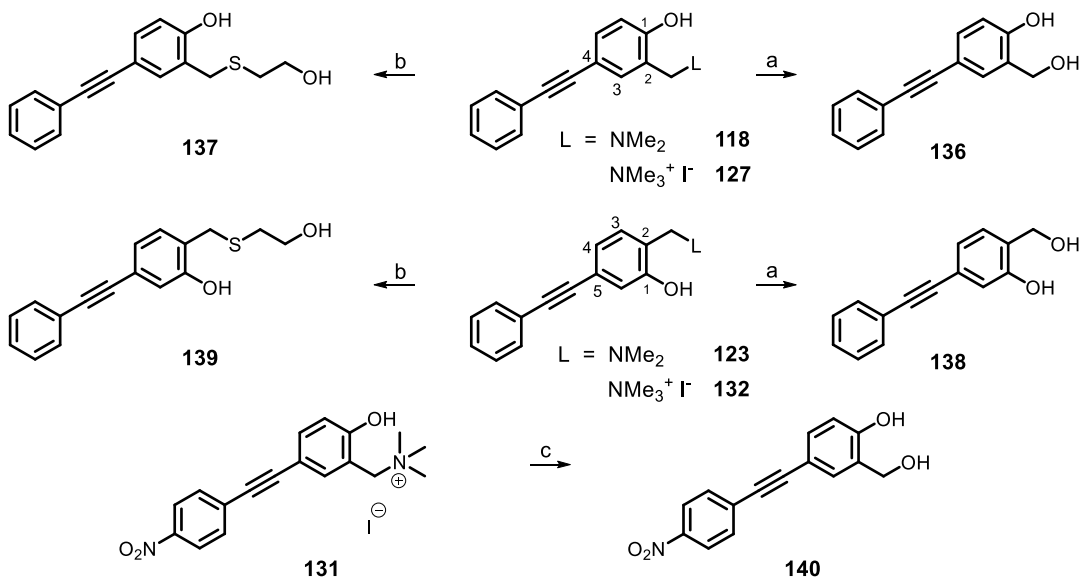


Figure 46: (a) Absorption spectra of compound **131** $7.30 \cdot 10^{-5}$ M in H₂O at different pH values; gray and yellow traces correspond to **131** and **131**⁻ respectively. (b) Molar absorptivity monitored at 420 nm; non-linear fitting of the experimental data yielded a pKa value of 7.55 ± 0.01 .

3.1.3 Photoreactivity and QM trapping

To investigate the photochemical reactivity of the putative QMPs, photohydrolysis reactions of six selected compounds were first performed by irradiating 10^{-4} M solutions in 1:1 aqueous ACN and buffered water (phosphate buffer), in the presence of molecular oxygen (Scheme 36, pathways a and c). In each case, the major product was isolated by column chromatography and reaction yields were derived by measuring the conversion by HPLC (Figure 47).



Scheme 36: QMs trapping products by photogeneration from QMPs. All reactions were performed in a Rayonet© multilamp reactor using 2 x 15 W UV lamps and 20 mL quartz tubes. (a) 10^{-4} M solution in ACN-H₂O 1:1, 310 nm, 5 min (yield: 35% from **118**, 10% from **123**, 89% from **127** and 64% from **132**); (b) 10^{-4} M solution in ACN-H₂O 9:1, 2-mercaptoethan-1-ol 10^{-2} M, 310 nm, 5 min (yield: 73% from **127** and 38% from **132**); (c) 10^{-4} M solution in ACN-H₂O 1:1, 360 nm, 450 min (yield: 98%).

The irradiations of unsubstituted systems **118**, **123**, **127** and **132** were performed in a Rayonet© multilamp reactor provided with two 15 W lamps centered at 310 nm, while two 15 W lamps centered at 360 nm were employed for the most red-shifted systems **122** and **131**. A duplicate of the same samples was kept in the dark and used as a reference: in every case the reactivity was completely quenched in the absence of light, thus demonstrating its photochemical nature. Furthermore, ferrioxalate actinometry was used to quantify the efficiency of the photohydration, in terms of quantum yield (Φ_R). To obtain an accurate value for Φ_R , based on actual reactant photochemistry and photophysics, these measurements

were performed at low conversion (<20%). Although both the irradiations of 4-arylethynyl QMPs **118** and **127** gave clean conversion to product **136** (Scheme 36), the quaternary ammonium salt (**127**) was a much more efficient QMP than its Mannich base (**118**), both in terms of chemical yield after 5 minutes of irradiation (86% vs 35%) and quantum yield ($\Phi_R=0.48\pm 0.02$ vs $\Phi_R=0.06\pm 0.01$). In buffered solution, at pH 7.4, the photoreactivity of both compounds was very similar with respect to aqueous ACN, yielding identical photoproducts with a slightly different efficiency, lower for the precursor **127** ($\Phi_R=0.30\pm 0.08$) and higher for **118** ($\Phi_R=0.08\pm 0.01$).

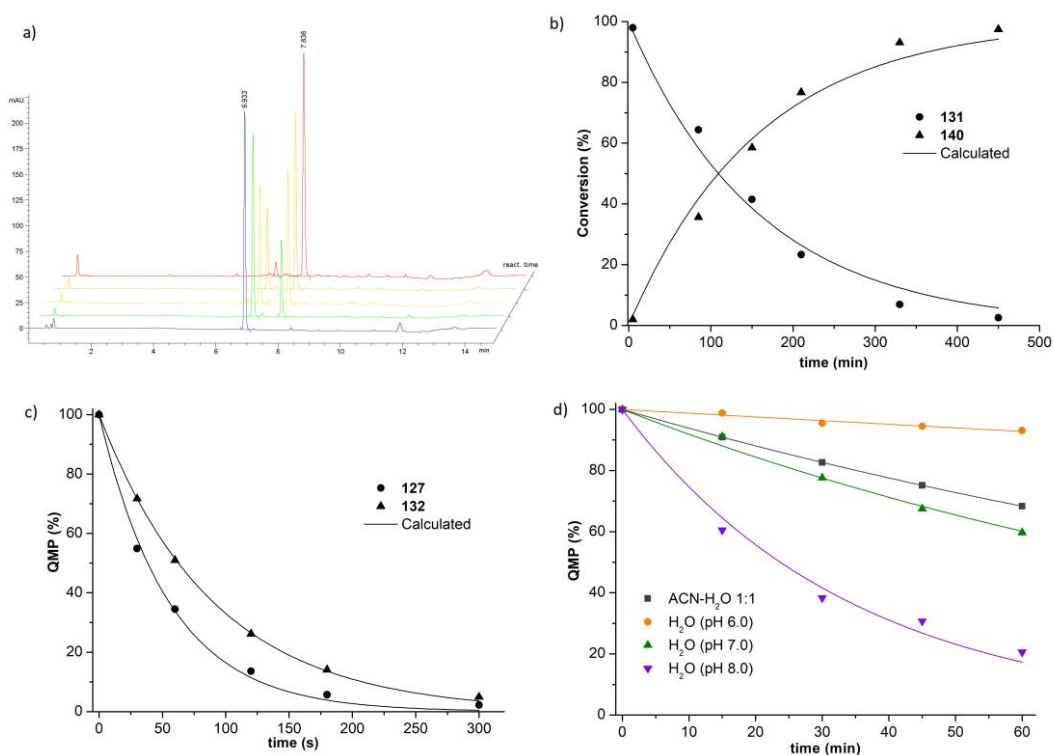


Figure 47: (a) Irradiation time-dependent HPLC chromatograms and (b) kinetic plot for conversion of **131** to **140** in ACN:H₂O 1:1. (c) Kinetic plot of depletion of **127** and **132** in ACN:H₂O 1:1. (d) Comparison of **131** depletion rate in ACN:H₂O 1:1 and in H₂O at different pHs.

Similarly, irradiation of isomeric 5-arylethynyl QMP **132** gave good conversion to product **138**, although with lower efficiency if compared to **127** ($\Phi_R=0.25\pm 0.01$ in 1:1 aqueous ACN, $\Phi_R=0.06\pm 0.01$ in water at pH 7.4). Besides, the related Mannich base **123** gave the same product in both very low reaction yield (10%) and efficiency ($\Phi_R=0.02\pm 0.01$ in 1:1 aqueous ACN, $\Phi_R=0.04\pm 0.01$ in water at pH 7.4). In all these cases, if the irradiation was extended

beyond 5 minutes the reaction yield lowered as a consequence of absorption and resulting reactions from the primary photoadduct, leading to the formation of a complex mixture of byproducts.

On the contrary, the nitro derivative **131** gave the photoproduct **140** very cleanly (Figure 47a and b) upon irradiation at 360 nm in ACN-H₂O 1:1. Despite the outstanding chemical yield (98%) the irradiation time was much longer (7.5 hours) reflecting a lower quantum yield ($\Phi_R=7\pm 1\cdot 10^{-4}$). The effect of the nitro substituent could be summarized with an overall decrease of the efficiency of QM generation by about 700 times. As a consequence, the photoreactivity of the corresponding Mannich base **122** was even lower and indeed it was recovered unreacted after 2 hours.

Photohydrolysis quantum yield of **131** was also measured in buffered water at pH 6.0, 7.0 and 8.0 (Figure 47d). Since at pH 8 and to a lesser extent at pH 7 other adducts formed together with **140**, most likely due to the competition of O- and C- nucleophilic phenolate with water for the electrophilic QM, in such cases the quantum yield was derived from QMP consumption rather than adduct formation. Despite still being very low, QM generation efficiency increased by raising solution pH (at pH 6.0 $\Phi_R=(1.4\pm 0.4)\cdot 10^{-4}$, at pH 7.0 $\Phi_R=(9\pm 1)\cdot 10^{-4}$ and at pH 8.0 $\Phi_R=(43\pm 8)\cdot 10^{-4}$). Considering that trapping of QM by a water molecule is by far the most probable event, even for low pH values, and it contributes by a constant factor (approximately 1) to the overall quantum yield, a higher Φ_R value cannot be ascribed to a higher concentration of OH⁻, but rather to the intrinsically higher quantum yield associated with the conjugated base **131**⁻. This is consistent to what observed by Basarić with some prototype cresol Mannich base QMPs^[213] and could be explained by the fact that proton abstraction is no more necessary to yield the QM, resulting in a more efficient overall process. Importantly, under physiological conditions, in buffered water at pH 7.4, **131** showed to be also reactive using visible light at longer wavelength ($\lambda > 400$ nm), where the only absorbing species was the zwitterionic conjugate base, **131**⁻. This evidence has remarkable implications in view of the application of these systems within a biological context.

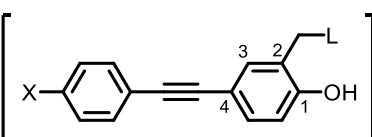
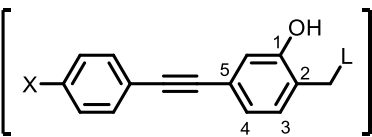
The general QMP photoreactivity of four selected QMPs was further investigated in the presence of thiols (Scheme 36, pathway b), which are well-known efficient QM traps. Thus,

thioethers **137** and **139** were isolated after irradiation of **127** and **132** in ACN-H₂O 1:1, in the presence of 10⁻² M of freshly distilled 2-mercaptoethan-1-ol. However, in these conditions the main products still were alcohols **136** and **138**, due to solvent competition for QM. On the contrary, the reactivity was considerably lower in neat ACN. Thus, a mixture of ACN-H₂O 9:1 was found as a good compromise so that **136** and **138** became minor by-products.

3.1.4 Laser flash photolysis QM and T₁ detection

Laser flash photolysis (LFP) measurements were performed to probe for quinone methides or additional competitive transient generation and elucidate the underlying photophysics and photochemistry. For the scope, 10⁻⁴ M solutions of putative QMPs **118-135** in ACN, ACN-H₂O 1:1 and buffered water (pH 7.4) were irradiated with a Nd:YAG laser at 266 nm. For the nitro-derivatives **122**, **126**, **131**, and **135**, an excitation wavelength of 354 nm was also used. Moreover, the measurements were performed both in Ar- and O₂-purged solutions.

Table 4: T-T absorption maxima in ACN:H₂O 1:1 of 4- and 5-arylethynyl Mannich bases and their quaternary ammonium salts.

	X	L=NMe ₂	λ _{max} (nm)	L=NMe ₃ ⁺ I ⁻	λ _{max} (nm)
	H	118	435	127	445
	F	119	440	128	440
	OCH ₃	120	450, 480	129	n.a.
	NMe ₂	121	545	-	-
	NMe ₃ ⁺	-	-	130	440
	NO ₂	122	600	131	570 broad
	H	123	415 broad	132	425
	F	124	415 broad	133	420
	OCH ₃	125	440	134	460
	NO ₂	126	590	135	550 broad

For all derivatives, a transient absorption with a maximum at 430–600 nm (as a function of the substituents X, Table 4) was observed in Ar-purged ACN solutions. In addition, the optical density at this wavelength was effectively quenched by molecular oxygen (Figure 48). Based on this evidence and considering the similarity with published triplet–triplet absorption spectra for phenol and naphthol, the observed spectral footprint was assigned to the lowest triplet excited state (T_1).

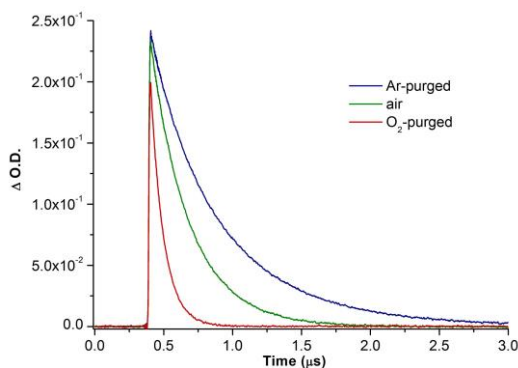


Figure 48: T_1 decay traces of **126** in Ar- and O_2 -purged ACN solutions, monitored at 590 nm.

Besides the fast decaying triplet at 435nm, the generation of an intense absorption band with a maximum at 365 nm, resembling that of a typical QM^[191, 254], was observed in the transient spectra of prototype compound **118** obtained in Ar-purged 1:1 aqueous ACN solution (Figure 49a). Compared to T_1 , this signal was much more stable being still observable after several ms (Figure 49b). In addition, the transient was not affected by the presence of molecular oxygen, but it was efficiently quenched by 2-mercaptoethan-1-ol (Figure 49c). As its lifetime increased in neat ACN, a quenching mechanism involving H_2O was also evident. Pseudo-first order rate constants (k_{obs}) were obtained after data fitting with a first order kinetic law from the LFP decay traces (Eqn 1 and 2).

$$-\frac{d[\text{Transient}]}{dt} = k_{obs} \cdot [\text{Transient}] \quad (1)$$

$$k_{obs} = k_2 \cdot [\text{RSH}] + k_{H_2O} \quad (2)$$

Hence, an observed rate constant $k_{obs} = (5.9 \pm 0.1) \cdot 10^2 \text{ s}^{-1}$ was measured for the hydration reaction, while second order rate constant for the quenching reaction with 2-mercaptoethan-1-ol was extracted from the slope of the k_{obs} vs thiol concentration plot, after

linear regression analysis. A value of $k_2 = (1.18 \pm 0.04) \cdot 10^5 \text{ M}^{-1} \text{ s}^{-1}$ was obtained in 1:1 aqueous ACN (Figure 49d). Both these values are typical for trapping reactions involving highly electrophilic QM intermediates^[187, 192]. Moreover, HPLC analysis of the LFP irradiated solution in the presence of thiol (after 50 pulses) revealed the formation of the adduct **23**. Overall, this evidences undoubtedly allowed the assignment of the transient at 365 nm to the quinone methide **QM1** (Table 5), suggesting the role of **118** as QMP.

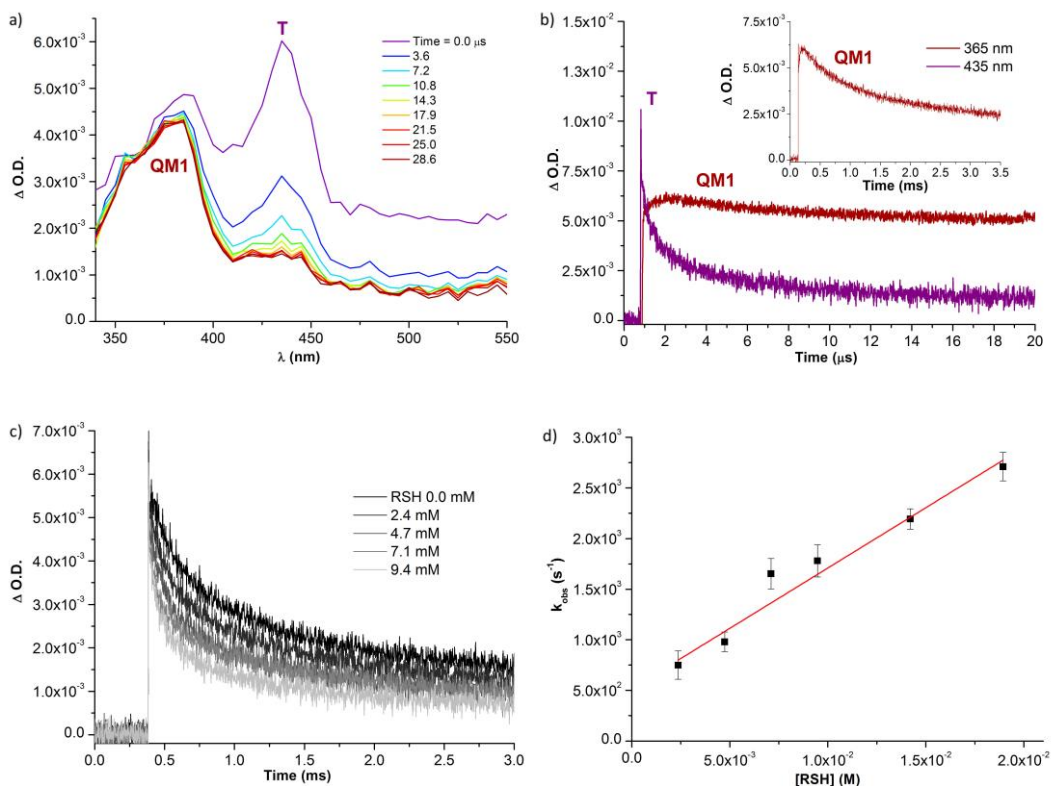
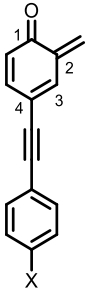
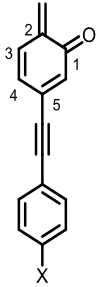


Figure 49: (a) Transient absorption spectra of Ar-purged ACN:H₂O 1:1 solution of **118**. (b) Decay traces monitored at 435 and 365 nm and relative to T₁ and **QM1**; inset: same decay trace within a longer time scale. (c) **QM1** decay traces monitored at 365 nm with increasing concentrations of 2-mercaptoethan-1-ol. (d) Linear regression of k_{obs} vs thiol concentration yielded a bimolecular rate constant of $(1.18 \pm 0.04) \cdot 10^5 \text{ M}^{-1} \text{ s}^{-1}$ for the quenching of **QM1** with 2-mercaptoethan-1-ol.

Likewise, the same LFP transient characterization was performed with all the compounds under study (**118-135**), leading to the identification of quinone methides **QM1-10** in both ACN and 1:1 aqueous ACN (Table 5). Overall, the LFP study confirmed the role of all the compounds **118-135** as QMPs, although they were characterized by rather different quantum efficiency. Importantly, the QM generation efficiency also showed to be influenced

by the absence or presence of a protic solvent. Moreover, the same structural differences on the generated quinone methides tuned their reactivity with trapping nucleophiles.

Table 5: Structures and absorption maxima of 4- and 5-arylethynyl quinone methides (**QM1-QM10**) photogenerated from QMPs **118-135** in ACN and in ACN:H₂O 1:1. Measured pseudo-first order and second order kinetic constants for QM trapping reactions with the aqueous solvent and 2-mercaptoethan-1-ol.

	X	QM	λ_{\max} (nm)		H ₂ O	RSH
			ACN	ACN:H ₂ O 1:1	k_{obs} (s ⁻¹)	k_2 (M ⁻¹ s ⁻¹)
	H	QM1	365, 375	380	$(5.9 \pm 0.1) \cdot 10^2$	$(1.18 \pm 0.02) \cdot 10^5$
	F	QM2	370, 530, 620	380, 540, 630	$(3.5 \pm 0.2) \cdot 10^2$	-
	OCH ₃	QM3	390	410	$(2.6 \pm 0.2) \cdot 10^2$	$(1.3 \pm 0.1) \cdot 10^3$
	NMe ₂	QM4	425, 475	440, 485	$(2.0 \pm 0.3) \cdot 10^2$	$(7.0 \pm 0.2) \cdot 10^2$
	NMe ₃ ⁺	QM5	350, 380	340, 350	$(1.77 \pm 0.05) \cdot 10^3$	-
	NO ₂	QM6	420	420	$(3.41 \pm 0.08) \cdot 10^4$	$(5.8 \pm 0.4) \cdot 10^5$
	H	QM7	350	350	$(9.8 \pm 0.1) \cdot 10^0$	-
	F	QM8	350	350	$(6.6 \pm 0.3) \cdot 10^2$	$(7.7 \pm 0.1) \cdot 10^2$
	OCH ₃	QM9	370	360	$(5.32 \pm 0.04) \cdot 10^1$	-
	NO ₂	QM10	370	400	$(4.39 \pm 0.08) \cdot 10^4$	$(3.5 \pm 0.1) \cdot 10^4$

3.1.5 Conjugation, leaving group and solvent effects

In neat acetonitrile, without aqueous cosolvent, the Mannich base **5** displayed transient spectra quite similar to those obtained in ACN:H₂O 1:1 by LFP irradiation at 266 nm, with absorption maxima at 430 nm for T₁ and 370 nm for **QM1** (Figure 50a). By contrast, the transient spectra of the isomeric 5-arylethynyl Mannich base **123** exhibited a much more intense absorption band centered at 430 nm, which was still assigned to the triplet excited state T₁ due to the efficient quenching by molecular oxygen. A second long-living absorption

centered at 350 nm was detected as well, but the signal was too weak to observe any significant difference in the presence of trapping nucleophiles (Figure 50b).

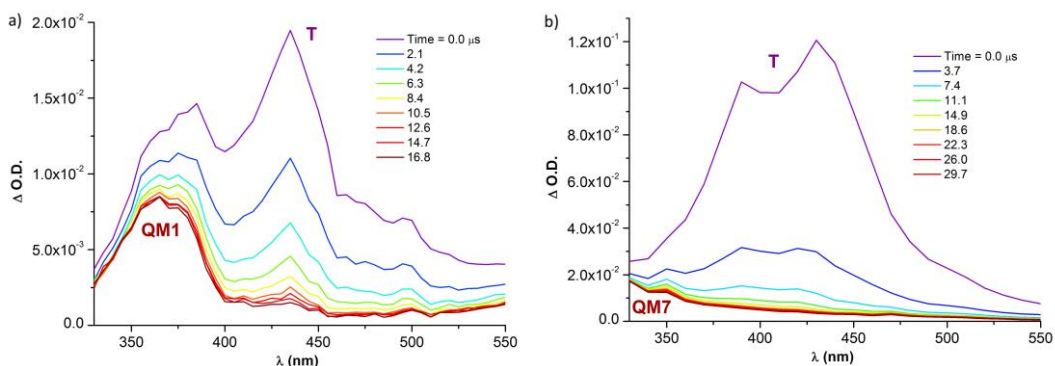


Figure 50: Transient absorption spectra of Ar-purged 10^{-4} M ACN solutions of (a) **118** and (b) **123** irradiated at 266 nm.

The very same LFP irradiations of **118** and **123** were performed in 1:1 aqueous acetonitrile and in buffered water solution at pH 7.4. In both cases, the protic conditions reduced the efficiency of T_1 generation. However, while on **118** this influence was limited and the efficiency of **QM1** generation remained substantially unaffected (Figure 51a), the detrimental effect on **123** triplet generation allowed the detection of **QM7** as a stable species within 1 ms, exhibiting an absorption maximum centered at 350 nm (Figure 51b). Importantly, no significant difference between buffered water and aqueous ACN was evident (Figure 52).

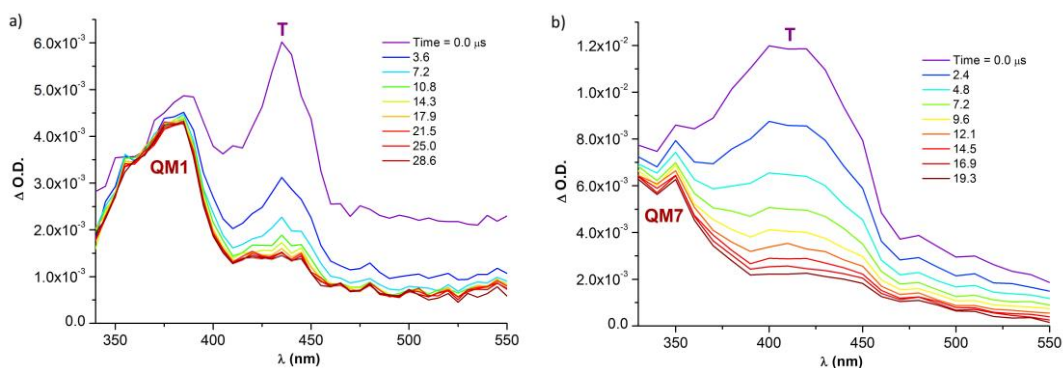


Figure 51: Transient absorption spectra of Ar-purged 10^{-4} M solutions in ACN:H₂O 1:1 of (a) **118** and (b) **123** irradiated at 266 nm.

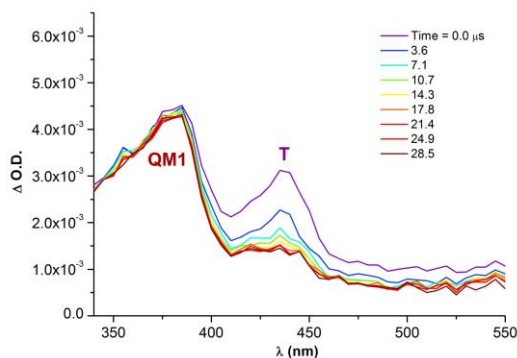


Figure 52: Transient absorption spectra of **118** in Ar-purged buffered water solution (pH 7.4), irradiated at 266 nm.

LFP irradiation of the quaternary ammonium salt **127** in 1:1 aqueous ACN generated a decaying transient absorption spectrum strongly resembling the one obtained from the corresponding Mannich base **118**. Indeed, the absorption band with a maximum at 380 nm which was stable within 1 ms time scale was easily assigned to **QM1**, while the faster decaying band centred at 450 nm was ascribed to the lowest triplet excited state (Figure 53a). Besides those similarities, the signal due to **QM1** was roughly 5 times more intense, implying a roughly same increase in its concentration.

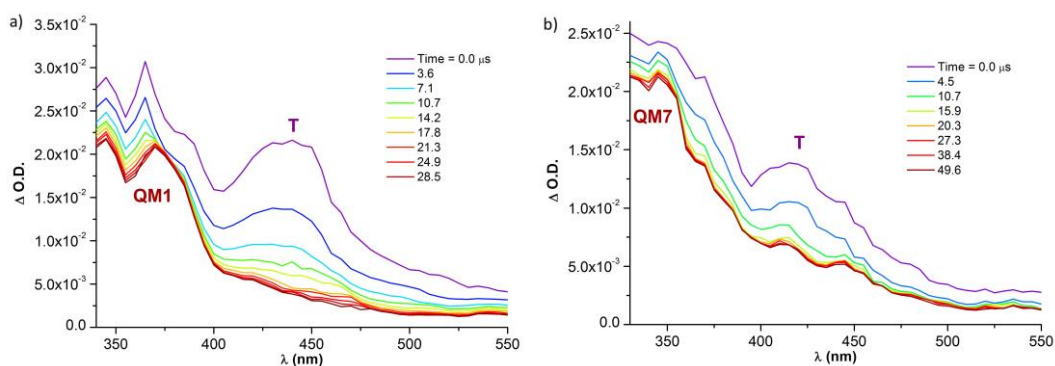
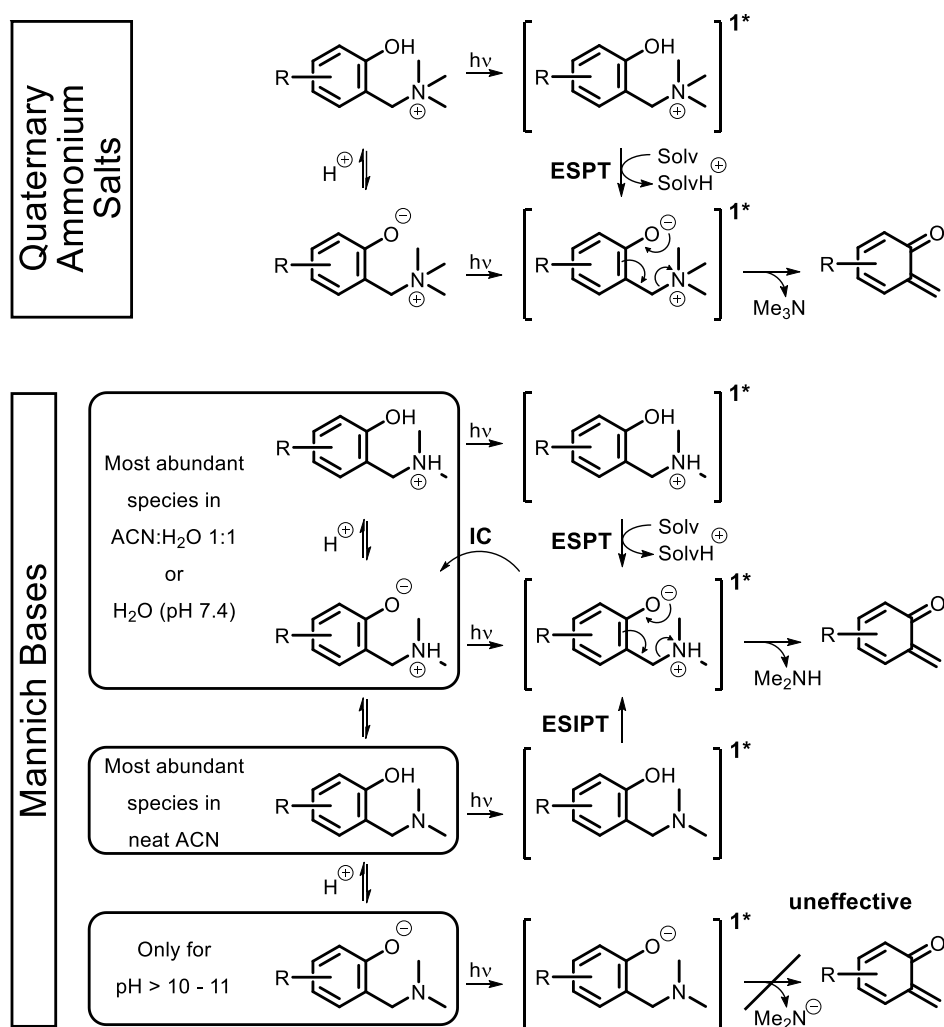


Figure 53: Transient absorption spectra of Ar-purged 10^{-4} M solutions in ACN:H₂O 1:1 of (a) **127** and (b) **132** irradiated at 266 nm.

Similarly, the quaternary ammonium salt **132** generated a transient absorption spectrum (Figure 53b) comparable with the one obtained from the corresponding Mannich base **123**, but the intensity of the signal ascribed to **QM7** immediately after the laser pulse was roughly 3.8 times more intense.

In summary, from preliminary LFP study performed on unsubstituted prototype system (X=H) both 4- and 5-substituted QMPs displayed similar capacity to generate the corresponding QM, although photohydration quantum yield measurement indicated that the 4-arylethynyl derivatives are generally better QMPs than the 5-isomer analogues. The electron-withdrawing inductive effect (-I) of the alkynyl substituent on QM photogeneration could rationalize the observed trend. In particular, the higher -I effect in 5-substituted QMPs implicates a lower acidity of the phenol in its S_1 excited state^[255] which in turn translates into lower efficient ESIPT and ESPT mechanisms (Scheme 37).



Scheme 37: Proposed mechanisms involved in the generation of QMs from Mannich bases and quaternary ammonium salts precursors. Competing T_1 states are not shown.

Besides a remarkable solvent effect was observed, namely the depletion of the T_1 population caused by water, no significant difference was recorded in the QM generation. However, preparative phototrapping reactions with 2-mercaptoethan-1-ol showed a generally increased QM generation under protic conditions if compared to neat ACN. This solvent effect on QMP photoreactivity is justifiable considering that QM formation proceed via ionic species and a basic atom is needed to allow ESPT to the solvent (Scheme 37). Suppression of T_1 population by the ISC process then might be an indirect consequence of more competing ESPT reaction from S_1 ^[256].

Definitely the most significant structural feature controlling the efficiency of QM generation was the nature of the leaving group, where the quaternary ammonium salts proved to be far better performing QMPs than the corresponding Mannich bases. Indeed, preparative photohydrations showed a 10-fold enhancement in the reactivity of the precursors when the quaternary ammonium salt was used in place of the Mannich base.

This latest observation could be rationalized considering that Me_3N is a better leaving group compared to Me_2NH as it is a worse nucleophile, therefore resulting in a faster elimination step which preceding QM formation (Scheme 37). Moreover, an excited-state deactivation by internal conversion exploiting the large amplitude stretching vibrations of the hydrogen in the O---H-N bond system^[257, 258] could be acting for the Mannich bases.

3.1.6 Substituent effect on QM photogeneration

When the 4-substituted nitro-group containing QMPs **122** and **131** were irradiated at 354 nm in aqueous ACN, a strong transient absorption ascribed to a T-T transition was observed at about 600 nm (Figure 54a and b). Besides the T_1 , an additional weak absorbing species was detected at 420 nm for Mannich base **122**. Considering the lack of influence of molecular oxygen and the quenching effect of 2-mercaptoethan-1-ol (Figure 55a), this species was assigned to **QM6**. In this case, the role of the leaving group was even more remarkable, as the very same transient became 10 times more intense by irradiating the quaternary ammonium salt **131**.

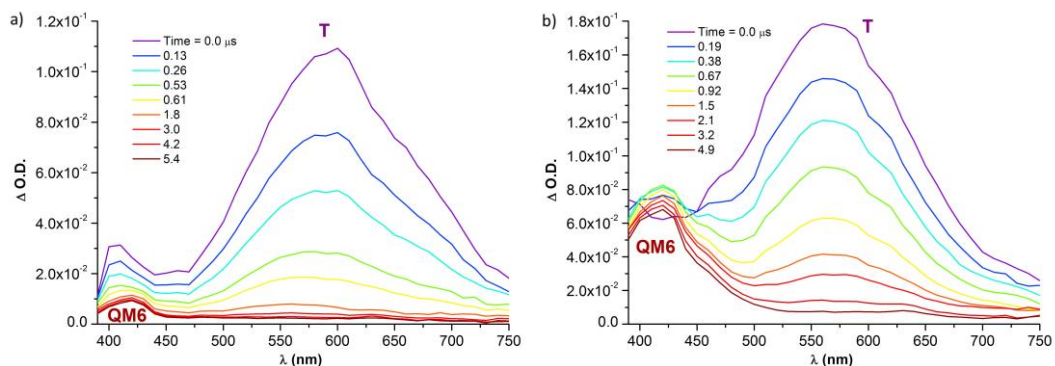


Figure 54: Transient absorption spectra of Ar-purged 10^{-4} M solutions in ACN:H₂O 1:1 of (a) **122** and (b) **131** irradiated at 354 nm.

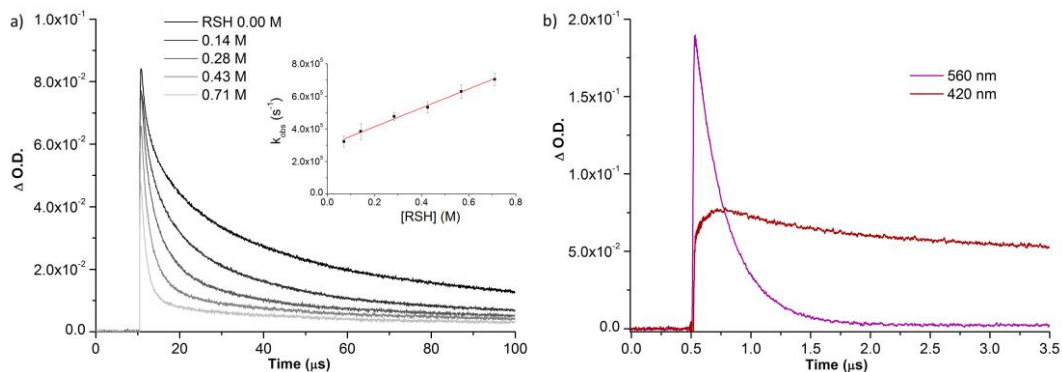
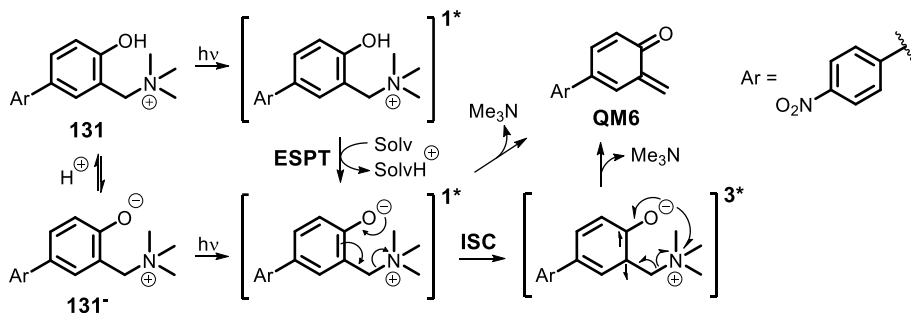


Figure 55: (a) Influence of increasing concentration of 2-mercaptoethan-1-ol on the decay trace of **QM6** at 420 nm. Inset: quenching plot k_{obs} vs thiol concentration, which yielded a bimolecular rate constant of $(5.8 \pm 0.4) \cdot 10^5 \text{ M}^{-1} \text{ s}^{-1}$. (b) Decay traces monitored at 560 and 420 nm, relative to T_1 and **QM6**, measured after irradiation at 354 nm of an Ar-purged 10^{-4} M solution in ACN:H₂O 1:1 of **131**.

Surprisingly, right after the laser pulse, the transient absorption trace monitored at 420 nm exhibits a rising which paralleled the decay trace of the T_1 (Figure 55b). This evidence could suggest a possible and unprecedentedly observed cogeneration of **QM6** from the lowest excited triplet state^[213, 259, 260]. A mechanism for the generation of this QM has been proposed, involving a radical fragmentation promoted by an initial electron transfer from **131** (T_1) (Scheme 38). However, extensive and more detailed surveys are needed to support this hypothesis. Potential hydrogen transfer reactions from **131** (T_1) have been ruled out as they usually involve higher energy barriers^[259].



Scheme 38: Proposed mechanism for the photogeneration of QM6 from **131** and **131⁺** accounting for the co-generation of QM6 from the lowest triplet excited state.

In line with what observed for the unsubstituted QMPs, the photogeneration of **QM6** was not significantly affected shifting from ACN-H₂O 1:1 to a buffered water solution at pH 7.4 (Figure 56a). Moreover, a parallel behaviour was observed for the NO₂ containing 5-isomer analogues **126** and **135**, with the latter being the only one acting as QMP, as a transient absorbing at 400 nm was observed in aqueous ACN and assigned to **QM10** (Figure 56b).

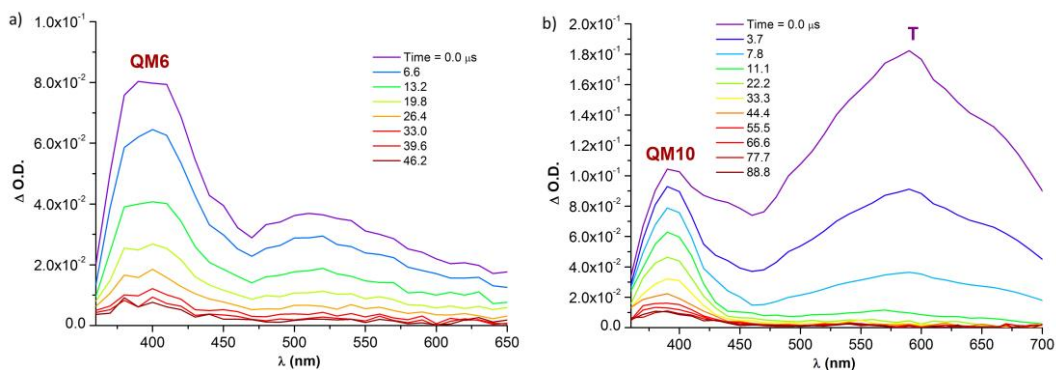


Figure 56: Transient absorption spectra obtained after irradiation at 354 nm of Ar-purged 10^{-4} M solutions of (a) **131** in buffered water (pH 7.4) and (b) **135** in ACN:H₂O 1:1.

The general decline of QM generation caused by the introduction of electron-withdrawing substituents was then confirmed by LFP studies performed on the NMe₃⁺ and F containing QMPs. In fact, the same detrimental effect encountered with Mannich bases **122** and **126** was found for **119** and **124**, for which exclusive photogeneration of the T₁ was evidenced. As previously shown for the strongly EWG NO₂ substituent, quinone methides could only be generated and detected by irradiating the quaternary ammonium salts **128**, **130** and **133**. The same compounds benefited of protic solvation, as an enhanced signal ascribed to the

QM paralleling a remarkable quenching of T_1 was established in aqueous ACN for **128** (Figure 57), **130** (Figure 58), and **131** (Figure 54b).

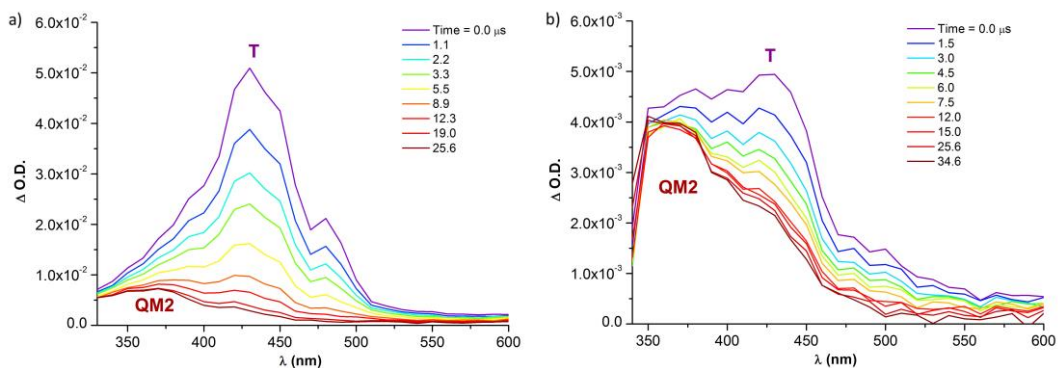


Figure 57: Transient absorption spectra of Ar-purged 10^{-4} M solutions of **128** irradiated at 266 nm in (a) neat ACN and (b) in ACN:H₂O 1:1.

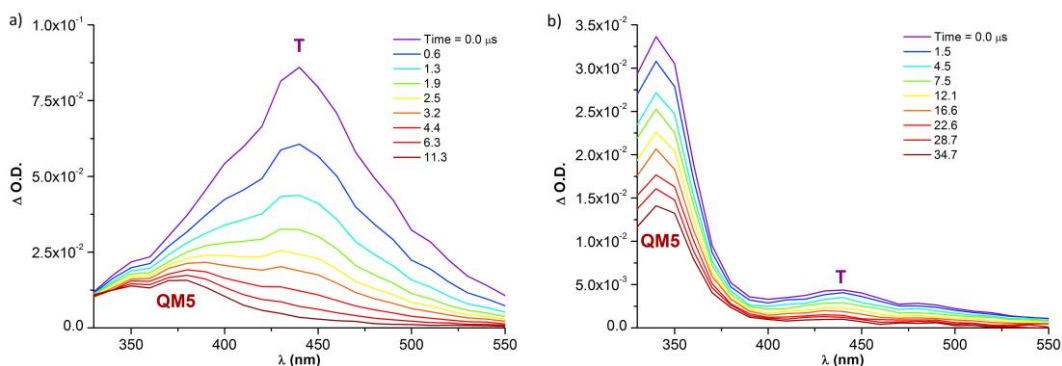


Figure 58: Transient absorption spectra of Ar-purged 10^{-4} M solutions of **130** irradiated at 266 nm in (a) neat ACN and (b) in ACN:H₂O 1:1.

Accordingly, a specular increase of QMP character was expected for precursors containing electron-donating groups. Indeed, among the 4-substituted arylethynyl Mannich bases **118-122**, the most effective QMP was the one bearing the strong electron-donating dimethylamino group. In particular, when **121** was irradiated in aqueous ACN the main detected species was **QM4**, with a broad absorption between 400 and 500 nm, although low T-T absorption was still visible at 550 nm (Figure 59a). Moreover, the same **QM4** spectrum was obtained in buffered water solution at pH 7.4, where it was still detectable after 3 ms (Figure 59b).

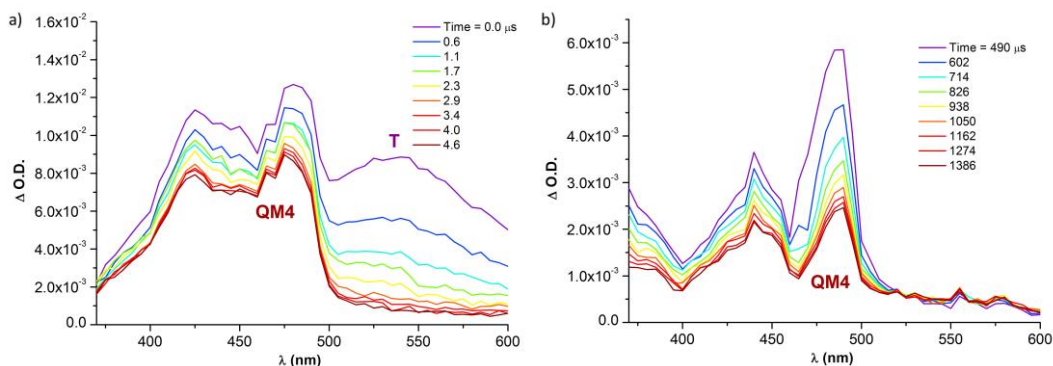


Figure 59: Transient absorption spectra of Ar-purged 10^{-4} M solutions of **121** irradiated at 266 nm in (a) ACN:H₂O 1:1 monitored in a μ s timescale and (b) buffered water at pH 7.4 monitored in a ms timescale.

A similar behaviour was observed for the Mannich base **120**, where **QM3** was effectively generated in neat ACN (Figure 60a) and the triplet was detectable only under Ar-purged conditions at shortened delay time. Under protic conditions, **QM3** became the dominant photogenerated transient with a negligible presence of the fast decaying triplet (Figure 60b).

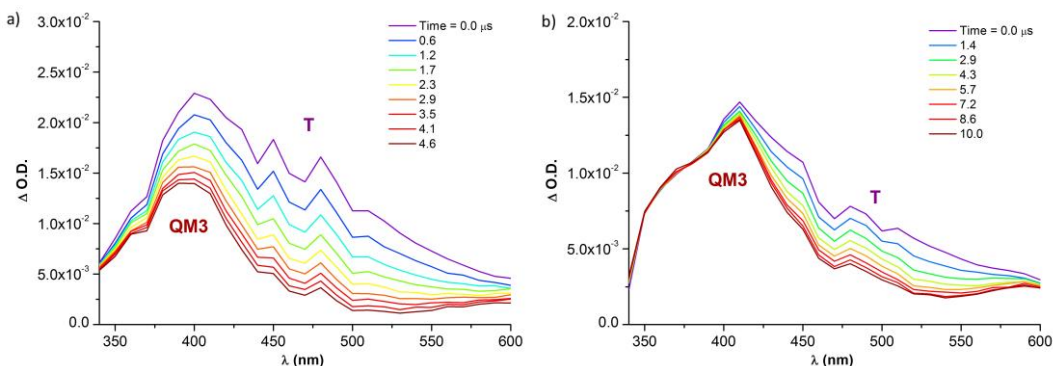


Figure 60: Transient absorption spectra of Ar-purged 10^{-4} M solutions of **120** irradiated at 266 nm in (a) neat ACN and (b) ACN:H₂O 1:1.

The same enhancing effect was observed when the donor substituent MeO was introduced in the 5-arylethynyl analogues. Therefore, **QM9** was produced by irradiation of the Mannich base **125** in 1:1 aqueous ACN, although an intense signal ascribed to T_1 was also evident (Figure 61a). Consistently, under the same conditions, the corresponding quaternary ammonium salt **134** displayed a 5-fold increase in the signal of **QM9** (Figure 61b).

Collectively, LFP data suggest that electronically conjugated Mannich bases are effective QMPs with less competing T_1 generation only in the presence of strong electron-donating

substituents. On the contrary the detrimental effect of electron-withdrawing substituents could be only partly contrasted by using more effective leaving groups and exploiting the water solvation effect.

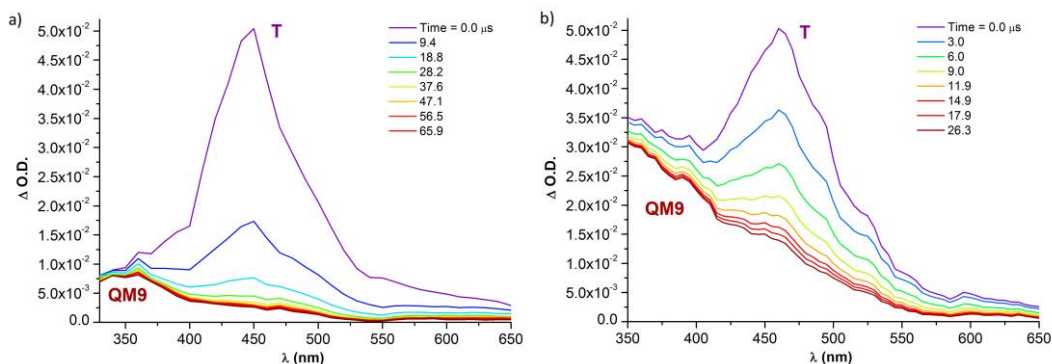


Figure 61: Transient absorption spectra of Ar-purged 10^{-4} M solutions in ACN:H₂O 1:1 of (a) **125** and (b) **134** irradiated at 266 nm.

3.1.7 Substituent and conjugation effect on QM reactivity

Observed and second order rate constants for quenching reactions by water and 2-mercaptoethan-1-ol were measured to assess transient QMs reactivity (Table 5). The observed overall trend was consistent with the expected electronic effect of the substituent X on the reactivity of the electrophilic Michael acceptor. Therefore, the shortest living and most reactive quinone methides were those containing electron-withdrawing moieties, i.e. nitro substituent (**QM6**, Figure 55a, and **QM10**) and trimethylammonium group (**QM5**). The effect was more intense with the former, acting both through inductive and resonance effects (-M, -I), and moderate with the latter, for which only inductive effect (-I) is operative. By contrast, the pseudo-first-order rate constants k_{obs} for the hydration reaction of the 4-arylethynyl **QM2-4** suggested only a moderate reduction of the electrophilicity by mesomeric effect (+M) of electron-donating groups, in comparison to **QM1**, with **QM4** being the least reactive. Indeed, in the presence of trapping thiol this was the longest leaving transient in aqueous solution, being 168 times less reactive than the prototype **QM1**, with a $k_2 = (7.0 \pm 0.2) \cdot 10^2 \text{ M}^{-1} \text{ s}^{-1}$ (Figure 62).

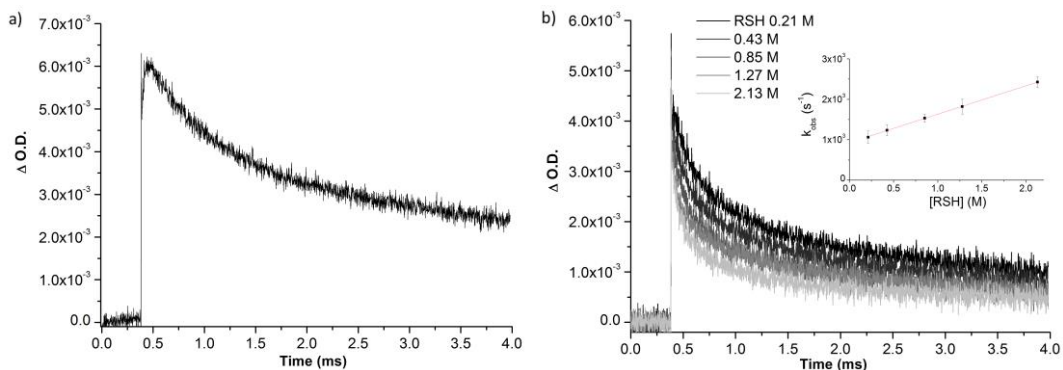


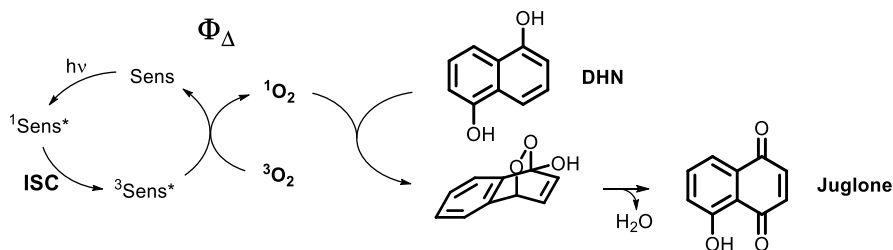
Figure 62: (a) Decay trace of **QM4** monitored at 485 nm after LFP irradiation at 354 nm of an Ar-purged 10^{-4} M solution in neat ACN of **121**. (b) Influence of increasing concentration of 2-mercaptoethan-1-ol on the decay trace of **QM4** at 485 nm in ACN:H₂O 1:1. Inset: quenching plot k_{obs} vs thiol concentration, which yielded a bimolecular rate constant of $(7.0 \pm 0.2) \cdot 10^2 \text{ M}^{-1} \text{ s}^{-1}$.

The hydration rate constant k_{obs} of unsubstituted 5-arylethynyl **QM7** described a much lower electrophilicity in comparison to isomeric **QM1** and the same trend was confirmed for the methoxy group containing 5-arylethynyl **QM9** compared to 4-arylethynyl **QM3**. The exception to this trend was **QM8**. In fact, unlike in **QM2**, there is no direct conjugation between fluorine and the exocyclic methylene moiety. Therefore, while the slight reduction of the **QM2** reactivity in comparison to **QM1** was rationalized in terms of +M effect, the fluorine atom in **QM8** could act only as an electron-withdrawing substituent with inductive effect (-I), thus explaining the higher reactivity of **QM8** in comparison to **QM7**.

3.1.8 Singlet oxygen photosensitization

The higher intersystem crossing efficiency encountered in QMPs bearing the strong electron-withdrawing NO₂ substituent, which effectively raised T₁ population, together with the fairly long living triplet excited state ($\tau = 4 \mu\text{s}$), and the absorption tail extending in the visible range (up to 420 nm) have prompted the interest for their possible exploitation as singlet oxygen sensitizers. ¹O₂ is a ROS that bears high cytotoxic activity and its production in living tissues is generally achieved through photosensitization in the so-called photodynamic therapy (PDT)^[261]. Thus, as a proof of concept, the quaternary ammonium salts **131** and **135** were investigated as singlet oxygen sensitizers in the photo-oxidation of 1,5-dihydroxynaphthalene in ACN, by irradiation at 360 nm (Scheme 39). In the presence of a

triplet sensitizer, in fact, **DHN** is effectively oxidized by $^1\text{O}_2$ to its naphthoquinone derivative 5-hydroxy-1,4-naphthalenedione, also known as **Juglone**, through its endoperoxide^[262].



Scheme 39: Mechanism for the photo-oxidation of **DHN** to **Juglone** through singlet oxygen sensitization. The compounds used as sensitizers were **131** ($\Phi_{\Delta} = 0.017 \pm 0.002$) and **135** ($\Phi_{\Delta} = 0.028 \pm 0.003$).

In neat acetonitrile compounds **131** and **135** were not subject to photobleaching after 1 hour of irradiation at 360 nm, as confirmed by HPLC analysis. A unique new HPLC peak formed and raised throughout the irradiation time at the expense of **DHN**, and it consistently matched a juglone reference. Showing a red-shifted absorption band in a free region of the UV-vis spectrum (400-480 nm), **Juglone** formation could be monitored spectrophotometrically (Figure 63a), while **DHN** consumption was independently monitored by HPLC analysis. The expected reaction rate equation followed a second order kinetics:

$$-\frac{d[\text{DHN}]}{dt} = k_2[{}^1\text{O}_2][\text{DHN}] \quad (3)$$

Since under the experimental conditions ${}^3\text{O}_2$ is far more abundant than the sensitizer and ${}^1\text{O}_2$ lifetime is very short (68 μs in ACN)^[263], the concentration of singlet oxygen could be considered constant throughout the experiment with good approximation. Therefore, eqn 3 could be simplified to a pseudo-first order kinetics. Indeed, the collected data were successfully fitted eqn 4 and 5 (Figure 63b).

$$\ln[\text{DHN}]_t = \ln[\text{DHN}]_0 - k_{obs}t \quad (4)$$

$$[\text{juglone}]_t = [\text{DHN}]_0(1 - e^{-k_{obs}t}) \quad (5)$$

$$k_{obs} = k_2[{}^1\text{O}_2] \quad (6)$$

In view of the fact that the second order rate constant for the cycloaddition step between **DHN** and ${}^1\text{O}_2$ does not depend on the sensitization process, the proportionality emerging

from eqn 6 was exploited to deduce singlet oxygen quantum yield (Φ_{Δ}) from the measured pseudo-first order rate constant (k_{obs}) by comparison with a well-established singlet oxygen sensitizer (Eqn 7).

$$\Phi_{\Delta} = \Phi_{\Delta}^{std} \cdot \frac{k_{obs}}{k_{obs}^{std}} \cdot \frac{I^{std}}{I} \quad (7)$$

In this relationship, Φ_{Δ}^{std} was the singlet oxygen quantum yield of a reference tetra-substituted naphthalelediimide used as standard sensitizer ($\Phi_{\Delta}^{std} = 0.30$)^[264], k_{obs} and k_{obs}^{std} were the pseudo-first order rate constants of **DHN** photo-oxidation measured under the same conditions for the tested compound and the reference respectively, while I and I^{std} were the fraction of incident photons effectively absorbed by the tested and reference sensitizers.

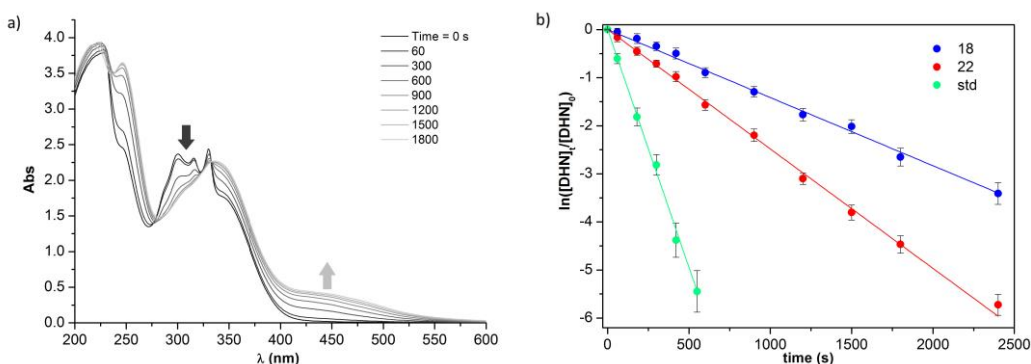
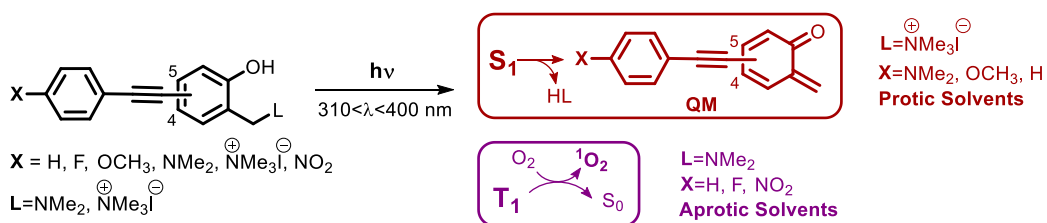


Figure 63: (a) Absorption spectra of an O₂-saturated ACN solution of DHN (1·10⁻⁴ M) irradiated at 360 nm, using 95 (1·10⁻⁴ M) as singlet oxygen photosensitizer. (b) ln([DHN]_t/[DHN]₀) vs irradiation time plot. Linear fitting yielded $k_{obs}=(142\pm 3)\cdot 10^{-5} \text{ s}^{-1}$ and $\Phi_{\Delta}=0.043\pm 0.001$ for **131**; $k_{obs}=(248\pm 3)\cdot 10^{-5} \text{ s}^{-1}$ and $\Phi_{\Delta}=0.075\pm 0.001$ for **135**; $k_{obs}=(99\pm 2)\cdot 10^{-4} \text{ s}^{-1}$ for the reference naphthalene diimide under the same conditions.

Based on the calculated quantum yields for **131** ($\Phi_{\Delta}=0.043\pm 0.001$) and **135** ($\Phi_{\Delta}=0.075\pm 0.001$), it could be inferred that the least effective QMP among the tested arylethynyl derivatives acted as the best singlet oxygen sensitizer in neat ACN, although the efficiency was rather low if compared to known sensitizers^[261]. Yet, this evidence further supported the above claimed competition of ISC with ESPT and ESIPT processes from S₁ of the QMP. Such a competition directly translates in T₁ versus QM relative population, which are usually co-generated transient species.

In summary, this study helped to clarify the factors affecting this dichotomy (Scheme 40). In particular, conjugating arylethynyl moieties on C4, together with strong electron-donating X substituents, good leaving group L, and protic conditions generally favor the selective photogeneration of the electrophilic QM intermediate, suppressing the T_1 generation. Conversely, conjugating arylethynyl moieties on C5, electron-withdrawing X substituents, bad leaving group L, and polar aprotic solvents tend to populate more effectively the T_1 .

Importantly, taking advantage of the red-shifted absorption of the conjugate base of **95** (**95⁻**, $\lambda_{\text{max}}=405$ nm), which is the main populated species at pH=7.6, the generation of a QM from a visible light harvesting precursor proved to be possible. However, it should be noted that the same electronic effect that positively affected the absorption properties and the pKa of the precursor also knocked down its reactivity as a QMP.

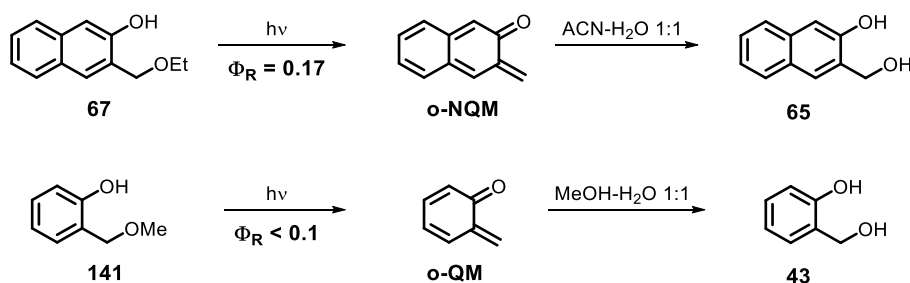


Scheme 40: General scheme summarizing the QMP structural features affecting T_1 population vs QM generation.

3.2 Design of a naphtho-QMP functional tool

In the previous section it has been shown how extending the conjugation of o-QMP through an arylethynyl moiety allowed to shift the absorption maximum in the 300–310 nm range, with a band tail that reached 360 nm. Only the introduction of suitable substituents could occasionally extend the absorption properties beyond 400 nm, although such modifications negatively affected the QM generation efficiency.

To overcome the issue of engineering red-shifted photo-triggerable QMPs, an alternative strategy is the exploitation of the extensively studied naphthol-based analogues. In fact, naphthol derivatives as quinone methide precursors (NQMPs) display an absorption band with a maximum at about 340 nm and a tail that extends over the visible spectral region^[209, 214]. Moreover, the higher excited state acidity of 2-naphthol ($pK_a^*=2.8$)^[212] compared to phenol ($pK_a^*=3.6$)^[211] should facilitate ESPT and ESIPT, therefore enhancing the efficiency of quinone methide formation. Indeed, Popik showed that the quantum yield of photolysis of 3-(ethoxymethyl)naphthalen-2-ol (**67**, $\Phi_R=0.17$)^[209] in aqueous solution was higher than that of the benzo-analogue (**141**, $\Phi_R<0.1$)^[185] (Scheme 41), despite the competing S_1 fluorescence decay was rather high ($\Phi_{FI}=0.23$). The chemical yields were almost quantitative for low conversions, mimicking benzo-QMP behaviour.



Scheme 41: Photolysis in aqueous solution of benzylic ethers **67**^[209] and **141**^[185].

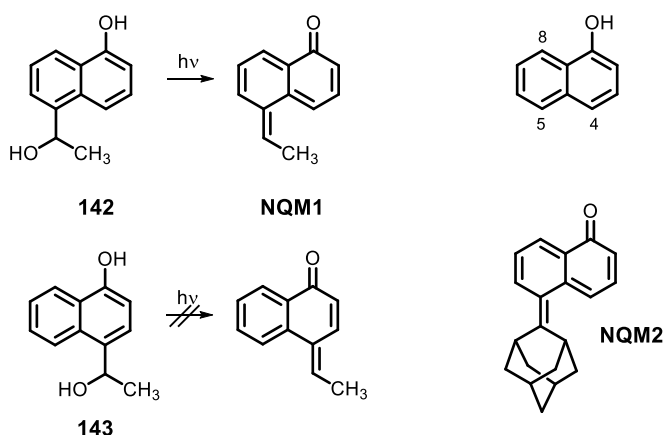
Additionally, Mannich bases and quaternary ammonium salts of these extended aromatic systems preserved excellent solubility under physiological conditions, as shown by direct photogeneration of naphthoquinone methides in the presence of DNA which allowed purine selective alkylation in buffered water^[214].

In this section, the synthesis of 6-substitued water-soluble o-NQMPs is presented. The aim of this project was to create an optimized photoalkylating molecular tool for biological applications which could readily be joint through a connecting spacer to a suitable targeting unit, to potentially create a variety of selective smart alkylating agents.

First, the synthetic approach to the precursors will be presented. Hence, the effect of different substituents on precursor photoreactivity will be evaluated to select the best functional group for effective NQMP ligation. Actual NQM generation will be assessed on the basis of LFP transient detection. Additionally, occurring ESPT mechanisms will be shown through fluorescence measurements.

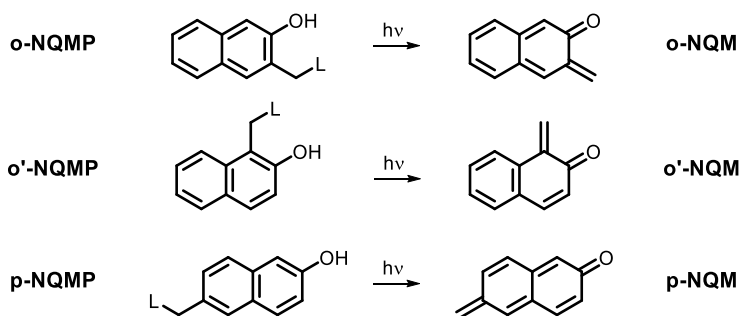
3.2.1 Synthesis of 6-substitued o-NQMPs

Even though in the singlet excited state (S_1) 1-naphthol display a higher acidity ($pK_a^*=0.4$) than 2-naphthol ($pK_a^*=2.8$)^[212], to date only two reactive QMs based on 1-naphthol have been reported (Scheme 42). Wan observed that unexpectedly, while irradiation of **142** did generate **NQM1**, this was not true for precursor **143**^[205]. Importantly, irradiation of 1-naphthol yielded deuterium incorporation in 5- and 8- ring positions as a consequence of solvent mediated ESPT which leads to tautomerization^[212]. This selectivity was thought to arise from local charge transfer from the naphthol OH to 5- and 8- ring positions. The failure of **143** to react through the 4-position has been therefore related to the lack of charge transfer which is thought to be crucial and precede photo-dehydration in such derivatives.



Scheme 42: **NQM1** and **NQM2** are the only NQMs derived from 1-naphthol reported to date^[265].

Moreover, no example of ortho-NQM derived from photolysis of 1-naphthols is known. Conversely, three classes of isomeric NQMs based on 2-naphthol have been successfully generated from a variety of precursors (Scheme 43). Popik reported the photochemical generation of both **o-NQM** and **o'-NQM** by photo-dehydration of 3-hydroxy-2-naphthalenemethanol and 2-hydroxy-1-naphthalenemethanol respectively, and their reactions with nucleophiles and electron-rich dienophiles to give addition products or and chromanes^[209]. Additionally, Freccero efficiently generated **p-NQM** from several precursors and bifunctional binol derivatives^[214]. However, due to the prohibitive distance between the naphthol OH and the leaving group, ESPT is not active and ESPT can occur only in the presence of a protic solvent, lowering the efficiency of **p-NQM** photogeneration. Similarly, although the almost identical generation efficiency and the similar reactivity as **o-NQM**, quinone methides of the **o'-NQM** family received little follow up in the recent past. This is likely a consequence of poor stability of the trapped adduct formation as confirmed by the intrinsically higher thermal reactivity of o'-NQMP. Therefore, in the last decade much more attention has been directed in the exploitation of the **o-NMQ** family, with applications ranging from DNA alkylation^[218, 220] to photolabile protecting groups^[179, 266], photoclick ligations^[267] and photolithography^[268].

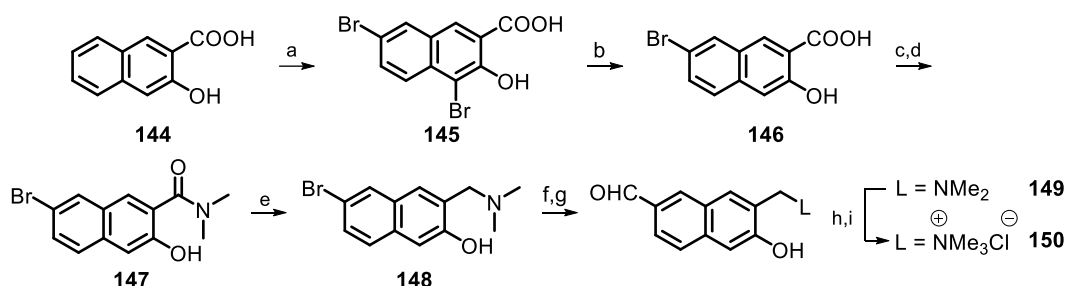


Scheme 43: The three classes of NQMs derived from 2-naphthol known to date.

Relying on this background knowledge, a 6-substitued o-NQMP scaffold was selected for the purpose of engineering a photoalkylating molecular tool for biological applications.

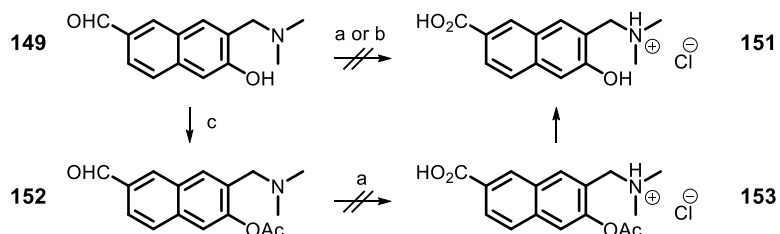
The synthesis of such scaffold started from commercially available 3-hydroxy-2-naphthoic acid **144** (Scheme 44). C-6 functionalization was obtained by introduction of a bromine atom in a two steps published protocol^[269]. Bromination of the naphthol with 2 equivalents of Br₂

afforded the dibromo derivative **145**, whereas subsequent treatment with Sn/HCl yielded **146** by reductive cleavage of the most reactive C-Br bond. The carboxylic acid was then converted in the dimethylamide **147**, through its acyl chloride, while amide reduction with lithium aluminium hydride finally afforded the Mannich base **148** with 73% yield over 5 steps.



Scheme 44: Synthesis of 6-carbaldehyde o-QMPs **149** and **150**. (a) Br₂, AcOH, reflux, 10 h (yield: 90%); (b) Sn, HCl 37%, AcOH, reflux, 12 h (yield: 97%); (c) SOCl₂, DMF, reflux, 15 m; (d) Me₂NH, THF, rt, 16 h (yield over 2 steps: 87%); (e) LiAlH₄, THF, reflux, 2 h (yield: 96%); (f) BuLi, THF, -78°C, 2 h; (g) DMF, -50°C; 45 m (yield over 2 steps: 71%); (h) MeI, ACN, rt, 48 h; (i) HCl, H₂O (yield over 2 steps: 99%).

Electron-rich naphthols containing strong EDG, such as amino and hydroxyl groups, are susceptible of oxidation by air and for this reason they are often difficult to handle. Conveniently, the introduction of an aldehyde or a carboxylic acid, which are particularly suited for further tethering, was considered. Therefore, following a protecting group-free protocol well-established for 6-bromo-2-naphthol^[270], direct lithiation with excess *n*-BuLi in dry THF and subsequent formylation with DMF and aqueous workup afforded the aldehyde **149** in good yields. Methylation of the tertiary amine was achieved with iodomethane in ACN to afford the quaternary ammonium salt **150**.



Scheme 45: Synthetic efforts in the attempt of converting aldehyde **149** into its carboxylic acid **151** by direct oxidation and naphtholic OH protection. (a) NaClO₂, H₂O₂, NaH₂PO₄, ACN-H₂O, 10°C; (b) NaClO₂, DMSO, 0°C; (c) Ac₂O, K₂CO₃, acetone, 55°C, 2 h (yield: 91%).

Unfortunately, every attempt of oxidizing the aldehyde **149** to the carboxylic acid **151** exploiting the Pinnick oxidation^[271] with sodium chlorite was unsuccessful (Scheme 45). When the reaction was carried out in aqueous ACN, in the presence of H₂O₂ as scavenger for the HOCl by-product, a complex mixture of unidentified products was obtained along with a negligible amount of **151** (yield < 5% by HPLC analysis, Figure 64a). Since the redox pair HOCl/Cl⁻ is a more powerful oxidant than ClO₂⁻/HOCl and electron-rich substrates can react with HOCl faster than H₂O₂, over-oxidation of naphthol at positions with high electronic density was the most probable side-reaction (e.g. leading to quinones). Accordingly, a modified procedure employing DMSO both as solvent and HOCl scavenger, which had been reported to be more convenient with electron-rich aryl aldehydes^[272], was used but still afforded some over-oxidation side-products at room temperature (yield = 43% by HPLC analysis, Figure 64b). Finally, when the temperature was reduced to 0 °C, a good conversion was observed. However, any attempt made to quench the reaction prior to purification were vain since, as soon as the temperature was raised, decomposition of the product occurred. Even acetylation of the naphthol OH, as a strategy to reduce its donor properties, resulted in unsatisfactory outcomes in the oxidative step (from **152** to **153**, Scheme 45).

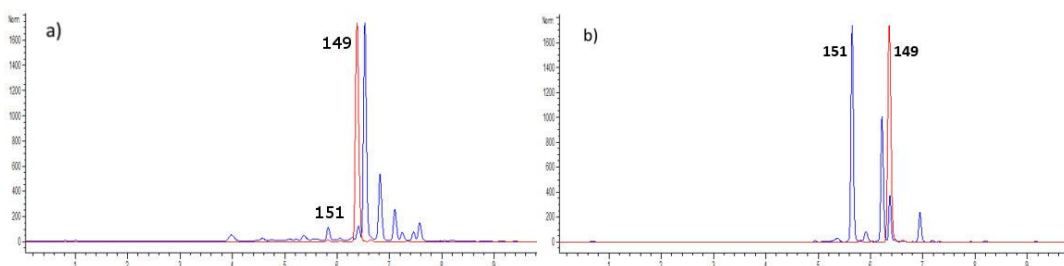
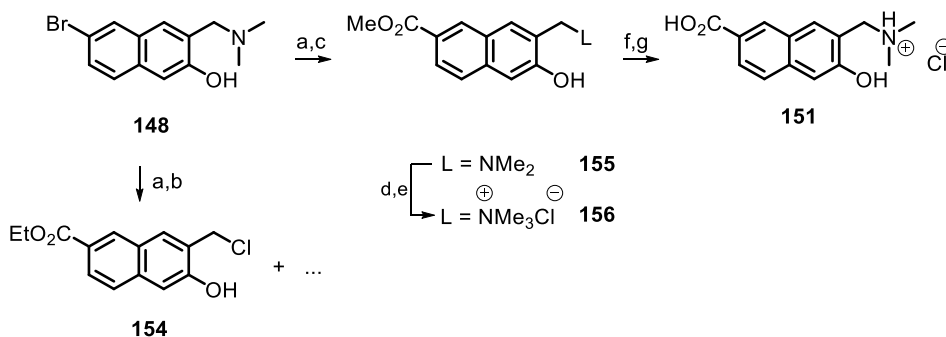


Figure 64: Superimposed chromatograms of reagent **149** (red) and the reaction mixture (blue) obtained by Pinnick oxidation under different conditions: (a) NaClO₂, H₂O₂, NaH₂PO₄, ACN-H₂O, 10°C; (b) NaClO₂, DMSO, 0°C.

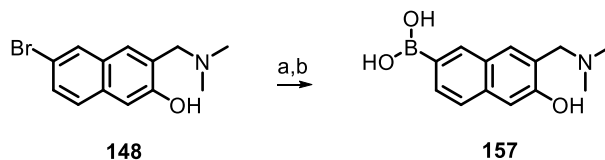
The logical consequence was the direct introduction of a carbon fragment at the carboxylic oxidation level on the bromo-derivative **148**. Unfortunately, bubbling CO₂ in a solution of the intermediate lithiated species led to the loss of the basic amino moiety. The same outcome was achieved by using ethyl chloroformate as the electrophile partner, and product **154** was identified in the rather dirty reaction mixture (Scheme 46). This evidence was rationalized by suggesting that the electrophile was also reacting with the tertiary amine, leading to the formation of a quaternary ammonium salt, so that substitution or elimination side-reactions

could take place. Therefore, use of less reactive electrophiles was more convenient. Indeed, trapping the lithium derivative of **148** with dimethyl carbonate afforded the desired methyl ester **155** and, upon exhaustive methylation, its quaternary ammonium salt **156**. To avoid the formation of the dimeric ketone, the lithium derivative obtained by metal-halogen exchange was added to a solution containing an excess of the electrophile in dry THF, and not *vice versa*. Finally, the carboxylic acid derivative **151** was obtained by basic hydrolysis of the ester in aqueous solution with good yields.



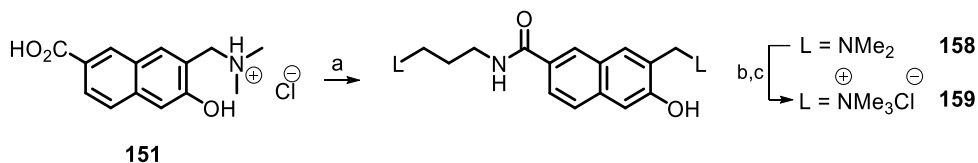
Scheme 46: Synthesis of the amino acid **151** through hydrolysis of an ester intermediate. (a) BuLi, THF, -78°C , 2 h; (b) ethyl chloroformate, -50°C ; 45 m (traces); (c) dimethyl carbonate, -50°C , 45 m (yield: 46%); (d) MeI, ACN, rt, 48 h; (e) HCl, H_2O (yield over 2 steps: 95%); (f) K_2CO_3 , THF- H_2O , reflux, 16 h; (g) HCl, H_2O (yield over 2 steps: 84%).

The lithium-derivative of **148** was also converted into the boronic acid **157**, although in lower yields, by trapping it with trimethyl borate (Scheme 47). Besides the synthetic utility as useful building-block for organometallic cross-couplings, **157** could also be employed to form boronic ester junctions with diols.



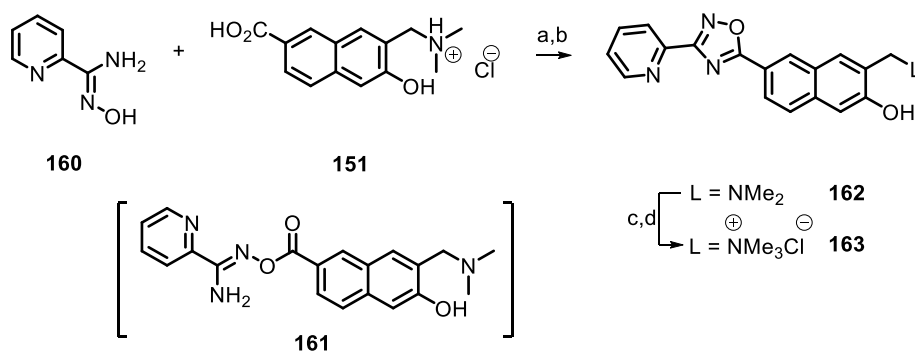
Scheme 47: Synthesis of the boronic acid **157**. (a) BuLi, THF, -78°C , 2 h; (b) trimethyl borate, -50°C ; 45 m (yield: 27%).

The amides **158** and **159** were obtained from the carboxylic acid **151** by direct condensation with 3-(dimethylamino)-1-propylamine, using PyBOP to activate the carboxylate, and subsequent exhaustive methylation (Scheme 48).



Scheme 48: Synthesis of the amides **158** and **159** (a) PyBOP, 3-(dimethylamino)-1-propylamine, rt, 1 h (yield: 79%); (b) MeI, ACN, rt, 48 h; (c) HCl, H₂O (yield over 2 steps: 98%).

Moreover, oxadiazole derivatives **162** and **163** were synthesized from the same intermediate to explore the opportunity to incorporate the photoalkylating scaffold in an oligo-heteroaromatic system capable of G-quadruplex binding. Therefore, the carboxylic acid **151** was activated with PyBOP in the presence of diisopropyl-ethyl-amine and condensed with N'-hydroxypicolinimidamide **160**. Unexpectedly, the reaction, which was monitored by reverse phase HPLC, proceeded by an initial fast oligomerization of **151** through intermolecular self-condensation. Though the monomer was still an activated ester, it was far less reactive. Despite the low reaction rate, eventually a single product formed after few days. Unfortunately, higher temperatures led to formation of by-products and diminished the overall yield. Hence, the intermediate, which had been assigned to O-acyl-amidoxime **161**, was not isolated, but rather it was subjected to ring-closing condensation in a one-pot process. The oxadiazole **162** was then treated with iodomethane to afford the quaternary ammonium salt **163**.



Scheme 49: Synthesis of the oxadiazoles **162** and **163**. (a) PyBOP, DIPEA, DMF, rt, 6 d; (b) K₂CO₃, DMF, 65°C, 2 h (yield over 2 steps: 61%); (c) MeI, ACN, rt, 48 h; (d) HCl, H₂O (yield over 2 steps: 90%).

3.2.2 Absorption and emission proprieties of a prototype NQMP

The spectroscopic proprieties of the new NQMP core were first investigated. Preliminary absorption spectra of **156** were recorded in ACN:H₂O 1:1 and buffered water (pH 7.4). The absorption was already remarkably red-shifted in aqueous ACN with respect to arylethynyl benzo-QMPs (Figure 65). However, this effect became even more evident in neat water, likely due to partial deprotonation of the naphthol. In this case the absorption tail extended up to 400 nm.

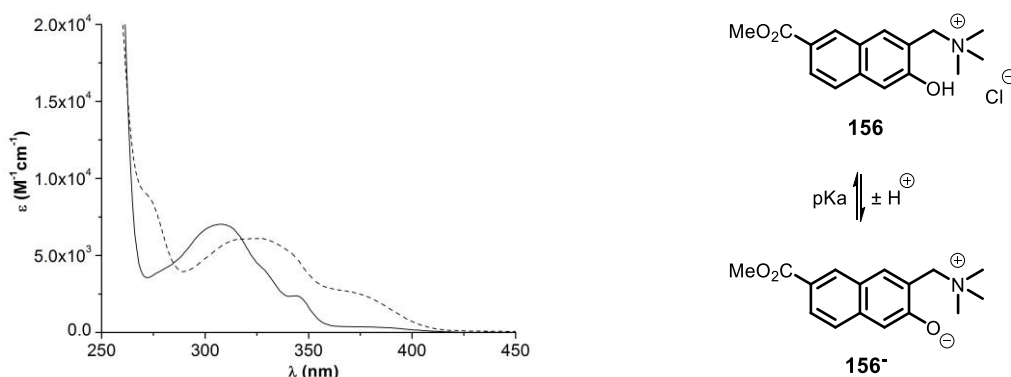


Figure 65: (left) UV-vis spectrum of **156** 10^{-5} M in ACN:H₂O 1:1 (solid line) and in buffered water at pH 7.4 (dashed line). (right) Protonation equilibrium for **156**.

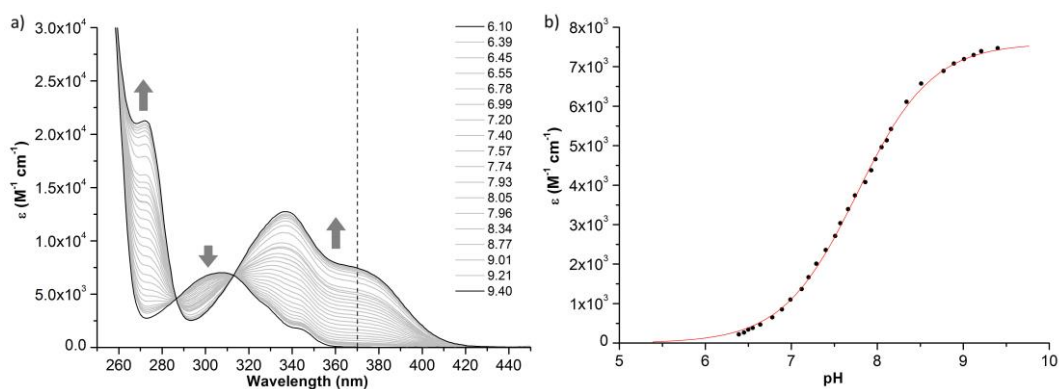


Figure 66: (a) Absorption spectra of compound **156** $5.00 \cdot 10^{-5}$ M in H₂O at different pH values. (b) Molar absorptivity monitored at 370 nm; non-linear fitting of the experimental data yielded $pK_a = 7.77 \pm 0.01$.

The effect of pH was further investigated by spectrophotometric titration, recording the compound absorption spectrum at increasing pH values (Figure 66). By shifting toward basic conditions a batho- and hyperchromic effect was observed. In more detail, a new band peaking at 340 nm and displaying a shoulder around 380 nm was formed and was assigned to the deprotonated species **156**⁻. Fitting of the molar extinction coefficient data at 370 nm as a function of pH yielded a pKa of 7.77 ± 0.01 . This likely indicated that, similarly to aryethynyl nitro-derivatives (Section 3.1), at physiological pH a considerable amount of the NQMP is present in the deprotonated form, which is the most interesting for its absorption properties.

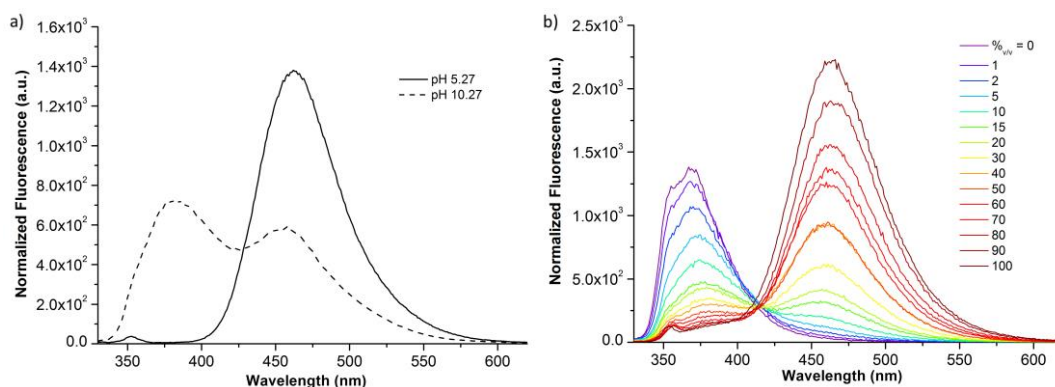


Figure 67: (a) Emission spectra of **156** $1.47 \cdot 10^{-5}$ M in ACN-H₂O 8:2 at different pH values ($\lambda_{\text{exc}}=318$ nm). At pH 5.27 (solid line) the only absorbing species is the acidic **156**, while at pH 10.27 (dashed line) the only species present at equilibrium is the conjugate base **156**⁻. (b) Emission spectra of **156** $1.5 \cdot 10^{-5}$ M in different ACN-H₂O mixtures ($\lambda_{\text{exc}}=318$ nm); %v/v is the percentage of H₂O.

The two species were also investigated by fluorescence spectroscopy. Despite the intrinsically low emission, as should be expected by the presence of a competing mechanism of consumption of S_1 , an interesting behaviour could be observed in buffered ACN-H₂O 8:2 (Figure 67a). In fact, while the deprotonated species **156**⁻ afforded the expected emission band centred at 470 nm, the situation for acidic **156** was more peculiar. In more detail, its fluorescence spectrum consisted in a convolution of two bands, respectively peaking at 380 and 470 nm. This observation suggested that structural changes might be occurring at the singlet excited state surface, and the deprotonated species could be forming *via* an excited state proton transfer (ESPT) mechanism involving the solvent as proton acceptor. This hypothesis was confirmed by recording the fluorescence spectra of the compound in

solutions at varying solvent composition (Figure 67b). Upon gradual substitution of polar aprotic ACN with water the emission spectrum shifted from that of the pure **156** (at 370 nm) to the one which was assigned to **156⁻** (480 nm), while the absorption spectrum remained mostly unchanged, displaying the features of **156**.

The same spectroscopic study was carried out on the corresponding Mannich base **155**, obtaining similar results. Interestingly, though, this dual emission behaviour was no more detected, not even in neat ACN (Figure 68). Only in ACN containing concentrated HCl the emission of the fully protonated species became detectable. This unambiguously indicated the intervention of an intramolecular proton transfer mechanism (ESIPT) from the naphthol to the proximal tertiary amine.

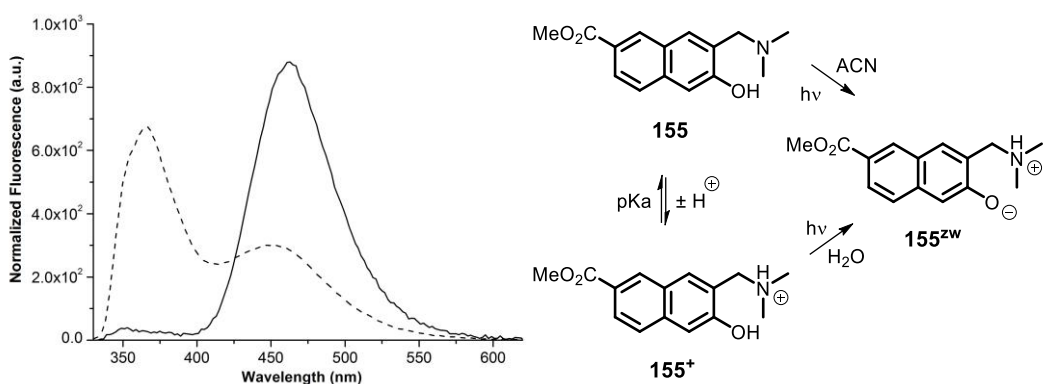


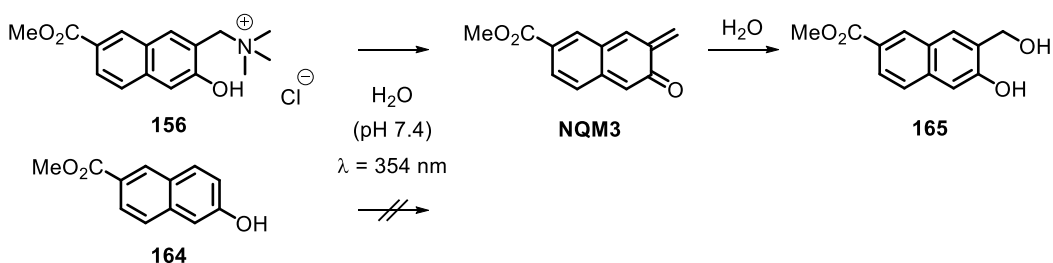
Figure 68: (Left) Emission spectra ($\lambda_{\text{exc}}=318$ nm) of **155** $1.5 \cdot 10^{-5}$ M in neat ACN before (solid line) and after addition of a drop of 37% HCl (dashed line). (Right) Protonation equilibrium between **155** and **155⁺** and generation of **155^{zw}**, which is the true emitting chromophore at 470 nm, through ESIPT.

3.2.3 LFP detection of a naphtho-QM

Following the preliminary results on occurring ESPT mechanisms, quaternary ammonium salt **156** was chosen as a prototype system to study the ability of the new class of naphtho-QMPs to effectively generate a quinone methide upon photochemical activation. Laser flash photolysis (LFP) measurements were carried out in order to detect any transient species generated upon irradiation at 354 nm. For the scope, an Ar-purged 10^{-4} M solution of **156** in buffered water (pH 7.4) was irradiated with a Nd:YAG laser. A transient band of remarkable intensity was observed centred around 650 nm and extending far beyond 700 nm (Figure

69a). However, its lifetime (.ca 30 μs) is relatively short if compared to previously reported naphtho-QM. Moreover, quenching studies with molecular oxygen and various nucleophiles did not allow to surely establish the nature of the transient species. In order to clarify whether it was actually a quinone methide, similar experiments were carried out on derivative **164**, which was missing the trimethylaminomethylene moiety (Scheme 50). As this compound is unable to generate a QM, a difference in the transient spectra obtained upon its irradiation with respect to **156** would confirm that the latter is actually generating a QM-type transient.

Indeed, the transient spectrum of **164** was quite different from that of **156** (Figure 69b). In fact, apart from displaying a much lower absorption intensity, it lacked the intense band in the NIR region. This was substituted by a less intense one, centred at 510 nm. It was thus concluded that the band generated by **156** can safely be assigned to **NQM3**.



Scheme 50: Generation of **NQM3** by photolysis of **156**. The analogue **164** was used as a reference compound, since it cannot generate any QM.

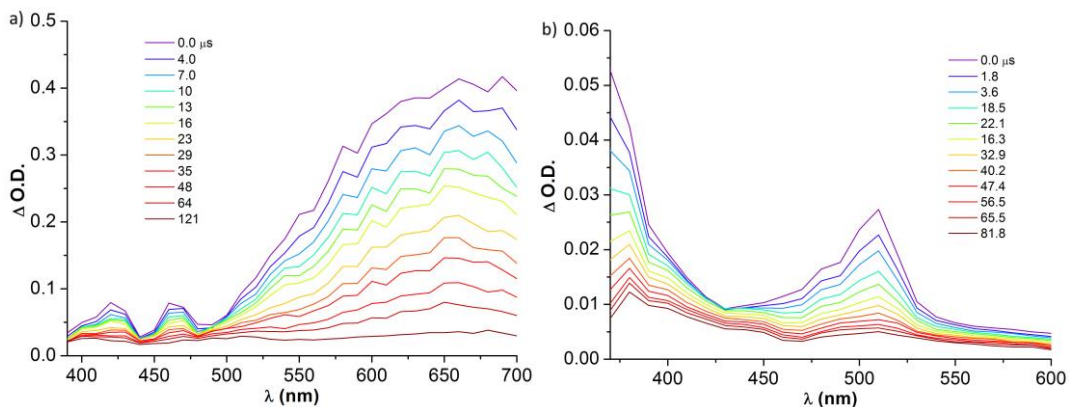


Figure 69: Transient absorption spectra of (a) **156** and (b) **164** 10^{-4} M in Ar-purged buffered water solution (pH 7.4), irradiated at 354 nm. To dissolve **164** ACN was used as a co-solvent in a 1:1 mixture.

Fitting of the transient decay trace (Figure 70) yielded a pseudo-first order rate constant $k_{obs} = (3.05 \pm 0.04) \cdot 10^4 \text{ s}^{-1}$. Such a high decay rate was indicative of a highly reactive and possibly electrophilic transient species. This reactivity was much more remarkable than those reported in the literature for unsubstituted NQMs, likely indicating that the ester functionality played a major role in it.

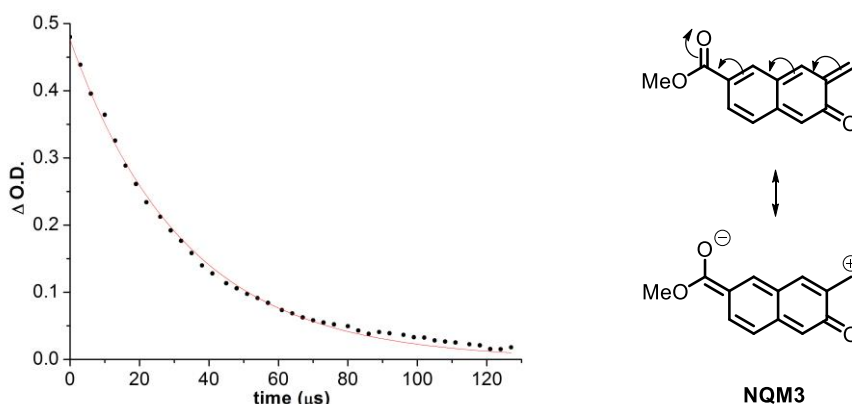
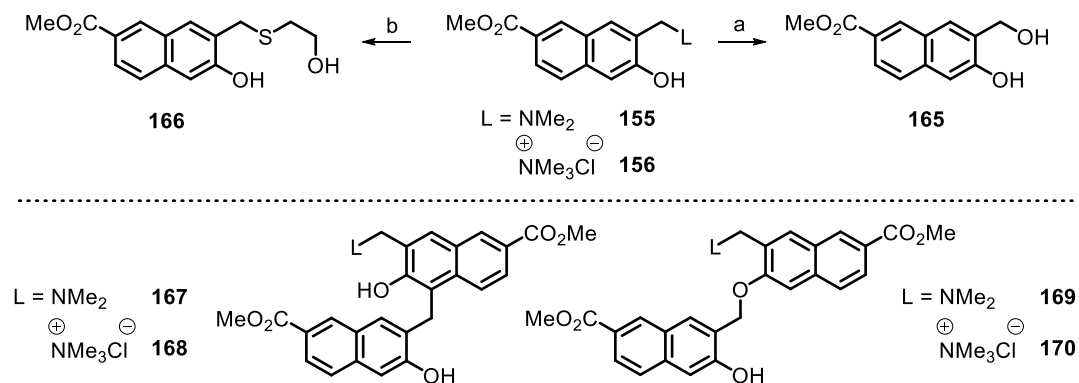


Figure 70: Decay trace monitored at 650 nm and relative to **NQM3**; fitting with a first order kinetic law yielded an observed rate constant of $(3.05 \pm 0.04) \cdot 10^4 \text{ s}^{-1}$ for the trapping of **NQM3** with H_2O to afford **165**. Such high reactivity could be explained by the effect of the carbomethoxy group in enhancing the electrophilic character.

3.2.4 Photoreactivity and QM trapping

As a following step for the reactivity investigation, photo-trapping experiments were carried out on the model derivatives **155** and **156** (Scheme 51). Upon irradiation of 10^{-4} M solutions in 1:1 aqueous ACN and buffered water (phosphate buffer), the expected photoreactivity of QMPs was observed.

In particular, in ACN:H₂O 1:1, the products obtainable from the trapping reactions with water and 2-mercaptoethan-1-ol were detected (**165** and **166** respectively). Moreover, two additional side-products were observed, resulting from the bimolecular reaction between **NQM3** and another QMP molecule at the most nucleophilic sites, namely the aromatic carbon in position 1 (**154** and **155**) and naphthol oxygen (**156** and **157**). As expected, these products disappeared by lowering the reagent concentration (Figure 71c).



Scheme 51: Photolysis adducts of QMPs **155** and **156**. All reactions were performed in a Rayonet® multilamp reactor using 2 x 15 W UV lamps and 20 mL quartz tubes centred at 310 nm. (a) 10⁻⁴ M solution in ACN-H₂O 1:1, 20 min (yield: 82% from **156**, 23% from **155**) (b) 10⁻⁴ M solution in ACN-H₂O 1:1, 2-mercaptoethan-1-ol 10⁻² M, 15 min (yield: 39% from **156** and 19% from **155**). Bimolecular side-products formed by both photolysis.

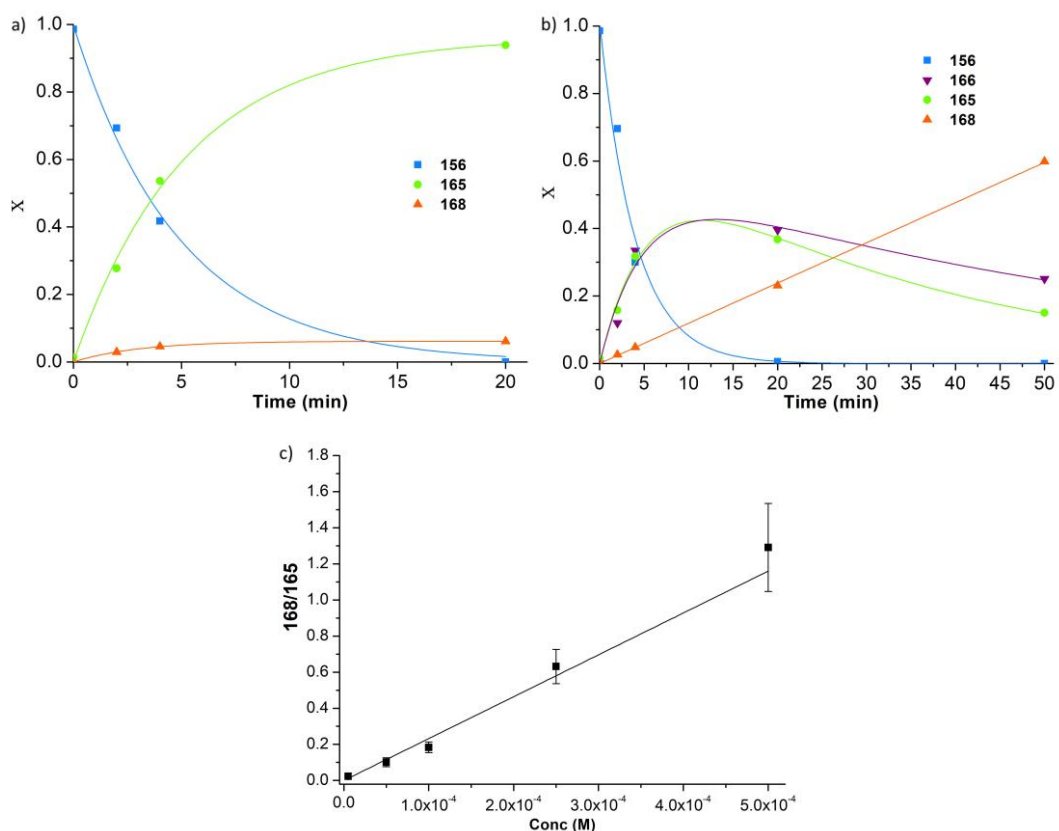


Figure 71: Kinetic plots for the photolysis of **156** 10⁻⁴ M in ACN:H₂O 1:1 (a) without and (b) with added 2-mercaptoethan-1-ol 10⁻² M. (c) Dependence of the ratio between products **168** and **165** obtained upon photolysis of **156** in ACN-H₂O 1:1 (after 20% conversion) on the total concentration.

Interestingly, the fact that upon prolonged irradiation some of the primary products started to fade to the advantage of secondary ones (Figure 71b), confirmed that these NQM derivatives display the typical photochemical reversibility of most QM adducts.

Photohydrolysis reaction quantum yields (Φ_R) were determined by monitoring the QMP conversion to the products by HPLC at low reaction conversion. In order to take into account the multiple photoalkylation products, the reagent consumption was monitored instead of the products formation. Since all the products had been demonstrated to be formed *via* QM generation, this parameter was the most suited to assess the actual reactivity of the QMP. Unexpectedly, in aqueous ACN Mannich base **155** proved to be more photoreactive than **156** ($\Phi_R=0.37$ vs 0.19). Additionally, when looking at the specific product formation, their distribution appeared different for the two derivatives (Figure 72). In fact, Mannich base **155** seemed to react preferentially via the alkylation of another molecule of QMP at carbon (**167**, $\Phi_R=0.24$), while **165** ($\Phi_R=0.08$) was formed as a minor product together with **169** ($\Phi_R=0.05$). Conversely, the quaternary ammonium salt **156** yielded for the major part the photohydrolysis product (**165**, $\Phi_R=0.16$), forming the bimolecular adduct **168** only in low amounts ($\Phi_R=0.03$) and **170** just in traces.

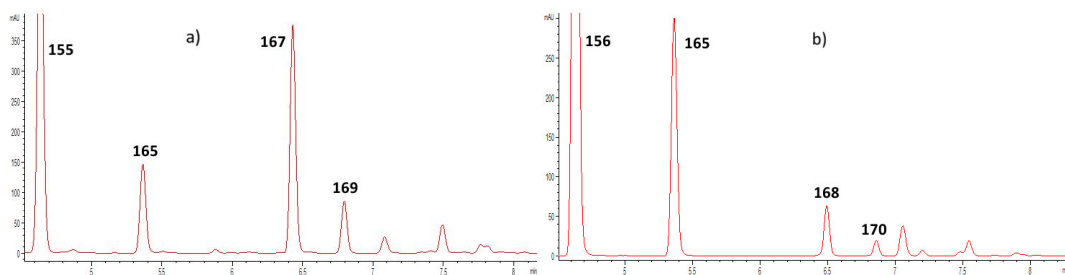
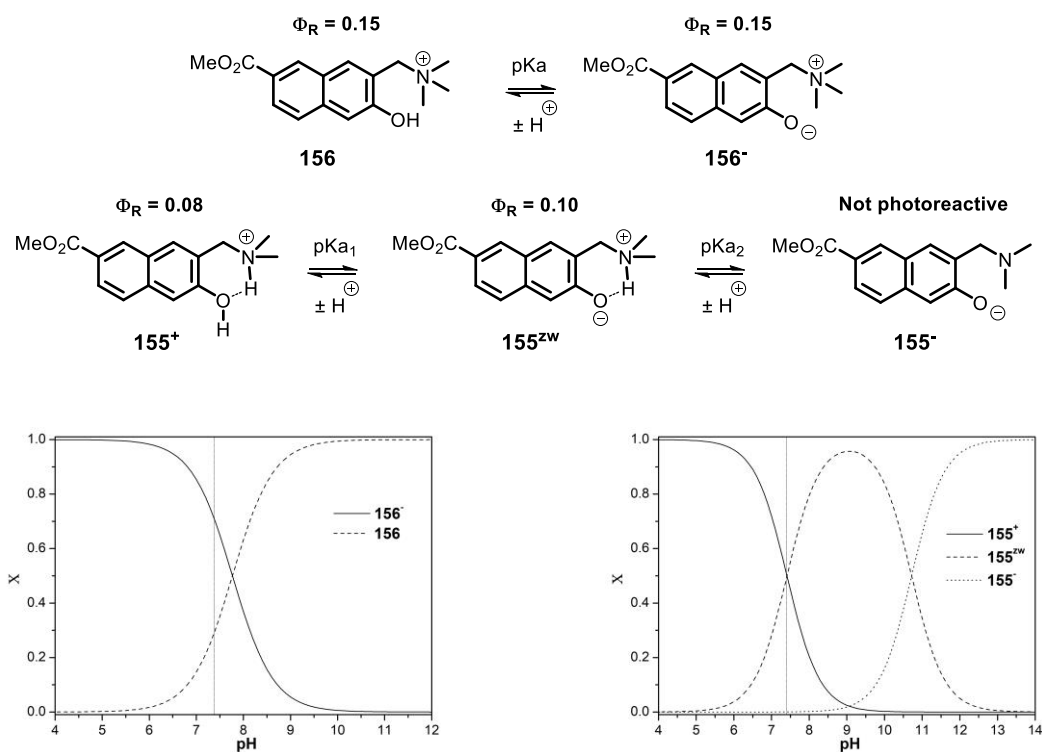


Figure 72: Enlarged HPLC chromatograms of photolysis reactions of (a) Mannich base **155** and (b) quaternary ammonium salt **156** 10^{-4} M in ACN:H₂O 1:1, after about 20% of conversion.

The photohydrolysis reactions of derivatives **155** and **156** were further investigated in buffered water. The overall reactivity was negatively affected moving from aqueous ACN to pure water, roughly decreasing by a factor of two. Although a clear explanation for the trend could not be found, this behavior is extremely general and is observed for most photochemically generated quinone methides.

As the compounds are involved in one or two protonation equilibria (deprotonation of the naphthol and protonation of the Mannich base), the photoreactivity was assessed at pH

values for which a single species was prevailing (Scheme 52). When testing **156** (naphthol $pK_a = 7.77$), pH 5.27 and 10.27 were selected as the conditions in which the fully protonated and deprotonated species would respectively be present. In this case, the neutral and anionic species proved to be equally reactive, since photohydration quantum yield was the same ($\Phi_R=0.15$), although at acidic pH only **165** was observed, whereas a mixture of **165** and **168** was formed in basic conditions ($\Phi_R=0.10$ and $\Phi_R=0.05$ respectively). On the other side, the corresponding Mannich base **155** could be present in three forms, the fully protonated **155⁺**, the zwitterionic **155^{zw}** and the anionic **155⁻**. Their distribution is governed by the two pK_a s (7.41 ± 0.01 and 10.72 ± 0.01) measured by spectrophotometric titration. The first two species proved again to have similar reactivity ($\Phi_R=0.08$ and $\Phi_R=0.10$ respectively at pH 4.91 and 9.07). Instead, the anionic species **155⁻** was completely unreactive, displaying uniquely a slow thermal hydrolysis of the ester. This was however expected as Me_2N^- is not a leaving group under these conditions ($pK_a \sim 35$).



Scheme 52: Protonation equilibria for **155** and **156** in neat water and species distribution at different pH values ($pK_a = 7.77 \pm 0.01$, $pK_{a1} = 7.41 \pm 0.01$, $pK_{a2} = 10.72 \pm 0.01$).

3.2.5 Substituent effect on NQMP photoreactivity

The reactivity study mentioned above was extended to NQMPs embedding different substituent in position 7. First, the absorption properties were checked for all compounds under study. In particular, the naphthol -OH acidity constant resulted to be slightly affected by the electron-withdrawing ability of the substituent R ($pK_a = 7 \div 8$), the extremities being represented by oxazole **162** ($pK_{a1} = 7.14$, Figure 73) and boronic acid **157** ($pK_{a\text{Naphthol}} = 8.03$).

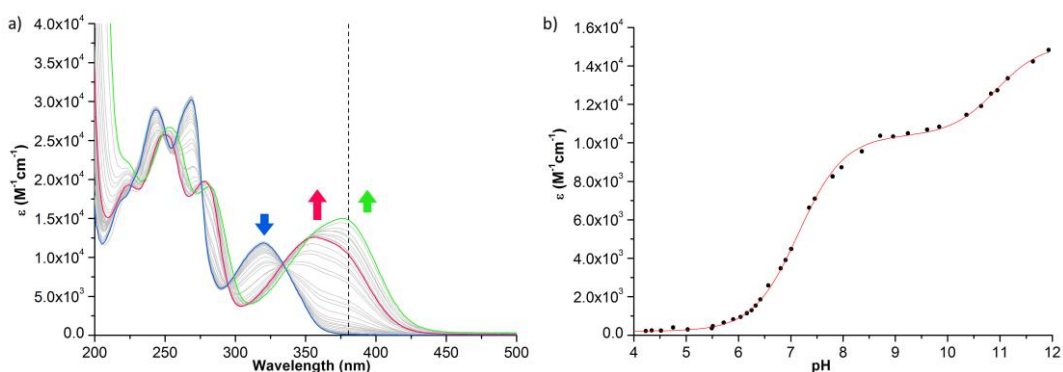


Figure 73: (a) Absorption spectra of compound **162** $2.75 \cdot 10^{-5}$ M in H_2O at different pH values. Blue spectrum corresponds to **162**⁺, red spectrum to **162**^z, green spectrum to **162**⁻. (b) Molar absorptivity monitored at 380 nm; non-linear fitting of the experimental data yielded $pK_{a1} = 7.14 \pm 0.01$ and $pK_{a1} = 10.93 \pm 0.04$.

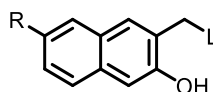
The resulting spectra showed that the absorption bands of the protonated and deprotonated reactive species are very similar for all the precursors (Table 6). More powerful electron-withdrawing groups red-shifted both absorption bands, despite such bathochromic effect was much more intense for the deprotonated species (.ca 40 nm vs 20 nm).

Table 6: Absorption maxima of 10^{-4} M solutions in H_2O of 7-substituted 2-naphthol Mannich bases and quaternary ammonium salts. λ^+ and λ^{z^w} correspond to the absorptions relative to the fully protonated Mannich base and the zwitterion respectively; λ and λ^- correspond to the absorptions relative to the quaternary ammonium salt and the deprotonated conjugated base respectively.

^a R = $CONH(CH_2)_3NHMe_2^+$

^b R = COO^-

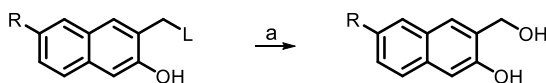
^c R = $B(OH)O^-$



R	L=NMe ₂	λ^+ (nm)	λ^{z^w} (nm)	L=NMe ₃ ⁺ Cl ⁻	λ (nm)	λ^- (nm)
	158 ^a	298	324	-	-	-

R	L=NMe ₂	λ ⁺ (nm)	λ ^{zw} (nm)	L=NMe ₃ ⁺ Cl ⁻	λ (nm)	λ ⁻ (nm)
	-	-	-	159	298	328
COOMe	155	306	334	156	307	336
COOH	151	306	320 ^b	-	-	-
CHO	149	317	365	150	320	370
B(OH) ₂	157	287, 337	351 ^c	-	-	-
	162	324	355	163	322	357

The effect of the substituent on quinone methide generation efficiency was thus investigated. Since all the compounds paralleled the spectral behavior of **155** and **156**, irradiation in the near UV was possible in every case. Therefore, simple photohydrolysis experiments in ACN-H₂O 1:1 using 310 nm centered light source were performed to assess NQMP photoreactivity (Scheme 53). In analogy to what have been observed in arylethynyl benzo-QMPs, the effect of the substituent attached to the naphtho-core was governed by its electron-withdrawing character (Table 7). In fact, the carboxylic acid **151**, the aldehyde **149** and the oxadiazole **162** were less reactive than the ester **155**. However, in contrast to this trend, amide **158** was markedly less reactive than the ester **155**, despite the lower electron-withdrawing ability. The same trend was confirmed for the quaternary ammonium salts. Interestingly, though, direct comparison with the analogous Mannich bases showed an unexpected lower reactivity, with the only exception of amide **159**. This is rather in contrast with what was observed for the parent *o*-QMP system (see Section 3.1) and might be a unique feature of such naphtho-derivatives, which should be taken into account for subsequent implementation into the ligand scaffolds.



Scheme 53: NQMs hydration products by photogeneration from NQMPs. All reactions were performed in a Rayonet® multilamp reactor using 2 x 15 W UV lamps and 20 mL quartz tubes. (a) 10⁻⁴ M solution in ACN-H₂O 1:1, 310 nm, 20 min – 6 h depending on Φ_R (yields: 18 - 95%).

Table 7: Quantum yield of photohydration (Φ_R) of 10^{-4} M solutions of 7-substituted NQMPs in ACN:H₂O 1:1 irradiated at 310 nm.

R	L=NMe ₂	Φ_R	L=NMe ₃ ⁺ Cl ⁻	Φ_R	L=OH
	158	0.084	-	-	171
	-	-	159	0.17	172
COOMe	155	0.37	156	0.19	165
COOH	151	0.049	-	-	173
CHO	149	0.010	150	0.0016	174
B(OH) ₂	157	0.042	-	-	175
	162	0.016	163	0.0054	176

In conclusion, 7-substituted naphtho-QMPs were shown to be capable of generating highly electrophilic QM intermediates through ESPT mechanisms. The nature of the remote substituent influenced the efficiency of the naphtho-QM generation process in a rather similar way to the substituted arylethynyl benzo-QMPs (Section 3.1). In particular, powerful electron-withdrawing groups had a detrimental effect on QM generation, although providing a convenient red-shift in the absorption properties of the precursor. However, the nature of the leaving group had a much less clear influence on the elimination process which precedes QM formation.

3.3 Towards selective G4 photo-alkylation

The ability to form a covalent bond, giving rise to an irreversible immobilization of the ligand on the G4 structure, could open up new perspectives for the development of novel quadruplex-binding molecular tools for in cell applications^[84]. Ligand-mediated photoreactivity on G4 has been prompted by the potential applications of G4 tagging and “pull-down” processes by covalent modifications.

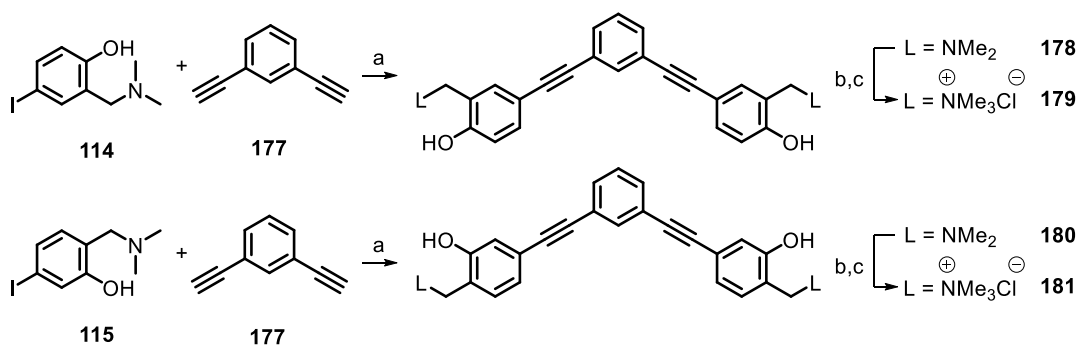
To date, only two classes of alkylating G4 ligands upon photoactivation have been described^[136, 137], and were based on benzophenone and arylazide excited state chemistry in one case, photo-induced electrontransfer and phenoxy radical generation in the other. This innovative photoaffinity labeling of G4-ligand interactions encloses the potential of obtaining spatial and temporal control over the alkylation event, providing an added value for diagnostic and therapeutic strategies. However, due to the irreversible nature of the newly formed bond, such photoaffinity labels cannot be exploited for G4 genome sequencing, which requires ligand detachment after pull-down. Conversely, the unique reversibility – upon irradiation – of the alkylation adducts formed with phototriggerable quinone methides, could offer a precious tool for mapping G4-forming sites in the strict cell context.

Apart from better analyze ligand-G4 interactions or capture a particular DNA sequence, it is also mandatory to get more corroborating proofs of G4 alkylation as a valuable therapeutic strategy. In this context, the design of new reversible ligand/alkylating agent hybrids is highly desirable. Based on the results discussed in the previous sections, a series of putative ligands embedding multiple photoactivatable quinone methide precursors have been developed.

First, the synthetic approach to 3 classes of water-soluble putative G4 ligands will be presented. Hence, the result of several screening biophysical assays will be shown and some conclusion will be derived concerning their binding mode. Additionally, the photoalkylation proprieties of the same compounds will be evaluated by PAGE analysis of the irradiated mixtures with two selected G4-forming oligonucleotides and in the presence of ds-DNA competitor. Stability of the newly formed covalent bond under heating will be determined. Finally, three lead compounds will be selected for assessing the sites of alkylation. Preliminary data will be presented in this regard.

3.3.1 Synthesis of V-shaped bifunctional o-QMPs

Based on the results achieved in Section 3.1, the synthesis of an extended aromatic compound embedding the arylethynyl structural motif was prompted. The evidences supporting target preference for planar V-shaped small molecules suggested the possible exploitation of a 1,3-diarylethynylbenzene scaffold^[126] (Scheme 54). Besides simplifying the overall synthetic approach, the design of a symmetrical structure enabled the introduction of two QMPs at the same time. The presence of more than one QMP within the same molecule was proposed to enhance the photoreactivity. In fact, although the single chromophore quantum yield is not affected, the overall cross-section results doubled. In addition, considering the typical reversibility of QM alkylation adducts promoted both thermally and photochemically, the use of bifunctional QMPs could potentially lead to cross-links between G-quadruplex nucleobases, thus lowering considerably the probability of off-target migration, which would require simultaneous QM generation and ligand detachment. Finally, directly conjugated electronrich QMPs should enhance each other's photoreactivity, as previously shown.



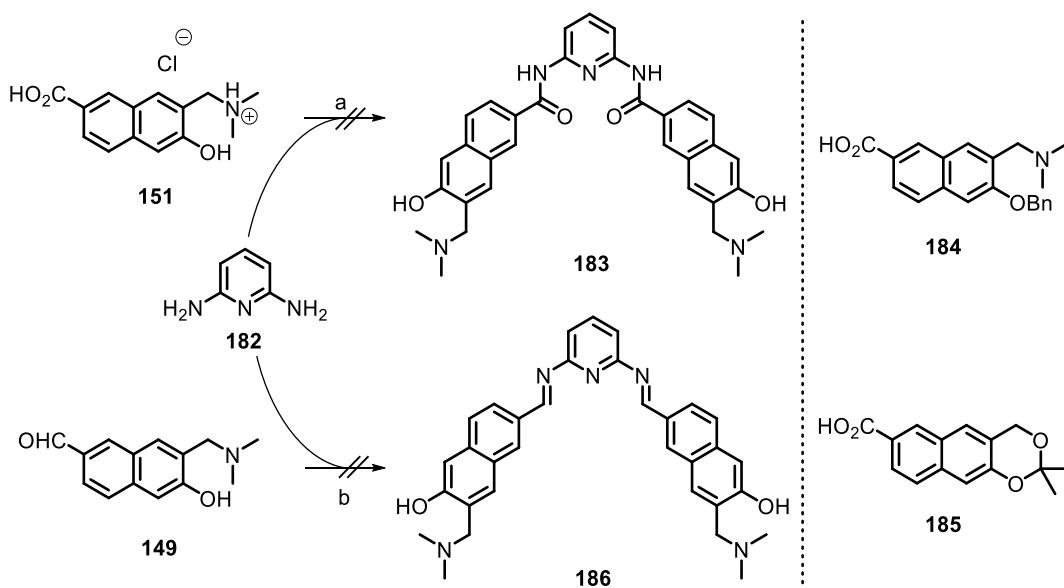
Scheme 54: Synthesis of V-shaped bifunctional o-QMPs **178–181**. (a) Pd(PPh₃)₂Cl₂ 10%, CuI 20%, TEA, DMF, rt, 9 h (yields: 25-38%); (b) MeI, ACN, rt, 48 h; (c) HCl, H₂O (yields over 2 steps: 97-99%).

The synthesis of V-shaped bifunctional o-QMPs followed straightforwardly the protocol used in Section 3.1. Therefore, the isomeric iodo-derivatives **114** and **115** were coupled with commercially available 1,3-diethynylbenzene (**177**) through Sonogashira cross-coupling in DMF to afford Mannich bases **178** and **180** (Scheme 54). This time, a high catalyst loading was needed and the low isolated yields reflected low substrate reactivity and catalyst turnover. Methylation of the tertiary amines was achieved by addition of excess

iodomethane in ACN affording the quaternary ammonium salts **179** and **181**. Hence, the affinity for quadruplex DNA and the subsequent photoreactivity was studied in vitro for both Mannich bases and quaternary ammonium salts.

3.3.2 Synthesis of V-shaped bifunctional NQMPs

The preliminary study described in Section 3.2 suggested that for efficient QM generation from 7-substituted naphtho-QMP the best functional group is the ester. Unfortunately, this functionality cannot be used as a central structural motif when it comes to build a G4 ligand. In order to get a planar arrangement for the whole ligand all the atoms of the central core must be sp^2 hybridized, but both arylesters and vinylsters suffer of hydrolytic instability. Conversely, arylamides have been extensively used as G4 binders, as fully demonstrated by the PDC series^[80], **Phen-DC3** and **Pyridostatin**, which are still considered among the most powerful and selective ligands. Therefore, the first attempts were made towards the synthesis of dicarboxamide **183** (Scheme 55).

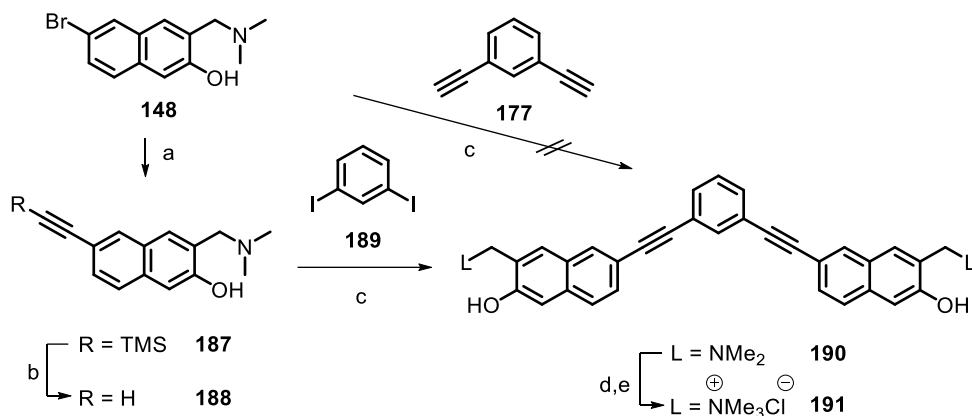


Scheme 55: Unsuccessful synthesis of dicarboxamide **183** and diimine **186**. (a) PyBOP, DIPEA, DMF, 60°C, 3 d; (b) MeOH, reflux, 22 h. Neither protected carboxylic acids **184** and **185** reacted with 2,6-diaminopyridine **182**.

Unfortunately, the condensation was unsuccessful, and even when the hydroxyl group was protected as a benzylether (**184**) or in the absence of the tertiary amine (**185**) no reaction was observed between the carboxylic acid and 2,6-diaminopyridine (**182**). Imine formation

between aldehyde **149** and **182** was also endeavored to afford compound **186** with little success.

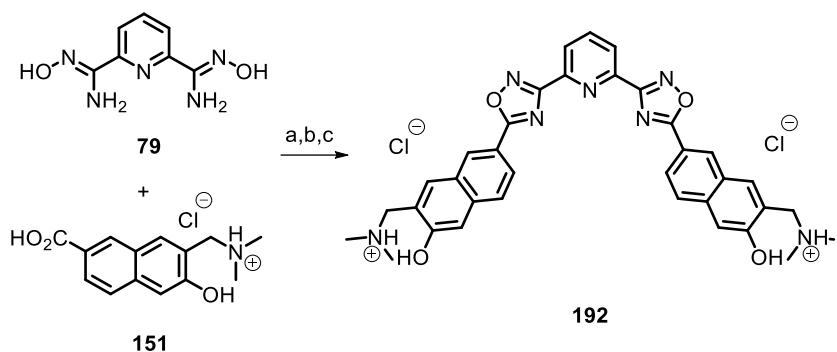
Therefore, two alternative strategies were considered. The first was the exploitation of the arylethynyl motif used successfully with the benzo-QMPs (Scheme 56). Unfortunately, any attempt of obtaining compound **190** through direct cross-coupling between bromo-derivative **148** and **177** was vain. Luckily, employing less sterically demanding ethynyltrimethylsilane afforded the desired arylethynyltrimethylsilane **187** in good yield. Subsequent TMS cleavage by basic methanol and Sonogashira cross-coupling with highly reactive 1,3-diiodobenzene (**189**) afforded the desired compound **190** in excellent yield. The quaternary ammonium salt **191** was achieved by addition of excess iodomethane in ACN. To get over the low kinetics observed at room temperature, exhaustive methylation was accomplished at reflux temperature to solubilize the reagent.



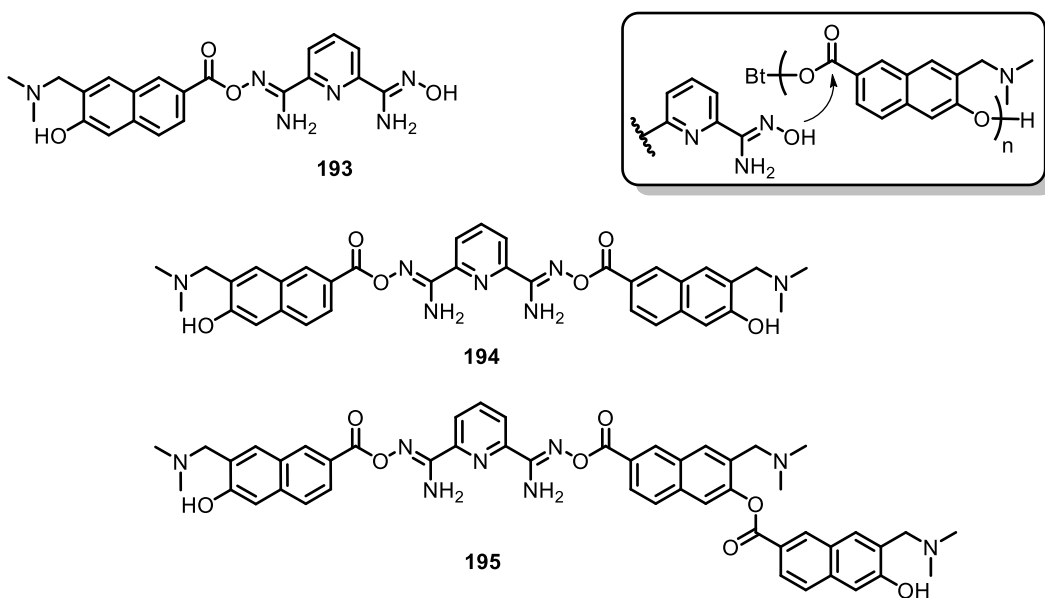
Scheme 56: Synthesis of V-shaped bifunctional arylethynyl NQMPs **190** and **191**. a) PdCl₂(PPh₃)₂ 4%, CuI 4%, TMS-CCH, TEA, 80°C, 1 h (yield: 86%); (b) K₂CO₃, MeOH, rt, 16 h (yield: 59%); (c) PdCl₂(PPh₃)₂ 4%, CuI 4%, TEA, 80°C, 2 h (yield: 81%); (d) MeI, ACN, reflux, 2 h; (e) HCl, H₂O (yield over 2 steps: 68%).

The second strategy relied on extending the synthesis of oxadiazole **162** for a bifunctional derivative **192** (Scheme 57), which closely mimics the structure of oligo-heteroaromatic compounds of Chapter 2. The same protocol was applied, but diamidoxime **79** was used in the place of monofunctional analogue **160**. After the acylation step (Scheme 57a) three major products **193-195** were isolated and characterized by ESI-MS. Their structure (Scheme 58) was consistent with a reaction mechanism involving a slow transacylation step following the fast formation of an oligomeric arylester by condensation of the carboxylic acid of one

molecule with the naphthol hydroxyl of another. Eventually, ring closing cyclodehydration was achieved under basic conditions, affording the Mannich base **192**.



Scheme 57: Synthesis of V-shaped bifunctional oligo-heteroaryl NQMP **192**. a) PyBOP, DIPEA, DMF, rt, 6 d; (b) K_2CO_3 , DMF, $65^\circ C$, 2 h; (c) HCl, H_2O (yield over 3 steps: 34%).



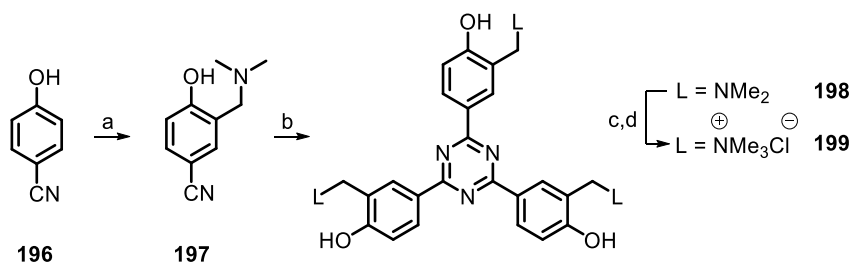
Scheme 58: Structures of the intermediates identified during the step (a) in Scheme 57. Proposed transacylation mechanism accounting for the observed intermediate **195**.

Despite the fact that it would have been worth to synthesize the quaternary ammonium salt as the effect of the leaving group on the reactivity of the prototype NQMPs was much less clear if compared to the benzo-analogues, the low isolated yield for compound **192**, together with the long multi-step procedure, did not allow its achievement.

3.3.3 Synthesis of trifunctional o-QMPs

To realize the tempting synthesis of a trifunctional QMP as G4 alkylating agent, the choice fell upon the C_3 -symmetric 2,4,6-triaryl-1,3,5-triazine scaffold. The most convenient route towards symmetrically trisubstituted triazines is based on the cyclotrimerization of aryl nitriles under highly acidic conditions (triflic acid or anhydride are mostly used) and has been widely described in the literature^[273]. Moreover, the central triazine ring ensured the effective planar arrangement of the oligoaryl system, while its electronic properties should control the overall electron-poor nature of the putative ligand.

Following a two steps protocol (Scheme 59), commercially available 4-cyanophenol **196** was first converted into its Mannich base **197** through the same procedure used for iodo-derivatives **114** and **115**. Subsequently, the nitrile was treated with triflic acid in chloroform, yielding the cyclotrimerization product **198** in good yield. Methylation of the tertiary amines was achieved by addition of excess iodomethane in ACN affording the quaternary ammonium salt **199**.



Scheme 59: Synthesis of trifunctional o-QMPs **198** and **199**. (a) PFA, NHMe₂ 33% in EtOH, EtOH, reflux, 2 h (yield: 50%); (b) TfOH, CHCl₃, rt, 48 h (yield: 83%); (c) MeI, ACN, rt, 24 h; (d) HCl, H₂O (yield over 2 steps: 97%).

3.3.4 QMPs as G-quadruplex reversible ligands

To evaluate the ability of the tested compounds to stabilize quadruplex structures, a preliminary FRET-melting assay was performed with a panel of seven G4-forming oligonucleotides. The assay was carried out under standard conditions, where labelled DNA 0.2 μM was incubated with the tested compound 1.0 μM .

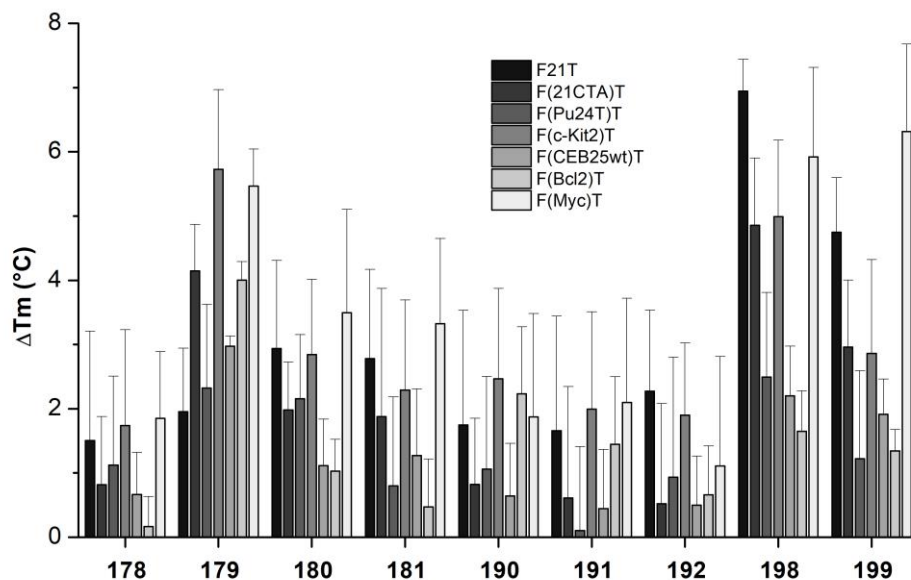


Figure 74: FRET-melting assay for photoalkylating agents **178-181**, **190-192**, **198-199** with a panel of G4s. Conditions: DNA 0.2 μ M, compounds 1 μ M, LiCaco 10 mM (pH 7.2), LiCl 99 mM and KCl 1 mM (LiCl 90 mM and KCl 10 mM for F21T and F(21CTA)T).

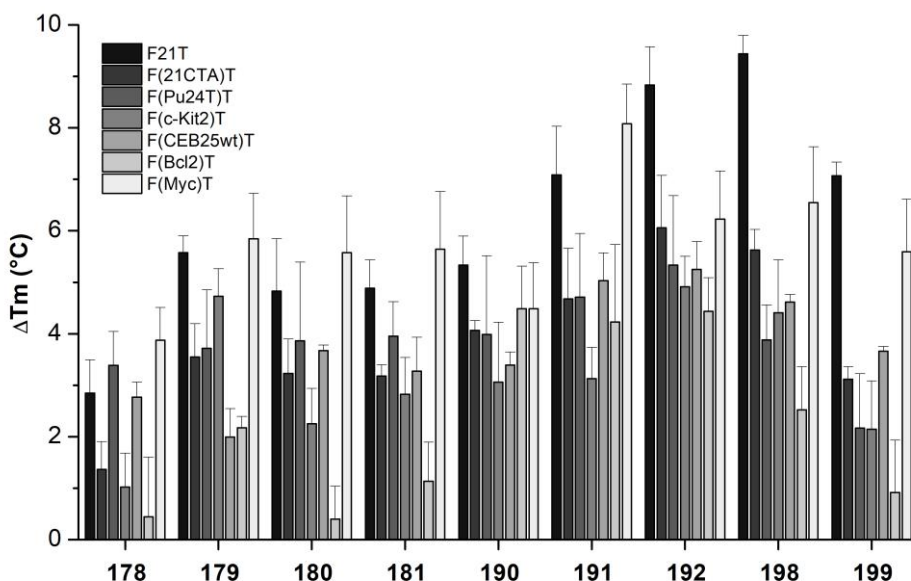


Figure 75: FRET-melting assay after doubling the concentration of the compounds. Conditions: DNA 0.2 μ M, compounds 2 μ M, LiCaco 10 mM (pH 7.2), LiCl 99 mM and KCl 1 mM (LiCl 90 mM and KCl 10 mM for F21T and F(21CTA)T).

The measured melting stabilization temperatures (Figure 74) were quite low and did not exceed 8°C even in the best cases (i.e. triazines **198** and **199**). Moreover, the standard deviation was often comparable to the ΔT_m value itself. Therefore, this first assay did not allow the proper characterization of the affinity of such structures for quadruplex DNA. Hence, the same screening was performed after doubling the concentration of the tested compounds (DNA 0.2 μM , compound 2 μM). A significant increase of the G4 stabilization was observed (Figure 75), even if ΔT_m values did not exceed 10°C in every case studied. Moreover, keeping in mind that ΔT_m values for different structures should not be directly compared as they depend on the intrinsic stability of any particular G4, no significant differences were observed in the relative selectivity among different G4-forming sequences. The only evident discrepancy could be attributed to F(Bcl2)T, for which naphtho-QMPs **190-192** showed to be better ligands if compared to benzo-QMPs.

As a further evidence for the actual interaction with quadruplex DNA, the same compounds were screened with two selected sequences, namely F21T and F(Pu24T)T, at a concentration as high as 20 μM , corresponding to 100 equivalents. The ΔT_m values were plotted against ligand concentration, showing a clear dose-response correlation (Figure 76). In both cases a similar pattern was observed, which allowed to rank the compounds for their ability to stabilize a general G-quadruplex.

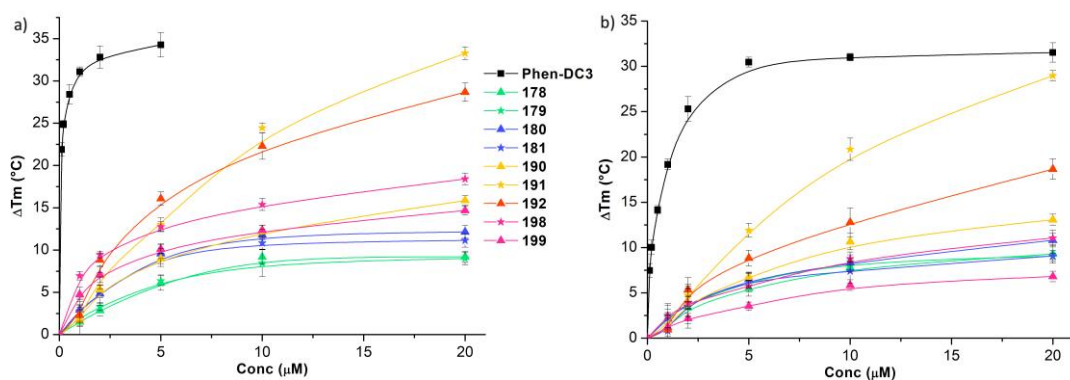


Figure 76: Dependence of ΔT_m of (a) F21T and (b) F(Pu24T)T on the concentration of the putative ligands. Conditions: (a) DNA 0.2 μM , LiCaco 10 mM (pH 7.2), LiCl 90 mM and KCl 10 mM; (b) DNA 0.2 μM , LiCaco 10 mM (pH 7.2), LiCl 99 mM and KCl 1 mM. **Phen-DC3** has been used as a reference.

In particular, naphtho-QMPs **190-192** were found to be better ligands than benzo-QMPs **178-181** and **198-199**, and among them the quaternary ammonium salt **191** was the more

effective at 20 μM , while oligoarylic compound **192** situates between **191** and the corresponding Mannich base **190**. Among bifunctional benzo-QMPs **178-181**, the binding was substantially unaffected by the nature of the leaving group, while 5-arylethynyl **180-181** were slightly more performing than 4-arylethynyl derivatives **178-179**. Trifunctional benzo-QMPs based on the triazine core **198** and **199** showed a similar behavior and meanly the same affinity as their bifunctional counterpart, but with a slight preference for the telomeric sequence F21T. Definitely, none of the tested compounds were vaguely comparable to benchmark **Phen-DC3** in its ability to stabilize G4 even at very low concentration. In this context, it should be remembered that the upper limit of ΔT_m in melting assays normally lies between 30 and 40°C – depending on the actual sequence – as melting temperatures above 90°C are not measurable.

To assess the selectivity of the ligands for G-Quadruplex secondary structures over duplex DNA, FRET-based competition assays were performed for the same G4-folding sequences (F21T and F(Pu24T)T) with increasing concentration of a competitor *ds*-DNA (ds26). Notably, despite the general low affinity, all the compounds under study displayed good selectivity for the tested G4s, as the ΔT_m was poorly affected by the addition of the competitor (Figure 77). In the worst case, i.e. oligoarylic NQMP **192** and sequence Pu24T, the melting stabilization temperature diminished from 19.9°C to 9.4°C after addition of 10 μM of ds26, which correspond to about 118 base pairs equivalents.

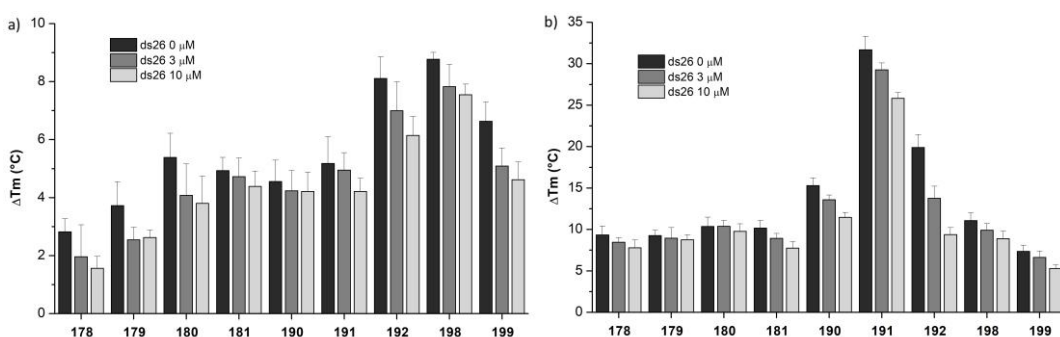


Figure 77: FRET-melting competition assay for photoalkylating agents **178-181**, **190-192**, **198-199** with (a) F21T and (b) F(Pu24T)T in the absence and in the presence of double-stranded DNA competitor (ds26). Conditions: (a) DNA 0.2 μM , compounds 1 μM , ds26 0, 3, or 10 μM , LiCaco 10 mM (pH 7.2), LiCl 90 mM and KCl 10 mM; (b) DNA 0.2 μM , compounds 20 μM , ds26 0, 3, or 10 μM , LiCaco 10 mM (pH 7.2), LiCl 99 mM and KCl 1 mM.

Fluorescence intercalator displacement (FID) was used as a further G4 affinity screening assay. Fluorescence titrations of the 2:1 complex between thiazole orange (TO) and eight DNA sequences (seven G4 and one *ds*-DNA) were performed with all the QMPs under study. Thiazole orange displacement (TOD) was hence inferred by fluorescence quenching (Figure 78). Remarkably, in most of the cases no significant displacement was observed even after addition of 10 equivalents of ligand. The only exceptions to this trend were observed for triazines **198** and **199** and 22AG and Myc sequences (those with the highest ΔT_m on FRET-melting assay, Figure 74), for which a still low 40% of displacement was obtained after the addition of 10 equivalents of ligand.

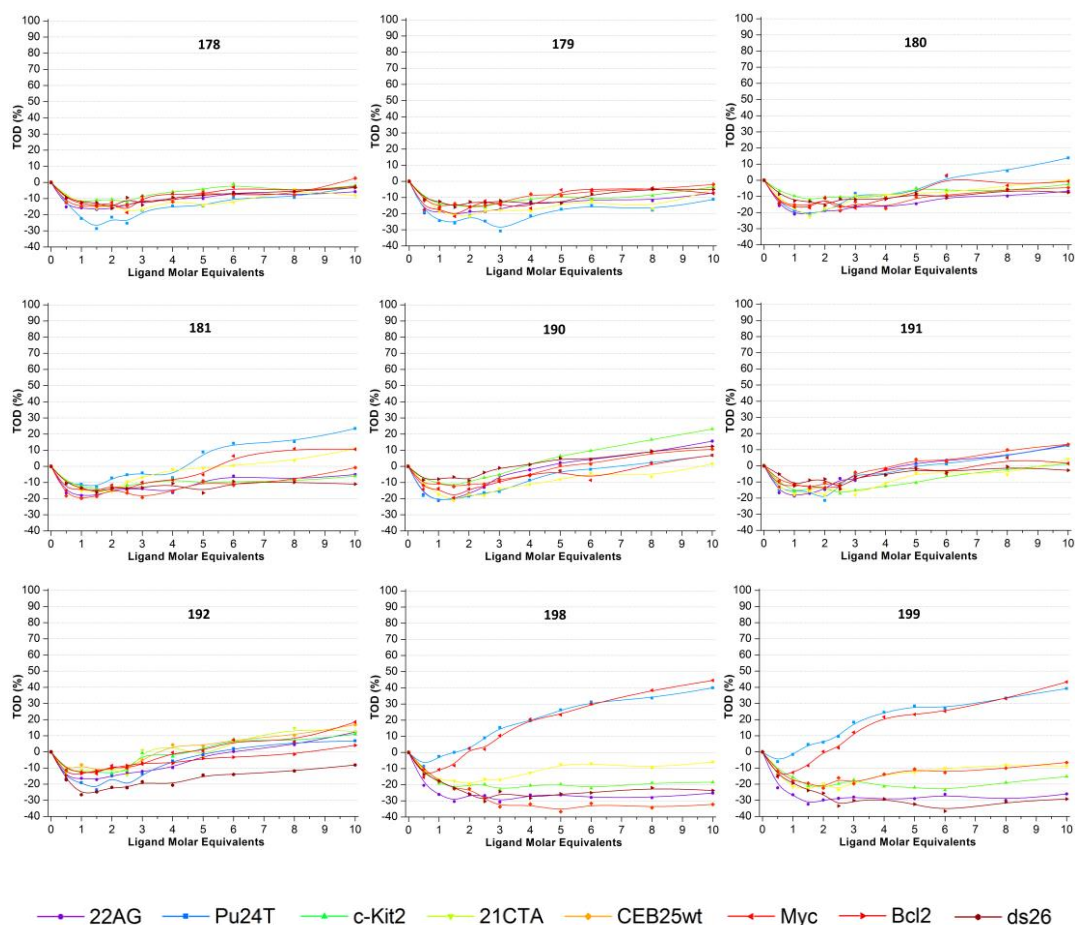


Figure 78: FID titration assay for photoalkylating agents **178-181**, **190-192**, **198-199** with a panel of seven G4s and one *ds*-DNA control sequence (ds26). Conditions: DNA 0.25 μ M, TO 0.5 μ M, compounds 0–2.5 μ M, LiCaco 10 mM (pH 7.2), KCl 100 mM.

The complete absence of TO displacement, along with the relatively low values of ΔT_m under standard conditions led to consider the possibility that the affinity of the QMPs for DNA in general is very weak, far lower than that of thiazole orange.

In order to investigate this aspect and gain a better understanding on the actual affinity of the QMPs as reversible binders, UV-vis absorption measurements were performed. In particular, a slight red-shift at about 320-340 nm in the absorption spectrum of **181** was noticed upon addition of DNA, and assigned to the bound species (Figure 79a). Importantly, this bathochromic shift was enough intense to allow the monitoring of complex formation during a titration. Therefore, binding constants for the complexes of **181** with different DNA structures were extrapolated from UV-vis titrations (Figure 79b-d).

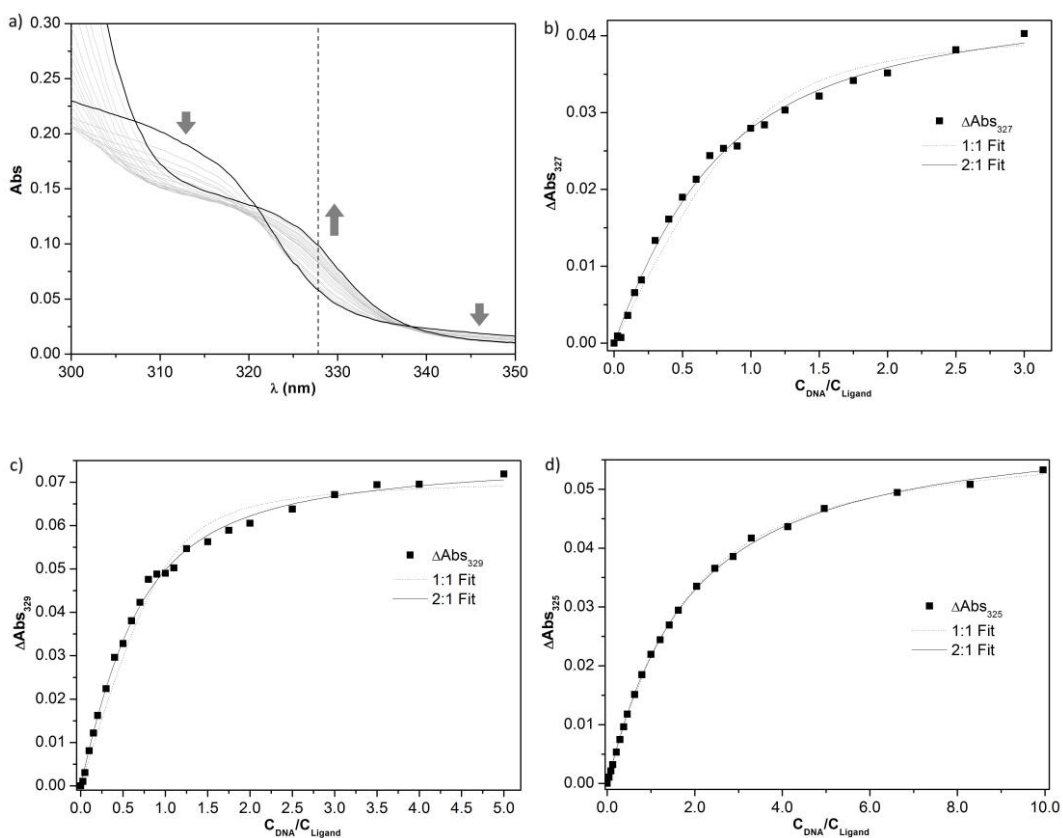


Figure 79: (a) Change in the UV-vis absorption spectrum of **181** (5 μM) upon addition of 22AG G4. Conditions: LiCaco 10 mM (pH 7.2), KCl 100 mM. (b-d) Titration plots of the absorption enhancement at the most convenient λ vs DNA equivalents; fitting analysis yielded 2:1 ligand-DNA stoichiometry in each case. (b) 22AG, $K_a = (2.3 \pm 0.2) \cdot 10^5 \text{ M}^{-1}$. (c) Pu24T, $K_a = (2.8 \pm 0.1) \cdot 10^5 \text{ M}^{-1}$. (d) ds26, $K_a = (6.6 \pm 0.1) \cdot 10^4 \text{ M}^{-1}$.

For simplicity, the absorption enhancement plots were fitted with a model that considers n independent host (DNA) binding sites for which the guest (QMP) exhibits the same binding constant K_a (see Appendix B). The parameter n was fixed as an integer and the best fit was obtained for a 2:1 guest-host stoichiometry for all the cases. The affinity of **181** for quadruplex structures is well depicted by the extrapolated mean binding constants $K_a = (2.3 \pm 0.2) \cdot 10^5 \text{ M}^{-1}$ for its complex with 22AG and $K_a = (2.8 \pm 0.1) \cdot 10^5 \text{ M}^{-1}$ with Pu24T. According to the aforementioned selectivity, the binding constant for the complex with duplex DNA ds26 is about 5-fold lower ($K_a = (6.6 \pm 0.1) \cdot 10^4 \text{ M}^{-1}$).

Since the reported affinity constant for TO-G4 complexes is in the order of 10^5 - 10^6 (e.g. $K_a = 2.1 \cdot 10^6 \text{ M}^{-1}$ for 22AG in K^+ buffer)^[146], the measured K_a could account for low TOD values and/or curve slope, but not for the observed complete absence of any displacement. Probably an independent binding site was involved for QMP **181**, so that TO stacking interactions with the external quartets were not affected by QMP complexation. Likely, the conclusion held true for the other QMPs, although the K_a were not measured.

The interaction of the putative ligands with quadruplex DNA was further established by circular dichroic spectroscopy. The CD spectra of six G4 sequences were measured before and after incubation with increasing concentration of QMPs. In almost all cases a significant change in the G4 dichroic signature was observed as a consequence of complex formation (Figure 80).

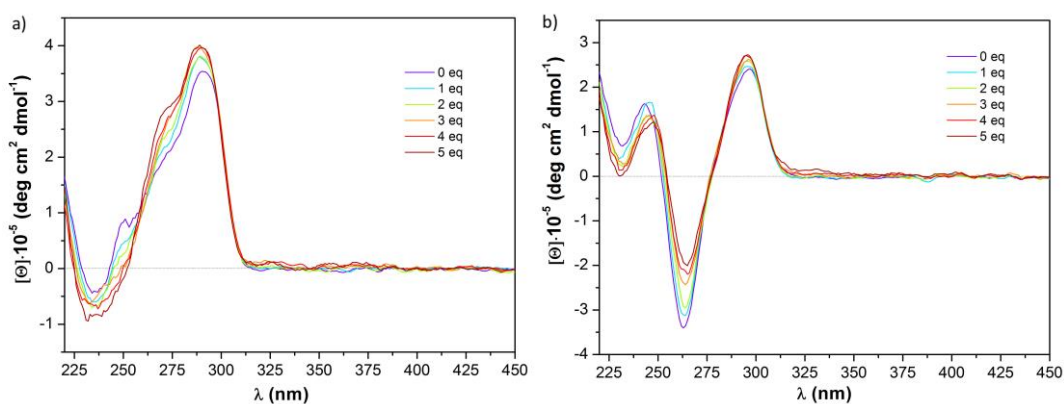


Figure 80: CD titration of 22AG in (a) K^+ and (b) Na^+ rich buffers, with trifunctional QMP **198**. Conditions: DNA $3 \mu\text{M}$, compounds up to $15 \mu\text{M}$, LiCaco 10 mM (pH 7.2), KCl or NaCl 100 mM .

Remarkably, the formation of a signal associated with ligand transitions was also evident in some cases. For instance, addition of arylethynyl naphtho-QMP **190** to both hybrid (in K^+ -rich buffer) and antiparallel (Na^+ -rich buffer) 22AG G4 clearly showed the appearance of a new band ascribable to an induced CD (Figure 81). Remarkably, such an intense ICD is the typical signature of an electronic transition arising from a helical arrangement of conjugated π systems.

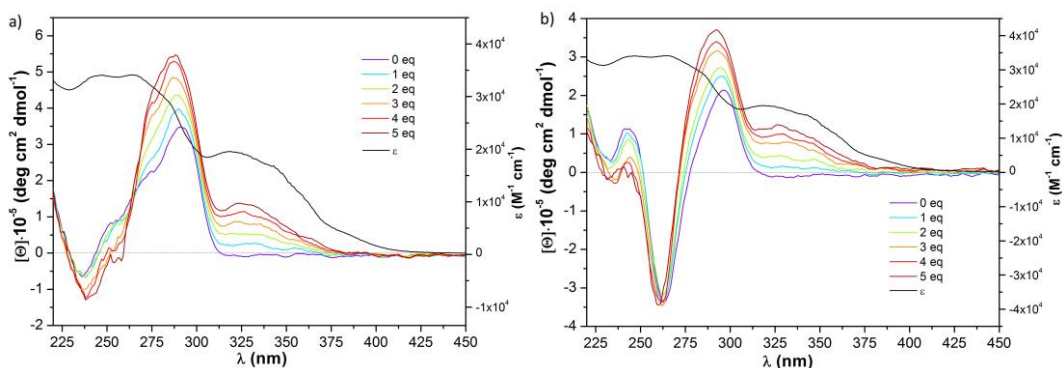


Figure 81: CD titration of 22AG in (a) K^+ and (b) Na^+ rich buffers, with arylethynyl naphtho-QMP **190**. Conditions: DNA $3 \mu M$, compounds up to $15 \mu M$, LiCaco 10 mM (pH 7.2), KCl or NaCl 100 mM . Ligand molar absorptivity has been superimposed for a clearer comparison.

This ICD is common to most arylethynyl QMPs (both benzo- and naphtho-), although some distinctions must be made among the different compounds. In particular, 5-arylethynyl benzo-QMPs **180** and **181** displayed a marked ICD band – positive or negative depending on the particular sequence – whereas isomeric 4-arylethynyl **178** and **179** did not (Figure 82).

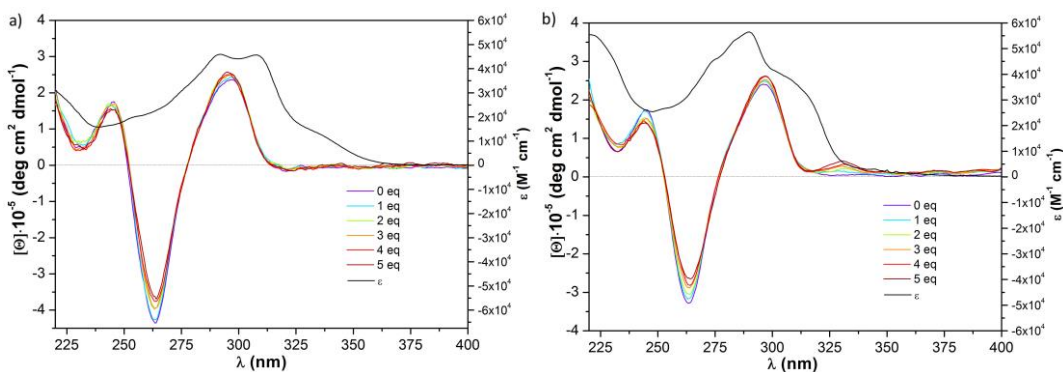


Figure 82: CD titration of 22AG in Na^+ rich buffer with arylethynyl quaternary ammonium salts (a) **179** and (b) **181**. Conditions: DNA $3 \mu M$, compounds up to $15 \mu M$, LiCaco 10 mM (pH 7.2), NaCl 100 mM . Ligand molar absorptivity has been superimposed for a clearer comparison.

The ICD arousal for oligoaryl QMP **192** was particularly interesting as it was observed in a topological dependent manner (Figure 83). More specifically, a remarkable negative ICD signal was observed upon complexation of hybrid and antiparallel G4, namely 22AG in K^+ , 22AG in Na^+ , and 21CTA. Conversely, no additional transition was detected with parallel conformations, namely c-Kit2, Myc and Pu24T. The fact that the former group of G4 has less hindered grooves, as they are not occupied by propeller-type loops, suggested that the binding might occur precisely at such site and thus produce an ICD signal, usually associated with helical distortion. On the contrary, the encumbered grooves of parallel G4s make such interaction mode less feasible, which was in agreement with the lack of ICD.

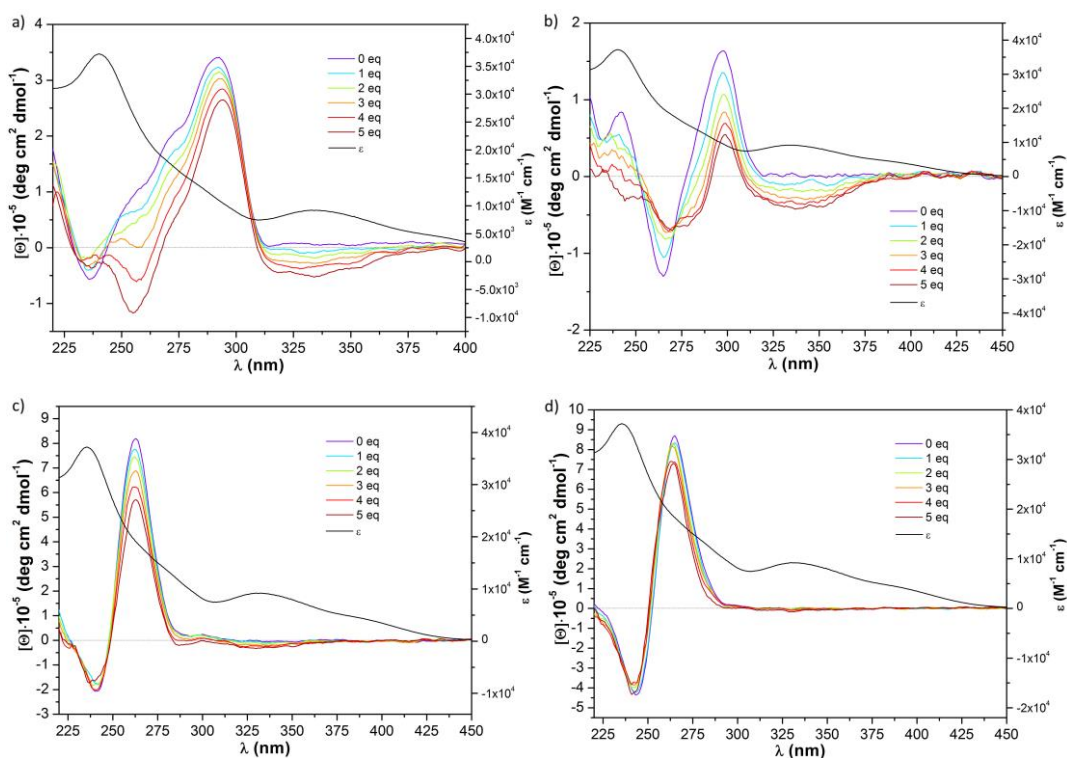


Figure 83: CD titration of (a) 22AG in K^+ rich buffer, (b) 22AG in Na^+ rich buffer, (c) c-Kit2, (d) Myc with oligoaryl QMP **192**. Conditions: DNA $3 \mu M$, compounds up to $15 \mu M$, LiCaco 10 mM (pH 7.2), KCl or NaCl 100 mM (if not specified KCl was used). Ligand molar absorptivity λ has been superimposed for a clearer comparison.

Differently from the other QMP ligands, trifunctional benzo-QMP **198** and **199** did not feature any ICD signal (Figure 80). However, this opposite behavior was in line with what had already been observed in FID and FRET-melting assays, and might be justified by the markedly different structure.

3.3.5 Photoalkylation of G-quadruplex

As biophysical assays confirmed a certain degree of interaction with the targets, the tests proceeded to assess the alkylating activity of the compounds. First, the UV-visible absorption spectra of all the synthesized compounds were measured under the same conditions needed for G-quadruplex formation, namely lithium cacodylate and KCl buffered water (pH 7.2), in order to choose the appropriate irradiation conditions for the following experiments.

Table 8: Absorption maxima in H₂O – lithium cacodylate 10 mM (pH 7.2), KCl 100 mM – of putative G4 photoalkylating agents.

		L=NMe ₂	λ_{\max} (nm)	L=NMe ₃ ⁺ Cl ⁻	λ_{\max} (nm)
Bifunctional QMP	4-ethynyl	178	308	179	308
	5-ethynyl	180	288	181	290
Bifunctional NQMP	7-ethynyl	190	319	191	322
	7-oxazole	192	333	-	-
Trifunctional QMP	Triazine	198	358	199	360

Besides the absorption maxima located around 310 nm (Table 8), the bifunctional arylethynyl benzo-QMPs **178-181** featured an absorption band extending up to 370 nm (Figure 84), which is in line with what had been observed for the prototype system (Section 3.1). The substitution of the benzo-QMP with the naphtho-analogue (**190** and **191**) already broadened the absorption tail up to 400 nm, proving itself a successful strategy to achieve a red-shift in the visible region. The additional electron-poor oxadiazole system enhanced this bathochromic effect further extending the absorption band up to 430 nm (**192**). Despite bearing benzo-QMPs, the trifunctional triazines **198** and **199** exhibited a remarkably red-shifted band due to the intervention of a charge transfer mechanism from the phenol to the central triazine ring. In this case, the absorption extended up to 400 nm and the maxima fell at higher wavelengths than those of all the other derivatives (360 nm).

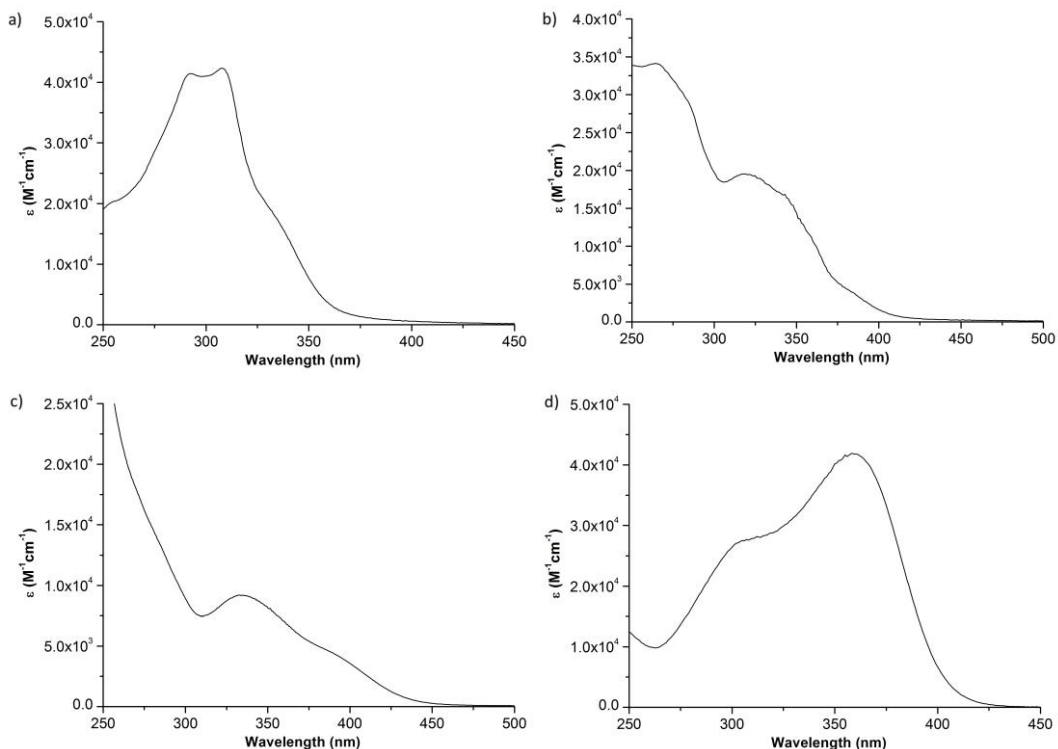


Figure 84: Absorption spectra of compound (a) **178**, (b) **190**, (c) **192** and (d) **198** 10^{-5} M in H_2O under the same conditions used in the biophysical and biochemical assays with DNA, i.e. lithium cacodylate 10 mM (pH 7.2), KCl 100 mM.

Next, the ability to alkylate the bound target upon an external light stimulus was tested on two G4-folding sequences (22AG and Pu24T). The reaction mixtures were exposed to 365 nm filtered and collimated light beam. After irradiation, the reaction mixtures were analyzed by denaturing polyacrylamide gel electrophoresis (PAGE). 5'-end ^{32}P -labelled oligonucleotides were used to detect and quantify the separated bands.

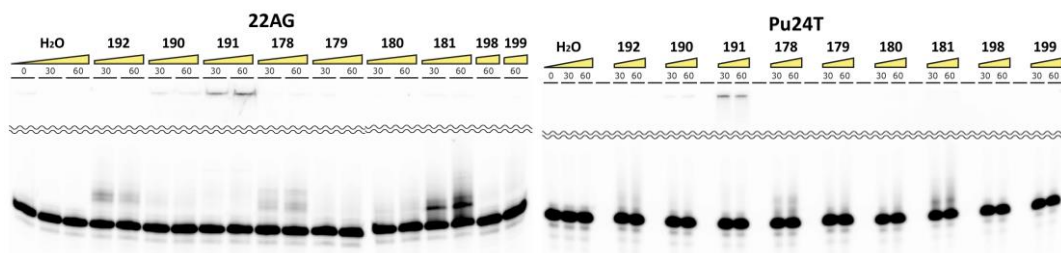


Figure 85: Denaturing 15% PAGE analysis of the irradiated 22AG and Pu24T G4s alone and incubated with the QMPs. Conditions: DNA 10 μ M, compounds 20 μ M, LiCaco 10 mM (pH 7.2), KCl 100 mM, 365 nm, 0.1 mW, 30 and 60 minutes irradiations.

As a first screening, all the compounds were irradiated in the presence of both G4s. Blank samples containing only DNA were used as a reference. In almost all cases a new slowly migrating band was detected, consistently with the expected alkylated adduct formation (Figure 85). Triazines **198** and **199** were the only QMPs displaying negligible photoreactivity, likely due to a competitive excited state deactivation mechanism (e.g. tautomerization).

The four compounds that displayed the highest photoreactivities, regardless of the sequence, were **178**, **181**, **191** and **192**. However, arylethynyl naphtho-QMP **191** produced a non-migrating band, whose intensity depended on the irradiation time and compound concentration (data not shown). This was likely due to wide DNA clustering caused by adduct precipitation. The detection of such a band indicated itself that the compound was effectively photoreactive, but the precipitation hampered further investigation of the phenomenon as it impeded gel analysis. Such compound was hence discarded and the investigation was focused on the remaining three.

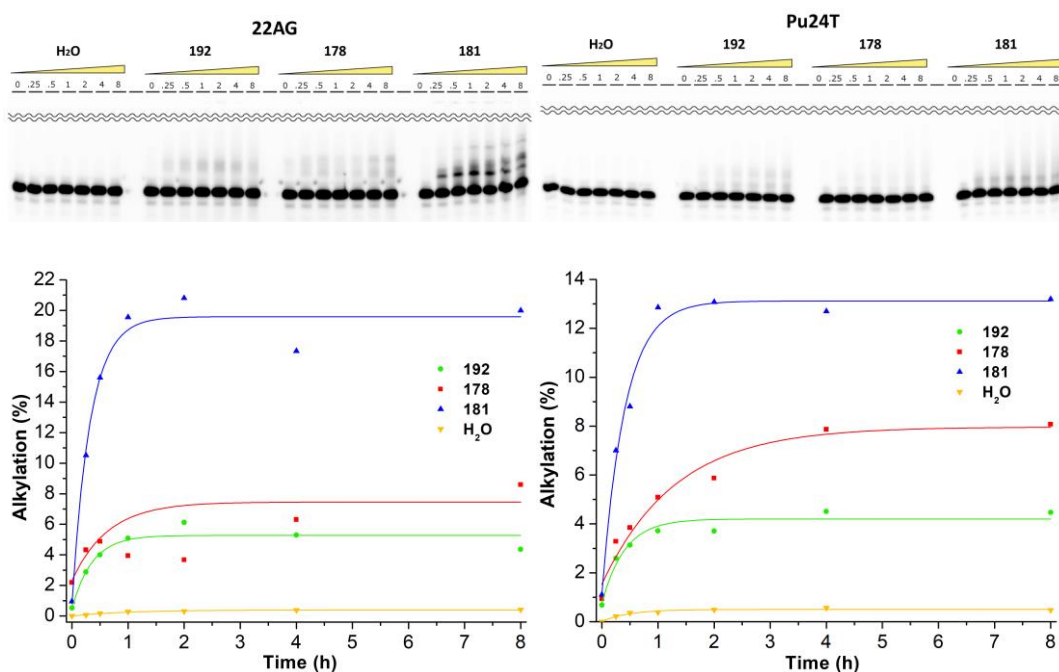


Figure 86: (above) Denaturing 15% PAGE analysis of the irradiated 22AG and Pu24T G4s alone and incubated with the more reactive QMPs **178**, **181** and **192**. Conditions: DNA 10 μ M, QMP 20 μ M, LiCaco 10 mM (pH 7.2), KCl 100 mM, 365 nm, 0.1 mW, irradiation time up to 8 hours. (below) Corresponding kinetic plots obtained after bands quantification.

The alkylation produced by the three selected compounds was assessed regarding the influence of the irradiation time, while fixing the compound molar ratio. As a reference, DNA

alone was irradiated for the corresponding amount of time. Quantification of the bands was performed to obtain the kinetic plot (Figure 86). In all cases alkylation increased with exposure time, before reaching saturation after 1-2 hours for **181** and **192**, and 2-4 hours for **178**. The general lower reactivity observed towards all-parallel Pu24T if compared to hybrid 22AG, under the same conditions, indicated a less efficient QM trapping by proximal nucleobases. However, it is difficult to elucidate the reason of this empirical finding without knowing the exact position occupied by the ligand, the nature of the closer nucleobases and their orientation with respect to the compound.

The highest percentage of photoalkylation was observed for compound **181**. In more detail, 20% of alkylated products was detected with 22AG, and 13% with Pu24T. In the first case, three bands could clearly be distinguished forming with rather different kinetics (Figure 87). The band which was closest to the unmodified 22AG was assigned to the mono-alkylated adduct as it formed more readily. The second and third bands formed more slowly, after the first band had already reached its maximum. These bands were thus assigned to the bis- and tris-alkylated adducts.

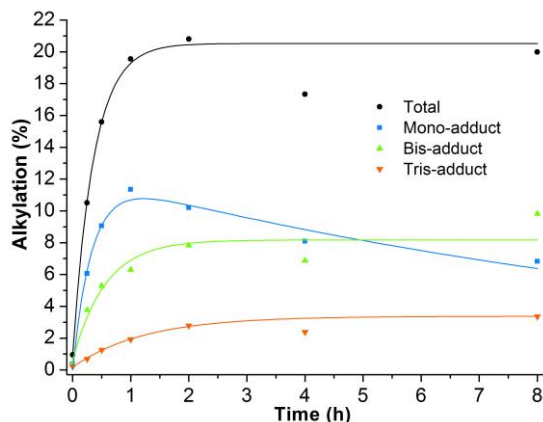


Figure 87: Kinetic plot of adducts formed by irradiation of **181**-22AG complex.

Subsequently, the optimal molar ratio of ligand was assessed in a concentration dependent experiment (Figure 88). Increasing concentrations of the three compounds were thus irradiated with 22AG for one hour. As a reference, equally composed samples were kept in the dark. Bands quantification revealed that the alkylation percentage increased with the concentration of the ligands, regardless of their identity. Five equivalents appeared to be the

optimal value as when more than 50 μM compound was added a non-migrating band ascribable to DNA clustering and precipitation started to be observed.

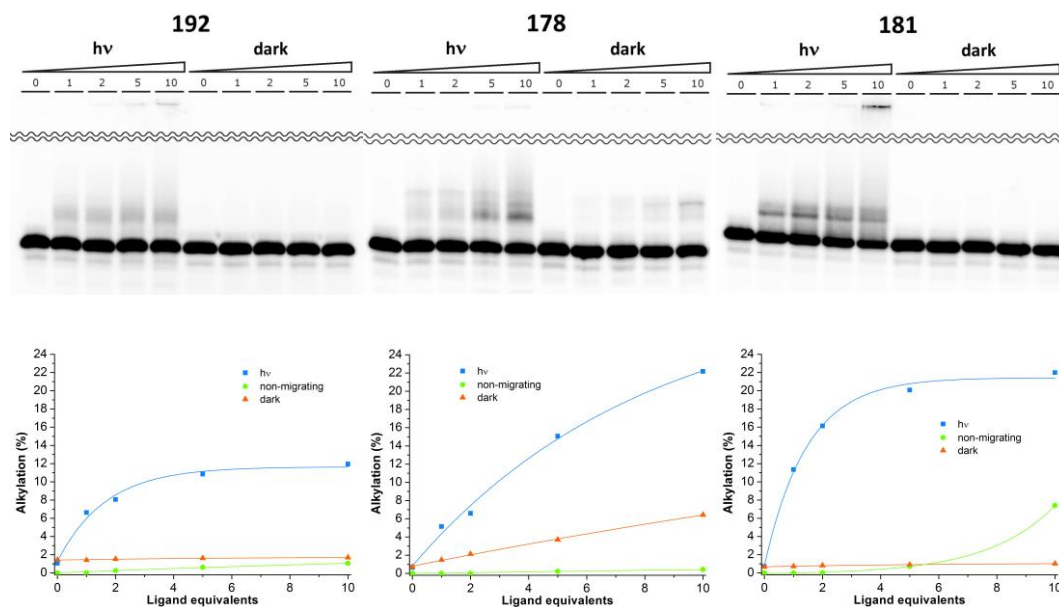
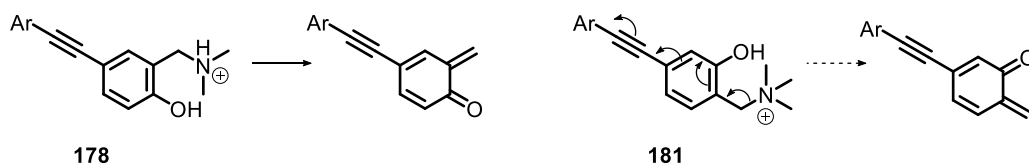


Figure 88: (above) Denaturing 15% PAGE of 22AG incubated with increasing concentrations of QMPs **178**, **181** and **192**, irradiated or not. Conditions: DNA 10 μM , QMP 20 μM , LiCaco 10 mM (pH 7.2), KCl 100 mM, 365 nm, 0.1 mW, 1 hour irradiations. (below) Concentration dependent plots obtained after bands quantification.

Since **178** produced an alkylation band also when the samples were kept in the dark, some kind of competing thermal reactivity had to be operating in this specific case, although a different product was apparently generated. Interestingly, **181** did not exhibit the same behavior, despite having a chemical structure similar to **178** and being a quaternary ammonium salt, theoretically more reactive as Me_3N is a better leaving group than Me_2NH . It is reasonable that the electron-withdrawing properties of the alkynyl moiety rise the free energy of the intermediate quinone methide, and thus the transition state that leads to it. Therefore, the general effect of the substituent is to lower the thermal reactivity of the precursor. However, such an influence was more effective in the 5-substituted derivative **181** than in the 4-substituted derivative **178**. This observation was consistent with the findings reported by Rokita and Freccero^[192] for *ortho*-QMPs substituted with different groups at the 5- or 4-position. The proposed rationalization takes into account resonance and hyperconjugation effects between the substituent and the benzylic bond with the leaving

group in the QMP. Such conjugation can in fact occur only when the substituent is located at the 5-position (Scheme 60).



Scheme 60: Schematic representation of the hyperconjugation effect in **181**, which prevents thermal QM generation. Such stabilization is less important in **178**, for which the EWG arylethynyl substituent displays only an inductive effect.

Alkylation of 22AG was also monitored upon addition of a duplex DNA competitor (Figure 89). As the percentage of G4 alkylation is only slightly affected by the presence of as high as 10 molar equivalents of ds26, corresponding to about 25 base pair equivalents, the assay indicated that the selectivity of the QMPs for quadruplex over duplex DNA was retained even during QM generation and directly translated into a selective alkylation.

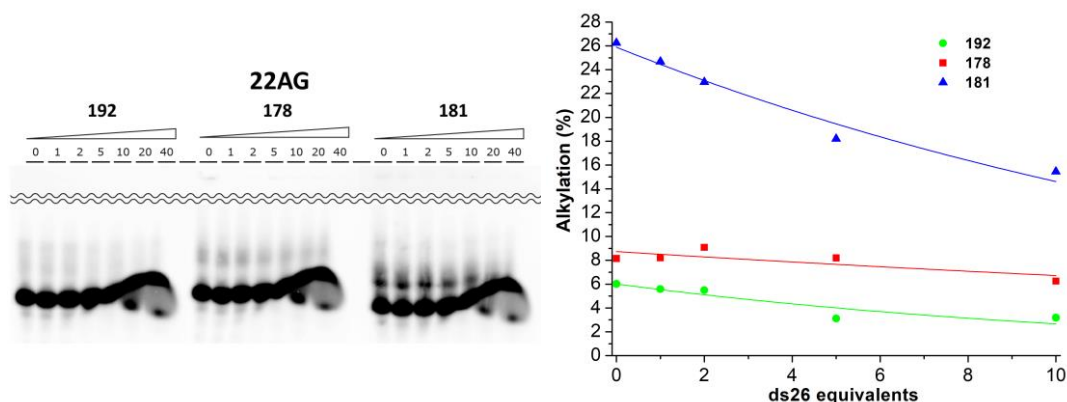


Figure 89: (left) Denaturing 15% PAGE analysis of the irradiated mixtures of 22AG incubated with QMPs **178**, **181** and **192** in the presence of increasing concentration of a non-labelled double strand competitor (ds26). Conditions: 22AG 10 μ M, QMP 20 μ M, ds26 up to 400 μ M, LiCaco 10 mM (pH 7.2), KCl 100 mM, 365 nm, 0.1 mW, 1 hour irradiations. (right) Competition plot obtained after bands quantification (wells 20 and 40 were discarded as well overloading hampered proper DNA migration and separation).

Finally, thermal stability of the alkylated DNA adducts was checked by heating the reaction mixtures at 37°C and 95°C after the irradiation (Figure 90). The results showed a complete stability of the three DNA adducts under physiological conditions for over 4 hours. Remarkably, even upon heating in denaturing conditions, the same adducts showed only a partial reversibility of the alkylation.

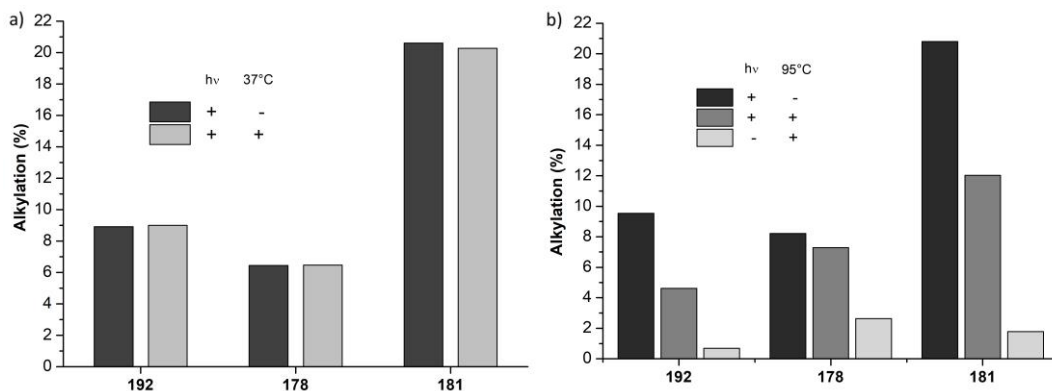


Figure 90: Percentage of alkylated adducts between 22AG and QMPs **178**, **181** and **192** before and after heating at (a) 37°C for 4 hours or (b) 95°C for 15 minutes. The mixtures were analysed by denaturing 15% PAGE. Conditions of irradiation: DNA 10 μ M, QMP 20 μ M, LiCaco 10 mM (pH 7.2), KCl 100 mM, 365 nm, 0.1 mW, 1 hour irradiations.

3.3.6 Assessment of the alkylation site

In order to gain a better insight on the alkylation mechanism at the molecular level, further investigation was carried out to identify the reaction site. For the scope additional biochemical studies were performed exclusively on 22AG G4, which proved to be the most reactive. The photoalkylation was thus carried out under the same conditions using a higher radioactive loading. The alkylation bands were isolated and the adduct was eluted and precipitated.

The isolated bands were submitted to 3'-5' exonuclease digestion. The enzyme degrades the DNA sequence moving in the 3'-5' direction, but becomes less efficient when it encounters a modified nucleobase, such as an alkylated one. Therefore, a stop band would be detected by PAGE corresponding to the alkylated site. A reference ladder was obtained from the partial digestion of the unmodified 22AG. Although these bands cannot be assigned to a specific nucleobase alkylation, as the obtained fragment has a different mobility with respect to the unmodified one, some qualitative information could be gathered from the results obtained through this assay.

Notably, few predominant stop signals were observed in the gel (Figure 91), meaning that there must be some site-specificity in the alkylation event.

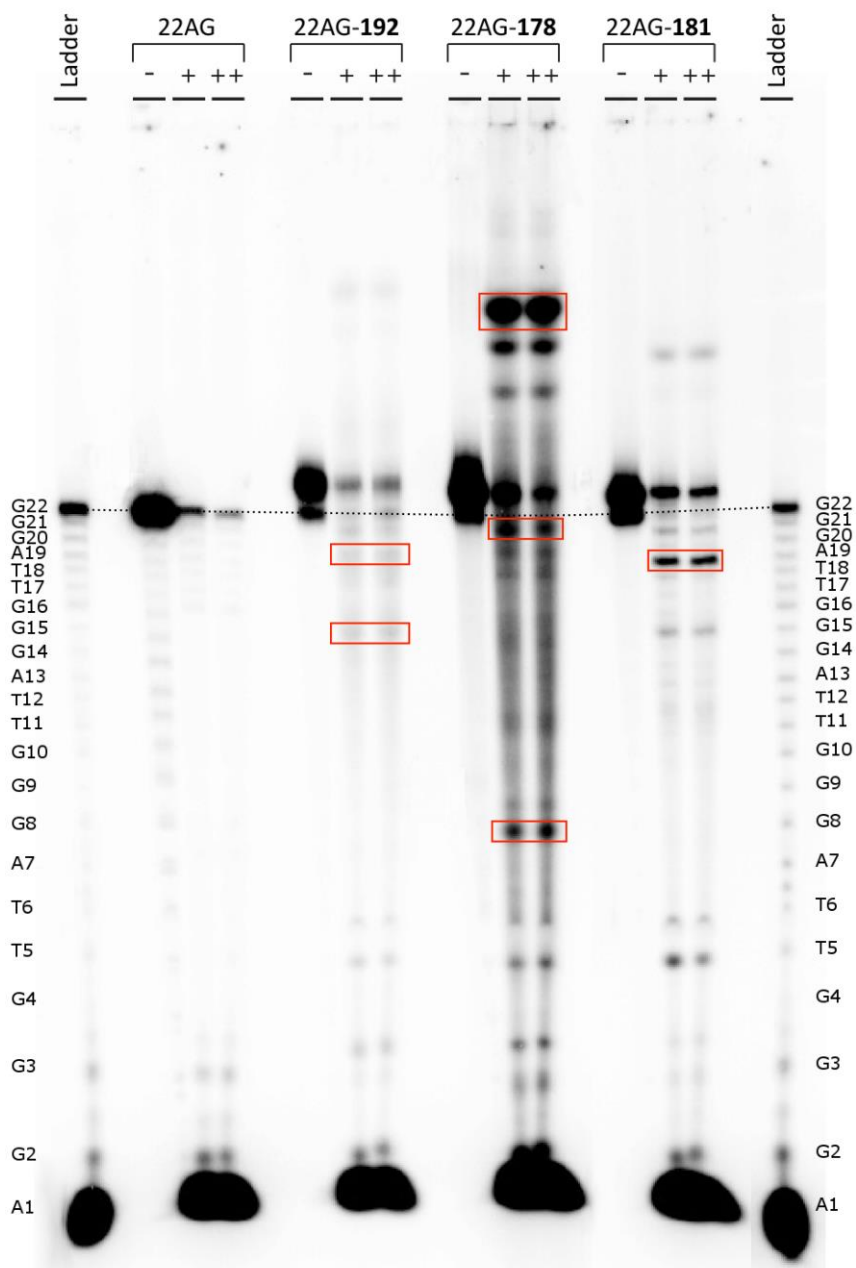


Figure 91: Denaturing 20% PAGE of 3'-5' exonuclease digestion assay performed on the isolated alkylation adducts obtained from 22AG-QMP mixtures. The prevailing stop signals have been underlined.

More in detail, the following remarks could be made.

- For the adduct between **192** and 22AG, two major stop signals could be identified located at the 3'-end (likely between A13 and A19).
- With **178** three major stop signals were observed, one located at the 3'-end (A19÷G22), one in the middle (G4÷A7) and one in the 5'-end (A1÷G2). This last stop band migrated quite slowly, being even slower than the alkylated whole sequence. This might be justified by the introduction of a positive charge on a small fragment bearing few negative ones.
- With **181** just one major stop signal was identified, located at the 3'-end (G16÷A19).

In order to identify the precise alkylation sites by comparison with the ladder, release of the nucleic acid fragments was attempted by heating the single isolated adducts at 95°C for 15 minutes. Besides the difficulties encountered in the isolation of the smallest adducts, all of them proved to be thermally stable, impeding the dealkylation process.

With the aim of addressing the identification site issue otherwise, two alternative treatments were attempted. One was dimethylsulphate (DMS) footprinting. DMS selectively methylates the N⁷ position of purines (guanines and to a lower extent adenines). Subsequent heating of the DNA in piperidine (Pip) leads to the excision of the N⁷ alkylated nucleobase and cleavage of the single strand at that position. Comparison of the shifts of the degradation products of the unmodified 22AG with those of the alkylated one should give an insight on the position of the QMP alkylation. In particular, if alkylation involved any nucleobase of the sequence, an upward shift should appear for all the fragments that still contain the alkylating moiety. The second assay was simpler and consisted in bare heating with piperidine of the untreated adducts. In this case an excision product would be identified by PAGE corresponding to the alkylation site, exclusively in case this occurred at the N⁷ of a purine.

In practice, PAGE analysis of the treated and untreated samples along with the reference ladders showed ambiguous patterns (Figure 92). Unfortunately, the gathered information was often in disagreement with previous assays and therefore could be misleading.

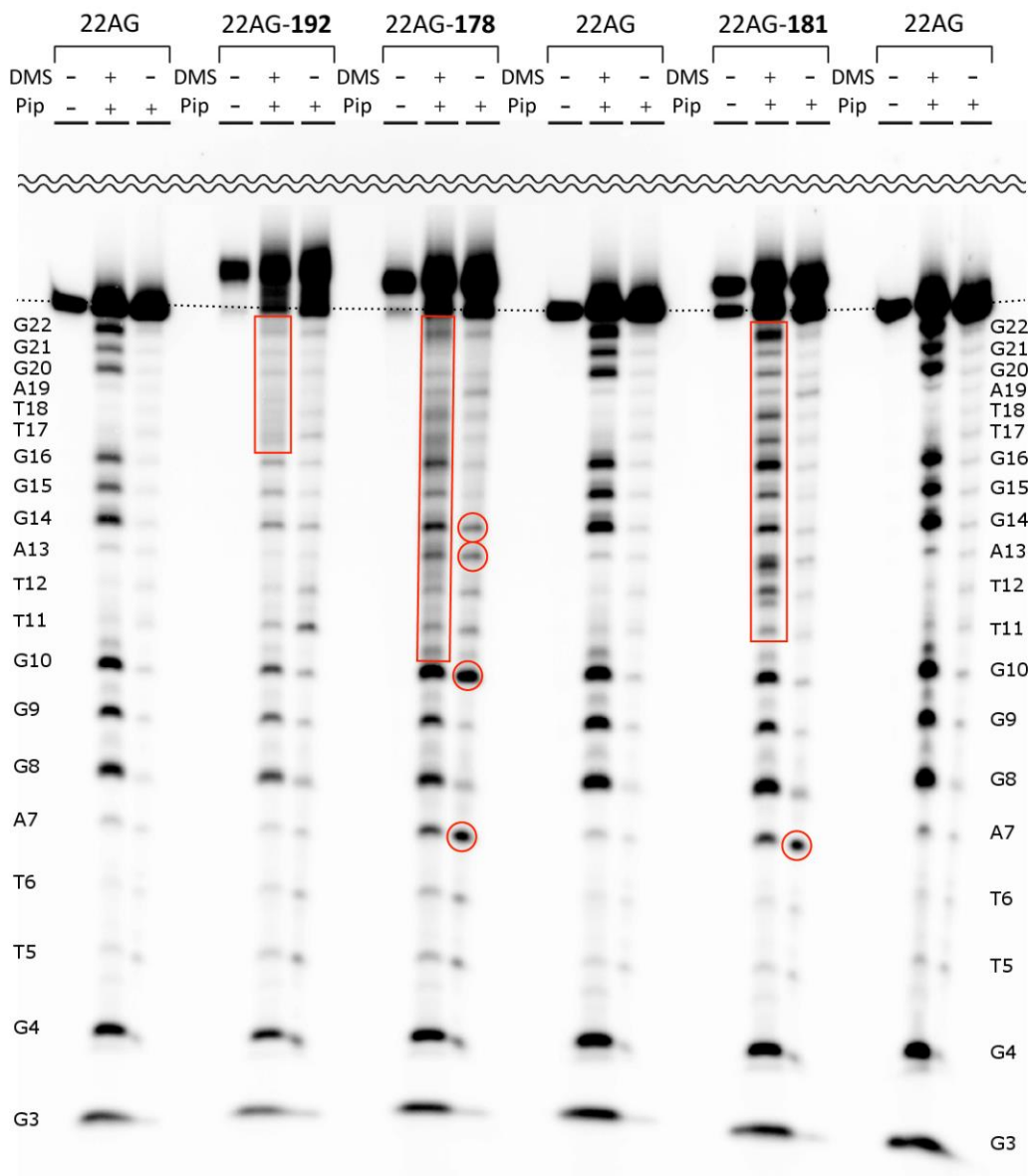


Figure 92: Denaturing 20% PAGE of DMS + Pip and Pip treatment assays performed on the isolated alkylation adducts obtained from 22AG-QMP mixtures. The prevailing signals and shifts have been underlined.

In particular, the following conclusions were inferred.

- For the adduct between **192** and 22AG, piperidine treatment did not show any significant difference upon comparison with the unmodified sequence. Instead, DMS + Pip treatment showed an upward shift starting from G20. Moreover, the presence of a blurred band corresponding to the T17÷A19 loop might indicate that an alkylation process was ongoing close to that site.
- With **178**, piperidine treatment showed two major spots at A7 and G10 and two minor ones at A13 and G14. Conversely, DMS + Pip treatment showed a complete upward shift of the G20÷G22 triad and a complicate pattern of bands from G10 to G22. Taken together, this data might suggest that the alkylation occurred somewhere between G10 and A13. However, the footprinting pattern might also indicate an alkylation in the T17÷A19 loop, so that conclusive deduction cannot be made.
- With **181**, piperidine treatment showed one major spot at A7. Instead, DMS + Pip treatment showed the presence of intense bands which had to be assigned to guanines preceding the T11÷A13 and T17÷A19 loops, indicative of a shift starting from G9 or G10. This suggests that an alkylation event occurred probably at such guanines, although not involving their N⁷.

In conclusion, although getting some qualitative information about some possible alkylation sites, their unambiguous identification was not possible by these means.

Conclusions and Remarks

This thesis was focused on the design of new small molecules targeting G-quadruplex nucleic acids and on the investigation of their interactions with such NA structures. In order to extend the panel of tools available to date and provide new therapeutic strategies based on G-quadruplex stabilization, two approaches were proposed and studied.

As a first strategy, a new family of eight oligo-heteroaromatic compounds has been synthesized based on the structure of a promising class of G4 ligands, namely non-macrocyclic telomestatin analogues. A convergent and strategically versatile synthetic process was designed to easily implement single structural modifications and study the contribute of the single features on target binding. These new molecules were also designed to contain tertiary amine pendals, which made them water-soluble at physiological pH, differently from the previously reported compounds. FRET-melting analysis on the whole family revealed a good affinity and selectivity for G4s over *ds*-DNA. Among these, four heptacyclic derivatives were compared to assess the role of the 6-membered rings in target recognition, since data on the true involvement of pyridine nitrogen for this class of open-chain oligo-heteroaryl ligands was missing. Indeed, the results showed higher G4 stabilization with compounds featuring pyridine rings, in particular in the central position. Further biophysical studies were used to get an insight on the binding mode. These suggested that the interaction preferentially occurs with the G-quadruplex grooves. In particular, this was highlighted by the formation of an induced CD band ascribable to the ligand, the only partial displacement of end-stacker thiazole orange, and the detection of a ternary complex between the target G4, thiazole orange and the ligand by MS. Docking studies further confirmed this hypothesis, suggesting a mixed binding mode for the heptacyclic compounds, which accommodate one half of the structure in the groove while protruding the other half on the end quartet.

The synthesized family offers further functionalization options, as the central ring has also been equipped with a primary amine group, which could provide a possible tethering point for functional moieties (e.g. fluorophore tags, QMPs). Therefore, this thesis offers a toolbox of new molecules that can be implemented for various applications.

The second strategy that was proposed was based on G4 selective alkylation with photo-activatable moieties. Besides the intrinsic interest in using an externally controlled trigger for the process, covalent binding was proposed not only as a mean to irreversibly stabilize G4s, but also as a new approach to implement a number of applications (e.g. fluorescent tagging and G4 pull-down). Due to the poor number of reports on such methods in the literature, this thesis served to lay the basis of this approach. Two types of photoactivatable building blocks, arylethynyl benzo-QMPs and 7-substitued naphtho-QMPs, have been proposed, which have then been combined in minimal G4-binding structures to preliminarily evaluate the alkylation feasibility.

An issue often encountered when considering the *in vivo* application of any photoactive molecule is the need of long excitation wavelength ($\lambda \geq 350 - 400$ nm), in order to limit damage of the biological matrix through direct or photosensitized reactions. Quinone methide precursors featuring an extended conjugated structure were thus proposed, which were demonstrated to absorb light and be photoactive in the near UV-vis region. The quinone methide transient species was identified in all cases by means of spectroscopic methods. Photoreactivity was investigated in detail, showing which are the most important features in terms of substituents and leaving groups to implement them in the putative ligands. These new molecules were designed so as to contain at least two alkylating moieties and thus increase the process efficiency and prevent off-target migration. Their G4 binding activity was preliminarily investigated by biophysical assays, revealing modest but selective stabilization. Combination of an ICD band observed during circular dichroic titrations, and poor performance in FID likely suggests a different binding mode with respect to the end tetrad, possibly *via* groove binding. G4 photo-alkylation experiments revealed three particularly active species which alkylated the target NAs with a maximum efficiency of roughly 20%. Interestingly this photoalkylation was not affected by the presence of a duplex competitor and proved to have a remarkable thermal stability. Unfortunately, due to this intrinsic stability the alkylation sites could not be identified by simple experiments.

Despite this limit in understanding the process details, these new alkylating moieties proved to be moderately efficacious and might be thus profitably used for subsequent applications, both to construct new G4 irreversible ligands, and as functional tools to anchor fragments of interest to the G4 target.

CHAPTER 4 : Experimental Section

4.1 Materials and methods

4.1.1 Purification

Reverse phase HPLC analysis was performed using an Agilent Technologies 1260 Infinity analytical HPLC provided with single channel UV-vis detector. The column was either XSelect CSH C18 (2.5 μ m, 150 x 4.6 mm) or XSelect CSH Phenyl-Hexyl (2.5 μ m, 150 x 4.6 mm).

Analytical method (might vary)

time (min)	A	B	time (min)	A	B
	H ₂ O + 0.1% TFA	ACN		H ₂ O + 0.1% TFA	ACN
0	95.0	5.0	11	0.0	100.0
2	95.0	5.0	12	95.0	5.0
10	0.0	100.0	15	95.0	5.0

Flow: 1.0 mL/min

Solvent A: 0.1% trifluoroacetic acid in water

Injection volume: 10 μ L

Solvent B: acetonitrile

Detector wavelength: 256 nm

Reverse phase HPLC purifications were performed using an Agilent Technologies 1260 Infinity preparative HPLC provided with a diode array UV-vis detector. The column was either SunFire C18 OBD (5 μ m, 150 x 30 mm) or SunFire Phenyl-Hexyl OBD (5 μ m, 150 x 30 mm).

Preparative Method (might vary)

time (min)	A	B	time (min)	A	B
	H ₂ O + 0.1% TFA	ACN		H ₂ O + 0.1% TFA	ACN
0	95.0	5.0	22	0.0	100.0
3	95.0	5.0	24	95.0	5.0
15	50.0	50.0	26	95.0	5.0

Flow: 30.0 mL/min

Solvent A: 0.1% trifluoroacetic acid in water

Injection volume: 10 mL

Solvent B: acetonitrile

Collection wavelength: 256 nm

Direct phase flash column chromatography purifications were performed using a Biotage Isolera One system provided with a dual-channel UV detector and an automated collection system. The Biotage® SNAP KP-Sil cartridges were packed with 50 µm silica particles with a surface area of 500 m²/g. The size was either 10, 25, 50 or 100 g, depending on the sample size and the separation factor.

TLC analysis were carried out on silica gel (60 F₂₅₄) with visualization at 254 and 366 nm.

4.1.2 Characterization

¹H, ¹³C, NMR spectra were recorded with a 300 MHz Bruker spectrometer, and the chemical shifts are reported relative to TMS. The structures of the new compounds were deduced from the results of ¹H, and ¹³C NMR. Elemental analyses were made on a Carlo Erba CNH analyzer, model 1106.

4.1.3 Reactivity studies and transients detection

- **Preparative trapping of photochemically generated QMs**

The photochemical reactions were performed by using Ar-purged solutions in 10 mL quartz tubes and a multi-lamp Rayonet© reactor equipped with two or four fluorescent UV-Vis lamps (15 W) with maximum emission centred at 310 or 360 or 450 nm. Photo-hydrations were performed on 10⁻⁴ M solutions in 1:1 aqueous acetonitrile or buffered water (phosphate buffer 50 mM) whereas photo-trapping with thiol were performed using 100-fold 2-mercaptoethan-1-ol (10⁻² M) in 90% aqueous acetonitrile. 2-mercaptoethan-1-ol was freshly distilled prior to use.

- **Quantum yield measurement.**

Reaction quantum yields (Φ_R) were measured by irradiating 3 mL 10⁻⁴ M solutions of QMP (ACN:H₂O = 1:1) in 1 cm optical path quartz cells after flushing with argon. The lamp source was a focalized 150 W high-pressure mercury arc fitted with a transmittance filter (either

315 nm or 360 nm centred transmission). Reaction conversion (1-X) was obtained by HPLC analysis of the reaction mixture and converted into Φ_R after linear regression analysis of multiple time measurements:

$$\Phi_R = \frac{\text{molecules of reactant consumed}}{\text{photons absorbed}} = -\frac{dX}{dt} \cdot \frac{V \cdot c}{q_p \cdot (1 - 10^{-\epsilon bc})}$$

where dX/dt (s^{-1}) is the initial QMP consumption rate, e.g. the reactant conversion per unit of time obtained by linear regression of the QMP fraction vs time at low conversions ($X > 0.80$); V (L) is the volume and c (M) is the molar concentration of the irradiated solution; ϵ ($M^{-1}cm^{-1}$) is the reactant molar absorptivity and b (cm) is the optical path length; q_p (E) is the photon flux, measured by potassium ferrioxalate^[274] and nitrate/benzoic acid^[275] actinometry.

Singlet oxygen quantum yields (Φ_Δ) were measured by irradiating 3 mL of ACN solutions of DHN (10^{-4} M) and the sensitizer (10^{-4} M, **131** or **135**) in 1 cm optical path quartz cells. Prior to irradiation O_2 was bubbled in the solution for 10 minutes. The lamp source was a focalized 150 W high-pressure mercury arc fitted with a transmittance filter centred at 360 nm. Time resolved DHN consumption was monitored by HPLC analysis of the reaction mixture, while juglone formation was inferred by UV-vis spectrophotometry ($\epsilon_{450}=4.38 \cdot 10^3$ $M^{-1}cm^{-1}$). Pseudo-first order rate constants (k_{obs}) were obtained by linear regression of $\ln[\text{DHN}]$ vs time and converted to singlet oxygen quantum yields by comparison with a known singlet oxygen sensitizer used as a reference under the same conditions:

$$\Phi_\Delta = \Phi_\Delta^{std} \cdot \frac{k_{obs}}{k_{obs}^{std}} \cdot \frac{I^{std}}{I}$$

where I is the fraction of photons effectively absorbed by the sensitizer, which were measured using a photon counting detector located downstream of the sample.

- **Nanosecond laser flash photolysis**

LP 920 Edinburgh Instrument photolysis system has been employed to carry out all the detection experiments of the transient species. The minimum response time of the detection system was about 10 ns. A Nd/YAG laser beam operated at 266 or 354 nm was focused on a

3 mm wide circular area on the quartz cell and the first 5 mm in depth were analyzed at right angle geometry. The incident energies used were 5-7 mJ/pulse. Normally the samples were purged with argon prior to laser irradiation. The solutions, whose concentration was assuring an absorbance of 1.0-1.2, were replaced every .ca 20 pulses. The spectra were built from time decay profiles taken each 5 nm.

4.1.4 Biophysical assays

- **Spectrophotometric measurements and titrations**

UV-visible spectra were measured in a JASCO Cary-300 or an HITACHI U-2900 spectrophotometer equipped with a Peltier temperature controller. The absorbance was recorded for the appropriate wavelength interval at a scan rate of 200 nm/min and a slit width of 1.5 nm.

Protonation constants were determined by pH spectrophotometric titrations in a water solution, 0.1 M in NaH_2PO_4 , at 25.0 ± 0.1 °C. In a typical experiment, 2 mL of a 10^{-4} M compound solution were titrated by addition of 2-5 μL aliquots of carbonate-free standard 0.1 M NaOH in a 3 mL quartz cell.

Ligand-G4 binding constants were determined by titrating a solution of the ligand with the DNA. Black-walled 1 mL rectangular quartz cells with 1 cm path length were used for the scope. In a typical experiment, 1 mL of a 5 μM compound solution were titrated by addition of aliquots of 200 μM G4 in 10 mM lithium cacodylate (pH 7.2) and 100 mM KCl previously heat denatured and folded.

- **FRET-melting assay**

FRET-melting assays were performed with 0.2 μM FAM (6-carboxyfluorescein) 5'-end- and Tamra (6-carboxy-tetramethylrhodamine) 3'-end-labelled oligonucleotides (Appendix A) in 10 mM lithium cacodylate buffer (pH 7.2), 99 mM LiCl and 1 mM KCl (90 mM LiCl and 10 mM KCl for F21T and F(21CTA)T oligonucleotides), heat denatured for 5 min at 95°C, and folded

in G4 structure by cooling the solutions at 0°C for 30 minutes or 4°C for 16 hours. Before the analysis, the proper amount of competitor (ds26) was added, followed by the tested compound (usually 1 μM) or water as a reference. Fluorescence melting curves were measured with a 7900HT Fast Real-Time quantitative PCR machine (Applied Biosystems, Thermo Fischer Scientific), using 96-well plates and a total reaction volume of 25 μL. After a first equilibration step at 25°C for 5 minutes, a stepwise increase of 0.5°C every 30 seconds for 140 cycles was performed to reach 95°C. A measurement was completed after each cycle by using 470 nm excitation and 530 nm detection. Oligonucleotide melting was monitored by observing 6-carboxyfluorescein (6-FAM) emission, which was normalized between 0 and 1. The melting temperature (T_m) was defined as the temperature at the inflection point of the sigmoid dose-response best fitting curve. For the cases in which a double sigmoid dose-response fitting was required, the second inflection point has been chosen. When the upper plateau was not reached, the melting temperature was underestimated by the abscissa at which the normalized fluorescence was 0.5.

- **FID titration assay**

FID assays were performed in a 96-well flat bottom polystyrene Nonbinding Surface (NBS™) microplate (Corning) and the reaction volume was 200 μL. In each well DNA (0.25 μM), Thiazole Orange (0.50 μM for G4 DNA and 0.75 μM for ds26) and tested compound (up to 2.5 μM) were mixed in 10 mM lithium cacodylate buffer (pH 7.2) and 100 mM KCl. Prior to sample preparation, 5 μM Oligonucleotides in 10 mM lithium cacodylate buffer and 100 mM KCl were heat denatured for 5 min at 95°C, and folded in G4 structure by cooling the solutions at 0°C for 30 minutes. Fluorescence was measured with a FLUOstar Omega microplate reader (BMG LABTECH GmbH), using an excitation filter centered at 485 nm and an emission filter centered at 520 nm. Before plate reading, 5 minutes of shaking were necessary for equilibration. All measurements were carried out in duplicate and average of data was subsequently used. The percentage of TO displacement was then calculated using:

$$\text{TOD}\% = 100 \cdot \left(1 - \frac{F}{F_0}\right)$$

where F is the fluorescence of the well and F₀ the fluorescence of the corresponding negative control well, i.e. in the absence of the compound.

- **Circular dichroic spectroscopy**

CD titrations were performed using a JASCO J-710 spectropolarimeter equipped with a Peltier temperature controller (Jasco PTC-348WI) and 1 mL black-walled rectangular quartz cells with 1 cm path length. The reaction volume was 1 mL. Prior to measurements, 3 μM oligonucleotide (2 μM for control ds26) in 10 mM lithium cacodylate buffer (pH 7.2) and 100 mM KCl or NaCl were heat denatured for 5 min at 95°C, and folded in G4 structure by cooling the solution at 0°C for 30 minutes or 4°C for 16 hours. This solution was titrated with 2 mM solution of the tested compound to get a final concentration in the range of 1–5 eq. Scans were recorded, from 220 to 450 nm with 50 nm min⁻¹ scan speed, 1.0 nm band width, 0.5 s integration time, 0.5 nm data pitch, and were corrected by a baseline obtained from the buffer in the same conditions. The signal, as an average of 4 accumulations, was further smoothed with a Savitzky-Golay method (2 order, 20 points window).

4.1.5 Biochemical assays

- **Oligonucleotide 5'-end labelling and purification**

³²P-5'-end labelling was achieved by incubating at 37°C for 30 minutes a solution prepared by mixing 1 μL of 20 μM PAGE-purified oligonucleotide, 3 μL of 3.33 μM (.ca 10 mCi/mL) [γ -³²P]-ATP (PerkinElmer), 2 μL of T4 Polynucleotide Kinase (T4 PNK), 1 μL of 10X T4 PNK reaction buffer and 3 μL of water. The oligonucleotides were subsequently purified by gel filtration on Sephadex® G-25 centrifugal filters after addition of 190 μL of water. Radioactivity incorporation was eventually measured on 1 μL samples by β -emission counting on a Tri-Carb® 2910TR Liquid Scintillator Analyzer. For a simple irradiation-PAGE analysis an amount of solution corresponding to about 5·10⁴ cpm was used. For subsequent band isolation and secondary gels or sequencing assays the freshly prepared labelled oligonucleotide was used in its entirety after concentration in a SpeedVac™ system ($\approx 10^7$ cpm).

T4 PNK: enzyme 10⁴ Richardson units/mL, Tris-HCl 10 mM, KCl 50 mM, 1,4-Dithiothreitol (DTT) 1 mM, EDTA 0.1 mM, 50%_{v/v} Glycerol, ATP 0.1 μM , pH 7.4 at 25°C.

10X T4 PNK Reaction Buffer: Tris-HCl 700 mM, MgCl₂ 100 mM, DTT 50 mM, pH 7.6 at 25°C.

- **Irradiation of the DNA-Ligand complexes**

The irradiations were performed with a MAX-303 Xenon light source (Asahi) provided with a filter centered at 365 nm, a quartz light guide and a collimator lens. The apparatus was setup in a top-down fashion (Figure 93), exposing an ice-cooled uncapped 1.5 mL eppendorf tube to the UV beam at a distance of approximately 120 mm measured from the collimator extremity to the eppendorf top (at this distance, the irradiance is approximately 1.8 mW/cm² at 365 nm). The reaction volume was 20 μ L. PAGE-purified ³²P-5'-end-labelled (.ca 100 Bq/ μ L) 10 μ M oligonucleotides (obtained by mixing the appropriate amount of labelled and label-free dna) in 10 mM lithium cacodylate buffer (pH 7.2) and 100 mM KCl were heat denatured for 10 min at 95°C, and folded in G4 structure by cooling the solutions at room temperature over 3 hours. Prior to irradiation, the G4 was incubated with the compound and the competitor.

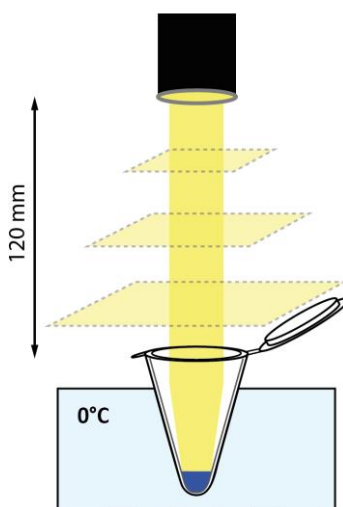


Figure 93: Schematic representation of the irradiation setup.

- **Thermal reversibility of the DNA-ligand covalent adducts**

To thermally revert the alkylation adducts, the samples were heated at 95°C for 10 minutes.

- **PAGE analysis**

Denaturing 15% (20%) polyacrylamide solution was prepared by dissolving 250 g of urea in 50 mL of 10X TBE (Tris-Borate, EDTA buffer) and 187.5 mL (250 mL) of 40% polyacrylamide

solution (19:1) at 40°C. MilliQ water was then added to the solution to reach a total volume of 500 mL. Urea denaturing 15% polyacrylamide gel was used to analyze DNA-ligand reaction mixtures and alkylation events, whereas urea denaturing 20% polyacrylamide gel was preferred for sequencing assays.

To initiate gelification, 200 µL of 10%_{w/v} ammonium persulfate solution (APS) and 20 µL of tetramethylethylenediamine (TEMED) were sequentially added to 60 mL of polyacrylamide solution. The forming gel was poured gently between two Sigmacote® treated 35x40 cm glass plates separated by 0.5 mm thick spacers, avoiding air bubble formation. A 15, 20 or 32 wells comb was inserted and the gel was let polymerize for 30-60 minutes. After polymerization was complete the comb was removed and the gel was assembled to the gel apparatus. 1 L of 1X TBE was used to fill lower and upper buffer chambers. After urea was gently removed from the wells, the gel was prerun for 30 minutes at 20 W (1300 V, 15 mA).

Before sample loading, the sample volume was reduced to 5-8 µL in a SpeedVac™ concentrator and 3 µL of a solution made of 80% formamide, 0.1 M EDTA, 0.1% xylene cyanol and 0.1% bromphenol blue (blue loading dye) were added to each sample. The gel was run at 20 W (1300 V, 15 mA) until the front marker dye had reached the lower end of the gel. The gel was exposed to a storage phosphor screen for 16 hours in the dark, which was converted to a digital image with a Typhoon Trio variable-mode imager (GE Healthcare).

The digital image was further processed with ImageQuant™ TL software to determine the counts corresponding to selected areas. The yield of alkylation was defined as the ratio between the counts corresponding to the alkylation band and the sum of the counts corresponding to both the alkylation and the non-modified dna bands, corrected by the background noise.

- **DNA-Ligand covalent adduct purification**

Freshly prepared ³²P-5'-end-labelled oligonucleotide (.ca 50000 Bq/µL) was incubated with 5 µM ligand and irradiated for 1 hour. The reaction mixture was purified by denaturing 15% PAGE using a 15-wells comb. The exposure to the phosphor screen was shortened to 10 minutes. To isolate the bands, prior to gel exposure, some reference dots of mixed ³²P-γ-ATP

and ink were deposited at the margins of the run lanes. These both radioactive and visible dots were used to create and finely position a mold indicating the exact position of any band of interest. After its cutting, the gel band was treated with 200 μL 0.15 M NaCl for 5 hours to elute DNA. The aqueous phase was isolated from solid gel pieces and cooled to 0°C; 1.1 mL of -20°C cold ethanol was added to this solution to cause DNA precipitation over 16 hours at -20°C. Centrifugation at 125000 rpm and 4°C for 2 hours and supernatant removal led finally to band isolation. 20 μL of water were subsequently added to dissolve DNA. Before further manipulations, its radioactivity was inferred by liquid scintillator analysis.

- **3' to 5' Exonuclease digestion**

PAGE-purified alkylated DNA was concentrated to a volume of 7 μL and divided in three portions: 1 μL for the untreated negative control, and two portions of 3 μL for digestion with two different concentration of Phosphodiesterase I from *Crotalus adamanteus* venom. 1 μL of reaction buffer and 1 μL of enzyme (from stock or 1:5 diluted solutions) were added to the treated samples at 0°C, so that the reaction volume was 5 μL ; in parallel, 1 μL of reaction buffer and 3 μL of water were added to the negative controls. The treated solutions were incubated for 25 minutes at 37°C, subsequently cooled in an ice bath and added with 3 μL of blue loading dye. Before gel electrophoresis the samples were stored at -20°C to prevent exonuclease from overreacting.

For each adduct both treated and untreated samples were analyzed by urea denaturing 20% polyacrylamide gel electrophoresis, along with treated and untreated unmodified DNA and a reference ladder. The main bands corresponding to an arrest of the exonuclease activity have been isolated and eluted in 200 μL of NaCl 0.15 M for 5 hours at room temperature; the gel particles were eliminated and DNA precipitation was afforded adding 1.1 mL of ethanol and 1 μL of Glycogen 20 $\mu\text{g}/\mu\text{L}$ and storing the solutions at -20°C for 16 hours. After centrifugation at 125000 rpm and 4°C for 2 hours and supernatant removal, 20 μL of water were added to dissolve DNA and radioactivity was inferred by liquid scintillation analysis.

Subsequently, the samples were heated at 95°C for 15 minutes to afford partial thermal reversion of the alkylation adduct. For each DNA-Ligand adduct both treated stop signal bands and untreated original alkylation band were analyzed by urea denaturing 20%

polyacrylamide gel electrophoresis, along with a reference ladder. Gel exposure time depends strongly by the amount of radioactivity loaded in each sample, but generally, after 2 consecutive bad isolation, it could reach up to 4 days.

Ladder: an amount of PAGE-purified unmodified DNA corresponding to a radioactivity 2 times higher than that of the most concentrated sample was added with 1 μL of reaction buffer and 1 μL of 1:20 or 1:30 diluted exonuclease solutions at 0°C. If necessary, water was added to obtain a total volume of 5 μL . The solution was incubated 25 minutes at 37°C, immediately cooled down to 0°C and added with 3 μL of blue loading dye. The solution was stored at -20°C until gel analysis.

Exonuclease: Phosphodiesterase I from *Crotalus adamanteus* venom 0.2 U/ μL , Tris-HCl 110 mM, NaCl 100 mM, MgCl_2 15 mM, 50%_{v/v} Glycerol.

5X Reaction Buffer: Tris-HCl 250 mM, MgCl_2 5 mM, pH 7.5 at 25°C.

- **Basic heating digestion**

An amount of PAGE-purified alkylated DNA corresponding to .ca $5 \cdot 10^4$ cpm was needed for each sample and untreated negative controls. Concentrations were adjusted by using a SpeedVacTM concentrator. 50 μL of piperidine 1 M were added to 1 μL of alkylated oligonucleotide and the mixture was heated at 90°C for 25 minutes. The solvent was removed by evaporation under reduced pressure, then 200 μL of water were added and subsequently removed under vacuo and these 2 steps were repeated 3 times to effectively remove piperidine traces. The samples were dissolved in 5 μL of water and added with 3 μL of blue loading dye before gel electrophoresis analysis. For each adduct both treated and untreated samples were analyzed by urea denaturing 20% polyacrylamide gel electrophoresis, along with treated and untreated unmodified DNA and a reference ladder.

Ladder: an amount of PAGE-purified unmodified DNA corresponding to an activity of .ca $1 \cdot 10^5$ cpm was diluted to 19 μL , pre-heated at 37°C, mixed with 1 μL of dimethylsulfate (DMS), and heated at 37°C for 90 seconds to afford guanine methylation at N⁷. Thus, 60 μL of ice-cold DMS stop solution were immediately added, followed by 600 μL of prechilled ethanol. The solution was kept at -20°C for 16 hours to afford DNA precipitation. After low

temperature centrifugation and solvent removal, the DNA was treated with piperidine 1 M as already described.

DMS stop solution: ammonium acetate 1.5 M (pH 7.0), β -mercaptoethanol 1 M, tRNA 100 $\mu\text{g}/\text{mL}$.

- **DMS-Piperidine digestion**

PAGE-purified alkylated DNA was dissolved in 20 μL of water and divided in three portions: 2 μL for the untreated negative control, 9 μL for piperidine treated negative control and 9 μL for fully treated DMS-piperidine sample.

The fully treated sample was diluted to 19 μL , pre-heated at 37°C, mixed with 1 μL of dimethylsulfate (DMS), and heated at 37°C for 90 seconds to afford guanine methylation at N⁷. Thus, 60 μL of ice-cold DMS stop solution were immediately added, followed by 600 μL of prechilled ethanol. The solution was kept at -20°C for 16 hours to afford DNA precipitation. The solvent was then removed after low temperature centrifugation.

Piperidine treatment was subsequently performed on both the fully treated sample and the piperidine treated negative control by adding 50 μL of piperidine 1 M and incubating at 90°C for 25 minutes. The solvent was then removed by evaporation under reduced pressure. 200 μL of water were added and subsequently removed under vacuo and these 2 steps were repeated 3 times to effectively remove piperidine traces. The samples were dissolved in 5 μL of water and added with 3 μL of blue loading dye before gel electrophoresis analysis.

For each adduct both treated samples and negative controls were analyzed by urea denaturing 20% polyacrylamide gel electrophoresis, along with treated and untreated unmodified DNA as a reference ladder.

Ladder: an amount of PAGE-purified unmodified DNA corresponding to an activity of .ca 1·10⁵ cpm was diluted to 19 μL , pre-heated at 37°C, mixed with 1 μL of dimethylsulfate (DMS), and heated at 37°C for 90 seconds to afford guanine methylation at N⁷. Thus, 60 μL of ice-cold DMS stop solution were immediately added, followed by 600 μL of prechilled ethanol. The solution was kept at -20°C for 16 hours to afford DNA precipitation. After low

temperature centrifugation and solvent removal, the DNA was treated with piperidine 1 M as already described.

DMS stop solution: ammonium acetate 1.5 M (pH 7.0), β -mercaptoethanol 1 M, tRNA 100 $\mu\text{g}/\text{mL}$.

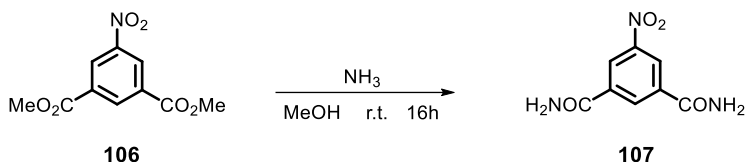
4.1.6 Molecular docking

MGL tools 1.5.6 with AutoGrid4 and AutoDock Vina were used to set up and exert blind docking calculations between the heptacyclic compounds and the DNA sequence Pu24T (PDB ID: 2A5P). The geometries of the ligands were optimized prior to the docking studies: the solubilizing chains were first replaced by methyl groups and the ligands were geometry optimized by DFT calculations at 6-31+G** level of theory by using Gaussian09; the solubilizing chains were appended and geometry optimized by using Spartan 08 keeping the core structure frozen. DNA and ligand files were provided using AutoDock Tools. The DNA was enclosed in a box with number of grid points in x_y_z directions, 42_32_40 and an exhaustiveness of 128. Lamarckian genetic algorithms, as accomplished in AutoDock Vina, were employed to perform docking calculations. All other parameters were default settings. For each of the docking cases, the lowest energy docked conformation, according to the Autodock scoring function, was selected as the binding mode. Visualization of the docked pose has been carried out by using UCSF Chimera molecular graphics program.

4.2 Synthetic protocols

4.2.1 Synthesis of heptacycles

- Synthesis of 5-nitroisophthalamide (**107**)

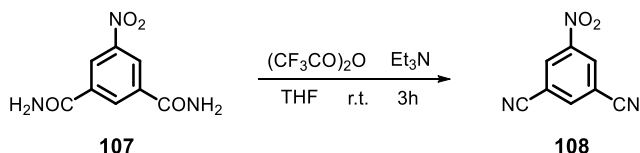


Dimethyl 5-nitroisophthalate **106** (2.51 g, 10.0 mmol) was dissolved in methanol (10 mL), added with methanolic ammonia 7 M (10 mL, 70 mmol), and stirred at room temperature for 16 hours. After addition of water (100 mL) the precipitate was filtered off, washed with water (3x50 mL), dried, and recrystallized from ethanol/water.

TLC (CHCl₃/MeOH 9:1) R_f 0.95 (reagent), 0.20 (product).

5-nitroisophthalamide (107): white solid (yield = 94%); mp = °C. **¹H-NMR** (300 MHz, DMSO-d₆, 25°C, TMS) δ (ppm) 8.81 (s, 3H), 8.43 (bs, 2H), 7.80 (bs, 2H). **¹³C-NMR** (75 MHz, DMSO-d₆, 25°C, TMS) δ (ppm) 165.4, 147.9, 136.0, 132.7, 124.5.

- Synthesis of 5-nitroisophthalonitrile (**108**)



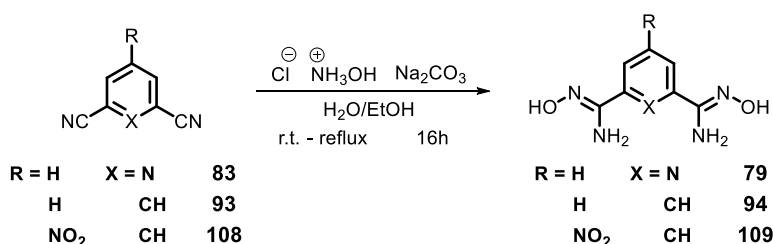
5-nitroisophthalamide **107** (1.16 g, 5.54 mmol) was dissolved in anhydrous THF (30 mL), added with triethylamine (2.3 mL, 16.6 mmol), and cooled in an ice bath. Trifluoroacetic anhydride (2.3 mL, 16.6 mmol) was added dropwise to the stirring solution over 1 hour. Hence, the ice bath was removed and the mixture was stirred at room temperature for additionally 3 hours. The reaction mixture was cooled in an ice bath and quenched with saturated NaHCO₃ (20 mL). The solvent was removed under reduced pressure and the residue was extracted with DCM (3x20 mL). The combined organic phases were dried over

MgSO₄, and the solvent was removed under reduced pressure. The crude was purified by flash chromatography (cyclohexane/CHCl₃ gradient).

TLC (CHCl₃/MeOH 9:1) R_f 0.20 (reagent), 0.86 (product).

5-nitroisophthalonitrile (108): white solid (yield = 87%); mp = °C. **¹H-NMR** (300 MHz, DMSO-d₆, 25°C, TMS) δ (ppm) 9.17 (s, 2H), 9.01 (s, 1H). **¹³C-NMR** (75 MHz, DMSO-d₆, 25°C, TMS) δ (ppm) 148.1, 142.1, 131.8, 115.7, 114.1.

- **Synthesis of diamidoximes (79, 94 and 109)**



A solution of hydroxylamine hydrochloride (1.74 g, 25.1 mmol) and sodium carbonate (1.33 g, 12.5 mmol) in water (25 mL) was added to a solution of the corresponding dinitrile (10.7 mmol) in ethanol (25 mL), and the resulting solution was stirred at the appropriate temperature (room temperature for **83** and **108**, reflux temperature for **93**) for 16 hours. Hence, the mixture was cooled in an ice bath, the solid was filtered off, washed with water (3 x 50 mL), dried and recrystallized from ethanol/water.

TLC (CHCl₃/MeOH 9:1) R_f 0.82 (**83**), 0.15 (**79**).

TLC (CHCl₃/MeOH 9:1) R_f 0.85 (**93**), 0.26 (**94**).

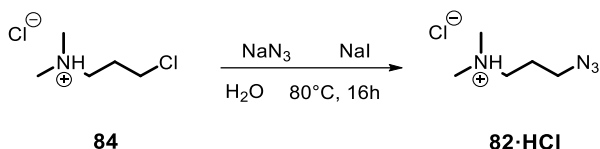
TLC (CHCl₃/MeOH 9:1) R_f 0.86 (**108**), 0.31 (**109**).

N'2,N'6-dihydroxypyridine-2,6-bis(carboximidamide) (79): white solid (yield = 78%); mp = °C. **¹H-NMR** (300 MHz, DMSO-d₆, 25°C, TMS) δ (ppm) 9.88 (s, 2H), 7.86–7.75 (m, 3H), 6.31 (bs, 4H). **¹³C-NMR** (75 MHz, DMSO-d₆, 25°C, TMS) δ (ppm) 149.6, 149.0, 136.7, 119.2.

N'1,N'3-dihydroxyisophthalimidamide (94): white solid (yield = 78%); mp = 179–182 °C. **¹H-NMR** (300 MHz, acetone-d₆, 25°C, TMS) δ (ppm) 8.98 (s, 2H), 8.04 (t, J = 1.5 Hz, 1H), 7.73 (dd, J = 7.6, 1.5 Hz, 2H), 5.53 (bs, 4H). **¹³C-NMR** (75 MHz, acetone-d₆, 25°C, TMS) δ (ppm) 152.2, 134.7, 128.9, 127.1, 123.8.

N'1,N'3-dihydroxy-5-nitroisophthalimidamide (109): yellow solid (yield = 86%); mp = °C. ¹H-NMR (300 MHz, DMSO-d₆, 25°C, TMS) δ (ppm) 10.02 (s, 2H), 8.49 (d, J = 1.3 Hz, 2H), 8.42 (t, J = 1.3 Hz, 1H), 6.12 (s, 4H). ¹³C-NMR (75 MHz, DMSO-d₆, 25°C, TMS) δ (ppm) 149.1, 147.7, 134.9, 128.2, 120.0.

- **Synthesis of N,N-Dimethyl-N-(3-azidopropyl)amine hydrochloride (82-HCl)**

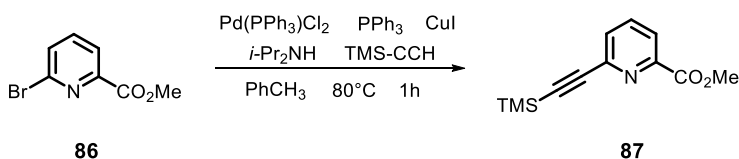


N,N-dimethyl-3-chloropropylamine hydrochloride (2.20 g, 13.9 mmol), sodium iodide (0.10 g, 0.70 mmol), and sodium azide (1.81 g, 27.8 mmol) were dissolved in water (50 mL) and the solution was stirred at 80°C for 16 hours. The solution was cooled to room temperature, basified with NaOH (0.56 g, 13.9 mmol), and the product was extracted with diethyl ether (4x50 mL). The combined organic phases were dried over Na₂SO₄ and filtrated. A solution of HCl 4 M in dioxane was added until complete precipitation. The solid was filtered off, washed with diethyl ether, dried and recrystallized from methanol/ether.

TLC (AcOEt/MeOH/acetone/water 7:1:1:1) R_f 0.20.

N,N-Dimethyl-N-(3-azidopropyl)amine hydrochloride (82-HCl): white solid (yield = 85%); mp = 109–111 °C. ¹H-NMR (300 MHz, DMSO-d₆, 25°C, TMS) δ (ppm) 11.16 (bs, 1H), 3.47 (t, J = 7.2 Hz, 2H), 3.05 (m, 2H), 2.70 (s, 6H), 1.93 (m, 2H). ¹³C-NMR (75 MHz, DMSO-d₆, 25°C, TMS) δ (ppm) 54.0, 48.2, 42.0, 23.6.

- **Synthesis of methyl 6-((trimethylsilyl)ethynyl)picolinate (87)**



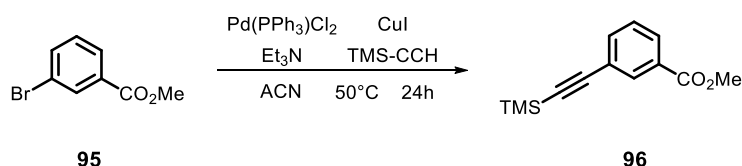
Methyl 6-bromopicolinate **86** (1.20 g, 5.56 mmol) was dissolved in toluene (30 mL), and nitrogen was bubbled for 1 minute. Pd(PPh₃)₂Cl₂ (80 mg, 2% mol), copper (I) iodide (24 mg, 1% mol), triphenylphosphine (60 mg, 4% mol), diisopropylamine (10.0 mL, 71.4 mmol), and

ethynyltrimethylsilane (1.16 mL, 8.37 mmol) were added in sequence under nitrogen atmosphere, and the mixture was stirred at 80°C for 1 hour. The insoluble salts were filtered off and washed with toluene (2x10 mL). The filtrate was washed with water (3 x 50 mL), dried over Na₂SO₄, and the solvent was removed under reduced pressure. The crude was purified by flash chromatography (cyclohexane/CHCl₃ gradient).

TLC (cyclohexane/AcOEt 8:2) R_f 0.28 (reagent), 0.39 (product).

methyl 6-((trimethylsilyl)ethynyl)picolinate (87): colourless sticky liquid (yield = 92%). ¹H-NMR (300 MHz, CDCl₃, 25°C, TMS) δ (ppm) 7.89 (d, J = 7.8 Hz, 1H), 7.68 (t, J = 7.8 Hz, 1H), 7.48 (d, J = 7.8 Hz, 1H), 3.84 (s, 3H), 0.11 (s, 9H). ¹³C-NMR (75 MHz, CDCl₃, 25°C, TMS) δ (ppm) 164.9, 148.0, 143.0, 137.0, 130.3, 124.0, 102.7, 96.0, 52.6, -0.62.

- **Synthesis of methyl 3-((trimethylsilyl)ethynyl)benzoate (96)**

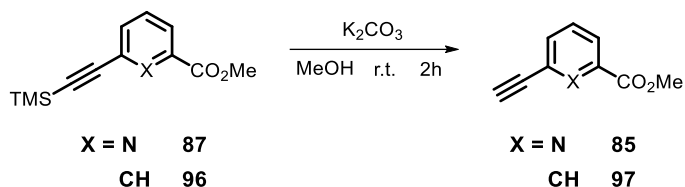


Methyl 3-bromobenzoate **95** (2.00 g, 9.30 mmol) was dissolved in acetonitrile (50 mL), and nitrogen was bubbled for 1 minute. Pd(PPh₃)₂Cl₂ (130 mg, 2% mol), copper (I) iodide (18 mg, 1% mol), triethylamine (2.6 mL, 18.6 mmol), and ethynyltrimethylsilane (1.6 mL, 11.3 mmol) were added in sequence under nitrogen atmosphere, and the mixture was stirred at 50°C for 24 hours. After solvent removal under reduced pressure, the residue was dissolved in AcOEt (75 mL), and the insoluble salts were filtered off. The filtrate was washed with water (3 x 50 mL), dried over Na₂SO₄, and the solvent was removed under reduced pressure. The crude was purified by flash chromatography (cyclohexane/CHCl₃ gradient).

TLC (cyclohexane/CHCl₃ 8:2) R_f 0.32 (reagent), 0.25 (product).

3-((trimethylsilyl)ethynyl)benzoate (96): colourless sticky liquid (yield = 88%). ¹H-NMR (300 MHz, CDCl₃, 25°C, TMS) δ (ppm) 8.13 (s, 1H), 7.97 (dd, J = 8.3, 2.3 Hz, 1H), 7.61 (dd, J = 8.5, 2.2 Hz, 1H), 7.37 (t, J = 8.5 Hz, 1H), 3.91 (s, 3H), 0.26 (s, 9H). ¹³C-NMR (75 MHz, CDCl₃, 25°C, TMS) δ (ppm) 166.5, 136.1, 133.2, 130.6, 129.8, 128.5, 123.7, 104.0, 95.5, 52.3, 0.00.

• **Synthesis of methyl 6-ethynylpicolinate (85) and methyl 3-ethynylbenzoate (97)**



The corresponding trimethylsilyl derivative (5.00 mmol) was dissolved in methanol (20 mL), and potassium carbonate (68 mg, 10% mol) was added in one portion. The resulting suspension was stirred at room temperature for 2 hours. Hence, the solvent was removed under reduced pressure, and the crude was purified by flash chromatography (cyclohexane/AcOEt 9:1).

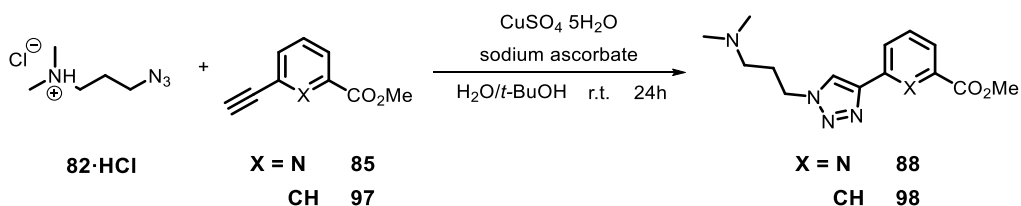
TLC (cyclohexane/AcOEt 8:2) R_f 0.42 (**87**), 0.25 (**85**).

TLC (cyclohexane/AcOEt 8:2) R_f 0.78 (**96**), 0.67 (**97**).

methyl 6-ethynylpicolinate (85): white solid (yield = 87%); mp = °C. $^1\text{H-NMR}$ (300 MHz, CDCl_3 , 25°C, TMS) δ (ppm) 8.10 (d, $J = 7.8$ Hz, 1H), 7.84 (t, $J = 7.8$ Hz, 1H), 7.65 (dd, $J = 7.8, 0.7$ Hz, 1H), 4.00 (s, 3H), 3.21 (s, 1H). $^{13}\text{C-NMR}$ (75 MHz, CDCl_3 , 25°C, TMS) δ (ppm) 165.0, 148.3, 142.4, 137.2, 130.4, 124.5, 81.9, 78.4, 52.9.

methyl 3-ethynylbenzoate (97): pale yellow solid (yield = 86%); mp = 49–51 °C. $^1\text{H-NMR}$ (300 MHz, CDCl_3 , 25°C, TMS) δ (ppm) 8.16 (s, 1H), 7.96 (d, $J = 7.9$ Hz, 1H), 7.66 (d, $J = 7.7$ Hz, 1H), 7.40 (t, $J = 7.8$ Hz, 1H), 3.92 (s, 3H), 3.13 (s, 1H). $^{13}\text{C-NMR}$ (75 MHz, CDCl_3 , 25°C, TMS) δ (ppm) 166.2, 136.2, 133.2, 130.5, 129.8, 128.4, 122.7, 82.5, 78.2, 52.3.

• **Synthesis of methyl 3-(1-(3-(dimethylamino)propyl)-1H-1,2,3-triazol-4-yl)aryl carboxylates (88 and 98)**



The corresponding alkyne (1.24 mmol) was dissolved in *tert*-butanol (10 mL) and added to a solution of *N,N*-Dimethyl-*N*-(3-azidopropyl)amine hydrochloride **82·HCl** (226 mg, 1.37

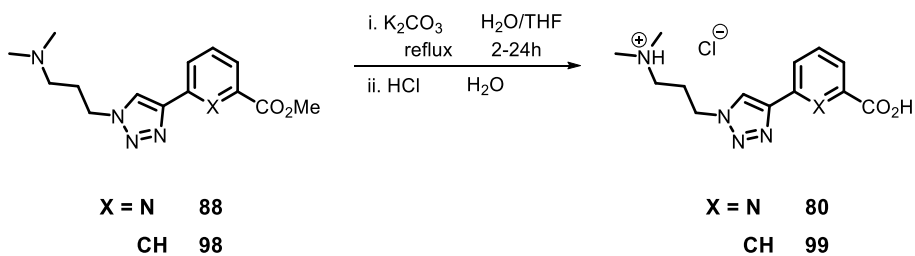
mmol), copper (II) sulphate pentahydrate (31 mg, 10% mol), and sodium ascorbate (246 mg, 1.24 mmol) in water (10 mL). The resulting solution was stirred at room temperature for 24 hours. The organic solvent was removed under reduced pressure and the residue was diluted with saturated NaHCO_3 (10 mL) and extracted with DCM (3x20 mL). The combined organic phases were dried over Na_2SO_4 , and the solvent was removed under reduced pressure. The crude was purified by flash chromatography ($\text{CHCl}_3/\text{MeOH}$ 95:5).

TLC ($\text{CHCl}_3/\text{MeOH}$ 8:2) R_f 0.95 (reagent), 0.32 (product).

methyl 6-(1-(3-(dimethylamino)propyl)-1H-1,2,3-triazol-4-yl)picolinate (88): colorless liquid (yield = 90%). $^1\text{H-NMR}$ (300 MHz, CDCl_3 , 25°C , TMS) δ (ppm) 8.39 (d, $J = 7.9$ Hz, 1H), 8.36 (s, 1H), 8.06 (d, $J = 7.7$ Hz, 1H), 7.95 (t, $J = 7.8$ Hz, 1H), 4.53 (t, $J = 7.0$ Hz, 2H), 4.02 (s, 3H), 2.34 (t, $J = 6.8$ Hz, 2H), 2.25 (s, 6H), 2.14 (quint, $J = 6.9$ Hz, 2H). $^{13}\text{C-NMR}$ (75 MHz, CDCl_3 , 25°C , TMS) δ (ppm) 165.4, 150.7, 147.5, 147.3, 137.7, 123.9, 123.2, 122.9, 55.7, 52.6, 48.2, 45.2, 28.0.

methyl 3-(1-(3-(dimethylamino)propyl)-1H-1,2,3-triazol-4-yl)benzoate (98): colorless liquid (yield = 95%). $^1\text{H-NMR}$ (300 MHz, CDCl_3 , 25°C , TMS) δ (ppm) 8.42 (s, 1H), 8.11 (d, $J = 7.8$ Hz, 1H), 7.99 (d, $J = 7.8$ Hz, 1H), 7.89 (s, 1H), 7.51 (t, $J = 7.8$ Hz, 1H), 4.49 (t, $J = 6.9$ Hz, 2H), 3.94 (s, 3H), 2.31 (t, $J = 6.7$ Hz, 2H), 2.24 (s, 6H), 2.11 (quint, $J = 6.8$ Hz, 2H). $^{13}\text{C-NMR}$ (75 MHz, CDCl_3 , 25°C , TMS) δ (ppm) 166.7, 146.6, 131.0, 130.6, 129.9, 128.92, 128.88, 126.6, 120.3, 55.6, 52.1, 48.1, 45.2, 28.0.

- **Synthesis of 3-(4-(3-carboxyaryl)-1H-1,2,3-triazol-1-yl)-N,N-dimethylpropan-1-aminium chlorides (80 and 99)**



The corresponding methyl ester (1.20 mmol) and potassium carbonate (248 mg, 1.80 mmol) were dissolved in 1:1 aqueous THF (10 mL), and the solution was stirred at reflux

temperature for the appropriate amount of time (2 hours for **88**, 24 hours for **98**). Hence, 1% HCl (10 mL) was added until cease of gas evolution, and the solvent was removed under reduced pressure. The crude was dissolved in isopropanol (5 mL) and filtered. The solid was collected, added with isopropanol (5 mL) and filtered, and these two steps were repeated a third time. The filtrates were combined and the solvent was removed under reduced pressure. A purified sample for NMR characterization was obtained by reverse phase HPLC (H₂O 0.1% TFA/ACN gradient) and exchanging the anion with 1% HCl (1 mL).

TLC (CHCl₃/MeOH 8:2) R_f 0.32 (reagent), 0 (product).

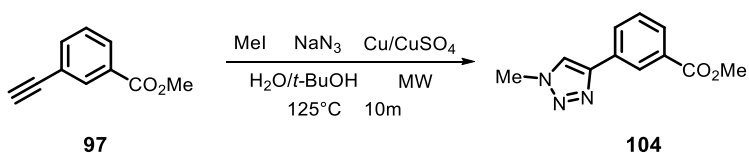
3-(4-(6-carboxypyridin-2-yl)-1H-1,2,3-triazol-1-yl)-N,N-dimethylpropan-1-aminium chloride (80):

white solid (yield = 98%); mp = . ¹H-NMR (300 MHz, DMSO-d₆, 25°C, TMS) δ (ppm) 8.81 (s, 1H), 8.25 (d, J = 7.7 Hz, 1H), 8.09 (t, J = 7.8 Hz, 1H), 8.00 (d, J = 7.6 Hz, 1H), 4.8–5.8 (bs), 4.58 (t, J = 6.7 Hz, 2H), 3.11 (t, J = 7.8 Hz, 2H), 2.78 (s, 6H), 2.33 (quint, J = 7.8 Hz, 2H). ¹³C-NMR (75 MHz, DMSO-d₆, 25°C, TMS) δ (ppm) 165.8, 149.9, 148.3, 146.7, 138.6, 124.2, 123.6, 122.5, 53.9, 47.0, 42.1, 24.6.

3-(4-(3-carboxyphenyl)-1H-1,2,3-triazol-1-yl)-N,N-dimethylpropan-1-aminium chloride (99):

white solid (yield = 97%); mp = . ¹H-NMR (300 MHz, CDCl₃, 25°C, TMS) δ (ppm) 10.71 (bs, NH), 8.79 (s, 1H), 8.42 (s, 1H), 8.09 (d, J = 7.7 Hz, 1H), 7.91 (d, J = 7.8 Hz), 7.60 (t, J = 7.7 Hz, 1H), 4.55 (t, J = 6.7 Hz, 2H), 3.09 (t, J = 7.6 Hz, 2H), 2.74 (s, 6H), 2.33 (quint, J = 7.2 Hz, 2H). ¹³C-NMR (75 MHz, CDCl₃, 25°C, TMS) δ (ppm) 167.1, 145.6, 131.5, 131.1, 129.3 (x2), 128.6, 125.8, 122.1, 53.7, 47.0, 42.0, 24.5.

- **Synthesis of methyl 3-(1-methyl-1H-1,2,3-triazol-4-yl)benzoate (104)**



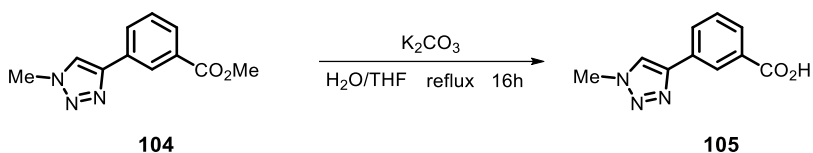
Methyl 3-ethynylbenzoate **97** (112 mg, 0.70 mmol) was put in a 10 mL MW reaction vessel and dissolved in a 1:1 mixture of water and *tert*-butanol (3 mL). Iodomethane (42 μL, 0.67 mmol), sodium azide (46 mg, 0.70 mmol), copper powder (50 mg, 0.79 mmol) and 1 M CuSO₄ water solution (200 μL, 0.20 mmol) were added, the vessel was sealed and heated under

microwave irradiation (100 W) at 125°C for 10 minutes. After cooling down to room temperature, the reaction mixture was diluted with water (30 mL) and extracted with DCM (3x30 mL). The combined organic phases were dried over Na₂SO₄ and the solvent was removed under reduced pressure. The crude was purified by flash chromatography (cyclohexane/CHCl₃ gradient).

TLC (CHCl₃) Rf 0.85 (reagent), 0.22 (product).

methyl 3-(1-methyl-1H-1,2,3-triazol-4-yl)benzoate (104): white solid (yield = 39%); mp = .
¹H-NMR (200 MHz, CDCl₃, 25°C, TMS) δ (ppm) 8.38 (s, 1H), 8.04 (d, J = 7.7 Hz, 1H), 7.95 (d, J = 7.8 Hz, 1H), 7.82 (s, 1H), 7.46 (t, J = 7.8 Hz, 1H), 4.11 (s, 3H), 3.89 (s, 3H).

- **Synthesis of 3-(1-methyl-1H-1,2,3-triazol-4-yl)benzoic acid (105)**

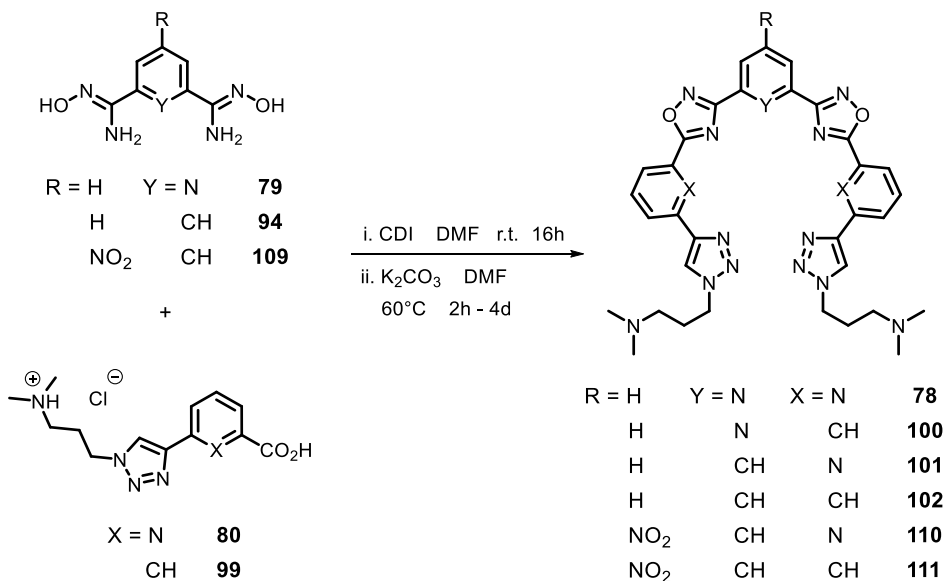


Methyl 3-(1-methyl-1H-1,2,3-triazol-4-yl)benzoate **104** (59 mg, 0.27 mmol) and potassium carbonate (52 mg, 0.38 mmol) were dissolved in a 1:1 mixture of water and THF (10 mL), and the solution was stirred at reflux temperature for 16 hours. The organic solvent was removed under reduced pressure, the residue was diluted with water (20 mL), acidified with 1% HCl (0.5 mL) and extracted with ethyl acetate (3x20 mL). The combined organic phases were dried over Na₂SO₄ and the solvent was removed under reduced pressure. The crude was recrystallized from ethanol/water.

TLC (CHCl₃) Rf 0.22 (reagent), 0 (product).

3-(1-methyl-1H-1,2,3-triazol-4-yl)benzoic acid (105): white solid (yield = 98%); mp = .
¹H-NMR (200 MHz, CDCl₃, 25°C, TMS) δ (ppm) 8.47 (s, 1H), 8.34 (s, 1H), 8.06–7.99 (m, 2H), 7.55 (t, J = 7.8 Hz, 1H), 4.17 (s, 3H).

• **Synthesis of heptacyclic oligo-heteroaryls (78, 100, 101, 102, 110, 111)**



The corresponding carboxylic acid (1.00 mmol) was dissolved in DMF (5 mL). 1,1'-carbonyldiimidazole (243 mg, 1.50 mmol) was added and the mixture was stirred at room temperature for 1 hour. The corresponding diamidoxime (0.50 mmol) was added and the solution was stirred at room temperature for 16 hours. Hence, potassium carbonate (167 mg, 1.2 eq) was added and the mixture was stirred at 60°C for the appropriate amount of time (from 2 to 4 hours when carboxylic acid **80** was used, from 2 to 4 days when carboxylic acid **99** was used). The reaction was monitored by reverse phase analytical HPLC (H₂O 0.1% TFA/ACN gradient). Hence, the solvent was removed under reduced pressure, the residue was dissolved in 1% HCl (15 mL), and purified by reverse phase HPLC (H₂O 0.1% TFA/ACN gradient). The collected aqueous fractions were neutralized with a saturated NaHCO₃ solution, extracted with chloroform (3x50 mL), the combined organic phases were dried over Na₂SO₄ and the solvent was removed under reduced pressure.

3,3'-(((pyridine-2,6-diylbis(1,2,4-oxadiazole-3,5-diyl)))bis(pyridine-6,2-diyl)))bis(1H-1,2,3-triazole-4,1-diyl))bis(N,N-dimethylpropan-1-amine) (78): white solid (yield = 34%); mp = .

¹H-NMR (300 MHz, CDCl₃, 25°C, TMS) δ (ppm) 8.56 (s, 2H), 8.46 (d, J = 7.9 Hz, 2H), 8.45 (d, J = 7.8 Hz, 2H), 8.37 (d, J = 7.6 Hz, 2H), 8.15 (t, J = 7.8 Hz, 1H), 8.07 (t, J = 7.9 Hz, 2H), 4.60 (t, J = 6.8 Hz, 4H), 2.51 (t, J = 6.8 Hz, 4H), 2.37 (s, 12H), 2.26 (quint, J = 6.7 Hz, 4H). ¹³C-NMR (75 MHz, CDCl₃, 25°C, TMS) δ (ppm) 175.2, 168.3, 151.5, 147.2, 146.8, 142.8, 138.4, 138.1, 125.1,

123.6, 123.3, 123.2, 55.7, 48.3, 44.9, 27.6. **ESI-MS**: 1369.3 (2M+Na), 712.5 (M+K), 696.5 (M+Na).

3,3'-(((pyridine-2,6-diylbis(1,2,4-oxadiazole-3,5-diyl))bis(3,1-phenylene))bis(1H-1,2,3-triazole-4,1-diyl))bis(N,N-dimethylpropan-1-amine) (100): white solid (yield = 40%); mp = .
¹H-NMR (300 MHz, CDCl₃, 25°C, TMS) δ (ppm) 8.66 (t, J = 1.5 Hz, 2H), 8.37 (d, J = 7.8 Hz, 2H), 8.21 (dd, J = 7.8, 1.5 Hz, 2H), 8.20 (dd, J = 7.8, 1.6 Hz, 2H), 8.10 (t, J = 7.9 Hz, 1H), 8.05 (s, 2H), 7.63 (t, J = 7.8 Hz, 2H), 4.53 (t, J = 6.9 Hz, 4H), 2.35 (t, J = 6.8 Hz, 4H), 2.26 (s, 12H), 2.15 (quint, J = 6.8 Hz, 4H). **¹³C-NMR** (75 MHz, CDCl₃, 25°C, TMS) δ (ppm) 176.2, 168.1, 146.9, 146.1, 138.3, 131.9, 129.9, 129.7, 127.5, 125.3, 125.0, 124.2, 120.8, 55.7, 48.2, 45.2, 28.0. **ESI-MS**: 1365.7 (2M+Na), 711.6 (M+K), 695.0 (M+Na), 673.1 (M+1).

3,3'-(((1,3-phenylenebis(1,2,4-oxadiazole-3,5-diyl))bis(pyridine-6,2-diyl))bis(1H-1,2,3-triazole-4,1-diyl))bis(N,N-dimethylpropan-1-amine) (101): white solid (yield = 31%); mp = .
¹H-NMR (300 MHz, CDCl₃, 25°C, TMS) δ (ppm) 9.11 (s, 1H), 8.47 (d, J = 7.8 Hz, 2H), 8.46 (s, 2H), 8.43 (dd, J = 7.8, 1.5 Hz, 2H), 8.32 (d, J = 7.7 Hz, 2H), 8.07 (t, J = 7.9 Hz, 2H), 7.73 (t, J = 7.8 Hz, 1H), 4.57 (t, J = 6.9 Hz, 4H), 2.39 (t, J = 6.8 Hz, 4H), 2.29 (s, 12H), 2.19 (quint, J = 6.8 Hz, 4H). **¹³C-NMR** (75 MHz, CDCl₃, 25°C, TMS) δ (ppm) 174.6, 168.6, 151.5, 147.2, 143.2, 138.1, 130.2, 129.5, 127.5, 126.8, 123.3, 123.2, 123.1, 55.8, 48.4, 45.2, 28.0. **ESI-MS**: 1367.3 (2M+Na), 1345.1 (2M+1), 695.3 (M+Na), 673.6 (M+1).

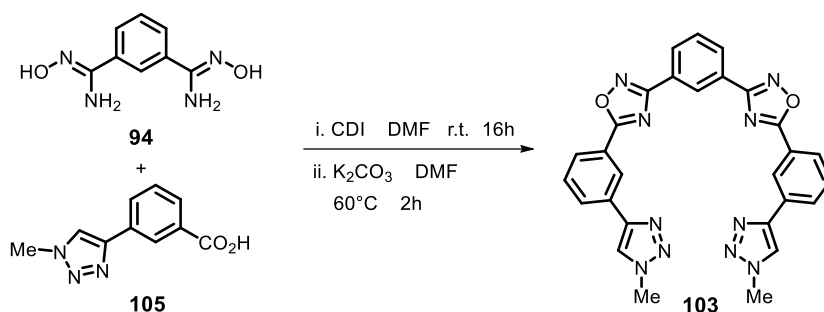
3,3'-(((1,3-phenylenebis(1,2,4-oxadiazole-3,5-diyl))bis(3,1-phenylene))bis(1H-1,2,3-triazole-4,1-diyl))bis(N,N-dimethylpropan-1-amine) (102): white solid (yield = 37%); mp = .
¹H-NMR (300 MHz, CDCl₃, 25°C, TMS) δ (ppm) 9.03 (s, 1H), 8.65 (s, 2H), 8.37 (d, J = 7.8 Hz, 2H), 8.23–8.19 (m, 4H), 8.02 (s, 2H), 7.69 (t, J = 8.0 Hz, 1H), 7.66 (t, J = 7.8 Hz, 2H), 4.55 (t, J = 6.8 Hz, 4H), 2.35 (t, J = 6.7 Hz, 4H), 2.27 (s, 12H), 2.17 (quint, J = 6.8 Hz, 4H). **¹³C-NMR** (75 MHz, CDCl₃, 25°C, TMS) δ (ppm) 175.6, 168.4, 146.2, 131.9, 130.0, 129.8, 129.7, 129.4, 127.7, 127.5, 126.6, 125.1, 124.6, 120.6, 55.7, 48.2, 45.2, 28.1. **ESI-MS**: 693.9 (M+Na), 671.9 (M+1).

3,3'-(((5-nitro-1,3-phenylene)bis(1,2,4-oxadiazole-3,5-diyl))bis(pyridine-6,2-diyl))bis(1H-1,2,3-triazole-4,1-diyl))bis(N,N-dimethylpropan-1-amine) (110): white solid (yield = 45%); mp = .
¹H-NMR (300 MHz, CDCl₃, 25°C, TMS) δ (ppm) 9.32 (s, 1H), 9.19 (s, 2H), 8.46–8.44 (m, 4H), 8.28 (d, J = 7.6 Hz, 2H), 8.05 (t, J = 7.8 Hz, 2H), 4.57 (t, J = 6.9 Hz, 4H), 2.37 (t, J = 6.6 Hz, 4H), 2.27 (s, 12H), 2.18 (quint, J = 6.8 Hz, 4H). **¹³C-NMR** (75 MHz, CDCl₃, 25°C, TMS) δ

(ppm) 175.2, 167.0, 151.6, 149.0, 147.0, 142.7, 138.1, 131.4, 129.3, 124.7, 123.4, 123.3, 55.8, 48.4, 45.2, 28.1.

3,3'-((((5-nitro-1,3-phenylene)bis(1,2,4-oxadiazole-3,5-diyl))bis(3,1-phenylene))bis(1H-1,2,3-triazole-4,1-diyl))bis(N,N-dimethylpropan-1-amine) (111): white solid (yield = 30%); mp = . ¹H-NMR (300 MHz, CDCl₃, 25°C, TMS) δ (ppm) 9.29 (s, 1H), 9.17 (s, 2H), 8.65 (s, 2H), 8.22 (d, J = 7.9 Hz, 4H), 8.07 (s, 2H), 7.67 (t, J = 7.8 Hz, 2H), 4.57 (t, J = 6.9 Hz, 4H), 2.46 (t, J = 7.0 Hz, 4H), 2.33 (s, 12H), 2.23 (quint, J = 6.9 Hz, 4H). ¹³C-NMR (75 MHz, CDCl₃, 25°C, TMS) δ (ppm) 176.3, 166.8, 149.0, 146.1, 132.0, 131.3, 130.2, 129.8, 129.6, 127.5, 125.2, 124.4, 124.1, 120.6, 55.5, 48.2, 44.8, 27.6. **ESI-MS**: 1431.1 (2M+1), 738.7 (M+Na), 716.7 (M+1).

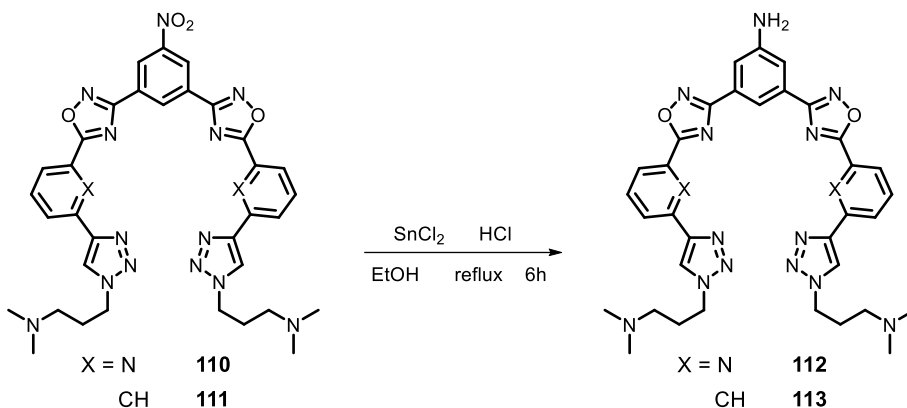
- **Synthesis of 1,3-bis(5-(3-(1-methyl-1H-1,2,3-triazol-4-yl)phenyl)-1,2,4-oxadiazol-3-yl)benzene (103)**



Carboxylic acid **105** (55 mg, 0.27 mmol) was dissolved in DMF (5 mL). 1,1'-carbonyldiimidazole (66 mg, 0.41 mmol) was added and the mixture was stirred at room temperature for 1 hour. Diamidoxime **94** (21 mg, 0.11 mmol) was added and the solution was stirred at room temperature for 16 hours. Hence, potassium carbonate (10 mg) was added and the mixture was stirred at 60°C for 2 hours, whereupon a white solid precipitated. The solid was filtered off, washed with water (2x30 mL) and dried.

1,3-bis(5-(3-(1-methyl-1H-1,2,3-triazol-4-yl)phenyl)-1,2,4-oxadiazol-3-yl)benzene (103): white solid (yield = 49%); mp = . ¹H-NMR (300 MHz, TFA-d, 25°C, TMS) δ (ppm) 8.66 (s, 1H), 8.53 (s, 2H), 8.51 (s, 2H), 8.32 (d, J = 7.6 Hz, 2H), 8.18 (d, J = 7.7 Hz, 2H), 7.93 (d, J = 7.5 Hz, 2H), 7.71 (t, J = 7.8 Hz, 2H), 7.61 (t, J = 7.7 Hz, 1H), 4.30 (s, 6H). ¹³C-NMR (75 MHz, TFA-d, 25°C, TMS) δ (ppm) 177.5, 170.5, 144.4, 133.5, 133.3, 133.1, 132.9, 132.1, 128.4, 128.3, 128.2, 127.9, 126.8, 125.2, 41.3. **ESI-MS** 551.6 (M+Na), 529.6 (M+1).

• **Synthesis of heptacyclic arylamines (112, 113)**



The appropriate nitro derivative (0.10 mmol) was dissolved in ethanol (5 mL), and 37% HCl (0.5 mL) was added. Subsequently, tin (II) chloride (134 mg, 0.6 mmol) was added in one portion and the suspension was stirred at reflux temperature for 6 hours. The reaction was monitored by reverse phase analytical HPLC (H₂O 0.1% TFA/ACN gradient) until completion. Hence, the solvent was removed under reduced pressure, the residue was added with NaOH 1 M (20 mL), and extracted with chloroform (3x20 mL). The combined organic phases were dried over Na₂SO₄, and the solvent was removed under reduced pressure. The crude was purified by reverse phase HPLC (H₂O 0.1% TFA/ACN gradient). The collected aqueous fractions were neutralized with a saturated NaHCO₃ solution, extracted with chloroform (3x50 mL), the combined organic phases were dried over Na₂SO₄ and the solvent was removed under reduced pressure.

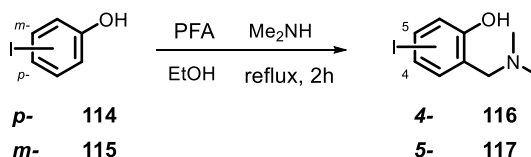
3,3'-((((5-amino-1,3-phenylene)bis(1,2,4-oxadiazole-3,5-diyl))bis(pyridine-6,2-diyl))bis(1H-1,2,3-triazole-4,1-diyl))bis(N,N-dimethylpropan-1-amine) (112): white solid (yield = 82%); mp = . ¹H-NMR (300 MHz, TFA-d, 25°C, TMS) δ (ppm) 8.45–8.40 (m, 5H), 8.25 (d, J = 7.7 Hz, 2H), 8.02 (t, J = 7.8 Hz, 2H), 7.68 (s, 2H), 4.55 (t, J = 6.9 Hz, 4H), 4.15 (bs, 2H), 2.36 (t, J = 6.7 Hz, 4H), 2.26 (s, 12H), 2.16 (quint, J = 6.9 Hz, 4H). ¹³C-NMR (75 MHz, TFA-d, 25°C, TMS) δ (ppm) 174.4, 168.8, 151.5, 147.5, 147.3, 143.3, 138.2, 128.4, 123.5, 123.2, 123.1, 116.9, 116.3, 55.9, 48.5, 45.4, 28.2.

3,3'-((((5-amino-1,3-phenylene)bis(1,2,4-oxadiazole-3,5-diyl))bis(3,1-phenylene))bis(1H-1,2,3-triazole-4,1-diyl))bis(N,N-dimethylpropan-1-amine) (113): white solid (yield = 86%); mp = . ¹H-NMR (300 MHz, TFA-d, 25°C, TMS) δ (ppm) 8.64 (s, 2H), 8.41 (s, 1H), 8.20 (d, J

= 7.8 Hz, 4H), 8.02 (s, 2H), 7.67–7.62 (m, 4H), 4.55 (t, $J = 6.9$ Hz, 4H), 2.36 (t, $J = 6.8$ Hz, 4H), 2.28 (s, 12H), 2.17 (quint, $J = 6.9$ Hz, 4H). $^{13}\text{C-NMR}$ (75 MHz, TFA-d, 25°C, TMS) δ (ppm) 175.4, 168.5, 147.3, 146.2, 131.8, 129.7, 129.6, 128.5, 127.4, 125.1, 124.7, 120.1, 116.8, 116.0, 55.7, 48.2, 45.2, 28.0. **ESI-MS** 708.7 (M+Na), 686.7 (M+1).

4.2.2 Synthesis of 4- and 5-Arylethynyl-ortho-QMPs

- Synthesis of 4- and 5- iodo Mannich bases (116-117)



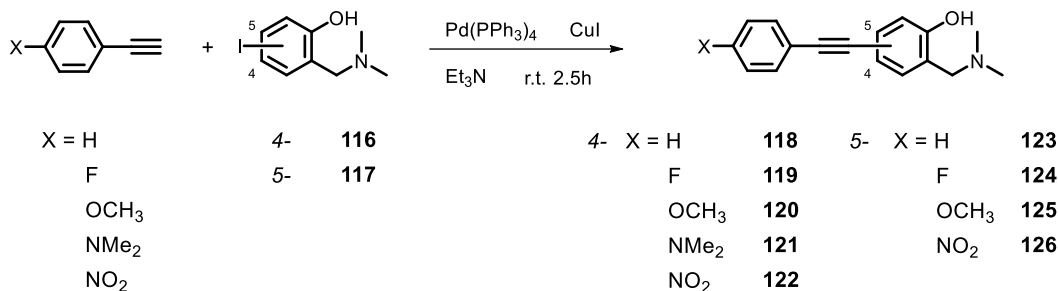
The corresponding (para- or meta-) iodophenol (3.00 g, 13.6 mmol) was dissolved in absolute ethanol (200 mL). Paraformaldehyde (9.00 g, 0.30 mol) and 33% solution of dimethylamine in ethanol (17.8 mL, 0.10 mol) were added under stirring. The mixture was heated to reflux under a nitrogen atmosphere for 2 hours. The solution was cooled to room temperature and the solvent removed by evaporation. The residue was dissolved in DCM (150 mL) and washed with an acidic aqueous solution (HCl 1%, 3x150 mL) to selectively extract the Mannich base product. The aqueous phases were collected and neutralized with solid NaHCO_3 and extracted with DCM (3x300 mL). The combined organic phases were dried over Na_2SO_4 , and the solvent was removed under reduced pressure. The crude was purified by flash chromatography ($\text{CHCl}_3/\text{MeOH}$ gradient).

TLC (AcOEt/MeOH 8:2) R_f 0.30.

2-((dimethylamino)methyl)-4-iodophenol (116): colorless oil (yield = 30%). $^1\text{H-NMR}$ (300 MHz, CDCl_3 , 25°C, TMS) δ (ppm) 10.43 (s, 1H), 7.35 (dd, $J = 8.5, 2.1$ Hz 1H), 7.18 (d, $J = 2.2$ Hz, 1H), 6.53 (d, $J = 8.5$ Hz, 1H), 3.51 (s, 2H), 2.23 (s, 6H).

2-((dimethylamino)methyl)-5-iodophenol (117): colorless oil (yield = 35%). $^1\text{H-NMR}$ (300 MHz, CDCl_3 , 25°C, TMS) δ (ppm) 10.90 (s, 1H), 7.17 (s, 1H), 7.07 (d, $J = 7.9$ Hz, 1H), 6.65 (d, $J = 7.9$ Hz, 1H), 3.56 (s, 2H), 2.29 (s, 6H).

• **Synthesis of 4- and 5- arylethynyl Mannich bases (118-126)**



The corresponding aryl iodide **116** or **117** (0.200 g, 0.72 mmol), Pd(PPh₃)₄ (3 mol %, 25.0 mg, 0.022 mmol), and copper (I) iodide (17 mol %, 23 mg, 0.12 mmol) were suspended in neat triethylamine (23 mL). After 5 minutes of bubbling with argon, a solution of the corresponding 1-ethynyl-4-substituted benzene (0.90 mmol) in neat triethylamine (2 mL) was added with a syringe under Ar atmosphere, and the mixture was stirred at room temperature for 2.5 hours. The solvent was then removed under reduced pressure. The residue was added with water (100 mL) and extracted with DCM (3x100 mL). The combined organic phases were dried over Na₂SO₄ and the solvent was removed under reduced pressure to afford a brown-yellow oil. The crude products were subsequently purified by flash chromatography (cyclohexane/AcOEt gradient).

TLC (AcOEt/MeOH 8:2) R_f = 0.35-0.40.

2-((Dimethylamino)methyl)-4-(phenylethynyl)phenol (118): colorless oil (yield = 94%). ¹H-NMR (300 MHz, CDCl₃, 25°C, TMS) δ (ppm) 10.86 (bs, 1 OH), 7.57–7.54 (m, 2H), 7.44–7.38 (m, 4H), 7.21 (s, 1H), 6.86 (d, J = 8.3 Hz, 1H), 3.62 (s, 2H), 2.30 (s, 6H). ¹³C-NMR (75 MHz CDCl₃, 25°C, TMS) δ (ppm) 158.6; 132.3; 131.6; 131.3; 128.2; 127.7; 123.6; 121.9; 116.2; 113.3; 89.5; 87.4; 62.4; 44.3. **Anal. calcd** for C₁₇H₁₇NO: C, 81.24; H, 6.82; N, 5.57; O, 6.37. **Found**: C, 81.19; H, 6.89; N, 5.61.

2-((Dimethylamino)methyl)-4-((4-fluorophenyl)ethynyl)phenol (119): white solid (yield = 88%); mp = 88–90 °C. ¹H-NMR (300 MHz, CDCl₃, 25°C, TMS) δ (ppm) 7.51–7.46 (m, 2H), 7.36 (dd, J = 2.0 Hz, J = 8.3 Hz, 1H), 7.18 (d, J = 2.0 Hz, 1H), 7.07–7.01 (m, 2H), 6.82 (d, J = 8.3 Hz, 1H), 3.66 (s, 2H), 2.35 (s, 6H). ¹³C-NMR (75 MHz, CDCl₃, 25°C, TMS) δ (ppm) 161.7 (d, JCF = 246.7 Hz), 158.2; 132.7 (d, JCF = 8.2 Hz); 131.9; 131.2; 121.5; 119.3 (d, JCF = 3 Hz); 115.9;

115.1 (d, JCF = 21.7 Hz); 112.7; 88.8; 85.9; 61.9; 43.9. **Anal. calcd** for C₁₇H₁₆FNO: C, 75.82; H, 5.99; F, 7.05; N, 5.20; O, 5.94. **Found:** C, 75.84; H, 6.05; N, 5.18.

2-((Dimethylamino)methyl)-4-((4-methoxyphenyl)ethynyl)phenol (120): white solid (yield = 70%); mp = 122–124 °C. ¹H-NMR (300 MHz, CDCl₃, 25°C, TMS) δ (ppm) 7.45 (AA'XX' system, J = 8.8 Hz, 2H), 7.36 (dd, J = 2.1 Hz, J = 8.3 Hz, 1H), 7.18 (d, J = 2.1 Hz, 1H), 6.88 (AA'XX' system, J = 8.8 Hz, 2H), 6.84 (d, J = 8.3 Hz, 1H), 3.84 (s, 3H); 3.67 (s, 2H), 2.37 (s, 6H). ¹³C-NMR (75 MHz, CDCl₃, 25°C, TMS) δ (ppm) 159.1; 158.2; 132.7; 132.2; 131.6; 121.7; 116.3; 115.7; 113.8; 113.7; 88.0; 87.3; 62.2; 55.1; 44.3. **Anal. calcd** for C₁₈H₁₉NO₂: C, 76.84; H, 6.81; N, 4.98; O, 11.37. **Found:** C, 76.89; H, 6.76; N, 5.05.

2-((Dimethylamino)methyl)-4-((4-(dimethylamino)-phenyl)-ethynyl)phenol (121): white solid (yield = 71%); mp = 149–150 °C. ¹H-NMR (300 MHz, CDCl₃, 25°C, TMS) δ (ppm) 7.39 (AA'XX' system, J = 9 Hz, 2H), 7.35 (dd, J = 1.8 Hz, J = 8.3 Hz, 1H), 7.18 (d, J = 1.8 Hz, 1H), 6.83 (d, J = 8.3 Hz, 1H), 6.67 (AA'XX' system, J = 9 Hz, 2H), 3.69 (s, 2H), 3.00 (s, 6H), 2.35 (s, 6H). ¹³C-NMR (75 MHz, CDCl₃, 25°C, TMS) δ (ppm) 157.7; 149.7; 132.4; 132.2; 131.7; 121.3; 116.4; 114.5; 111.8; 110.4; 88.5; 87.0; 61.9; 44.1; 40.1. **Anal. calcd** for C₁₉H₂₂N₂O: C, 77.52; H, 7.53; N, 9.52; O, 5.43. **Found:** C, 77.54; H, 7.58; N, 9.49.

2-((Dimethylamino)methyl)-4-((4-nitrophenyl)ethynyl)phenol (122): yellow solid (yield = 77%); mp = 111–113 °C. ¹H-NMR (300 MHz, CDCl₃, 25°C, TMS) δ (ppm) 11.19 (bs, OH); 8.17 (AA'XX' system, J = 9 Hz, 2H), 7.58 (AA'XX' system, J = 9 Hz, 2H), 7.37 (dd, J = 1.8 Hz, J = 8.3 Hz, 1H), 7.19 (d, J = 1.8 Hz, 1H), 6.82 (d, J = 8.3 Hz, 1H), 3.66 (s, 2H), 2.34 (s, 6H). ¹³C-NMR (75 MHz, CDCl₃, 25°C, TMS) δ (ppm) 159.6; 146.5; 132.7; 131.9; 131.7; 130.7; 123.5; 116.5; 113.8; 112.1; 95.5; 86.1; 62.3; 44.3. **Anal. calcd** for C₁₇H₁₆N₂O₃: C, 68.91; H, 5.44; N, 9.45; O, 16.20. **Found:** C, 68.81; H, 5.47; N, 9.49.

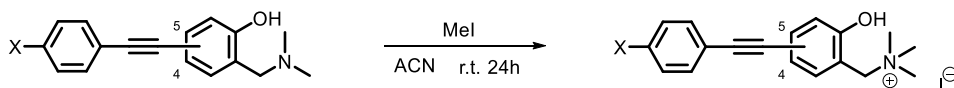
2-((Dimethylamino)methyl)-5-(phenylethynyl)phenol (123): white solid (yield = 93%); mp = 66–68 °C. ¹H-NMR (300 MHz, CDCl₃, 25°C, TMS) δ (ppm) 10.86 (bs, 1OH), 7.58–7.55 (m, 2H), 7.38–7.35 (m, 3H), 7.06 (s, 1H), 7.02–6.94 (m, 2H), 3.66 (s, 2H), 2.34 (s, 6H). ¹³C-NMR (75 MHz, CDCl₃, 25°C, TMS) δ (ppm) 157.8; 131.5; 128.2; 128.0; 123.4; 123.3; 122.4; 122.3; 118.8; 89.3; 88.8; 62.5; 44.3. **Anal. calcd** for C₁₇H₁₇NO: C, 81.24; H, 6.82; N, 5.57; O, 6.37. **Found:** C, 81.28; H, 6.79; N, 5.59.

2-((Dimethylamino)methyl)-5-((4-fluorophenyl)ethynyl)phenol (124): white solid (yield = 85%); mp = 104–106 °C. ¹H-NMR (300 MHz, CDCl₃, 25°C, TMS) δ (ppm) 7.54–7.49 (m, 2H), 7.08–6.96 (m, 5H), 3.68 (s, 2H), 2.36 (s, 6H). ¹³C-NMR (75 MHz, CDCl₃, 25°C, TMS) δ (ppm) 162.3 (d, JCF = 247.5 Hz), 157.8; 133.3 (d, JCF = 8.2 Hz); 128.3; 123.2; 122.4; 112.3; 119.4; 118.9; 115.4 (d, JCF = 21.7 Hz); 88.9; 87.8; 62.4; 44.3. **Anal. calcd** for C₁₇H₁₆FNO: C, 75.82; H, 5.99; F, 7.05; N, 5.20; O, 5.94. **Found:** C, 75.81; H, 6.00; N, 5.22.

2-((Dimethylamino)methyl)-5-((4-methoxyphenyl)ethynyl)phenol (125): white solid (yield = 70%); mp = 89–91 °C. ¹H-NMR (300 MHz, CDCl₃, 25°C, TMS) δ (ppm) 7.48 (AA'XX' system, J = 8.8 Hz, 2H), 7.00 (s, 1H), 6.96–6.95 (m, 2H); 6.89 (AA'XX' system, J = 8.8 Hz, 2H), 3.84 (s, 3H); 3.67 (s, 2H), 2.36 (s, 6H). ¹³C-NMR (75 MHz, CDCl₃, 25°C, TMS) δ (ppm) 159.4; 157.7; 132.9; 128.2; 123.7; 122.2; 122.1; 118.7; 115.4; 113.8; 88.9; 87.9; 62.4; 55.2; 44.3. **Anal. calcd** for C₁₈H₁₉NO₂: C, 76.84; H, 6.81; N, 4.98; O, 11.37. **Found:** C, 76.92; H, 6.88; N, 4.95.

2-((Dimethylamino)methyl)-5-((4-nitrophenyl)ethynyl)phenol (126): yellow solid (yield = 75%); mp = 89–91 °C. ¹H-NMR (300 MHz, CD₃OD, 25°C, TMS) δ (ppm) 8.39 (AA'XX' system, J = 8.9 Hz, 2H), 7.87 (AA'XX' system, J = 8.9 Hz, 2H), 7.50 (d, J = 7.3 Hz, 1H), 7.29–7.25 (m, 2H), 4.45 (s, 2H), 2.99 (s, 6H). ¹³C-NMR (75 MHz, CD₃OD, 25°C, TMS) δ (ppm) 158.1; 149.1; 134.1; 133.9; 131.1; 127.1; 125.1; 124.9; 119.5; 119.4; 94.2; 89.5; 58.2; 43.6. **Anal. calcd** for C₁₇H₁₆N₂O₃: C, 68.91; H, 5.44; N, 9.45; O, 16.20. **Found:** C, 68.95; H, 5.42; N, 9.49.

• **Synthesis of 4- and 5- arylethynyl quaternary ammonium salts (127-135)**



4- X = H	118	5- X = H	123	4- X = H	127	5- X = H	132
F	119	F	124	F	128	F	133
OCH ₃	120	OCH ₃	125	OCH ₃	129	OCH ₃	134
NMe ₂	121	NO ₂	126	[⊕] NMe ₃ I [⊖]	130	NO ₂	135
NO ₂	122			NO ₂	131		

The corresponding 4- or 5-arylethynyl Mannich base (0.72 mmol) was dissolved in ACN (10 mL) and excess methyl iodide (280 μL, 4.5 mmol) was subsequently added. The resulting

solution was stirred under N₂ atmosphere. After 24 hours, the solvent was completely removed under reduced pressure to yield quantitatively the quaternary ammonium salt.

TLC (AcOEt/MeOH 8:2 + 2% Et₃N) R_f 0.10–0.15.

1-(2-Hydroxy-5-(phenylethynyl)phenyl)-N,N,N-trimethylmethanaminium iodide (127): white solid (yield = 99%); mp = 218–220 °C. **¹H-NMR** (300 MHz, CD₃OD, 25°C, TMS) δ (ppm) 7.68 (d, J = 1.59 Hz, 1H), 7.57–7.48 (m, 3H), 7.39–7.36 (m, 3H), 7.01 (d, J = 8.4 Hz, 1H), 4.58 (s, 2H), 3.18 (s, 9H). **¹³C-NMR** (75 MHz, CD₃OD, 25°C, TMS) δ (ppm) 157.4; 137.3; 135.2; 130.7; 127.9; 127.7; 122.9; 116.0; 114.6; 114.5; 87.7; 87.6; 63.3; 52.1; 52.0; 51.9. **Anal. calcd** for C₁₈H₂₀INO: C, 54.97; H, 5.13; I, 32.27; N, 3.56; O, 4.07. **Found:** C, 54.94; H, 5.19; N, 3.54.

1-(2-Hydroxy-5-(4-fluorophenylethynyl)phenyl)-N,N,N-trimethylmethanaminium iodide (128): white solid (yield = 99%); mp = 209–211 °C. **¹H-NMR** (300 MHz, CD₃OD, 25°C, TMS) δ (ppm) 7.65 (d, J = 2.02 Hz, 1H), 7.57–7.50 (m, 3H), 7.16–7.10 (m, 2H), 7.02 (d, J = 8.5 Hz, 1H), 4.57 (s, 2H), 3.18 (s, 9H). **¹³C-NMR** (75 MHz, CD₃OD, 25°C, TMS) δ (ppm) 164.2 (d, JCF = 246.7 Hz), 159.4; 139.2; 137.1; 134.7 (d, JCF = 8.2 Hz); 121.1; 117.9; 116.9 (d, JCF = 22.5 Hz); 116.5; 116.3; 89.3; 88.5; 65.3; 53.8. **Anal. calcd** for C₁₈H₁₉FINO: C, 52.57; H, 4.66; F, 4.62; I, 30.86; N, 3.41; O, 3.89. **Found:** C, 52.59; H, 4.71; N, 3.44.

1-(2-Hydroxy-5-(4-methoxyphenylethynyl)phenyl)-N,N,N-trimethylmethanaminium iodide (129): white solid (yield = 97%); mp = 197–200 °C. **¹H-NMR** (300 MHz, CD₃OD, 25°C, TMS) δ (ppm) 7.61 (d, J = 2.0 Hz, 1H); 7.53 (dd, J = 2.0 Hz, J = 8.5 Hz, 1H), 7.42 (AA'XX' system, J = 8.9 Hz, 2H), 7.00 (d, J = 8.5 Hz, 1H), 6.94 (AA'XX' system, J = 8.9 Hz, 2H), 4.55 (s, 2H); 3.83 (s, 3H); 3.17 (s, 9H). **¹³C-NMR** (75 MHz, CD₃OD, 25°C, TMS) δ (ppm) 161.5; 159.1; 138.9; 136.9; 134.1; 117.8; 117.0; 116.8; 116.4; 115.4; 89.7; 88.0; 65.1; 56.1; 53.8; 53.7. **Anal. calcd** for C₁₉H₂₂INO₂: C, 53.91; H, 5.24; I, 29.98; N, 3.31; O, 7.56. **Found:** C, 53.94; H, 5.22; N, 3.35.

4-((4-Hydroxy-3-((trimethylammonio)methyl)phenyl)ethynyl)-N,N,N-trimethylbenzenaminium iodide (130): white solid (yield = 95%); mp dec >150 °C. **¹H-NMR** (300 MHz, CD₃OD, 25°C, TMS) δ (ppm) 7.99 (AA'XX' system, J = 8.6 Hz, 2H), 7.77 (AA'XX' system, J = 9 Hz, 2H), 7.75 (s, 1H), 7.62 (dd, J = 2.0, J = 8.6 Hz, 1H), 7.04 (d, J = 8.6 Hz, 1H), 4.60 (s, 2H), 3.74 (s, 9H), 3.21 (s, 9H). **¹³C-NMR** (75 MHz, CD₃OD, 25°C, TMS) δ (ppm) 160.0; 147.9; 139.7; 137.4; 134.5;

127.5; 122.1; 118.0; 116.7; 115.4; 92.6; 87.4; 65.2; 58.2; 54.0; 53.9. **Anal. calcd** for $C_{21}H_{28}I_2N_2O$: C, 43.62; H, 4.88; I, 43.89; N, 4.84; O, 2.77. **Found**: C, 43.64; H, 4.51; N, 4.87.

1-(2-Hydroxy-5-(4-nitrophenylethynyl)phenyl)-N,N,N-trimethylmethanaminium Iodide (131): yellow solid (yield = 98%); mp = 220–222 °C. **1H -NMR** (300 MHz, DMSO- d_6 , 25°C, TMS) δ (ppm) 11.05 (bs, OH); 8.27 (AA'XX' system, J = 8.9 Hz, 2H), 7.77 (AA'XX' system, J = 8.9 Hz, 2H), 7.72 (d, J = 2.1 Hz, 1H), 7.63 (dd, J = 2.1 Hz, J = 8.5 Hz, 1H), 7.07 (d, J = 8.5 Hz, 1H), 4.48 (s, 2H), 3.08 (s, 9H). **^{13}C -NMR** (75 MHz, DMSO- d_6 , 25°C, TMS) δ (ppm) 158.7; 146.6; 138.4; 135.6; 132.2; 129.4; 123.9; 116.8; 115.6; 111.9; 94.3; 86.7; 62.5; 52.2. **Anal. calcd** for $C_{18}H_{19}IN_2O_3$: C, 49.33; H, 4.37; I, 28.96; N, 6.39; O, 10.95. **Found**: C, 49.37; H, 4.36; N, 6.41.

1-(2-Hydroxy-4-(phenylethynyl)phenyl)-N,N,N-trimethylmethanaminium Iodide (132): white solid (yield = 99%); mp = 189–191 °C. **1H -NMR** (300 MHz, CD $_3$ OD, 25°C, TMS) δ (ppm) 7.55–7.51 (m, 2H), 7.48 (d, J = 8.4 Hz, 1H), 7.42–7.39 (m, 3H), 7.16–7.13 (m, 2H), 4.58 (s, 2H), 3.32 (s, 9H). **^{13}C -NMR** (75 MHz, CD $_3$ OD, 25°C, TMS) δ (ppm) 158.9; 136.2; 132.9; 130.2; 129.9; 128.9; 124.2; 119.8; 116.4; 91.9; 89.4; 65.4; 65.3; 53.9; 53.4. **Anal. calcd** for $C_{18}H_{20}INO$: C, 54.97; H, 5.13; I, 32.27; N, 3.56; O, 4.07. **Found**: C, 54.91; H, 5.19; N, 3.57.

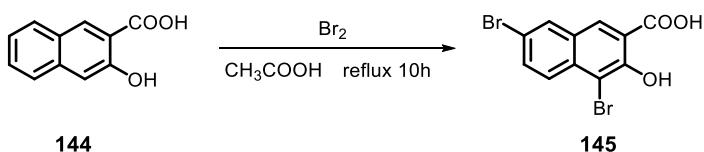
1-(2-Hydroxy-4-(4-fluorophenylethynyl)phenyl)-N,N,N-trimethylmethanaminium Iodide (133): white solid (yield = 98%); mp = 187–190 °C. **1H -NMR** (300 MHz, CD $_3$ OD, 25°C, TMS) δ (ppm) 7.58 (m, 2H), 7.47 (d, J = 7.7 Hz, 1H), 7.19–7.12 (m, 4H); 4.57 (s, 2H), 3.17 (s, 9H). **^{13}C -NMR** (75 MHz, CD $_3$ OD, 25°C, TMS) δ (ppm) 164.5 (d, JCF = 247.5 Hz), 159.0; 136.2; 135.1 (d, JCF = 8.2 Hz); 128.8; 124.4; 120.5 (d, JCF = 3.7 Hz); 119.8; 117.1 (d, JCF = 22.5 Hz); 116.5; 90.8; 89.1; 65.4; 53.8; 53.7. **Anal. calcd** for $C_{18}H_{19}FINO$: C, 52.57; H, 4.66; F, 4.62; I, 30.86; N, 3.41; O, 3.89. **Found**: C, 52.59; H, 4.64; N, 3.44.

1-(2-Hydroxy-4-(4-methoxyphenylethynyl)phenyl)-N,N,N-trimethylmethanaminium Iodide (134): white solid (yield = 99%); mp = 198–200 °C. **1H -NMR** (300 MHz, CD $_3$ OD, 25°C, TMS) δ (ppm) 7.46 (AA'XX' system, J = 8.8 Hz, 2H), 7.43 (d, J = 7.9 Hz, 1H), 7.11 (d, J = 7.9 Hz, 1H); 7.10 (s, 1H); 6.96 (AA'XX' system, J = 8.8 Hz, 2H), 4.55 (s, 2H); 3.84 (s, 3H), 3.16 (s, 9H). **^{13}C -NMR** (75 MHz, CD $_3$ OD, 25°C, TMS) δ (ppm) 162.0; 159.0; 136.1; 134.5; 129.5; 124.3; 119.7; 116.2; 116.0; 115.6; 92.3; 88.1; 65.5; 56.2; 53.8; 53.7. **Anal. calcd** for $C_{19}H_{22}INO_2$: C, 53.91; H, 5.24; I, 29.98; N, 3.31; O, 7.56. **Found**: C, 53.95; H, 5.28; N, 3.35.

1-(2-Hydroxy-4-(4-nitrophenylethynyl)phenyl)-N,N,N-trimethylmethanaminium Iodide (135): yellow solid (yield = 97%); mp = 212–215 °C. $^1\text{H-NMR}$ (300 MHz, CD_3OD , 25°C, TMS) δ (ppm) 8.29 (AA'XX' system, $J = 8.9$ Hz, 2H), 7.77 (AA'XX' system, $J = 8.9$ Hz, 2H), 7.49 (d, $J = 7.8$ Hz, 1H), 7.21–7.17 (m, 2H), 4.57 (s, 2H), 3.17 (s, 9H). $^{13}\text{C-NMR}$ (75 MHz, CD_3OD , 25°C, TMS) δ (ppm) 159.2; 149.1; 136.4; 134.0; 131.0; 127.9; 125.1; 124.6; 120.2; 117.4; 94.0; 89.9; 65.4; 53.9; 53.8. **Anal. calcd** for $\text{C}_{18}\text{H}_{19}\text{IN}_2\text{O}_3$: C, 49.33; H, 4.37; I, 28.96; N, 6.39; O, 10.95. **Found:** C, 49.37; H, 4.35; N, 6.41.

4.2.3 Synthesis of 7-substitued NQMPs

- Synthesis of 4,7-dibromo-3-hydroxy-2-naphthoic acid (145)^[269]

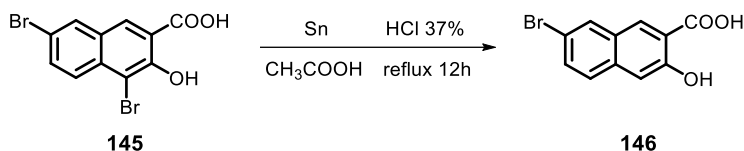


3-hydroxy-2-naphthoic acid (50 g, 0.27 mol) was added in a 1 L three-necked round-bottom flask, glacial acetic acid (600 mL) was added, and the mixture was stirred to be a solution. Bromine (34 mL, 0.67 mol) was dissolved in glacial acetic acid (100 mL) and slowly added dropwise to the reaction mixture through an addition funnel. Throughout the addition the temperature was kept at 20–30°C. Hence, the temperature was raised to 125°C, and the reaction mixture was refluxed for 10 hours under vigorous mechanical stirring. The mixture was slowly cooled down to room temperature upon which a large amount of solid precipitated. The solid was filtered off, and the filter cake was washed with water (2x200 mL). The solid was dissolved in ethyl acetate (300 mL), washed with water (3x200 mL) and with brine (100 mL). The organic phase was dried over Na_2SO_4 and the solvent was removed under reduced pressure to obtain 83 g of product.

TLC ($\text{CHCl}_3/\text{MeOH}$ 80:20) R_f 0.20.

4,7-dibromo-3-hydroxy-2-naphthoic acid (145): yellow solid (yield = 90%); mp = 257–264 °C. $^1\text{H-NMR}$ (200 MHz, acetone- d_6 , 25°C, TMS) δ (ppm) 10.41 (bs, 2H), 8.53 (s, 1H), 8.15 (s, 1H), 7.96 (d, $^3J(\text{H,H})=8$ Hz, 1H), 7.72 (d, $^3J(\text{H,H})=8$ Hz, 1H).

- **Synthesis of 7-bromo-3-hydroxy-2-naphthoic acid (146)**^[269]

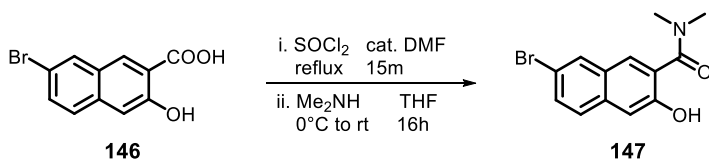


4,7-dibromo-3-hydroxy-2-naphthoic acid (72 g, 0.208 mol), glacial acetic acid (900 mL) and tin powder (32.4 g, 0.273 mol) were added in a 2 L three-necked round-bottom flask and stirred to be homogeneous. The mixture was then added with 37% hydrochloric acid (240 mL) through an addition funnel, heated to 125°C, and refluxed for 12 hours. Hence, the mixture was added with 550 mL of water, cooled down to room temperature and filtered. The filter cake was washed with water (3 x 200 mL) and dried in an oven to obtain 53 g of product.

TLC (CHCl₃/MeOH 80:20) R_f 0.05–0.20.

7-bromo-3-hydroxy-2-naphthoic acid (146): yellow solid (yield = 97%); mp = 269–271 °C. ¹H-NMR (200 MHz, DMSO-*d*₆, 25°C, TMS) δ (ppm) 8.50 (s, 1H), 8.22 (d, ⁴J(H,H)=2.0 Hz 1H), 7.71 (d, ³J(H,H)=8.9 Hz 1H), 7.59 (dd, ³J(H,H)=8.8 Hz, ⁴J(H,H)=2.0 Hz, 1H), 7.32 (s, 1H).

- **Synthesis of 7-bromo-3-hydroxy-N,N-dimethyl-2-naphthamide (147)**



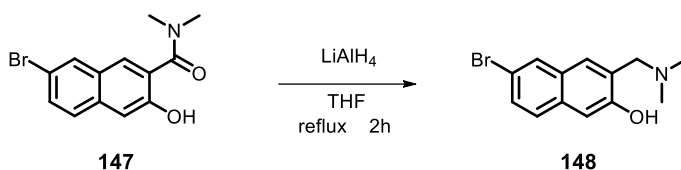
7-Bromo-3-hydroxynaphthalene-2-carboxylic acid (10.0 g, 37.4 mmol) was added in small portions to ice-cooled thionyl chloride (30 mL) under magnetic stirring. A catalytic amount of DMF (5 drops) were added to the stirring suspension and the mixture was heated at 80°C and refluxed for 15 minutes. Removal of the SOCl₂ was afforded under vacuum provided by a water pump. After complete elimination of the solvent, the crude acyl chloride was obtained as a yellow solid. Hence, the acyl chloride was dissolved in anhydrous THF (100 mL), transferred into a three-necked round-bottom flask and the solution was cooled to 0°C. A constant light flow of gaseous dimethylamine was then bubbled into the stirring solution at 0°C. Gaseous dimethylamine was generated by dropwise addition of NaOH 10 M (40 mL) in

a 30–50°C heated flask containing dimethylamine hydrochloride (30 g). A gentle N₂ flux was used to let the vapors pass through a condenser and a CaCl₂/NaOH drying column to the stirring solution. After 3 hours the flask was sealed and keeping the stirring for additional 16 hours at room temperature, whereupon a white solid precipitated. After addition of water (400 mL) and neutralization with 10% HCl, the solid was filtered, washed with water (3 x 50 mL) and dried. The crude solid was purified by recrystallization from acetone.

TLC (CHCl₃/MeOH 95:5) R_f 0.46.

7-bromo-3-hydroxy-N,N-dimethyl-2-naphthamide (147): white solid (yield = 87%); mp = °C. **¹H-NMR** (200 MHz, DMSO-*d*₆, 25°C, TMS) δ (ppm) 10.29 (s, 1H), 8.08 (d, ⁴J(H,H)=1.5 Hz, 1H), 7.70 (m, 2H), 7.50 (dd, ³J(H,H)=8.9 Hz, ⁴J(H,H)=1.9 Hz, 1H), 7.21 (s, 1H), 3.00 (s, 3H), 2.79 (s, 3H).

- **Synthesis of 6-bromo-3-((dimethylamino)methyl)naphthalene-2-ol (148)**

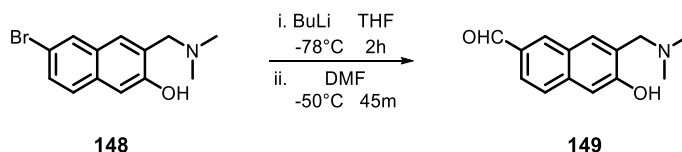


7-bromo-3-hydroxy-N,N-dimethyl-2-naphthamide (8.88 g, 30.2 mmol) was suspended in anhydrous THF (250 mL) and the mixture was cooled at 0°C. Lithium aluminium hydride (2.5 g, 65.9 mmol) was added in one portion under stirring and the reaction mixture was heated at 70 °C and refluxed for 2 hours. Hence, the mixture was cooled in an ice bath and quenched with a saturated aqueous NaHCO₃ solution (100 mL). The organic solvent was removed under reduced pressure and the aqueous phase was extracted with DCM (3x50 mL). The combined organic phases were washed with brine and dried over Na₂SO₄. The solvent was removed under reduced pressure, and the residue was purified by recrystallization in ethanol.

TLC (CHCl₃/MeOH 95:5) R_f 0.56.

6-bromo-3-((dimethylamino)methyl)naphthalene-2-ol (148): white solid (yield = 96%); mp = 134–142°C. **¹H-NMR** (200 MHz, CDCl₃, 25°C, TMS) δ (ppm) 9.66 (bs, 1H), 7.83 (d, ⁴J(H,H)=2 Hz, 1H), 7.55 (d, ³J(H,H)=8 Hz, 2H), 7.44 (dd, ³J(H,H)=8 Hz, ⁴J(H,H)=2 Hz, 1H), 7.16 (s, 1H), 3.81 (s, 2H), 2.37 (s, 6H).

- **Synthesis of 7-((dimethylamino)methyl)-6-hydroxy-2-naphthaldehyde (149)**

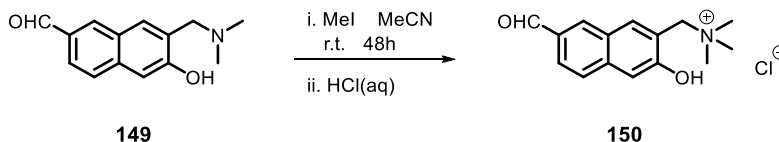


6-bromo-3-((dimethylamino)methyl)naphthalen-2-ol (1.00 g, 3.56 mmol) was dissolved in dry THF (25 mL). The magnetically stirred solution was cooled to -78°C and, under an argon atmosphere, a solution of *n*-BuLi 2.5 M in *n*-hexane (3.14 mL, 7.85 mmol) was added dropwise, keeping the temperature below -70°C . After 2 hours, dry *N,N*-dimethylformamide (1.10 mL, 14.2 mmol) was added dropwise, keeping the temperature below -50°C . After 45 minutes, the reaction mixture was let warm up and was poured into HCl/ice (pH<1) under vigorous stirring. Hence, the mixture was neutralized with NaHCO_3 and extracted with DCM (3x50 mL). The combined organic phases were washed twice with water, dried over Na_2SO_4 , and the solvent was removed under reduced pressure. The crude was purified by flash chromatography (cyclohexane/ CHCl_3 8:2).

TLC ($\text{CHCl}_3/\text{MeOH}$ 95:5) R_f 0.56. **TLC** (cyclohexane/ CHCl_3 6:4) R_f 0.20.

7-((dimethylamino)methyl)-6-hydroxy-2-naphthaldehyde (149): white solid (yield = 71%); mp = $146.1\text{--}148.7^{\circ}\text{C}$. $^1\text{H-NMR}$ (300 MHz, DMSO-d_6 , 25°C , TMS) δ (ppm) 10.07 (s, 1H), 8.18 (s, 1H), 7.87 (dd, $^3J(\text{H,H})=8.6$ Hz, $^4J(\text{H,H})=1.3$ Hz, 1H), 7.75 (d, $^3J(\text{H,H})=8.6$ Hz, 1H), 7.64 (s, 1H), 7.23 (s, 1H), 3.88 (s, 2H), 2.41 (s, 6H). $^{13}\text{C-NMR}$ (75 MHz, DMSO-d_6 , 25°C , TMS) δ (ppm) 191.5; 159.1; 137.7; 133.6; 131.4; 128.7; 126.7; 126.4; 125.4; 122.8; 110.3; 62.3; 44.0.

- **Synthesis of 1-(7-formyl-3-hydroxynaphthalen-2-yl)-*N,N,N*-trimethylmethanaminium chloride (150)**



Iodomethane (40 μL , 0.65 mmol) was added to a stirred solution of the Mannich base **149** (50 mg, 0.22 mmol) in ACN (5 mL) and the reaction mixture was stirred at room temperature for 48 hours. The solvent and excess iodomethane were removed under reduced pressure.

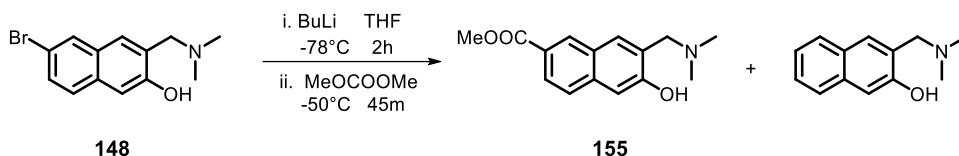
The product was purified by reverse phase HPLC (H₂O 0.1% TFA/ACN gradient) and the anion was exchanged with 1% HCl (1 mL).

TLC (CHCl₃/MeOH 8:2) R_f 0.77 (reagent), 0.05 – 0 (product).

1-(7-formyl-3-hydroxynaphthalen-2-yl)-N,N,N-trimethylmethanaminium chloride (150):

white solid (yield = 99%); mp = °C. ¹H-NMR (300 MHz, DMSO-d₆, 25°C, TMS) δ (ppm) 11.57 (s, 1H), 10.08 (s, 1H), 8.50 (s, 1H), 8.30 (s, 1H), 7.86 (s, 2H), 7.56 (s, 1H), 4.71 (s, 2H), 3.14 (s, 9H). ¹³C-NMR (75 MHz, DMSO-d₆, 25°C, TMS) δ (ppm) 192.4; 157.6; 138.6; 137.4; 135.3; 131.8; 126.9; 126.0; 123.9; 119.2; 110.3; 62.6; 52.2.

• **Synthesis of methyl 7-((dimethylamino)methyl)-6-hydroxy-2-naphthoate (155)**



6-bromo-3-((dimethylamino)methyl)naphthalen-2-ol (1.00 g, 3.56 mmol) was dissolved in dry THF (25 mL). The magnetically stirred solution was cooled to -78 °C and, under an argon atmosphere, a solution of n-BuLi 2.5 M in n-hexane (3.14 mL, 7.85 mmol) was added dropwise, keeping the temperature below -70 °C. After 2 hours, the organolithium solution was cannulated under an Ar pressure into a solution of dimethyl carbonate (3.0 mL, 35.7 mmol) in dry THF (50 mL) cooled to -78°C. The reaction mixture was stirred for additional 45 minutes keeping the temperature below -50 °C, after which it was let warm up and it was poured into HCl/ice (pH<1) under vigorous stirring. Hence, the mixture was neutralized with NaHCO₃ and extracted with EtOAc (3x50 mL). The combined organic phases were washed twice with water, dried over Na₂SO₄, and the solvent was removed under reduced pressure. The crude was purified by flash chromatography (cyclohexane/EtOAc gradient).

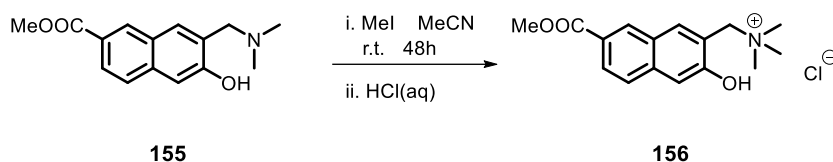
TLC (CHCl₃/MeOH 95:5) R_f 0.50 (reagent), 0.45 (dealogenated subproduct), 0.35 (product).

methyl 7-((dimethylamino)methyl)-6-hydroxy-2-naphthoate (155): white solid (yield = 46%); mp = 177.2–180.5°C. ¹H-NMR (300 MHz, CDCl₃, 25°C, TMS) δ (ppm) 8.48 (s, 1H), 7.98 (dd, J = 8.6 Hz, 1.6 Hz, 1H), 7.71 (d, J = 8.7 Hz, 1H), 7.60 (s, 1H), 7.23 (s, 1H), 3.97 (s, 3H), 3.88

(s, 2H), 2.42 (s, 6H). $^{13}\text{C-NMR}$ (75 MHz, CDCl_3 , 25°C , TMS) δ (ppm) 167.4; 158.4; 137.0; 130.6; 129.0; 126.7; 126.1; 125.4; 125.3; 124.5; 110.2; 62.6; 51.9; 44.3.

3-((dimethylamino)methyl)naphthalen-2-ol: white solid (yield = 42%). $^1\text{H-NMR}$ (200 MHz, CDCl_3 , 25°C , TMS) δ (ppm) 10.15 (bs, 1H), 7.75 (d, $J = 8.2$ Hz, 2H), 7.49–7.31 (m, 4H), 3.78 (s, 2H), 2.35 (s, 6H).

- **Synthesis of 1-(3-hydroxy-7-(methoxycarbonyl)naphthalene-2-yl)-N,N,N-trimethylmethanaminium chloride (156)**

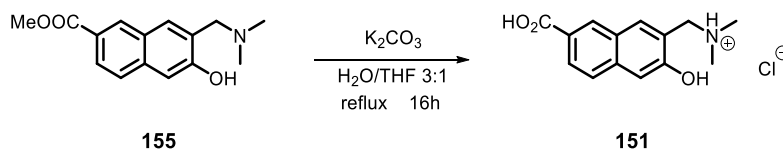


Iodomethane (122 μL , 2.0 mmol) was added to a stirred solution of the Mannich base **155** (85 mg, 0.33 mmol) in ACN (10 mL) and the reaction mixture was stirred at room temperature for 48 hours. The solvent and excess iodomethane were removed under reduced pressure. The product was purified by reverse phase HPLC (H_2O 0.1% TFA/ACN gradient) and the anion was exchanged with 1% HCl (1 mL).

TLC ($\text{CHCl}_3/\text{MeOH}$ 8:2) R_f 0.77 (reagent), 0.05 – 0 (product).

1-(3-hydroxy-7-(methoxycarbonyl)naphthalene-2-yl)-N,N,N-trimethylmethanaminium chloride (156): white solid (yield = 95%); mp = 220.8 – 229.3°C (decomposition with vapour evolution). $^1\text{H-NMR}$ (300 MHz, MeOD, 25°C , TMS) δ (ppm) 8.60 (s, 1H), 8.21 (s, 1H), 8.02 (d, $J = 8.6$ Hz, 1H), 7.78 (d, $J = 8.7$ Hz, 1H), 7.37 (s, 1H), 4.75 (s, 2H), 3.96 (s, 3H), 3.22 (s, 6H). $^{13}\text{C-NMR}$ (75 MHz, MeOD, 25°C , TMS) δ (ppm) 168.8; 158.0; 140.2; 138.7; 132.9; 128.37; 128.35; 127.7; 127.0; 119.9; 111.4; 65.6; 54.0; 53.0.

- **Synthesis of 1-(7-carboxy-3-hydroxynaphthalen-2-yl)-N,N-dimethylmethanaminium chloride (151)**

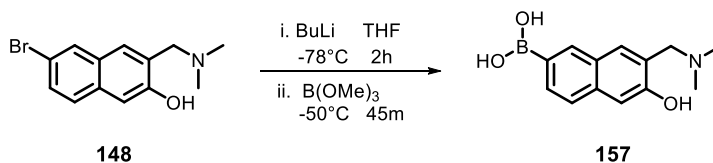


Methyl 7-((dimethylamino)methyl)-6-hydroxy-2-naphthoate **155** (100 mg, 0.38 mmol) was dissolved in water/THF 3:1 mixture (20 mL). Potassium carbonate (118 mg, 0.86 mmol) was added in one portion and the reaction mixture was heated to reflux for 16 hours. The solution was acidified with 10% HCl (1 mL) and the solvent was removed under reduced pressure. The crude was dissolved in isopropanol (5 mL) and filtered. The solid was collected, added with isopropanol (5 mL) and filtered, and these two steps were repeated a third time. The filtrates were combined and the solvent was removed under reduced pressure. A purified sample for NMR characterization was obtained by reverse phase HPLC (H₂O 0.1% TFA/ACN gradient) and exchanging the anion with 1% HCl (1 mL).

TLC (CHCl₃/MeOH 8:2) R_f 0.77 (reagent), 0 (product).

1-(7-carboxy-3-hydroxynaphthalen-2-yl)-N,N-dimethylmethanaminium chloride (151): white solid (yield = 84%); mp = °C. ¹H-NMR (300 MHz, MeOD, 25°C, TMS) δ (ppm) 8.59 (s, 1H), 8.09 (s, 1H), 8.05 (d, J = 8.7, 1H), 7.79 (d, J = 8.6 Hz, 1H), 7.34 (s, 1H), 4.53 (s, 2H), 2.94 (s, 6H). ¹³C-NMR (75 MHz, MeOD, 25°C, TMS) δ (ppm) 170.1, 157.3, 140.0, 135.7, 132.8, 128.7, 128.5, 127.7 (x2), 121.8, 110.8, 59.0, 43.9.

- **Synthesis of 7-((dimethylamino)methyl)-6-hydroxynaphthalen-2-ylboronic acid (157)**



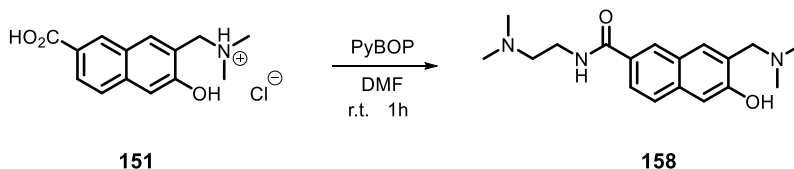
6-bromo-3-((dimethylamino)methyl)naphthalen-2-ol (1.00 g, 3.56 mmol) was dissolved in dry THF (25 mL). The magnetically stirred solution was cooled to -78 °C and, under an argon atmosphere, a solution of n-BuLi 2.5 M in n-hexane (3.14 mL, 7.85 mmol) was added

dropwise, keeping the temperature below $-70\text{ }^{\circ}\text{C}$. After 2 hours, trimethyl borate (3.0 mL, 26.9 mmol) was added dropwise, keeping the temperature below $-50\text{ }^{\circ}\text{C}$. After 45 minutes, the reaction mixture was let warm up and was poured into HCl/ice (pH<1) under vigorous stirring. Hence, the mixture was neutralized with NaHCO_3 and extracted with EtOAc (3x50 mL). The combined organic phases were washed twice with water, dried over Na_2SO_4 , and the solvent was removed under reduced pressure. The crude was purified by flash chromatography ($\text{CHCl}_3/\text{MeOH}$ gradient).

TLC ($\text{CHCl}_3/\text{MeOH}$ 7:3) Rf 0.79 (reagent), 0.48 (product).

(7-((dimethylamino)methyl)-6-hydroxynaphthalen-2-yl)boronic acid (157): white solid (yield = 54%); mp = $^{\circ}\text{C}$. $^1\text{H-NMR}$ (300 MHz, DMSO-d_6 , 25°C , TMS) δ (ppm) 10.96 (s, 1H), 10.39 (bs, 1H), 8.38 (s, 1H), 8.17 (s, 1H), 7.93 (d, $J = 8.3\text{ Hz}$, 1H), 7.75 (d, $J = 8.3\text{ Hz}$, 1H), 7.44 (s, 1H), 4.50 (s, 2H), 2.85 (s, 6H). $^{13}\text{C-NMR}$ (75 MHz, DMSO-d_6 , 25°C , TMS) δ (ppm) 154.6, 136.1, 135.2, 133.7, 131.9, 128.7, 126.7, 124.5, 119.3, 109.0, 54.8, 42.0.

- **Synthesis of 7-((dimethylamino)methyl)-N-(3-(dimethylamino)propyl)-6-hydroxy-2-naphthamide (158)**



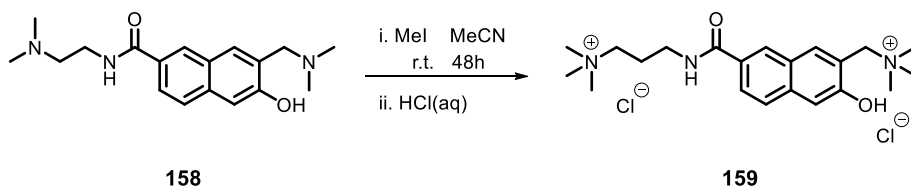
The amino acid **151** (100 mg, 0.35 mmol) was dissolved in dry DMF (5 mL). PyBOP (185 mg, 0.35 mmol) was added in one portion to the stirred solution and, after 1 minute, 3-(dimethylamino)-1-propylamine (133 μL , 0.106 mmol) was added. The reaction mixture was stirred at room temperature for 1 hour. The solvent was removed under vacuo and the crude was purified by reverse phase HPLC (H_2O 0.1% TFA/ACN gradient). The aqueous phase was neutralized with NaHCO_3 , extracted in DCM (3x10 mL), the combined organic phases were dried over Na_2SO_4 , and the solvent was removed under reduced pressure.

TLC ($\text{CHCl}_3/\text{MeOH}$ 8:2) Rf 0.77 (reagent), 0.20 (product).

7-((dimethylamino)methyl)-N-(3-(dimethylamino)propyl)-6-hydroxy-2-naphthamide (158)

: white solid (yield = 79%); mp = °C. ¹H-NMR (300 MHz, CDCl₃, 25°C, TMS) δ (ppm) 8.54 (s, 1H), 8.38 (s, 1H), 7.87-7.79 (m, 2H), 7.67 (s, 1H), 7.30 (s, 1H), 3.95 (s, 2H), 3.74 (q, J = 5.4 Hz, 2H), 2.76 (t, J = 5.9 Hz, 2H), 2.54 (s, 6H), 2.49 (s, 6H), 2.00 (quint, J = 6.0 Hz, 2H). ¹³C-NMR (75 MHz, CDCl₃, 25°C, TMS) δ (ppm) 167.2, 157.5, 135.9, 128.8, 128.5, 127.3, 127.0, 126.2, 125.5, 123.5, 110.0, 62.8, 58.5, 44.9, 44.4, 39.7, 25.0.

- **Synthesis of 1-(7-((3-dimethylamino)propyl)carbamoyl)-3-hydroxynaphthalen-2-yl)-N,N,N-trimethylmethanaminium chloride (159)**

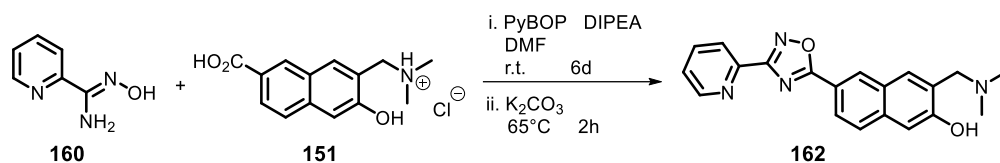


Iodomethane (43 μL, 0.68 mmol) was added to a stirred solution of the Mannich base **158** (50 mg, 0.15 mmol) in ACN (10 mL) and the reaction mixture was stirred at room temperature for 48 hours. The solvent and excess iodomethane were removed under reduced pressure. The product was purified by reverse phase HPLC (H₂O 0.1% TFA/ACN gradient) and the anion was exchanged with 1% HCl (1 mL).

TLC (CHCl₃/MeOH 8:2) R_f 0.77 (reagent), 0.05 – 0 (product).

1-(7-((3-dimethylamino)propyl)carbamoyl)-3-hydroxynaphthalen-2-yl)-N,N,N-trimethylmethanaminium chloride (159): white solid (yield = 98%); mp = °C. ¹H-NMR (300 MHz, MeOD, 25°C, TMS) δ (ppm) 8.44 (s, 1H), 8.16 (s, 1H), 7.94 (dd, J = 8.7, 1.6 Hz, 1H), 7.82 (d, J = 8.8 Hz, 1H), 7.38 (s, 1H), 4.75 (s, 2H), 3.57 (t, J = 6.7 Hz, 2H), 3.52–3.46 (m, 2H), 3.21 (s, 9H), 3.18 (s, 9H), 2.18 (quint, J = 8.4 Hz, 2H). ¹³C-NMR (75 MHz, MeOD, 25°C, TMS) δ (ppm) 170.5, 157.6, 139.5, 138.3, 130.9, 130.0, 128.5, 127.7, 127.1, 119.9, 111.4, 66.2, 65.6, 54.0, 53.9, 38.3, 24.9.

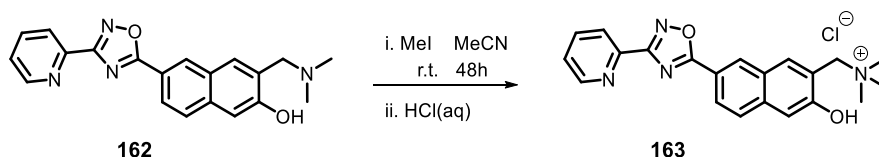
• **Synthesis of 3-((dimethylamino)methyl)-6-(3-(pyridin-2-yl)-1,2,4-oxadiazol-5-yl)naphthalen-2-ol (162)**



The amino acid **151** (100 mg, 0.35 mmol) and diisopropyl-ethyl-amine (124 μ L, 0.71 mmol) were dissolved in dry DMF (5 mL). PyBOP (185 mg, 0.35 mmol) was added in one portion to the stirred solution and, after 1 hour, N'-hydroxypicolinimidamide **160** (49 mg, 0.35 mmol) was added. The reaction mixture was stirred at room temperature for 6 days. The formation of a major peak was monitored by reverse phase HPLC (H₂O 0.1% TFA/ACN gradient). Ring closure was obtained by addition of anhydrous K₂CO₃ (5 mg, 10% mol) and heating the suspension at 65°C for 2 hours. The solvent was removed under reduced pressure and the crude was purified by reverse phase HPLC (H₂O 0.1% TFA/ACN gradient). The aqueous phase was neutralized with NaHCO₃, extracted in DCM (3x10 mL), the combined organic phases were dried over Na₂SO₄, and the solvent was removed under reduced pressure.

1-(3-hydroxy-7-(3-(pyridine-2-yl)-1,2,4-oxadiazol-5-yl)naphthalen-2-yl)-N,N-dimethylmethanaminium chloride (162·HCl): white solid (yield = 61%); mp = °C. ¹H-NMR (300 MHz, MeOD, 25°C, TMS) δ (ppm) 9.00 (d, J = 4.2 Hz, 1H), 8.81 (s, 1H), 8.72–8.68 (m, 2H), 8.24–8.16 (m, 3H), 7.95 (d, J = 8.6 Hz, 1H), 7.39 (s, 1H), 4.58 (s, 2H), 2.97 (s, 6H). ¹³C-NMR (75 MHz, MeOD, 25°C, TMS) δ (ppm) 179.3, 166.1, 158.1, 146.9, 146.7, 142.6, 140.0, 136.0, 131.6, 130.1, 129.0, 128.7, 127.1, 126.6, 122.8, 119.9, 111.1, 58.7, 44.0.

• **Synthesis of 1-(3-hydroxy-7-(3-(pyridine-2-yl)-1,2,4-oxadiazol-5-yl)naphthalen-2-yl)-N,N,N-trimethylmethanaminium chloride (163)**



Iodomethane (58 μ L, 0.90 mmol) was added to a stirred solution of the Mannich base **162** (50 mg, 0.15 mmol) in ACN (10 mL) and the reaction mixture was stirred at room temperature for 48 hours. The solvent and excess iodomethane were removed under reduced pressure.

The product was purified by reverse phase HPLC (H₂O 0.1% TFA/ACN gradient) and the anion was exchanged with 1% HCl (1 mL).

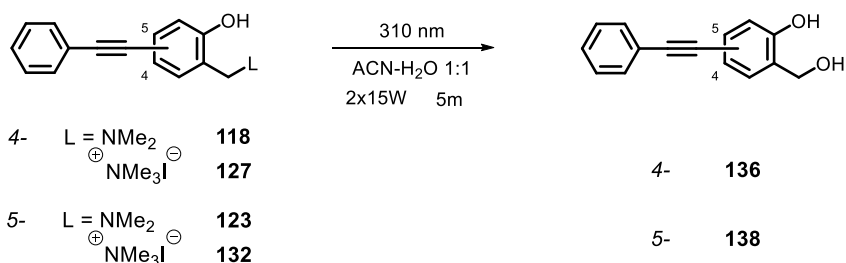
TLC (CHCl₃/MeOH 8:2) R_f 0.77 (reagent) 0.05 – 0 (product)

1-(3-hydroxy-7-(3-(pyridine-2-yl)-1,2,4-oxadiazol-5-yl)naphthalen-2-yl)-N,N,N-trimethylmethanaminium chloride (163): white solid (yield = 90%); mp = °C. ¹H-NMR (300 MHz, MeOD, 25°C, TMS) δ (ppm) 8.88 (s, 2H), 8.40–8.32 (m, 3H), 8.19 (t, J = 7.8 Hz, 1H), 8.02 (d, J = 8.7 Hz, 1H), 7.76 (t, J = 5.3 Hz, 1H), 7.48 (s, 1H), 4.85 (s, 2H), 3.33 (s, 9H). ¹³C-NMR (75 MHz, MeOD, 25°C, TMS) δ (ppm) 178.2, 169.9, 158.4, 151.3, 147.5, 140.0, 139.8, 138.6, 131.3, 128.7, 128.6, 127.9, 127.0, 125.1, 120.7, 120.5, 111.7, 65.5, 58.9.

4.2.4 Preparative phototrapping of prototype QMPs

QMs were photogenerated by irradiation of QMPs and were trapped with water and 2-mercaptoethan-1-ol. All the reactions were performed in a Rayonet® multilamp reactor using two 15 W UV lamps and 20 mL quartz tubes.

- **Preparative photohydrations of 118, 123, 127, 132 – Synthesis of benzylic alcohols 136 and 138**



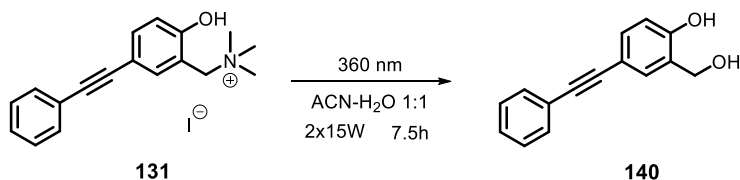
The corresponding QMP (**118**, **123**, **127** or **132**, 0.024 mmol) was dissolved in a 1:1 ACN-H₂O mixture (240 mL, 10⁻⁴ M). The solution was distributed into 20 mL quartz tubes (16x15 mL), sealed, bubbled with argon for 30 seconds, and irradiated at 310 nm for 5 minutes (2x15 W). Hence, the solvent was removed under reduced pressure, and the crude was purified by column chromatography (cyclohexane/AcOEt 1:1).

TLC (cyclohexane/AcOEt 7:3) R_f 0.67.

2-(Hydroxymethyl)-4-(phenylethynyl)phenol (136): white solid (yield = 35% from **118** and 89% from **127**); mp = 149–151 °C. ¹H-NMR (300 MHz, acetone-d₆, 25°C, TMS) δ (ppm) 9.00 (s, OH), 7.62–7.58 (m, 3H), 7.50–7.44 (m, 3H), 7.38 (dd, J = 2.1 Hz, J = 8.3 Hz, 1H), 6.96 (d, J = 8.3 Hz, 1H), 4.84 (s, 2H), 4.60 (bs, OH). ¹³C-NMR (75 MHz, acetone-d₆, 25°C, TMS) δ (ppm) 156.8; 132.6; 132.4; 132.0; 129.7; 129.6; 129.1; 125.0; 116.6; 115.1; 91.1; 88.3; 61.3. **Anal. calcd** for C₁₅H₁₂O₂: C, 80.34; H, 5.39; O, 14.27. **Found:** C, 80.37; H, 5.41.

2-(Hydroxymethyl)-5-(phenylethynyl)phenol (138): white solid (yield = 10% from **123** and 64% from **132**); mp = 135–138 °C. ¹H-NMR (300 MHz, acetone-d₆, 25°C, TMS) δ (ppm) 8.79 (s, OH), 7.65–7.62 (m, 2H), 7.52–7.50 (m, 3H), 7.43 (d, J = 7.7 Hz, 1H), 7.13 (dd, J = 1.6 Hz, J = 7.7 Hz, 1H), 7.09 (s, 1H); 4.86 (d, J = 5.3 Hz, 2H), 4.58 (t, J = 5.3 Hz, OH). ¹³C-NMR (75 MHz, acetone-d₆, 25°C, TMS) δ (ppm) 156.2; 132.6; 130.2; 129.8; 129.6; 128.8; 124.5; 124.1; 123.6; 118.8; 90.5; 89.6; 61.6. **Anal. calcd** for C₁₅H₁₂O₂: C, 80.34; H, 5.39; O, 14.27. **Found:** C, 80.32; H, 5.35.

- **Preparative photohydrations of 131 – Synthesis of benzylic alcohol 140**



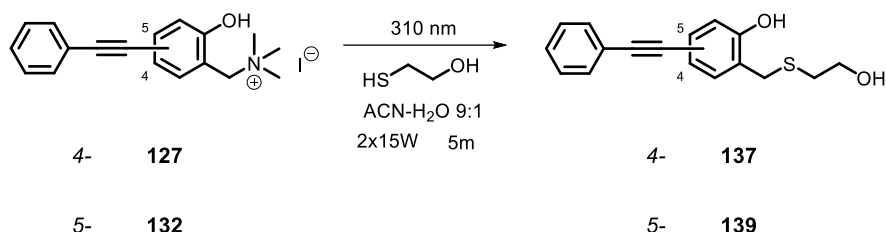
The quaternary ammonium salt **131** (10 mg, 0.024 mmol) was dissolved in a 1:1 ACN-H₂O mixture (240 mL, 10⁻⁴ M). The solution was distributed into 20 mL quartz tubes (16x15 mL), sealed, bubbled with argon for 30 seconds, and irradiated at 310 nm for 7.5 hours (2x15 W). Hence, the solvent was removed under reduced pressure, and the crude was purified by column chromatography (cyclohexane/AcOEt 1:1).

TLC (cyclohexane/AcOEt 7:3) R_f 0.78.

2-(Hydroxymethyl)-4-(4-nitrophenylethynyl)phenol (140): yellow solid (yield = 98%) mp = 148–150 °C. ¹H-NMR (300 MHz, acetone-d₆, 25°C, TMS) δ (ppm) 8.36 (AA'XX' system, J = 8.9 Hz, 2H), 7.84 (AA'XX' system, J = 8.9 Hz, 2H), 7.68 (d, J = 1.9 Hz, 1H), 7.47 (dd, J = 1.9 Hz, J = 8.3 Hz, 1H), 7.00 (d, J = 8.3 Hz, 1H), 4.85 (s, 2H), 3.04 (bs, OH). ¹³C-NMR (75 MHz, acetone-d₆, 25°C, TMS) δ (ppm) 157.5; 148.1; 133.3; 133.1; 132.4; 131.9; 129.9; 124.9; 116.6; 113.9; 96.7;

87.1; 61.0. **Anal. calcd** for $C_{15}H_{11}NO_4$: C, 66.91; H, 4.12; N, 5.20; O, 23.77. **Found**: C, 66.94; H, 4.11; N, 5.24.

- **Preparative phototrapping of 127 and 132 with 2-mercaptoethan-1-ol – Synthesis of thioethers 137 and 139**



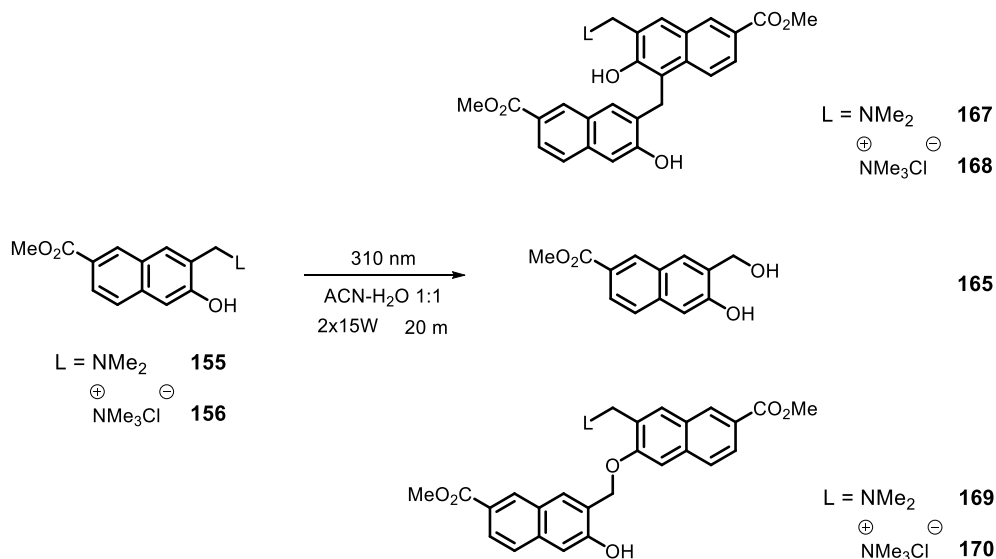
The corresponding quaternary ammonium salt (**127** or **132**, 0.024 mmol) was dissolved in a 9:1 ACN-H₂O mixture (240 mL, 10⁻⁴ M). Freshly distilled 2-mercaptoethan-1-ol (168 μL, 2.4 mmol, 10⁻² M). The solution was distributed into 20 mL quartz tubes (16x15 mL), sealed, bubbled with argon for 30 seconds, and irradiated at 310 nm for 5 minutes (2x15 W). Hence, the solvent was removed under reduced pressure, and the crude was purified by column chromatography (cyclohexane/AcOEt 1:1).

TLC (cyclohexane/AcOEt 7:3) *R_f* 0.54.

2-(((2-Hydroxyethyl)thio)methyl)-4-(phenylethynyl)phenol (137): colorless oil (yield = 73%); ¹H-NMR (300 MHz, CDCl₃, 25°C, TMS) δ (ppm) 7.54–7.50 (m, 2H), 7.40–7.32 (m, 5H), 6.87 (d, *J* = 8.1 Hz, 1H), 3.87–3.83 (m, 4H), 2.69 (t, *J* = 5.8 Hz, 2H). ¹³C-NMR (75 MHz, CDCl₃, 25°C, TMS) δ (ppm) 155.1; 133.9; 132.5; 131.3; 128.2; 127.9; 123.3; 116.9; 115.4; 88.9; 88.1; 61.5; 33.4; 31.6. **Anal. calcd** for C₁₇H₁₆O₂S: C, 71.80; H, 5.67; O, 11.25; S, 11.27. **Found**: C, 71.77; H, 5.68.

2-(((2-Hydroxyethyl)thio)methyl)-5-(phenylethynyl)phenol (139): white solid (yield = 38%); mp = 83–85 °C. ¹H-NMR (300 MHz, CDCl₃, 25°C, TMS) δ (ppm) 7.56–7.51 (m, 2H), 7.37–7.35 (m, 3H), 7.15–7.07 (m, 3H), 3.94–3.81 (m, 4H), 2.68 (t, *J* = 5.8 Hz, 2H). ¹³C-NMR (75 MHz, CDCl₃, 25°C, TMS) δ (ppm) 154.5; 131.5; 130.6; 128.2; 124.1; 123.8; 123.7; 123.0; 119.6; 89.5; 88.7; 61.5; 33.4; 31.6. **Anal. calcd** for C₁₇H₁₆O₂S: C, 71.80; H, 5.67; O, 11.25; S, 11.27. **Found**: C, 71.83; H, 5.65.

• Preparative photohydrations of **155** and **156** – Synthesis of alcohol **165**



The corresponding QMP (**155** or **156**, 0.032 mmol) was dissolved in a 1:1 ACN-H₂O mixture (100 mL, 3.2 · 10⁻⁴ M). The solution was distributed into 20 mL quartz tubes (7x15 mL), sealed, bubbled with argon for 30 seconds, and irradiated at 310 nm for 20 minutes (2x15 W). Hence, the organic solvent was removed under reduced pressure, the aqueous phase was acidified with 1% HCl (1 mL) and extracted with DCM (3x25 mL). The combined organic phases were dried over Na₂SO₄ and the solvent removed under reduced pressure. The crude was purified by flash column chromatography (CHCl₃/AcOEt 8:2) to obtain **165**.

The aqueous phase was purified by reverse phase HPLC (H₂O 0.1% TFA/ACN gradient) and the anion was exchanged with 1% HCl (1 mL) to obtain **167·HCl** and **169·HCl** (from **155**) or **168** and **170** (from **156**).

TLC (CHCl₃/AcOEt 7:3) R_f 0.36 (**165**).

Methyl 6-hydroxy-7-(hydroxymethyl)-2-naphthoate (165): white solid (yield = 18% from **120**, 53% from **121**) mp = °C. ¹H-NMR (300 MHz, DMSO-d₆, 25°C, TMS) δ (ppm) 10.44 (bs, 1H), 8.56 (s, 1H), 8.08 (s, 1H), 7.94 (dd, J = 8.6, 1.5 Hz, 1H), 7.86 (d, J = 8.7 Hz, 1H), 7.28 (s, 1H), 5.35 (bs, 1H), 4.73 (s, 2H), 3.98 (s, 3H). ¹³C-NMR (75 MHz, DMSO-d₆, 25°C, TMS) δ (ppm) 166.6, 155.6, 135.9, 133.2, 130.2, 127.0, 126.6, 126.0, 124.4, 123.6, 107.9, 58.4, 52.0.

1-(3-hydroxy-4-((3-hydroxy-7-(methoxycarbonyl)naphthalen-2-yl)methyl)-7-(methoxycarbonyl)naphthalen-2-yl)-N,N-dimethylmethanaminium chloride (167·HCl): white solid (yield = 48%) mp = °C. ¹H-NMR (300 MHz, DMSO-d₆, 25°C, TMS) δ (ppm) 10.87 (bs, 1H), 10.10 (bs, 2H), 8.57 (s, 1H), 8.30 (s, 1H), 8.12 (s, 1H), 7.88 (d, J = 8.9 Hz, 1H), 7.76–7.72 (m, 3H), 7.34 (s, 1H), 7.11 (s, 1H), 4.57 (s, 2H), 4.53 (s, 2H), 3.88 (s, 3H), 3.78 (s, 3H), 2.86 (s, 6H). ¹³C-NMR (75 MHz, DMSO-d₆, 25°C, TMS) δ (ppm) 166.4, 166.2, 156.5, 154.1, 136.3, 135.6, 133.7, 131.4, 130.7, 129.9, 128.4, 127.1, 126.5, 126.2, 125.9, 124.5, 124.4, 123.8, 123.5, 121.9, 118.9, 108.2, 55.9, 52.1, 51.8, 42.3, 25.2.

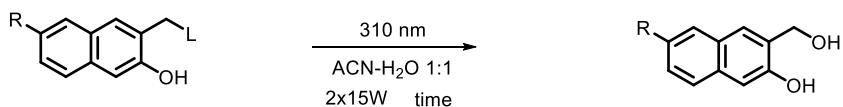
1-(3-hydroxy-4-((3-hydroxy-7-(methoxycarbonyl)naphthalen-2-yl)methyl)-7-(methoxycarbonyl)naphthalen-2-yl)-N,N,N-trimethylmethanaminium chloride (168): white solid (yield = 12%) mp = °C. ¹H-NMR (300 MHz, DMSO-d₆, 25°C, TMS) δ (ppm) 10.43 (bs, 1H), 9.86 (bs, 2H), 8.57 (s, 1H), 8.26 (s, 1H), 8.16 (s, 1H), 7.91 (d, J = 8.9 Hz, 1H), 7.79–7.70 (m, 3H), 7.36 (s, 1H), 7.10 (s, 1H), 4.93 (s, 2H), 4.55 (s, 2H), 3.91 (s, 3H), 3.76 (s, 3H), 3.26 (s, 9H). ¹³C-NMR (75 MHz, DMSO-d₆, 25°C, TMS) δ (ppm) 166.4, 166.2, 156.5, 154.1, 136.3, 135.6, 133.7, 131.4, 130.7, 129.9, 128.4, 127.1, 126.5, 126.2, 125.9, 124.5, 124.4, 123.8, 123.5, 121.9, 118.9, 108.2, 65.5, 53.9, 52.3, 52.0, 25.6.

1-(3-((3-hydroxy-7-(methoxycarbonyl)naphthalen-2-yl)methoxy)-7-(methoxycarbonyl)naphthalen-2-yl)-N,N-dimethylmethanaminium chloride (169·HCl): white solid (yield = 10%) mp = °C. ¹H-NMR (300 MHz, DMSO-d₆, 25°C, TMS) δ (ppm) 10.81 (bs, 1H), 9.36 (bs, 1H), 8.62 (s, 1H), 8.60 (s, 1H), 8.30–8.27 (m, 2H), 8.03 (s, 2H), 7.92–7.78 (m, 3H), 7.34 (s, 1H), 5.47 (s, 2H), 4.57 (s, 2H), 3.92 (s, 3H), 3.89 (s, 3H), 2.81 (s, 6H). ¹³C-NMR (75 MHz, DMSO-d₆, 25°C, TMS) δ (ppm) 166.5, 166.3, 155.9, 153.8, 136.8, 135.2, 133.9, 130.9, 130.6, 129.8, 128.0, 126.9, 125.5, 125.4, 125.3, 124.8, 122.8, 121.7, 120.5, 120.2, 118.9, 110.2, 73.2, 55.9, 52.1, 51.8, 42.4.

1-(3-((3-hydroxy-7-(methoxycarbonyl)naphthalen-2-yl)methoxy)-7-(methoxycarbonyl)naphthalen-2-yl)-N,N,N-trimethylmethanaminium chloride (170): white solid (yield = 4%) mp = °C. ¹H-NMR (300 MHz, DMSO-d₆, 25°C, TMS) δ (ppm) 10.68 (bs, 1H), 9.72 (bs, 1H), 8.60 (s, 1H), 8.60 (s, 1H), 8.30–8.27 (m, 2H), 8.03 (s, 2H), 7.92–7.78 (m, 3H), 7.34 (s, 1H), 5.39 (s, 2H), 4.83 (s, 2H), 3.96 (s, 3H), 3.91 (s, 3H), 3.21 (s, 9H). ¹³C-NMR (75 MHz, DMSO-d₆, 25°C, TMS) δ (ppm) 166.5, 166.3, 155.9, 153.8, 136.8, 135.2, 133.9, 130.9, 130.6, 129.8, 128.0,

126.9, 125.5, 125.4, 125.3, 124.8, 122.8, 121.7, 120.5, 120.2, 118.9, 110.2, 73.2, 62.9, 54.4, 52.1, 51.8.

• **Preparative photohydrations of 149-151,157-159,162-163 – Synthesis of alcohols 171-176**



R = CONH(CH ₂) ₃ NMe ₂	L = NMe ₂	158	time = 45 m	R = CONH(CH ₂) ₃ NMe ₂	171
CONH(CH ₂) ₃ NMe ₃ Cl	[⊕] NMe ₃ Cl [⊖]	159	50 m	[⊕] CONH(CH ₂) ₃ NMe ₃ Cl [⊖]	172
COOH	NMe ₂	151	45 m	COOH	173
CHO	NMe ₂	149	6 h	CHO	174
CHO	[⊕] NMe ₃ Cl [⊖]	150	40 h	CHO	174
B(OH) ₂	NMe ₂	157	30 m	B(OH) ₂	175
(C ₂ N ₂ O)(C ₅ H ₄ N)	NMe ₂	162	4 h	(C ₂ N ₂ O)(C ₅ H ₄ N)	176
(C ₂ N ₂ O)(C ₅ H ₄ N)	[⊕] NMe ₃ Cl [⊖]	163	10 h	(C ₂ N ₂ O)(C ₅ H ₄ N)	176

The corresponding QMP (0.020 mmol) was dissolved in a 1:1 ACN-H₂O mixture (200 mL, 10⁻⁴ M). The solution was distributed into 20 mL quartz tubes (15x15 mL), sealed, bubbled with argon for 30 seconds, and irradiated at 310 nm for the appropriate amount of time (2x15 W). For derivatives **173-176**, the organic solvent was removed under reduced pressure, the aqueous phase was acidified with 1% HCl (1 mL) and extracted with DCM (3x25 mL). The combined organic phases were dried over Na₂SO₄ and the solvent removed under reduced pressure. The crude was purified by flash column chromatography (CHCl₃/AcOEt/MeOH gradient).

Derivatives **171** and **172** were instead purified by reverse phase HPLC (H₂O 0.1% TFA/ACN gradient). To obtain **172**, the anion was exchanged with 1% HCl (1 mL). To obtain **171**, the aqueous phase was neutralized with NaHCO₃, extracted in DCM (3x10 mL), the combined organic phases were dried over Na₂SO₄, and the solvent was removed under reduced pressure.

N-(3-(dimethylamino)propyl)-6-hydroxy-7-(hydroxymethyl)-2-naphthamide (171): white solid (yield = 18%) mp = °C. ¹H-NMR (300 MHz, CDCl₃, 25°C, TMS) δ (ppm) 8.22 (bs, 1H), 7.80 (s, 1H), 7.57–7.45 (m, 2H), 7.26 (s, 1H), 7.09 (s, 1H), 4.88 (s, 2H), 3.56 (t, J = 5.6 Hz, 2H), 2.56 (t, J = 6.2 Hz, 2H), 2.34 (s, 6H), 1.82 (quint, J = 6.0 Hz, 2H). ¹³C-NMR (75 MHz, CDCl₃, 25°C,

TMS) δ (ppm) 167.5, 157.6, 131.8, 131.2, 130.9, 130.2, 128.2, 127.9, 126.1, 123.2, 108.9, 59.1, 58.7, 47.2, 37.2, 25.9.

3-(6-hydroxy-7-(hydroxymethyl)-2-naphthamido)-N,N,N-trimethylpropan-1-aminium chloride (172): white solid (yield = 91%) mp = °C. $^1\text{H-NMR}$ (300 MHz, MeOD, 25°C, TMS) δ (ppm) 8.31 (s, 1H), 7.93 (s, 1H), 7.81 (dd, J = 8.6, 1.7 Hz, 1H), 7.71 (d, J = 8.7 Hz, 1H), 7.16 (s, 1H), 4.83 (s, 2H), 3.56 (t, J = 6.6 Hz, 2H), 3.50–3.45 (m 2H), 3.17 (s, 9H), 2.17 (quint, 7.5 Hz, 2H). $^{13}\text{C-NMR}$ (75 MHz, MeOD, 25°C, TMS) δ (ppm) 171.2, 157.1, 137.8, 133.5, 129.7, 129.1, 129.0, 128.8, 127.4, 125.0, 109.6, 66.2, 61.2, 53.9, 38.2, 25.0.

6-hydroxy-7-(hydroxymethyl)-2-naphthoic acid (173): white solid (yield = 68%) mp = °C. $^1\text{H-NMR}$ (300 MHz, MeOD, 25°C, TMS) δ (ppm) 8.50 (s, 1H), 7.95–7.88 (m, 2H), 7.67 (d, J = 8.6 Hz, 1H), 7.15 (s, 1H), 4.81 (s, 2H). $^{13}\text{C-NMR}$ (75 MHz, MeOD, 25°C, TMS) δ (ppm) 169.3, 157.8, 134.2, 130.1, 129.5, 127.8, 127.6, 126.1, 125.4, 124.6, 107.8, 58.9.

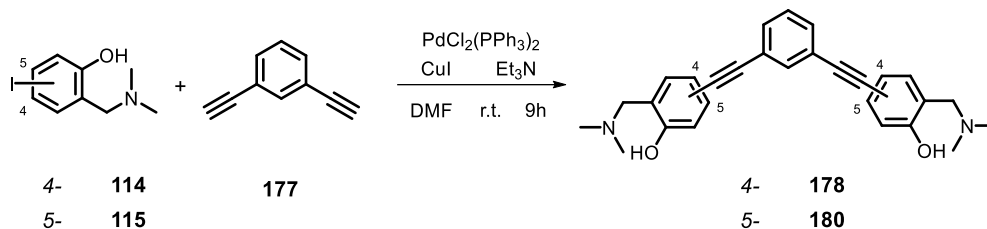
6-hydroxy-7-(hydroxymethyl)-2-naphthaldehyde (174): white solid (yield = 32% from **114**, 95% from **115**) mp = °C. $^1\text{H-NMR}$ (300 MHz, DMSO- d_6 + DCI in D_2O , 25°C, TMS) δ (ppm) 9.95 (s, 1H), 8.38 (s, 1H), 7.98 (s, 1H), 7.74 (s, 2H), 7.21 (s, 1H), 4.63 (s, 2H). $^{13}\text{C-NMR}$ (75 MHz, DMSO- d_6 + DCI in D_2O , 25°C, TMS) δ (ppm) 194.6, 157.0, 138.1, 136.0, 133.4, 132.3, 128.9, 127.8, 127.7, 123.3, 109.6, 59.4.

(6-hydroxy-7-(hydroxymethyl)naphthalen-2-yl)boronic acid (175): white solid (yield = 79%) mp = °C. $^1\text{H-NMR}$ (300 MHz, DMSO- d_6 , 25°C, TMS) δ (ppm) 10.18 (bs, 1H), 8.18 (s, 1H), 8.02 (s, 1H), 7.89 (d, J = 8.3 Hz, 1H), 7.75 (d, J = 8.3 Hz, 1H), 7.38 (s, 1H), 5.38 (bs, 1H), 4.93 (s, 2H). $^{13}\text{C-NMR}$ (75 MHz, DMSO- d_6 , 25°C, TMS) δ (ppm) 154.6, 136.1, 135.2, 133.7, 131.9, 128.7, 126.7, 124.5, 119.3, 109.0, 59.8.

3-(hydroxymethyl)-6-(3-(pyridin-2-yl)-1,2,4-oxadiazol-5-yl)naphthalen-2-ol (176): white solid (yield = 59% from **127**, 88% from **128**) mp = °C. $^1\text{H-NMR}$ (300 MHz, DMSO- d_6 , 25°C, TMS) δ (ppm) 10.58 (s, 1H), 8.91 (d, J = 4.5 Hz, 1H), 8.83 (s, 1H), 8.31 (d, J = 7.9 Hz, 1H), 8.20–8.14 (m, 3H), 8.02 (d, J = 8.9 Hz, 1H), 7.75 (t, J = 5.8 Hz, 1H), 7.34 (s, 1H), 5.41 (d, J = 5.5 Hz, 1H), 4.76 (d, J = 4.9 Hz, 2H). $^{13}\text{C-NMR}$ (75 MHz, DMSO- d_6 , 25°C, TMS) δ (ppm) 182.1, 168.3, 155.9, 150.3, 146.9, 137.7, 135.8, 133.8, 128.7, 127.0, 126.9, 126.5, 126.2, 125.8, 123.4, 123.2, 108.2, 58.4.

4.2.5 Synthesis of QMPs for G4 binding

- Synthesis of V-shaped 4- and 5- arylethynyl benzo- Mannich bases (**178** and **180**)



The corresponding aryl iodide **114** or **115** (0.300 g, 1.08 mmol), $\text{PdCl}_2(\text{PPh}_3)_2$ (76 mg, 10 mol %), and copper (I) iodide (41 mg, 20 mol %) were dissolved in dry DMF (15 mL). After 5 minutes of bubbling with argon, a solution of 1,3-diethynylbenzene (72 μL , 0.54 mmol) in neat triethylamine (1.5 mL, 10.8 mmol) was added with a syringe under Ar atmosphere, and the mixture was stirred at room temperature for 9 hours. The solvent was then removed under reduced pressure. The residue was dissolved in DCM (50 mL) and washed with 1% NaHCO_3 (3x30 mL). The organic phase was dried over Na_2SO_4 and the solvent was removed under reduced pressure. The crude was purified by reverse phase HPLC (H_2O 0.1% TFA/ACN gradient). The aqueous phase was neutralized with NaHCO_3 , extracted in DCM (3x10 mL), the combined organic phases were dried over Na_2SO_4 , and the solvent was removed under reduced pressure.

TLC (AcOEt/MeOH 8:2) R_f 0.20.

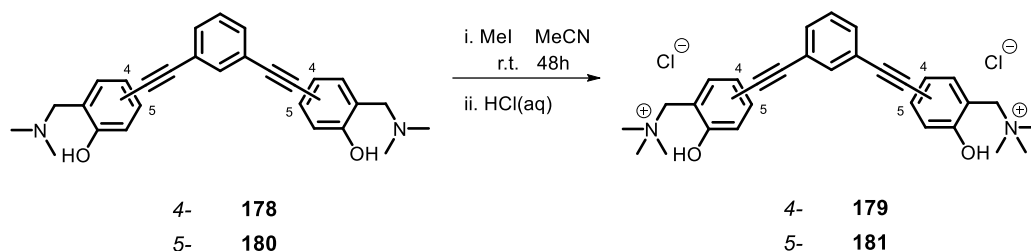
4,4'-(1,3-phenylenebis(ethyne-2,1-diyl))bis(2-((dimethylamino)methyl)phenol) (**178**):

white solid (yield = 38%); mp = $^{\circ}\text{C}$. $^1\text{H-NMR}$ (300 MHz, CDCl_3 , 25°C , TMS) δ (ppm) 10.28 (bs, 2H), 7.65 (s, 1H), 7.45–7.28 (m, 5H), 7.19 (d, $J = 1.7$ Hz, 2H), 6.84 (d, $J = 8.4$ Hz, 2H), 3.66 (s, 4H), 2.36 (s, 12H). $^{13}\text{C-NMR}$ (75 MHz, CDCl_3 , 25°C , TMS) δ (ppm) 158.7, 134.0, 132.4, 131.7, 130.5, 128.3, 123.9, 121.9, 116.3, 113.1, 90.1, 86.8, 62.3, 44.3.

5,5'-(1,3-phenylenebis(ethyne-2,1-diyl))bis(2-((dimethylamino)methyl)phenol) (**180**):

white solid (yield = 25%); mp = $^{\circ}\text{C}$. $^1\text{H-NMR}$ (300 MHz, CDCl_3 , 25°C , TMS) δ (ppm) 8.64 (bs, 2H), 7.71 (s, 1H), 7.49 (d, $J = 7.8$ Hz, 2H), 7.34 (t, $J = 7.3$ Hz, 1H), 7.02–6.96 (m, 6H), 3.67 (s, 4H), 2.35 (s, 12H). $^{13}\text{C-NMR}$ (75 MHz, CDCl_3 , 25°C , TMS) δ (ppm) 159.7, 136.3, 132.9, 130.1, 130.0, 125.4, 124.9, 124.5, 124.3, 120.7, 91.7, 89.9, 64.4, 46.2.

- Synthesis of V-shaped 4- and 5- arylethynyl benzo- ammonium salts (**179** and **181**)



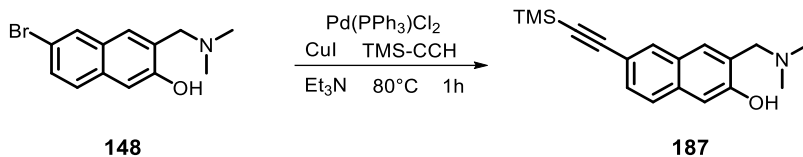
Iodomethane (11 μ L, 0.17 mmol) was added to a stirred solution of the corresponding Mannich base (10 mg, 0.029 mmol) in ACN (10 mL) and the reaction mixture was stirred at room temperature for 48 hours. The solvent and excess iodomethane were removed under reduced pressure. The product was purified by reverse phase HPLC (H_2O 0.1% TFA/ACN gradient) and the anion was exchanged with 1% HCl (1 mL).

TLC ($CHCl_3/MeOH$ 8:2) R_f 0.25 (reagent) 0.05 – 0 (product)

1,1'-((1,3-phenylenebis(ethyne-2,1-diyl))bis(6-hydroxy-3,1-phenylene))bis(N,N,N-trimethylmethanaminium) chloride (179**):** white solid (yield = 97%); mp = °C. **1H -NMR** (300 MHz, $CDCl_3$, 25°C, TMS) δ (ppm) 10.28 (bs, 2H), 7.65 (s, 1H), 7.45–7.28 (m, 5H), 7.19 (d, J = 1.7 Hz, 2H), 6.84 (d, J = 8.4 Hz, 2H), 3.66 (s, 4H), 2.36 (s, 12H). **^{13}C -NMR** (75 MHz, $CDCl_3$, 25°C, TMS) δ (ppm) 158.7, 134.0, 132.4, 131.7, 130.5, 128.3, 123.9, 121.9, 116.3, 113.1, 90.1, 86.8, 62.3, 44.3.

1,1'-((1,3-phenylenebis(ethyne-2,1-diyl))bis(2-hydroxy-4,1-phenylene))bis(N,N,N-trimethylmethanaminium) chloride (181**):** white solid (yield = 99%); mp = °C. **1H -NMR** (300 MHz, $CDCl_3$, 25°C, TMS) δ (ppm) 8.64 (bs, 2H), 7.71 (s, 1H), 7.49 (d, J = 7.8 Hz, 2H), 7.34 (t, J = 7.3 Hz, 1H), 7.02–6.96 (m, 6H), 3.67 (s, 4H), 2.35 (s, 12H). **^{13}C -NMR** (75 MHz, $CDCl_3$, 25°C, TMS) δ (ppm) 159.7, 136.3, 132.9, 130.1, 130.0, 125.4, 124.9, 124.5, 124.3, 120.7, 91.7, 89.9, 64.4, 46.2.

- **Synthesis of 3-((dimethylamino)methyl)-6-((trimethylsilyl)ethynyl)naphthalen-2-ol (187)**

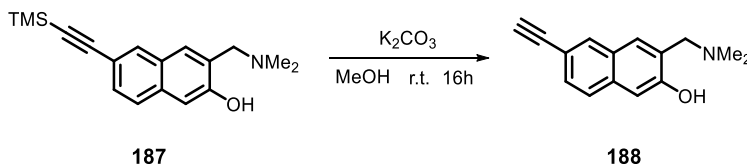


6-bromo-3-((dimethylamino)methyl)naphthalen-2-ol **148** (500 mg, 1.78 mmol), PdCl₂(PPh₃)₂ (50 mg, 4% mol), copper (I) iodide (13.6 mg, 4% mol) were added into a three necked round-bottomed flask equipped with a condenser and a magnetic stirrer and kept under Ar atmosphere. Trimethylsilylacetylene (378 μL, 2.68 mmol) was dissolved in triethylamine (20 mL), degassed with Ar for 5 minutes, and added in the reaction flask. The reaction mixture was stirred at 80°C for 1 hour. The mixture was filtered through a thin pad of celite, washed with chloroform (3x20 mL), and the solvent was removed under reduced pressure. The crude was purified by flash chromatography (cyclohexane/AcOEt gradient)

TLC (CHCl₃/MeOH 9:1) R_f 0.75 (reagent), 0.69 (product).

3-((dimethylamino)methyl)-6-((trimethylsilyl)ethynyl)naphthalen-2-ol (187): white solid (yield = 86%); mp = 123–125°C. ¹H-NMR (200 MHz, CDCl₃, 25°C, TMS) δ (ppm) 7.86 (s, 1H), 7.60 (d, J = 8.5 Hz, 1H), 7.46–7.39 (m, 2H), 7.16 (s, 1H), 3.83 (s, 2H), 2.40 (s, 6H), 0.30 (s, 9H). ¹³C-NMR (75 MHz, CDCl₃, 25°C, TMS) δ (ppm) 157.0, 134.1, 131.4, 128.7, 127.3, 127.2, 126.0, 125.2, 117.3, 110.3, 105.9, 93.2, 62.7, 44.3, 0.0.

- **Synthesis of 3-((Dimethylamino)methyl)-6-ethynynaphthalen-2-ol (188)**



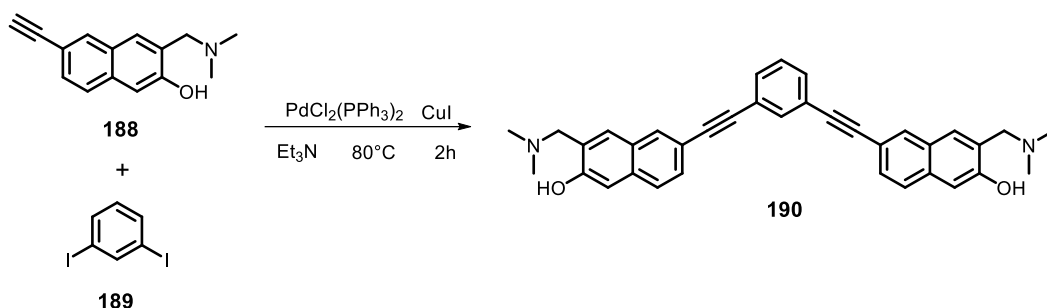
3-((dimethylamino)methyl)-6-((trimethylsilyl)ethynyl)naphthalen-2-ol **187** (400 mg, 1.34 mmol) was dissolved in methanol (25 mL) and potassium carbonate (204 mg, 1.608 mmol) was added in one portion. The suspension was stirred at room temperature for 16 hours. The solvent was removed under reduced pressure, the crude was added with 1% HCl (10 mL) and neutralized with NaHCO₃. The product was extracted in DCM (3x20 mL), the combined

organic phases were dried over Na_2SO_4 and the solvent was removed under reduced pressure. The crude was purified by flash chromatography (cyclohexane/AcOEt gradient).

TLC ($\text{CHCl}_3/\text{MeOH}$ 9:1) R_f 0.69 (same for reagent and product).

3-((Dimethylamino)methyl)-6-ethynynaphthalen-2-ol (188**):** white solid (yield = 59%); mp = 153–155°C. $^1\text{H-NMR}$ (200 MHz, CDCl_3 , 25°C, TMS) δ (ppm) 9.85 (bs, 1H), 7.88 (s, 1H), 7.63 (d, $J = 8.5$ Hz, 1H), 7.45 (d, $J = 7.8$, 1H), 7.44 (s, 1H), 7.17 (s, 1H), 3.82 (s, 2H), 3.11 (s, 1H), 2.38 (s, 6H). $^{13}\text{C-NMR}$ (75 MHz, CDCl_3 , 25°C, TMS) δ (ppm) 156.9, 133.9, 131.3, 128.3, 128.0, 126.9, 125.8, 125.1, 115.8, 109.9, 84.0, 76.0, 62.5, 44.0.

- **Synthesis of 6,6'-(1,3-phenylenebis(ethyne-2,1-diyl))bis(3-((dimethylamino)methyl)naphthalen-2-ol) (**190**)**

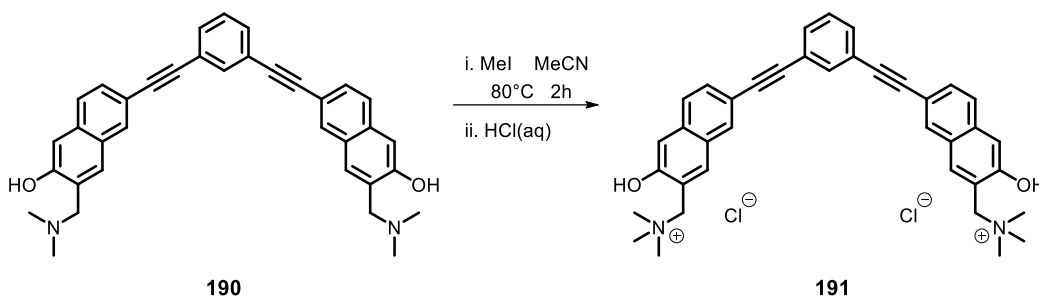


1,3-diiodobenzene **189** (73 mg, 0.22 mmol), $\text{PdCl}_2(\text{PPh}_3)_2$ (12.4 mg, 4% mol), copper (I) iodide (3.4 mg, 4% mol) were added into a three necked round-bottomed flask equipped with a condenser and a magnetic stirrer and kept under Ar atmosphere. 3-((dimethylamino)methyl)-6-ethynynaphthalen-2-ol **188** (100 mg, 0.44 mmol) was dissolved in triethylamine (10 mL), degassed with Ar for 5 minutes and added in the reaction flask. The reaction mixture was stirred at 80°C for 2 hours. The residue was dissolved in DCM (25 mL) and washed with 1% NaHCO_3 (3x20 mL). The organic phase was dried over Na_2SO_4 and the solvent was removed under reduced pressure. The crude was purified by reverse phase HPLC (H_2O 0.1% TFA/ACN gradient). The aqueous (H_2O) phase was neutralized with NaHCO_3 , extracted in DCM (3x10 mL), the combined organic phases were dried over Na_2SO_4 , and the solvent was removed under reduced pressure.

TLC ($\text{CHCl}_3/\text{MeOH}$ 95:5) R_f 0.54 (reagent), 0.44 (product).

6,6'-(1,3-phenylenebis(ethyne-2,1-diyl))bis(3-((dimethylamino)methyl)naphthalen-2-ol) (190): white solid (yield = 81%); mp = °C. ¹H-NMR (300 MHz, DMSO-d₆, 25°C, TMS) δ (ppm) 8.06 (s, 2H), 7.77–7.74 (m, 5H), 7.62 (d, J = 7.2 Hz, 2H), 7.53–7.49 (m, 3H), 7.19 (s, 2H), 3.89 (s, 4H), 2.39 (s, 12H). ¹³C-NMR (75 MHz, DMSO-d₆, 25°C, TMS) δ (ppm) 156.6, 133.8, 133.7, 131.2, 131.1, 129.4, 128.7, 128.2, 127.0, 126.3, 125.9, 123.2, 116.0, 109.2, 91.0, 87.8, 59.6, 44.0.

- **Synthesis of 1,1'-((1,3-phenylenebis(ethyne-2,1-diyl))bis(3-hydroxynaphthalene-7,2-diyl))bis(N,N,N-trimethylmethanaminium) chloride (191)**

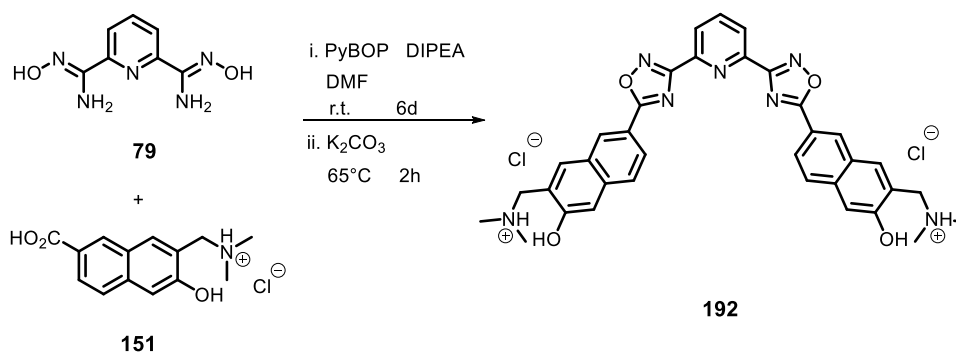


Iodomethane (268 μL, 4.3 mmol) was added to a stirred solution of the Mannich base **190** (94 mg, 0.18 mmol) in ACN (10 mL) and the reaction mixture was stirred at reflux for 2 hours. After cooling at room temperature, sodium acetate (14.8 mg, 0.18 mmol) was added in one portion, followed by further iodomethane (67 μL, 1.08 mmol), and the suspension was stirred at room temperature for additional 16 hours. Hence, the solvent and excess iodomethane were removed under reduced pressure. The product was purified by reverse phase HPLC (H₂O 0.1% TFA/ACN gradient) and the anion was exchanged with 1% HCl (1 mL).

TLC (CHCl₃/MeOH 95:5) R_f 0.44 (reagent) 0.05 – 0 (product)

1,1'-((1,3-phenylenebis(ethyne-2,1-diyl))bis(3-hydroxynaphthalene-7,2-diyl))bis(N,N,N-trimethylmethanaminium) chloride (191): white solid (yield = 68%); mp = °C. ¹H-NMR (300 MHz, MeOD, 25°C, TMS) δ (ppm) 8.06 (s, 4H), 7.73–7.69 (m, 3H), 7.59–7.52 (m, 4H), 7.41 (dd, J = 8.3, 7.0 Hz, 1H), 7.33 (s, 2H), 4.72 (s, 4H), 3.21 (s, 18H). ¹³C-NMR (75 MHz, MeOD, 25°C, TMS) δ (ppm) 156.7, 137.4, 137.0, 135.5, 133.3, 132.7, 131.6, 130.3, 129.0, 127.7, 125.4, 119.7, 119.6, 111.6, 91.5, 89.7, 65.6, 53.9.

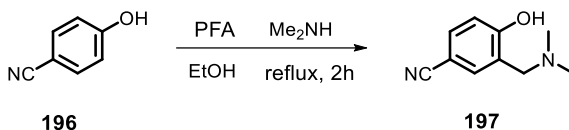
- **Synthesis of 1,1'-((pyridine-2,6-diylbis(1,2,4-oxadiazole-3,5-diyl))bis(3-hydroxynaphthalene-7,2-diyl))bis(N,N-dimethylmethanaminium) chloride (192)**



1-(7-carboxy-3-hydroxynaphthalen-2-yl)-N,N-dimethylmethanaminium chloride **151** (100 mg, 0.35 mmol) and diisopropyl-ethyl-amine (124 μ L, 0.71 mmol) were dissolved in dry DMF (5 mL). PyBOP (185 mg, 0.35 mmol) was added in one portion to the stirred solution and, after 1 hour, N',N'6-dihydroxypyridine-2,6-bis(carboximidamide) **79** (35 mg, 0.18 mmol) was added. The reaction mixture was stirred at room temperature for 6 days. The formation of a major peak was monitored by reverse phase HPLC (H₂O 0.1% TFA/ACN gradient). Ring closure was obtained by addition of anhydrous K₂CO₃ and heating the suspension at 65°C for 2 hours. The solvent was removed under reduced pressure and the crude was purified by reverse phase HPLC (H₂O 0.1% TFA/ACN gradient) and the anion was exchanged with 1% HCl (1 mL).

1,1'-((pyridine-2,6-diylbis(1,2,4-oxadiazole-3,5-diyl))bis(3-hydroxynaphthalene-7,2-diyl))bis(N,N-dimethylmethanaminium) chloride (192): pale yellow solid (yield = 34%); mp = °C. ¹H-NMR (300 MHz, CDCl₃, 25°C, TMS) δ (ppm) 8.72 (s, 2H), 8.40 (d, J = 7.8 Hz, 2H), 8.22 (dd, J = 8.6, 1.2 Hz, 2H), 8.11 (t, J = 7.8 Hz, 1H), 7.84 (d, J = 8.7 Hz, 2H), 7.67 (s, 2H), 7.25 (s, 2H), 3.90 (s, 4H), 2.42 (s, 12H). ¹³C-NMR (75 MHz, CDCl₃, 25°C, TMS) δ (ppm) 176.7, 167.8, 158.6, 146.9, 137.8, 136.5, 128.9, 128.4, 126.7, 126.6, 125.7, 124.5, 123.8, 117.8, 110.1, 62.4, 44.0. ESI-MS 614.5 (M+1), 636.4 (M+Na), 652.6 (M+1).

- **Synthesis of 3-((dimethylamino)methyl)-4-hydroxybenzonitrile (197)**

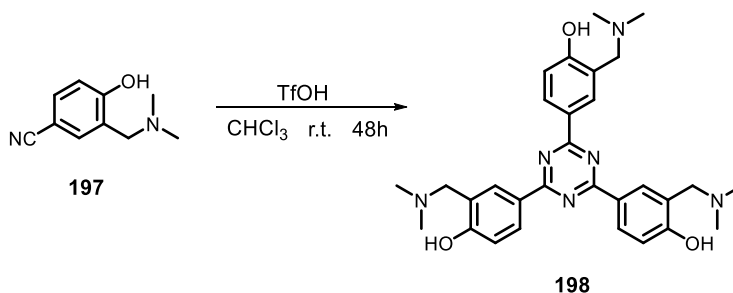


4-hydroxybenzonitrile (500 mg, 4.2 mmol) was dissolved in absolute ethanol (10 mL). Paraformaldehyde (1.30 g, 42 mmol) and 33% solution of dimethylamine in ethanol (2.2 mL, 12.9 mmol) were added under stirring. The mixture was heated to reflux under a nitrogen atmosphere for 2 hours. The solution was cooled to room temperature and the solvent removed under reduced pressure. The residue was dissolved in AcOEt (50 mL) and washed with an acidic aqueous solution (HCl 1%, 3x50 mL) to selectively extract the Mannich base product. The aqueous phases were collected and neutralized with solid NaHCO₃ and extracted with AcOEt (3x25 mL). The combined organic phases were dried over Na₂SO₄, and the solvent was removed under reduced pressure. The crude was purified by flash chromatography (CHCl₃/MeOH gradient).

TLC (CHCl₃/MeOH 8:2) R_f 0.39.

3-((dimethylamino)methyl)-4-hydroxybenzonitrile (197): white solid (yield = 50%); mp = .
¹H-NMR (200 MHz, CDCl₃, 25°C, TMS) δ (ppm) 9.35 (bs, 1H), 7.46 (dd, J = 8.5, 1.6 Hz, 1H), 7.27 (d, J = 1.7 Hz, 1H), 6.84 (d, J = 8.5 Hz, 1H), 3.68 (s, 2H), 2.36 (s, 6H).

- **Synthesis of 4,4',4''-(1,3,5-Triazine-2,4,6-triyl)tris(2-((dimethylamino)methyl)phenol) (198)**



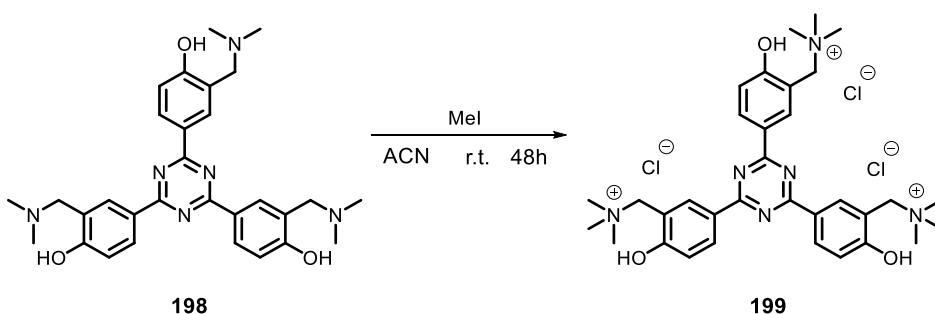
3-((dimethylamino)methyl)-4-hydroxybenzonitrile **197** (250 mg, 1.42 mmol) was dissolved in ice-cooled anhydrous chloroform (5 mL). Triflic acid (1.0 mL, 11.3 mmol) was added dropwise

and the reaction mixture was stirred for 30 min at 0°C. The ice bath was then removed and the mixture was stirred for additional 48 hours at room temperature. Hence, the solution was poured into ice, neutralized with NaHCO₃, extracted with DCM (3x20 mL) and dried over Na₂SO₄. The solvent was removed at the rotary evaporator and the crude was purified by reverse phase HPLC (H₂O 0.1% TFA/ACN gradient). The aqueous phase was neutralized with NaHCO₃, extracted in DCM (3x10 mL), the combined organic phases were dried over Na₂SO₄, and the solvent was removed under reduced pressure.

TLC (CHCl₃/MeOH 8:2) R_f 0.72 (reagent), 0.48 (product).

4,4',4''-(1,3,5-Triazine-2,4,6-triyl)tris(2-((dimethylamino)methyl)phenol) (198): yellow solid (yield = 83%); mp = . ¹H-NMR (300 MHz, MeOD, 25°C, TMS) δ (ppm) 8.69 (d, J = 8.5 Hz, 3H), 8.66 (d, J = 1.6 Hz, 3H), 7.04 (dd, J = 8.6 Hz, 1.7 Hz, 3H), 4.39 (s, 6H), 2.83 (s, 18H). ¹³C-NMR (75 MHz, MeOD, 25°C, TMS) δ (ppm) 172.2, 162.4, 135.0, 134.4, 129.7, 118.7, 117.0, 58.5, 43.7.

- **Synthesis of 1,1',1''-((1,3,5-triazine-2,4,6-triyl)tris(6-hydroxybenzene-3,1-diyl))tris(N,N,N-trimethylmethanaminium) chloride (199)**



Iodomethane (167 μL, 2.7 mmol) was added to a stirred solution of 4,4',4''-(1,3,5-Triazine-2,4,6-triyl)tris(2-((dimethylamino)methyl)phenol) **198** (158 mg, 0.30 mmol) in ACN (5 mL) and the reaction mixture was stirred at room temperature for 48 hours. The solvent and excess iodomethane were removed under reduced pressure. The product was purified by reverse phase HPLC (H₂O 0.1% TFA/ACN gradient) and the anion was exchanged with 1% HCl (5 mL).

TLC (CHCl₃/MeOH 8:2) R_f 0.48 (reagent), 0.05–0 (product).

1,1',1''-((1,3,5-triazine-2,4,6-triyl)tris(6-hydroxybenzene-3,1-diyl))tris(N,N,N-trimethylmethanaminium) chloride (199): yellow solid (yield = 67%); mp = . ¹H-NMR (300 MHz, MeOD, 25°C, TMS) δ (ppm) 9.01 (s, 3H), 8.81 (d, J = 8.4 Hz, 3H), 7.15 (d, J = 8.5 Hz, 3H), 4.94 (s, 6H), 3.28 (s, 27H). ¹³C-NMR (75 MHz, MeOD, 25°C, TMS) δ (ppm) 165.0, 148.3, 142.4, 137.2, 130.4, 124.5, 81.9, 78.4, 52.9

Appendix A – DNA sequences

G4-folding sequences

22AG	5'-A- GGG -TTA- GGG -TTA- GGG -TTA- GGG -3'
hTel21	5'- GGG -TTA- GGG -TTA- GGG -TTA- GGG -3'
21CTA	5'- GGG -CTA- GGG -CTA- GGG -CTA- GGG -3'
Pu24T	5'-TGA- GGG - TGG -TGA- GGG - TGG -GGA- AGG -3'
Myc	5'-TGA- GGG - TGG -GTA- GGG - TGG -GTA-A-3'
c-Kit2	5'- GGG - CGG - GCG -CGA- GGG - AGG -GG-3'
LTRIII	5'- GGG -AGG-CGT-GGC-CTG- GGC - GGG -ACT- GGG -G-3'

Self-complementary duplex and hairpin-folding sequence

ds26	5'-CAA-TCG-GAT-CGA-ATT-CGA-TCC-GAT-TG-3'
-------------	--

Labelled sequences for FRET-melting assays

F21T	5'-Fam- GGG -TTA- GGG -TTA- GGG -TTA- GGG -Tamra-3'
F(21CTA)T	5'-Fam- GGG -CTA- GGG -CTA- GGG -CTA- GGG -Tamra-3'
F(Pu24T)T	5'-Fam-TGA- GGG - TGG -TGA- GGG - TGG -GGA- AGG -Tamra-3'
F(c-Myc)T	5'-Fam-TTG-A GG -GTG- GGT -A GG -GTG- GGT -AA-Tamra-3'
F(c-Kit2)T	5'-Fam- GGG - CGG - GCG -CGA- GGG - AGG -GG-Tamra-3'
F(Bcl2)T	5'-Fam-AG GG - GGC - GGG -CGC-GGC-AGG-AAG- GGG - GCG - GGA -Tamra-3'
F(CEB25wt)T	5'-Fam-AAG- GGT - GGG -TGT-AAG-TGT- GGG - TGG -GT-Tamra-3'
F(LTRIII)T	5'-Fam- GGG -AGG-CGT-GGC-CTG- GGC - GGG -ACT- GGG -G-Tamra-3'
F(LTRIV)T	5'-Fam-T GG - GCG - GGA -CTG- GGG -AGT- GGT -Tamra-3'
F(ds26)T	5'-Fam-CAA-TCG-GAT-CGA-ATT-CGA-TCC-GAT-TG-Tamra-3'

Appendix B – Fitting Equations

Monoacid pKa measurement (UV-vis titration)

$$y = A1 \frac{10^{(pKa-x)}}{1 + 10^{(pKa-x)}} + A2 \frac{1}{1 + 10^{(pKa-x)}}$$

y	Solution molar absorptivity
x	pH
A1	Conjugated acid molar absorptivity
A2	Conjugated base molar absorptivity
Ka	Acidity constant

Diacid pKas measurements (UV-vis titration)

$$y = A1 \frac{10^{(pKa_1+pKa_2-2x)}}{1 + 10^{(pKa_2-x)} + 10^{(pKa_1+pKa_2-2x)}} + A2 \frac{10^{(pKa_2-x)}}{1 + 10^{(pKa_2-x)} + 10^{(pKa_1+pKa_2-2x)}} + A3 \frac{1}{1 + 10^{(pKa_2-x)} + 10^{(pKa_1+pKa_2-2x)}}$$

y	Solution molar absorptivity
x	pH
A1	Diacid molar absorptivity (H ₂ A)
A2	Monoacid molar absorptivity (HA ⁻)
A3	Base molar absorptivity (A ²⁻)
Ka ₁	First acidity constant
Ka ₂	Second acidity constant

Dose-Response Sigmoid (FRET-melting)

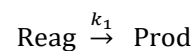
$$y = A1 + \frac{A2 - A1}{1 + 10^{(LOGx0-x)p}}$$

y	Signal (FAM fluorescence)
x	Temperature
A1	Bottom asymptote
A2	Top asymptote
LOGx0	Center (T _m)
p	Hill slope

Biphasic Dose-Response Sigmoid (FRET-melting)

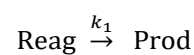
$$y = A1 + (A2 - A1) \left[\frac{p}{1 + 10^{(LOGx01-x)h1}} + \frac{1-p}{1 + 10^{(LOGx02-x)h2}} \right]$$

y	Signal (FAM fluorescence)
x	Temperature
A1	Bottom asymptote
A2	Top asymptote
LOGx01	First EC50
LOGx02	Second EC50 (T _m)
h1	First hill slope
h2	Second hill slope
p	Proportion

1st Order Kinetics – Reagent depletion

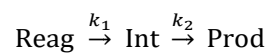
$$y = Ae^{-kx}$$

y	Signal
x	Time
A	Initial signal
k	Rate constant

1st Order Kinetics – Product formation

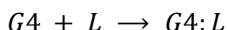
$$y = b + A(1 - e^{-kx})$$

y	Signal
x	Time
b	Ordinates intercept
A	Signal/Concentration ratio
k	Rate constant

1st Order Kinetics – Intermediate in consecutive reactions

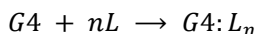
$$y = A \frac{k_1}{k_2 - k_1} (e^{-k_1x} - e^{-k_2x})$$

y	Signal
x	Time
A	Signal/Concentration ratio
k ₁	Rate constant of formation
k ₂	Rate constant of depletion

Complex formation – 1:1 stoichiometry (titration of ligand with G4)

$$y = b \left[\varepsilon_f \left(L_t - \frac{KL_t + Kx + 1 - \sqrt{(KL_t + Kx + 1)^2 - 4K^2 L_t x}}{2K} \right) + \varepsilon_b \frac{KL_t + Kx + 1 - \sqrt{(KL_t + Kx + 1)^2 - 4K^2 L_t x}}{2K} \right]$$

- y Absorbance
 x Total DNA molar concentration
 K Binding constant
 ε_f Molar absorptivity of free ligand
 ε_b Molar absorptivity of bound ligand
 b Optical path length (fixed)
 L_t Ligand total concentration (fixed)

Complex formation – general stoichiometry (titration of ligand with G4)

$$K_1 = \frac{[G4:L]}{[G4][L]} \quad K_2 = \frac{[G4:L_2]}{[G4:L][L]} \quad K_n = \frac{[G4:L_n]}{[G4:L_{n-1}][L]}$$

The n different equilibria are treated like a single equilibrium in which the ligand L can interact with n different independent binding sites, all exhibiting the same affinity and binding constant K.



$$y = \frac{\Delta\varepsilon \cdot L_t}{2} \left(A + xn + 1 - \sqrt{(A + xn + 1)^2 - 4xn} \right)$$

- y Absorbance enhancement $\Delta Abs = Abs - Abs_0$
 x DNA equivalents (with respect to ligand) C_{G4}/L_t
 L_t Ligand total concentration (fixed)
 $\Delta\varepsilon$ Instrumental response $\varepsilon_b - \varepsilon_f$
 A $1/(K \cdot L_t)$ where K is the mean binding constant
 n Number of independent binding sites per quadruplex

The model assumes that $K_{ij} = \frac{[G4:L_i]_j}{[G4:L_{i-1}]_{\neq j}[L]}$, which corresponds to the interaction of the ligand with binding sites $j = a, b, \dots, n$, has the same value:

for each $i = 1, 2, \dots, n$ (independent binding sites)

for each $j = a, b, \dots, n$ (same affinity = same energy of interaction for each binding site)

If such conditions are satisfied:

$$K_1 = \frac{[G4:L]_a + [G4:L]_b + \dots + [G4:L]_n}{[G4][L]} = K_{1a} + K_{1b} + \dots + K_{1n} = nK_{ij}$$

Demonstration that, in the simplified model, $K = K_{ij}$

Expressing the thermodynamic constants K_i in function of K_{ij} :

$$K_1 = \frac{[G4:L]_a + [G4:L]_b + \dots + [G4:L]_n}{[G4][L]} = K_{1a} + K_{1b} + \dots + K_{1n} = nK_{ij}$$

$$K_2 = \frac{[G4:L_2]_{ab} + [G4:L_2]_{ac} + \dots + [G4:L_2]_{an} + \dots + [G4:L_2]_{nn}}{([G4:L]_a + [G4:L]_b + \dots + [G4:L]_n)[L]} = \frac{n(n-1)}{2} \frac{[G4:L_2]_{ab}}{n[G4:L]_a[L]} = \frac{(n-1)}{2} K_{ij}$$

more in general,

$$K_i = \frac{\binom{n}{i}}{\binom{n}{i-1}} K_{ij} = \frac{n!}{(n-i)! i!} \frac{(n-i+1)! (i-1)!}{n!} K_{ij} = \frac{n-i+1}{i} K_{ij}$$

from which

$$K_i = \frac{n-i+1}{n-i} K_1 \quad (1)$$

Unrolling the equation which defines K :

$$\begin{aligned} K &= \frac{[G4_{1/n}:L]}{[G4_{1/n}][L]} = \frac{[G4:L] + 2[G4:L_2] + 3[G4:L_3] + \dots + n[G4:L_n]}{n[G4] + (n-1)[G4:L] + (n-2)[G4:L_2] + \dots + [G4:L_{n-1}]} \cdot \frac{1}{[L]} = \\ &= \frac{[G4:L] + 2[G4:L_2] + 3[G4:L_3] + \dots + n[G4:L_n]}{n[G4] + (n-1)K_1[G4][L] + (n-2)K_1K_2[G4][L]^2 + \dots + K_1K_2 \dots K_{n-1}[G4][L]^{n-1}} \cdot \frac{1}{[L]} = \\ &= \frac{[G4:L] + 2[G4:L_2] + 3[G4:L_3] + \dots + n[G4:L_n]}{[G4][L]} \cdot \frac{1}{n + (n-1)K_1[L] + (n-2)K_2K_1[L]^2 + \dots + K_{n-1} \dots K_2K_1[L]^{n-1}} \\ &= \frac{K_1 + 2K_2K_1[L] + 3K_3K_2K_1[L]^2 \dots + nK_nK_{n-1} \dots K_3K_2K_1[L]^{n-1}}{n + (n-1)K_1[L] + (n-2)K_2K_1[L]^2 + \dots + K_{n-1} \dots K_3K_2K_1[L]^{n-1}} \end{aligned}$$

and, following equation (1)

$$\begin{aligned} &= \frac{K_1 + 2 \frac{(n-1)}{2n} K_1 K_1 [L] + 3 \frac{(n-2)}{3n} K_1 \frac{(n-1)}{2n} K_1 K_1 [L]^2 \dots + n \frac{1}{n^2} K_1 \frac{2}{(n-1)n} K_1 \dots \frac{(n-2)}{3n} K_1 \frac{(n-1)}{2n} K_1 K_1 [L]^{n-1}}{n + (n-1)K_1[L] + (n-2) \frac{(n-1)}{2n} K_1 K_1 [L]^2 + \dots + \frac{2}{(n-1)n} K_1 \dots \frac{(n-2)}{3n} K_1 \frac{(n-1)}{2n} K_1 K_1 [L]^{n-1}} \\ &= \frac{K_1 \left(1 + \frac{(n-1)}{n} K_1 [L] + \frac{(n-2)(n-1)}{n} \frac{(n-1)}{2n} K_1^2 [L]^2 + \dots + \frac{1}{n} \frac{2}{(n-1)n} \dots \frac{(n-2)(n-1)}{3n} \frac{(n-1)}{2n} K_1^{n-1} [L]^{n-1} \right)}{n \left(1 + \frac{(n-1)}{n} K_1 [L] + \frac{(n-2)(n-1)}{n} \frac{(n-1)}{2n} K_1^2 [L]^2 + \dots + \frac{1}{n} \frac{2}{(n-1)n} \dots \frac{(n-2)(n-1)}{3n} \frac{(n-1)}{2n} K_1^{n-1} [L]^{n-1} \right)} \end{aligned}$$

In conclusion:

$$K = \frac{1}{n} K_1 = K_{ij}$$

Bibliography

- [1] Kaushik, M., Kaushik, S., Roy, K., Singh, A., Mahendru, S., Kumar, M., Chaudhary, S., Ahmed, S., and Kukreti, S., *Biochem Biophys Rep* (2016) 5, 388-395.
- [2] Neidle, S., *Curr Opin Struct Biol* (2009) 19, 239-250.
- [3] Rhodes, D., and Lipps, H. J., *Nucleic Acids Res* (2015) 43, 8627-8637.
- [4] Largy, E., Mergny, J.-L., and Gabelica, V. (2016) "Role of Alkali Metal Ions in G-Quadruplex Nucleic Acid Structure and Stability", In *The Alkali Metal Ions: Their Role for Life* (Sigel, A., Sigel, H., and Sigel, R. K. O., Eds.), pp 203-258, Springer International Publishing, Cham.
- [5] Bhattacharyya, D., Mirihana Arachchilage, G., and Basu, S., *Front Chem* (2016) 4, 38.
- [6] König, S. L., Evans, A. C., and Huppert, J. L., *Biomol Concepts* (2010) 1, 197-213.
- [7] Huppert, J. L., and Balasubramanian, S., *Nucleic Acids Res* (2005) 33, 2908-2916.
- [8] Todd, A. K., Johnston, M., and Neidle, S., *Nucleic Acids Res* (2005) 33, 2901-2907.
- [9] Chambers, V. S., Marsico, G., Boutell, J. M., Di Antonio, M., Smith, G. P., and Balasubramanian, S., *Nat Biotechnol* (2015) 33, 877-881.
- [10] Bedrat, A., Lacroix, L., and Mergny, J. L., *Nucleic Acids Res* (2016) 44, 1746-1759.
- [11] Scaria, V., Hariharan, M., Arora, A., and Maiti, S., *Nucleic Acids Res* (2006) 34, W683-685.
- [12] Burge, S., Parkinson, G. N., Hazel, P., Todd, A. K., and Neidle, S., *Nucleic Acids Res* (2006) 34, 5402-5415.
- [13] Esposito, V., Galeone, A., Mayol, L., Oliviero, G., Virgilio, A., and Randazzo, L., *Nucleosides, Nucleotides and Nucleic Acids* (2007) 26, 1155-1159.
- [14] Patel, D. J., Phan, A. T., and Kuryavyi, V., *Nucleic Acids Res* (2007) 35, 7429-7455.
- [15] Šponer, J., Mládek, A., Špačková, N., Cang, X., Cheatham, T. E., and Grimme, S., *Journal of the American Chemical Society* (2013) 135, 9785-9796.
- [16] Phan, A. T., *FEBS J* (2010) 277, 1107-1117.
- [17] Cayrou, C., Grégoire, D., Coulombe, P., Danis, E., and Méchali, M., *Methods* (2012) 57, 158-164.
- [18] Maizels, N., and Gray, L. T., *PLoS Genet* (2013) 9, e1003468.
- [19] Bugaut, A., and Balasubramanian, S., *Nucleic Acids Res* (2012) 40, 4727-4741.
- [20] Frees, S., Menendez, C., Crum, M., and Bagga, P. S., *Hum Genomics* (2014) 8, 8.
- [21] Perrone, R., Nadai, M., Frasson, I., Poe, J. A., Butovskaya, E., Smithgall, T. E., Palumbo, M., Palu, G., and Richter, S. N., *J Med Chem* (2013) 56, 6521-6530.
- [22] Beaume, N., Pathak, R., Yadav, V. K., Kota, S., Misra, H. S., Gautam, H. K., and Chowdhury, S., *Nucleic Acids Res* (2013) 41, 76-89.
- [23] Hershman, S. G., Chen, Q., Lee, J. Y., Kozak, M. L., Yue, P., Wang, L. S., and Johnson, F. B., *Nucleic Acids Res* (2008) 36, 144-156.
- [24] Leeder, W. M., Hummel, N. F., and Goring, H. U., *Sci Rep* (2016) 6, 29810.
- [25] Henderson, A., Wu, Y., Huang, Y. C., Chavez, E. A., Platt, J., Johnson, F. B., Brosh, R. M., Jr., Sen, D., and Lansdorp, P. M., *Nucleic Acids Res* (2014) 42, 860-869.
- [26] Biffi, G., Tannahill, D., McCafferty, J., and Balasubramanian, S., *Nat Chem* (2013) 5, 182-186.
- [27] Kazemier, H. G., Paeschke, K., and Lansdorp, P. M., *Nucleic Acids Res* (2017).
- [28] Sauer, M., and Paeschke, K., *Biochemical Society Transactions* (2017).
- [29] Lipps, H. J., and Rhodes, D., *Trends in Cell Biology* (2009) 19, 414-422.
- [30] Sundquist, W. I., and Heaphy, S., *Proceedings of the National Academy of Sciences* (1993) 90, 3393-3397.

- [31] Zahler, A. M., Williamson, J. R., Cech, T. R., and Prescott, D. M., *Nature* (**1991**) *350*, 718-720.
- [32] Kim, M.-Y., Vankayalapati, H., Shin-ya, K., Wierzba, K., and Hurley, L. H., *Journal of the American Chemical Society* (**2002**) *124*, 2098-2099.
- [33] Harrison, R. J., Gowan, S. M., Kelland, L. R., and Neidle, S., *Bioorganic & Medicinal Chemistry Letters* (**1999**) *9*, 2463-2468.
- [34] Paeschke, K., Simonsson, T., Postberg, J., Rhodes, D., and Lipps, H. J., *Nature Structural & Molecular Biology* (**2005**) *12*, 847.
- [35] Xin, H., Liu, D., and Songyang, Z., *Genome Biol* (**2008**) *9*, 232.
- [36] Cogoi, S., Shchekotikhin, A. E., and Xodo, L. E., *Nucleic Acids Res* (**2014**) *42*, 8379-8388.
- [37] Cogoi, S., and Xodo, L. E., *Nucleic Acids Res* (**2006**) *34*, 2536-2549.
- [38] Siddiqui-Jain, A., Grand, C. L., Bearss, D. J., and Hurley, L. H., *Proc Natl Acad Sci U S A* (**2002**) *99*, 11593-11598.
- [39] Halder, K., Benzler, M., and Hartig, J. S., *Methods* (**2012**) *57*, 115-121.
- [40] Gearhart, J., Pashos, E. E., and Prasad, M. K., *New England Journal of Medicine* (**2007**) *357*, 1469-1472.
- [41] Roskoski Jr, R., *Biochemical and Biophysical Research Communications* (**2005**) *337*, 1-13.
- [42] Malumbres, M., and Barbacid, M., *Nature Reviews Cancer* (**2003**) *3*, 459-465.
- [43] Xu, Y., Suzuki, Y., Ito, K., and Komiyama, M., *Proc Natl Acad Sci U S A* (**2010**) *107*, 14579-14584.
- [44] Kumari, S., Bugaut, A., Huppert, J. L., and Balasubramanian, S., *Nature Chemical Biology* (**2007**) *3*, 218.
- [45] Darnell, J. C., Jensen, K. B., Jin, P., Brown, V., Warren, S. T., and Darnell, R. B., *Cell* *107*, 489-499.
- [46] Guo, J. U., and Bartel, D. P., *Science* (**2016**) *353*.
- [47] Edwards, D. N., Machwe, A., Wang, Z., and Orren, D. K., *PLOS ONE* (**2014**) *9*, e80664.
- [48] London, T. B., Barber, L. J., Mosedale, G., Kelly, G. P., Balasubramanian, S., Hickson, I. D., Boulton, S. J., and Hiom, K., *J Biol Chem* (**2008**) *283*, 36132-36139.
- [49] Sun, D., Thompson, B., Cathers, B. E., Salazar, M., Kerwin, S. M., Trent, J. O., Jenkins, T. C., Neidle, S., and Hurley, L. H., *Journal of Medicinal Chemistry* (**1997**) *40*, 2113-2116.
- [50] Burger, A. M., Dai, F., Schultes, C. M., Reszka, A. P., Moore, M. J., Double, J. A., and Neidle, S., *Cancer Research* (**2005**) *65*, 1489.
- [51] Hansel-Hertsch, R., Beraldi, D., Lensing, S. V., Marsico, G., Zyner, K., Parry, A., Di Antonio, M., Pike, J., Kimura, H., Narita, M., Tannahill, D., and Balasubramanian, S., *Nat Genet* (**2016**) *48*, 1267-1272.
- [52] Hansel-Hertsch, R., Antonio, M. D., and Balasubramanian, S., *Nat Rev Mol Cell Biol* (**2017**) *18*, 279-284.
- [53] Besnard, E., Babled, A., Lapasset, L., Milhavet, O., Parrinello, H., Dantec, C., Marin, J. M., and Lemaitre, J. M., *Nat Struct Mol Biol* (**2012**) *19*, 837-844.
- [54] Holder, I. T., and Hartig, J. S., *Chem Biol* (**2014**) *21*, 1511-1521.
- [55] Rodriguez, R., Miller, K. M., Forment, J. V., Bradshaw, C. R., Nikan, M., Britton, S., Oelschlaegel, T., Xhemalce, B., Balasubramanian, S., and Jackson, S. P., *Nat Chem Biol* (**2012**) *8*, 301-310.
- [56] Monchaud, D., and Teulade-Fichou, M. P., *Org Biomol Chem* (**2008**) *6*, 627-636.
- [57] Campbell, N. H., Parkinson, G. N., Reszka, A. P., and Neidle, S., *Journal of the American Chemical Society* (**2008**) *130*, 6722-6724.
- [58] Randazzo, A., Galeone, A., and Mayol, L., *Chemical Communications* (**2001**), 1030-1031.

-
- [59] Martino, L., Virno, A., Pagano, B., Virgilio, A., Di Micco, S., Galeone, A., Giancola, C., Bifulco, G., Mayol, L., and Randazzo, A., *Journal of the American Chemical Society* (**2007**) *129*, 16048-16056.
- [60] Pagano, B., Fotticchia, I., De Tito, S., Mattia, C. A., Mayol, L., Novellino, E., Randazzo, A., and Giancola, C., *J Nucleic Acids* (**2010**) *2010*.
- [61] Cocco, M. J., Hanakahi, L. A., Huber, M. D., and Maizels, N., *Nucleic Acids Research* (**2003**) *31*, 2944-2951.
- [62] Perry, P. J., Read, M. A., Davies, R. T., Gowan, S. M., Reszka, A. P., Wood, A. A., Kelland, L. R., and Neidle, S., *Journal of Medicinal Chemistry* (**1999**) *42*, 2679-2684.
- [63] Moore, M. J. B., Schultes, C. M., Cuesta, J., Cuenca, F., Gunaratnam, M., Tanious, F. A., Wilson, W. D., and Neidle, S., *Journal of Medicinal Chemistry* (**2006**) *49*, 582-599.
- [64] Heald, R. A., Modi, C., Cookson, J. C., Hutchinson, I., Laughton, C. A., Gowan, S. M., Kelland, L. R., and Stevens, M. F. G., *Journal of Medicinal Chemistry* (**2002**) *45*, 590-597.
- [65] Guyen, B., Schultes, C. M., Hazel, P., Mann, J., and Neidle, S., *Organic & Biomolecular Chemistry* (**2004**) *2*, 981-988.
- [66] Mergny, J. L., Lacroix, L., Teulade-Fichou, M. P., Hounsou, C., Guittat, L., Hoarau, M., Arimondo, P. B., Vigneron, J. P., Lehn, J. M., Riou, J. F., Garestier, T., and Helene, C., *Proc Natl Acad Sci U S A* (**2001**) *98*, 3062-3067.
- [67] Parkinson, G. N., Ghosh, R., and Neidle, S., *Biochemistry* (**2007**) *46*, 2390-2397.
- [68] Goncalves, D. P., Rodriguez, R., Balasubramanian, S., and Sanders, J. K., *Chem Commun (Camb)* (**2006**), 4685-4687.
- [69] Rezler, E. M., Seenisamy, J., Bashyam, S., Kim, M.-Y., White, E., Wilson, W. D., and Hurley, L. H., *Journal of the American Chemical Society* (**2005**) *127*, 9439-9447.
- [70] Georgiades, S. N., Abd Karim, N. H., Suntharalingam, K., and Vilar, R., *Angew Chem Int Ed Engl* (**2010**) *49*, 4020-4034.
- [71] Dixon, I. M., Lopez, F., Tejera, A. M., Estève, J.-P., Blasco, M. A., Pratviel, G., and Meunier, B., *Journal of the American Chemical Society* (**2007**) *129*, 1502-1503.
- [72] Ren, L., Zhang, A., Huang, J., Wang, P., Weng, X., Zhang, L., Liang, F., Tan, Z., and Zhou, X., *Chembiochem* (**2007**) *8*, 775-780.
- [73] Reed, J. E., Arnal, A. A., Neidle, S., and Vilar, R., *Journal of the American Chemical Society* (**2006**) *128*, 5992-5993.
- [74] Bertrand, H., Monchaud, D., De Cian, A., Guillot, R., Mergny, J.-L., and Teulade-Fichou, M.-P., *Organic & Biomolecular Chemistry* (**2007**) *5*, 2555.
- [75] Stafford, V. S., Suntharalingam, K., Shivalingam, A., White, A. J., Mann, D. J., and Vilar, R., *Dalton Trans* (**2015**) *44*, 3686-3700.
- [76] Riou, J. F., Guittat, L., Mailliet, P., Laoui, A., Renou, E., Petitgenet, O., Megnin-Chanet, F., Helene, C., and Mergny, J. L., *Proc Natl Acad Sci U S A* (**2002**) *99*, 2672-2677.
- [77] Gomez, D., Lemarteleur, T., Lacroix, L., Mailliet, P., Mergny, J. L., and Riou, J. F., *Nucleic Acids Research* (**2004**) *32*, 371-379.
- [78] Lemarteleur, T., Gomez, D., Paterski, R., Mandine, E., Mailliet, P., and Riou, J. F., *Biochem Biophys Res Commun* (**2004**) *323*, 802-808.
- [79] De Cian, A., and Mergny, J. L., *Nucleic Acids Res* (**2007**) *35*, 2483-2493.
- [80] Granotier, C., Pennarun, G., Riou, L., Hoffschir, F., Gauthier, L. R., De Cian, A., Gomez, D., Mandine, E., Riou, J. F., Mergny, J. L., Mailliet, P., Dutrillaux, B., and Boussin, F. D., *Nucleic Acids Res* (**2005**) *33*, 4182-4190.
- [81] Rodriguez, R., Muller, S., Yeoman, J. A., Trentesaux, C., Riou, J. F., and Balasubramanian, S., *J Am Chem Soc* (**2008**) *130*, 15758-15759.
-

- [82] Shirude, P. S., Gillies, E. R., Ladame, S., Godde, F., Shin-ya, K., Huc, I., and Balasubramanian, S., *Journal of the American Chemical Society* (2007) 129, 11890-11891.
- [83] Di Antonio, M., Biffi, G., Mariani, A., Raiber, E. A., Rodriguez, R., and Balasubramanian, S., *Angew Chem Int Ed Engl* (2012) 51, 11073-11078.
- [84] Di Antonio, M., Rodriguez, R., and Balasubramanian, S., *Methods* (2012) 57, 84-92.
- [85] Muller, S., Kumari, S., Rodriguez, R., and Balasubramanian, S., *Nat Chem* (2010) 2, 1095-1098.
- [86] Guilbaud, G., Murat, P., Recolin, B., Campbell, B. C., Maiter, A., Sale, J. E., and Balasubramanian, S., *Nature Chemistry* (2017).
- [87] Sahakyan, A. B., Murat, P., Mayer, C., and Balasubramanian, S., *Nat Struct Mol Biol* (2017) 24, 243-247.
- [88] De Cian, A., Delemos, E., Mergny, J. L., Teulade-Fichou, M. P., and Monchaud, D., *J Am Chem Soc* (2007) 129, 1856-1857.
- [89] Chung, W. J., Heddi, B., Hamon, F., Teulade-Fichou, M. P., and Phan, A. T., *Angew Chem Int Ed Engl* (2014) 53, 999-1002.
- [90] Fedoroff, O. Y., Salazar, M., Han, H., Chemeris, V. V., Kerwin, S. M., and Hurley, L. H., *Biochemistry* (1998) 37, 12367-12374.
- [91] Rangan, A., Fedoroff, O. Y., and Hurley, L. H., *Journal of Biological Chemistry* (2001) 276, 4640-4646.
- [92] Cuenca, F., Greciano, O., Gunaratnam, M., Haider, S., Munnur, D., Nanjunda, R., Wilson, W. D., and Neidle, S., *Bioorg Med Chem Lett* (2008) 18, 1668-1673.
- [93] Lopergolo, A., Perrone, R., Tortoreto, M., Doria, F., Beretta, G. L., Zuco, V., Freccero, M., Borrello, M. G., Lanzi, C., Richter, S. N., Zaffaroni, N., and Folini, M., *Oncotarget* (2016) 7, 49649-49663.
- [94] Doria, F., Oppi, A., Manoli, F., Botti, S., Kandoth, N., Grande, V., Manet, I., and Freccero, M., *Chem Commun (Camb)* (2015) 51, 9105-9108.
- [95] Zuffo, M., Doria, F., Spalluto, V., Ladame, S., and Freccero, M., *Chemistry* (2015) 21, 17596-17600.
- [96] Zuffo, M., Ladame, S., Doria, F., and Freccero, M., *Sensors and Actuators B: Chemical* (2017) 245, 780-788.
- [97] Perrone, R., Doria, F., Butovskaya, E., Frasson, I., Botti, S., Scalabrin, M., Lago, S., Grande, V., Nadai, M., Freccero, M., and Richter, S. N., *J Med Chem* (2015) 58, 9639-9652.
- [98] Doria, F., Nadai, M., Zuffo, M., Perrone, R., Freccero, M., and Richter, S. N., *Chem Commun (Camb)* (2017) 53, 2268-2271.
- [99] Zuffo, M., Doria, F., Botti, S., Bergamaschi, G., and Freccero, M., *Biochim Biophys Acta* (2017) 1861, 1303-1311.
- [100] Shin-ya, K., Wierzba, K., Matsuo, K.-i., Ohtani, T., Yamada, Y., Furihata, K., Hayakawa, Y., and Seto, H., *Journal of the American Chemical Society* (2001) 123, 1262-1263.
- [101] Kim, M.-Y., Gleason-Guzman, M., Izbicka, E., Nishioka, D., and Hurley, L. H., *Cancer Research* (2003) 63, 3247.
- [102] Gomez, D., Paterski, R., Lemarteleur, T., Shin-Ya, K., Mergny, J. L., and Riou, J. F., *J Biol Chem* (2004) 279, 41487-41494.
- [103] Binz, N., Shalaby, T., Rivera, P., Shin-ya, K., and Grotzer, M. A., *Eur J Cancer* (2005) 41, 2873-2881.
- [104] Gomez, D., Wenner, T., Brassart, B., Douarre, C., O'Donohue, M. F., El Khoury, V., Shin-Ya, K., Morjani, H., Trentesaux, C., and Riou, J. F., *J Biol Chem* (2006) 281, 38721-38729.
- [105] Yamada, S. S., K.; Kitagawa, K.; Okajima, S.; Asao, T., *EP1350794-A1*, Taiho Pharmaceutical CO., L.

-
- [106] Doi, T., Yoshida, M., Shin-ya, K., and Takahashi, T., *Org Lett* (**2006**) *8*, 4165-4167.
- [107] Linder, J., Garner, T. P., Williams, H. E., Searle, M. S., and Moody, C. J., *J Am Chem Soc* (**2011**) *133*, 1044-1051.
- [108] Doi, T., Shibata, K., Yoshida, M., Takagi, M., Tera, M., Nagasawa, K., Shin-ya, K., and Takahashi, T., *Org Biomol Chem* (**2011**) *9*, 387-393.
- [109] Jantos, K., Rodriguez, R., Ladame, S., Shirude, P. S., and Balasubramanian, S., *Journal of the American Chemical Society* (**2006**) *128*, 13662-13663.
- [110] Pilch, D. S., Barbieri, C. M., Rzuczek, S. G., Lavoie, E. J., and Rice, J. E., *Biochimie* (**2008**) *90*, 1233-1249.
- [111] Rzuczek, S. G., Pilch, D. S., LaVoie, E. J., and Rice, J. E., *Bioorg Med Chem Lett* (**2008**) *18*, 913-917.
- [112] Iida, K., Tera, M., Hirokawa, T., Shin-ya, K., and Nagasawa, K., *Chem Commun (Camb)* (**2009**), 6481-6483.
- [113] Rzuczek, S. G., Pilch, D. S., Liu, A., Liu, L., LaVoie, E. J., and Rice, J. E., *J Med Chem* (**2010**) *53*, 3632-3644.
- [114] Minhas, G. S., Pilch, D. S., Kerrigan, J. E., LaVoie, E. J., and Rice, J. E., *Bioorg Med Chem Lett* (**2006**) *16*, 3891-3895.
- [115] Barbieri, C. M., Srinivasan, A. R., Rzuczek, S. G., Rice, J. E., LaVoie, E. J., and Pilch, D. S., *Nucleic Acids Res* (**2007**) *35*, 3272-3286.
- [116] Chung, W. J., Heddi, B., Tera, M., Iida, K., Nagasawa, K., and Phan, A. T., *J Am Chem Soc* (**2013**) *135*, 13495-13501.
- [117] Tera, M., Iida, K., Shin-ya, K., and Nagasawa, K., *Nucleic Acids Symp Ser (Oxf)* (**2009**), 231-232.
- [118] Hamon, F., Largy, E., Guedin-Beaurepaire, A., Rouchon-Dagois, M., Sidibe, A., Monchaud, D., Mergny, J. L., Riou, J. F., Nguyen, C. H., and Teulade-Fichou, M. P., *Angew Chem Int Ed Engl* (**2011**) *50*, 8745-8749.
- [119] Petenzi, M., Verga, D., Largy, E., Hamon, F., Doria, F., Teulade-Fichou, M. P., Guedin, A., Mergny, J. L., Mella, M., and Freccero, M., *Chemistry* (**2012**) *18*, 14487-14496.
- [120] Unpublished Data.
- [121] Medeiros-Silva, J., Guedin, A., Salgado, G. F., Mergny, J. L., Queiroz, J. A., Cabrita, E. J., and Cruz, C., *Biochim Biophys Acta* (**2017**) *1861*, 1281-1292.
- [122] Moorhouse, A. D., Santos, A. M., Gunaratnam, M., Moore, M., Neidle, S., and Moses, J. E., *Journal of the American Chemical Society* (**2006**) *128*, 15972-15973.
- [123] Moorhouse, A. D., Haider, S., Gunaratnam, M., Munnur, D., Neidle, S., and Moses, J. E., *Mol Biosyst* (**2008**) *4*, 629-642.
- [124] Moses, J. E., Ritson, D. J., Zhang, F., Lombardo, C. M., Haider, S., Oldham, N., and Neidle, S., *Org Biomol Chem* (**2010**) *8*, 2926-2930.
- [125] Dash, J., Shirude, P. S., and Balasubramanian, S., *Chem Commun (Camb)* (**2008**), 3055-3057.
- [126] Jyotirmayee Dash, P. S. S., Shang-Te Danny Hsu, and Shankar Balasubramanian, *J. Am. Chem. Soc.* (**2008**) *130*, 15950 – 15956.
- [127] Neidle, S., *FEBS J* (**2010**) *277*, 1118-1125.
- [128] Smith, N. M., Amrane, S., Rosu, F., Gabelica, V., and Mergny, J. L., *Chem Commun (Camb)* (**2012**) *48*, 11464-11466.
- [129] Di Antonio, M., McLuckie, K. I., and Balasubramanian, S., *J Am Chem Soc* (**2014**) *136*, 5860-5863.
- [130] Bertrand, H., Bombard, S., Monchaud, D., and Teulade-Fichou, M. P., *J Biol Inorg Chem* (**2007**) *12*, 1003-1014.
-

- [131] Bertrand, H., Bombard, S., Monchaud, D., Talbot, E., Guedin, A., Mergny, J. L., Grunert, R., Bednarski, P. J., and Teulade-Fichou, M. P., *Org Biomol Chem* (**2009**) *7*, 2864-2871.
- [132] Trajkovski, M., Morel, E., Hamon, F., Bombard, S., Teulade-Fichou, M. P., and Plavec, J., *Chemistry* (**2015**) *21*, 7798-7807.
- [133] Doria, F., Nadai, M., Folini, M., Scalabrin, M., Germani, L., Sattin, G., Mella, M., Palumbo, M., Zaffaroni, N., Fabris, D., Freccero, M., and Richter, S. N., *Chemistry – A European Journal* (**2013**) *19*, 78-81.
- [134] Di Antonio, M., Doria, F., Richter, S. N., Bertipaglia, C., Mella, M., Sissi, C., Palumbo, M., and Freccero, M., *Journal of the American Chemical Society* (**2009**) *131*, 13132-13141.
- [135] Doria, F., Nadai, M., Folini, M., Di Antonio, M., Germani, L., Percivalle, C., Sissi, C., Zaffaroni, N., Alcaro, S., Artese, A., Richter, S. N., and Freccero, M., *Org Biomol Chem* (**2012**) *10*, 2798-2806.
- [136] Verga, D., Hamon, F., Poyer, F., Bombard, S., and Teulade-Fichou, M. P., *Angew Chem Int Ed Engl* (**2014**) *53*, 994-998.
- [137] Nadai, M., Doria, F., Germani, L., Richter, S. N., and Freccero, M., *Chemistry* (**2015**) *21*, 2330-2334.
- [138] Murat, P., Singh, Y., and Defrancq, E., *Chem Soc Rev* (**2011**) *40*, 5293-5307.
- [139] Campbell, N. H., and Parkinson, G. N., *Methods* (**2007**) *43*, 252-263.
- [140] Bazzicalupi, C., Ferraroni, M., Bilia, A. R., Scheggi, F., and Gratteri, P., *Nucleic Acids Res* (**2013**) *41*, 632-638.
- [141] Adrian, M., Heddi, B., and Phan, A. T., *Methods* (**2012**) *57*, 11-24.
- [142] Miyoshi, D., Matsumura, S., Nakano, S.-i., and Sugimoto, N., *Journal of the American Chemical Society* (**2004**) *126*, 165-169.
- [143] Teulade-Fichou, M.-P., Carrasco, C., Guittat, L., Bailly, C., Alberti, P., Mergny, J.-L., David, A., Lehn, J.-M., and Wilson, W. D., *Journal of the American Chemical Society* (**2003**) *125*, 4732-4740.
- [144] Monchaud, D., Allain, C., and Teulade-Fichou, M. P., *Bioorg Med Chem Lett* (**2006**) *16*, 4842-4845.
- [145] Largy, E., Hamon, F., and Teulade-Fichou, M. P., *Anal Bioanal Chem* (**2011**) *400*, 3419-3427.
- [146] Monchaud, D., Allain, C., and Teulade-Fichou, M. P., *Nucleosides Nucleotides Nucleic Acids* (**2007**) *26*, 1585-1588.
- [147] Monchaud, D., Allain, C., Bertrand, H., Smargiasso, N., Rosu, F., Gabelica, V., De Cian, A., Mergny, J. L., and Teulade-Fichou, M. P., *Biochimie* (**2008**) *90*, 1207-1223.
- [148] Tran, P. L., Largy, E., Hamon, F., Teulade-Fichou, M. P., and Mergny, J. L., *Biochimie* (**2011**) *93*, 1288-1296.
- [149] Beauvineau, C., Guetta, C., Teulade-Fichou, M. P., and Mahuteau-Betzer, F., *Org Biomol Chem* (**2017**).
- [150] Hardin, C. C., Watson, T., Corregan, M., and Bailey, C., *Biochemistry* (**1992**) *31*, 833-841.
- [151] Kypr, J., Kejnovska, I., Rencuk, D., and Vorlickova, M., *Nucleic Acids Res* (**2009**) *37*, 1713-1725.
- [152] Eriksson, M., and Nordén, B. (**2001**) "*Linear and Circular Dichroism of Drug-Nucleic Acid Complexes*", In *Methods in Enzymology*, pp 68-98, Academic Press.
- [153] Randazzo, A., Spada, G. P., and da Silva, M. W., *Top Curr Chem* (**2013**) *330*, 67-86.
- [154] Paramasivan, S., Rujan, I., and Bolton, P. H., *Methods* (**2007**) *43*, 324-331.
- [155] Grajewski, J. G. a. J., *Organic Letters* (**2003**) *5*, 3301-3303.
- [156] Garbett, N. C., Ragazzon, P. A., and Chaires, J. B., *Nat Protoc* (**2007**) *2*, 3166-3172.
- [157] Prairie, W. C. K. a. M. D., *Chemico-Biological Interactions* (**1991**) *79*, 137-149.
- [158] Kimura, T., Kawai, K., Fujitsuka, M., and Majima, T., *Chem. Commun.* (**2006**), 401-402.
-

- [159] Rosu, F., De Pauw, E., and Gabelica, V., *Biochimie* (2008) 90, 1074-1087.
- [160] Singh, J., Petter, R. C., Baillie, T. A., and Whitty, A., *Nat Rev Drug Discov* (2011) 10, 307-317.
- [161] Rajski, S. R., and Williams, R. M., *Chemical Reviews* (1998) 98, 2723-2796.
- [162] Hurley, L. H., *Nat Rev Cancer* (2002) 2, 188-200.
- [163] Goodman, L. S., Wintrobe, M. M., Dameshek, W., Goodman, M. J., Gilman, A., and Mc, L. M., *Journal of the American Medical Association* (1946) 132, 126-132.
- [164] Gilman, A., and Philips, F. S., *Science* (1946) 103, 409.
- [165] Wolfe, A. R., Smith, T. J., and Meehan, T., *Chemical Research in Toxicology* (2004) 17, 476-491.
- [166] Park, K. K., Wishnok, J. S., and Archer, M. C., *Chemico-Biological Interactions* (1977) 18, 349-354.
- [167] Kroeger Smith, M. B., Taneyhill, L. A., Michejda, C. J., and Smith, R. H., *Chemical Research in Toxicology* (1996) 9, 341-348.
- [168] Ponti, M., Souhami, R. L., Fox, B. W., and Hartley, J. A., *British Journal of Cancer* (1991) 63, 743-747.
- [169] Johnstone, T. C., Park, G. Y., and Lippard, S. J., *Anticancer research* (2014) 34, 471-476.
- [170] Drabløs, F., Feyzi, E., Aas, P. A., Vaagbø, C. B., Kavli, B., Bratlie, M. S., Peña-Díaz, J., Otterlei, M., Slupphaug, G., and Krokan, H. E., *DNA Repair* (2004) 3, 1389-1407.
- [171] Tomasz, M., *Chemistry & Biology* (1995) 2, 575-579.
- [172] Cimino, G. D., Gamper, H. B., Isaacs, S. T., and Hearst, J. E., *Annual Review of Biochemistry* (1985) 54, 1151-1193.
- [173] Abdella, B. R., and Fisher, J., *Environmental Health Perspectives* (1985) 64, 4-18.
- [174] Mauro, F., *Mini-Reviews in Organic Chemistry* (2004) 1, 403-415.
- [175] Angle, S. R., and Yang, W., *Journal of the American Chemical Society* (1990) 112, 4524-4528.
- [176] Erdtman, H., *Journal of Polymer Science Part B: Polymer Letters* (1972) 10, 228-230.
- [177] Wan, P., Barker, B., Diao, L., Fischer, M., Shi, Y., and Yang, C., *Canadian Journal of Chemistry* (1996) 74, 465-475.
- [178] Singh, M. S., Nagaraju, A., Anand, N., and Chowdhury, S., *RSC Adv.* (2014) 4, 55924-55959.
- [179] Kulikov, A., Arumugam, S., and Popik, V. V., *The Journal of Organic Chemistry* (2008) 73, 7611-7615.
- [180] Gnaim, S., and Shabat, D., *Acc Chem Res* (2014) 47, 2970-2984.
- [181] Qiang, L., Ting, D., Xiaohui, L., Xiaoyun, Z., Xiaoying, Y., and Xiaoguang, L., *Current Organic Chemistry* (2014) 18, 86-92.
- [182] Arumugam, S., Guo, J., Mbua, N. E., Friscourt, F., Lin, N., Nekongo, E., Boons, G. J., and Popik, V. V., *Chem Sci* (2014) 5, 1591-1598.
- [183] Ping, W., Yang, S., Lixia, Z., Hanping, H., and Xiang, Z., *Current Medicinal Chemistry* (2005) 12, 2893-2913.
- [184] Claudia Percivalle, F. D. a. M. F., *Current Organic Chemistry* (2014) 18, 19-43.
- [185] Diao, L., Yang, C., and Wan, P., *Journal of the American Chemical Society* (1995) 117, 5369-5370.
- [186] K. Nakatani, N. Higashida, and Saito, I., *Tetrahedron Letters* (1997) 38, 5005-5008.
- [187] Chiang, Y., Kresge, A. J., and Zhu, Y., *J Am Chem Soc* (2001) 123, 8089-8094.
- [188] Rokita, S. E., Yang, J., Pande, P., and Greenberg, W. A., *The Journal of Organic Chemistry* (1997) 62, 3010-3012.
- [189] Zeng, Q., and Rokita, S. E., *The Journal of Organic Chemistry* (1996) 61, 9080-9081.
- [190] Li, T., and Rokita, S. E., *Journal of the American Chemical Society* (1991) 113, 7771-7773.
- [191] Modica, E., Zanaletti, R., Freccero, M., and Mella, M., *J Org Chem* (2001) 66, 41-52.

- [192] Emily E. Weinert, R. D., Stefano Colloredo-Melz,, Kristen N. Frankenfield, C. H. M., Mauro Freccero*, and, and Rokita*, S. E., *J Am Chem Soc* (**2006**) *128*, 11940 - 11947.
- [193] Freccero, M., Gandolfi, R., and Sarzi-Amade, M., *J Org Chem* (**2003**) *68*, 6411-6423.
- [194] Veldhuyzen, W. F., Pande, P., and Rokita, S. E., *Journal of the American Chemical Society* (**2003**) *125*, 14005-14013.
- [195] Zhou, Q., and Rokita, S. E., *Proc Natl Acad Sci U S A* (**2003**) *100*, 15452-15457.
- [196] Huang, C., and Rokita, S. E., *Frontiers of Chemical Science and Engineering* (**2015**) *10*, 213-221.
- [197] Huang, C., Liu, Y., and Rokita, S. E., *Signal Transduction and Targeted Therapy* (**2016**) *1*, 16009.
- [198] McCrane, M. P., Hutchinson, M. A., Ad, O., and Rokita, S. E., *Chem Res Toxicol* (**2014**) *27*, 1282-1293.
- [199] Du, Y., Weng, X., Huang, J., Zhang, D., Ma, H., Chen, D., Zhou, X., and Constant, J. F., *Bioorg Med Chem* (**2010**) *18*, 4149-4153.
- [200] Weng, X., Ren, L., Weng, L., Huang, J., Zhu, S., Zhou, X., and Weng, L., *Angewandte Chemie* (**2007**) *119*, 8166-8169.
- [201] Cao, S., Wang, Y., and Peng, X., *Chemistry* (**2012**) *18*, 3850-3854.
- [202] Sztatowski, T. P., and Nathan, C. F., *Cancer Research* (**1991**) *51*, 794-798.
- [203] Di Antonio, M., Doria, F., Mella, M., Merli, D., Profumo, A., and Freccero, M., *J Org Chem* (**2007**) *72*, 8354-8360.
- [204] Zhong, C. J., Kwan, W. S. V., and Miller, L. L., *Chemistry of Materials* (**1992**) *4*, 1423-1428.
- [205] Lukeman, M., Veale, D., Wan, P., Munasinghe, V. R. N., and Corrie, J. E. T., *Canadian Journal of Chemistry* (**2004**) *82*, 240-253.
- [206] Basaric, N., Doslic, N., Ivkovic, J., Wang, Y. H., Veljkovic, J., Mlinaric-Majerski, K., and Wan, P., *J Org Chem* (**2013**) *78*, 1811-1823.
- [207] Basaric, N., Doslic, N., Ivkovic, J., Wang, Y. H., Malis, M., and Wan, P., *Chemistry* (**2012**) *18*, 10617-10623.
- [208] Diao, L., and Wan, P., *Canadian Journal of Chemistry* (**2008**) *86*, 105-118.
- [209] Arumugam, S., and Popik, V. V., *J Am Chem Soc* (**2009**) *131*, 11892-11899.
- [210] Leo, E. A., Delgado, J., Domingo, L. R., Espinós, A., Miranda, M. A., and Tormos, R., *The Journal of Organic Chemistry* (**2003**) *68*, 9643-9647.
- [211] Gao, J., Li, N., and Freindorf, M., *Journal of the American Chemical Society* (**1996**) *118*, 4912-4913.
- [212] Webb, S. P., Philips, L. A., Yeh, S. W., Tolbert, L. M., and Clark, J. H., *The Journal of Physical Chemistry* (**1986**) *90*, 5154-5164.
- [213] Skalamera, D., Bohne, C., Landgraf, S., and Basaric, N., *J Org Chem* (**2015**) *80*, 10817-10828.
- [214] Verga, D., Nadai, M., Doria, F., Percivalle, C., Di Antonio, M., Palumbo, M., Richter, S. N., and Freccero, M., *J Am Chem Soc* (**2010**) *132*, 14625-14637.
- [215] Verga, D., Richter, S. N., Palumbo, M., Gandolfi, R., and Freccero, M., *Org Biomol Chem* (**2007**) *5*, 233-235.
- [216] Wang, P., Liu, R., Wu, X., Ma, H., Cao, X., Zhou, P., Zhang, J., Weng, X., Zhang, X.-L., Qi, J., Zhou, X., and Weng, L., *Journal of the American Chemical Society* (**2003**) *125*, 1116-1117.
- [217] Brousmitche, D. W., Xu, M., Lukeman, M., and Wan, P., *Journal of the American Chemical Society* (**2003**) *125*, 12961-12970.
- [218] Doria, F., Richter, S. N., Nadai, M., Colloredo-Mels, S., Mella, M., Palumbo, M., and Freccero, M., *J Med Chem* (**2007**) *50*, 6570-6579.
- [219] Colloredo-Mels, S., Doria, F., Verga, D., and Freccero, M., *The Journal of Organic Chemistry* (**2006**) *71*, 3889-3895.

-
- [220] Richter, S. N., Maggi, S., Mels, S. C., Palumbo, M., and Freccero, M., *J Am Chem Soc* (**2004**) *126*, 13973-13979.
- [221] Scaiano, J. C. (**2003**) "*Nanosecond Laser Flash Photolysis: A Tool for Physical Organic Chemistry*", In *Reactive Intermediate Chemistry*, pp 847-871, John Wiley & Sons, Inc.
- [222] Zhou, B., Liu, C., Geng, Y., and Zhu, G., *Sci Rep* (**2015**) *5*, 16673.
- [223] Cadet, J., Douki, T., Ravanat, J. L., and Di Mascio, P., *Photochem Photobiol Sci* (**2009**) *8*, 903-911.
- [224] Santagada, V., Frecentese, F., Perissutti, E., Cirillo, D., Terracciano, S., and Caliendo, G., *Bioorg Med Chem Lett* (**2004**) *14*, 4491-4493.
- [225] Wang, Y., Miller, R. L., Sauer, D. R., and Djuric, S. W., *Organic Letters* (**2005**) *7*, 925-928.
- [226] Lukin, K., and Kishore, V., *Journal of Heterocyclic Chemistry* (**2014**) *51*, 256-261.
- [227] Baykov, S., Sharonova, T., Osipyan, A., Rozhkov, S., Shetnev, A., and Smirnov, A., *Tetrahedron Letters* (**2016**) *57*, 2898-2900.
- [228] Tron, G. C., Pirali, T., Billington, R. A., Canonico, P. L., Sorba, G., and Genazzani, A. A., *Med Res Rev* (**2008**) *28*, 278-308.
- [229] Agalave, S. G., Maujan, S. R., and Pore, V. S., *Chem Asian J* (**2011**) *6*, 2696-2718.
- [230] Wang, W., Xu, H., Xu, Y., Ding, T., Zhang, W., Ren, Y., and Chang, H., *Org Biomol Chem* (**2016**) *14*, 9814-9822.
- [231] Klein, D. A., and Fouty, R. A., *Macromolecules* (**1968**) *1*, 318-324.
- [232] Fabre, B., Picha, J., Vanek, V., Selicharova, I., Chrudinova, M., Collinsova, M., Zakova, L., Budesinsky, M., and Jiracek, J., *ACS Comb Sci* (**2016**) *18*, 710-722.
- [233] Gao, M., Duan, L., Luo, J., Zhang, L., Lu, X., Zhang, Y., Zhang, Z., Tu, Z., Xu, Y., Ren, X., and Ding, K., *J Med Chem* (**2013**) *56*, 3281-3295.
- [234] Chinchilla, R., and Najera, C., *Chem Soc Rev* (**2011**) *40*, 5084-5121.
- [235] Chiou, S., and Shine, H. J., *Journal of Heterocyclic Chemistry* (**1989**) *26*, 125-128.
- [236] Neves Filho, R. A. W., Bezerra, N. M. M., Guedes, J. M., and Srivastava, R. M., *Journal of the Brazilian Chemical Society* (**2009**) *20*, 1365-1369.
- [237] Bruton, E. A., Brammer, L., Christopher Pigge, F., Aakeröy, C. B., and Leinen, D. S., *New J. Chem.* (**2003**) *27*, 1084-1094.
- [238] Zou, H., Zhou, L., Li, Y., Cui, Y., Zhong, H., Pan, Z., Yang, Z., and Quan, J., *J Med Chem* (**2010**) *53*, 994-1003.
- [239] Appukkuttan, P., Dehaen, W., Fokin, V. V., and Van der Eycken, E., *Organic Letters* (**2004**) *6*, 4223-4225.
- [240] Tondreau, A. M., Darmon, J. M., Wile, B. M., Floyd, S. K., Lobkovsky, E., and Chirik, P. J., *Organometallics* (**2009**) *28*, 3928-3940.
- [241] Data Not Shown.
- [242] Sinha, R. P., and Häder, D.-P., *Photochemical & Photobiological Sciences* (**2002**) *1*, 225-236.
- [243] Skalamera, D., Mlinaric-Majerski, K., Martin-Kleiner, I., Kralj, M., Wan, P., and Basaric, N., *J Org Chem* (**2014**) *79*, 4390-4397.
- [244] Doria, F., Nadai, M., Folini, M., Scalabrin, M., Germani, L., Sattin, G., Mella, M., Palumbo, M., Zaffaroni, N., Fabris, D., Freccero, M., and Richter, S. N., *Chemistry - A European Journal* (**2013**) *19*, 78-81.
- [245] Nadai, M., Doria, F., Di Antonio, M., Sattin, G., Germani, L., Percivalle, C., Palumbo, M., Richter, S. N., and Freccero, M., *Biochimie* (**2011**) *93*, 1328-1340.
- [246] Marchand, A., Strzelecka, D., and Gabelica, V., *Chemistry* (**2016**) *22*, 9551-9555.
- [247] Dumat, B., Bordeaux, G., Faurel-Paul, E., Mahuteau-Betzer, F., Saettel, N., Bombled, M., Metge, G., Charra, F., Fiorini-Debuisschert, C., and Teulade-Fichou, M. P., *Biochimie* (**2011**) *93*, 1209-1218.
-

- [248] Doria, F., Lena, A., Bargiggia, R., and Freccero, M., *J Org Chem* (2016) 81, 3665-3673.
- [249] Waldeck, D. H., *Chem Rev* (1991) 91, 415-436.
- [250] Schultz, T., Quenneville, J., Levine, B., Toniolo, A., Martinez, T. J., Lochbrunner, S., Schmitt, M., Shaffer, J. P., Zgierski, M. Z., and Stolor, A., *J Am Chem Soc* (2003) 125, 8098-8099.
- [251] Percivalle, C., Sissi, C., Greco, M. L., Musetti, C., Mariani, A., Artese, A., Costa, G., Perrore, M. L., Alcaro, S., and Freccero, M., *Org Biomol Chem* (2014) 12, 3744-3754.
- [252] Kammerer, B., Kahlich, R., Biegert, C., Gleiter, C. H., and Heide, L., *Phytochem Anal* (2005) 16, 470-478.
- [253] Epstein, J., Plapinger, R. E., Michel, H. O., Cable, J. R., Stephani, R. A., Hester, R. J., Billington, C., and List, G. R., *Journal of the American Chemical Society* (1964) 86, 3075-3084.
- [254] B. Barker, L. Diao, and Wan, P., *J. Photochem. Photobiol. A* (1997) 104, 91-96.
- [255] Wehry, E. L., and Rogers, L. B., *Journal of the American Chemical Society* (1965) 87, 4234-4238.
- [256] Ma, J., Zhang, X., Basaric, N., Wan, P., and Phillips, D. L., *Phys Chem Chem Phys* (2015) 17, 9205-9211.
- [257] Avouris, P., Gelbart, W. M., and El-Sayed, M. A., *Chemical Reviews* (1977) 77, 793-833.
- [258] Flom, S. R., and Barbara, P. F., *The Journal of Physical Chemistry* (1985) 89, 4489-4494.
- [259] Grellmann, K. H., Mordziński, A., and Heinrich, A., *Chemical Physics* (1989) 136, 201-211.
- [260] Lukeman, M., and Wan, P., *Journal of the American Chemical Society* (2002) 124, 9458-9464.
- [261] DeRosa, M. C., and Crutchley, R. J., *Coordination Chemistry Reviews* (2002) 233, 351-371.
- [262] Takizawa, S. Y., Aboshi, R., and Murata, S., *Photochem Photobiol Sci* (2011) 10, 895-903.
- [263] Hurst, J. R., McDonald, J. D., and Schuster, G. B., *Journal of the American Chemical Society* (1982) 104, 2065-2067.
- [264] Doria, F., Manet, I., Grande, V., Monti, S., and Freccero, M., *J Org Chem* (2013) 78, 8065-8073.
- [265] Veljkovic, J., Uzelac, L., Molcanov, K., Mlinaric-Majerski, K., Kralj, M., Wan, P., and Basaric, N., *J Org Chem* (2012) 77, 4596-4610.
- [266] Arumugam, S., and Popik, V. V., *Photochem Photobiol Sci* (2012) 11, 518-521.
- [267] Arumugam, S., and Popik, V. V., *J Am Chem Soc* (2011) 133, 5573-5579.
- [268] Arumugam, S., and Popik, V. V., *J Am Chem Soc* (2012) 134, 8408-8411.
- [269] Li, S., Zhong, W., Xiao, P. L. J., Zheng, Z., Xie, Y., Zhao, G., Wang, X., Wang, L., Li, X., and Zhou, X., *EP2573067 (A4)*, AMMS, I. P. T., Oct 29, 2014.
- [270] Verga, D., Percivalle, C., Doria, F., Porta, A., and Freccero, M., *J Org Chem* (2011) 76, 2319-2323.
- [271] Raach, A., and Reiser, O., *Journal für praktische Chemie* (2000) 342, 605-608.
- [272] Dalcanale, E., and Montanari, F., *The Journal of Organic Chemistry* (1986) 51, 567-569.
- [273] Samanta, J., and Natarajan, R., *Org Lett* (2016) 18, 3394-3397.
- [274] Aillet, T., Loubiere, K., Dechy-Cabaret, O., and Prat, L., *International Journal of Chemical Reactor Engineering* (2014) 12.
- [275] Jankowski, J. J., Kieber, D. J., and Mopper, K., *Photochemistry and Photobiology* (1999) 3, 319-328.

List of Abbreviations

ACN	acetonitrile
BINOL	1,1'-bi-2-naphthols
CD	circular dichroism
CDI	1,1'-carbonyldiimidazole
CuAAC	copper(I)-catalyzed azide-alkyne cycloaddition
DCM	dichloromethane
DHN	1,5-dihydroxynaphthalene
DIPEA	diisopropyl ethyl amine
DMF	dimethylformamide
DMS	dimethylsulphate
DMSO	dimethylsulfoxide
DNA	deoxyribonucleic acid
<i>ds</i> -DNA	double-stranded DNA
<i>ss</i> -DNA	single-stranded DNA
EDG	electron-donating group
ESIPT	excited state intramolecular proton transfer
ESPT	excited state intermolecular proton transfer
EWG	electron-withdrawing group
FID	fluorescence intercalator displacement
FRET	Förster resonance energy transfer
G4	G-quadruplex
GBA	glycosidic bond angle
HFIP	hexafluoroisopropanol
HPLC	high performance liquid chromatography
IC	internal conversion
ICL	interstrand crosslink
ICD	induced circular dichroism
ISC	intersystem crossing
ITC	isothermal titration calorimetry

LFP	laser flash photolysis
LTR	long terminal repeat
MS	mass spectroscopy
NDI	naphthalene diimide
NER	nucleotide excision repair
NMR	nuclear magnetic resonance
NOE	nuclear Overhauser effect
NQM	naphthoquinone methide
<i>o</i>-NQM	ortho-naphthoquinone methide
<i>p</i>-NQM	para-naphthoquinone methide
NQMP	naphthoquinone methide precursor
PAGE	polyacrylamide gel electrophoresis
PDS	pyridostatin
PDT	photodynamic therapy
Pip	piperidine
POT1	protection of telomeres 1 (component of shelterin complex)
PQS	putative quadruplex sequences
QM	quinone methide
<i>o</i>-QM	ortho-quinone methide
<i>p</i>-QM	para-quinone methide
QMA	quinone methide adduct
QMP	quinone methide precursor
ROS	reactive oxygen species
SPR	surface plasmon resonance
TEA	triethylamine
THF	tetrahydrofuran
TO	thiazole orange
UTR	untranslated region
XRD	X-ray diffraction

Acknowledgements

I would like to express my gratitude to Prof. Freccero, who has been an outstanding scientific mentor.

Thanks to all the Lab G teammates that I met in these years, to have shared great times together. I wish you achieve all your goals in the upcoming future.

I would also like to thank Dr.³ Grande, who had first trained me in the chemical laboratory to profitably learn basic techniques and synthetic procedures. He also played an important role as *The Master of Molecular Docking*. His catching irony gladdened my daytime in the lab. Working with him has been indeed a pleasure.

Thanks to Teulade-Fichou's group in Institute Curie, Orsay, who kindly welcomed me during my stay in Paris. In particular, thanks to Dr. Verga and Dr. Bombard, who introduced me into biophysics and guided me over many obstacles and difficulties. Optimism is the way.

Thanks to my family and friends who have kept betting on me even when I was submerged by doubts and discouragement. Still, their naive unconditional faith has been very important to me.

Finally, a special thank goes to Michela, without whom this thesis would not have seen any printer before [today's date]. More importantly, she had a challenging and crucial role in maintaining my focus and mental strength during the toughest moments. She has been a fundamental support and a light in the tunnel. On top, it is a fortune to be able to constructively share different opinions, perspectives and choices.

Besides,

[...] horses are terrible people.

Pavia, 19 February 2018

